Richardson, Euan James (2018) *A multiphysics finite element model of the wood cell wall*. PhD thesis.

https://theses.gla.ac.uk/9150/

A Multiphysics Finite Element Model of the Wood Cell Wall

Euan James Richardson

Infrastructure & Environment Research Division
College of Science and Engineering
University of Glasgow

A thesis presented for the degree of
Doctor of Philosophy

June 2017

Abstract

Timber is a highly complex naturally occurring material, with properties adapted to its local environment. These properties, on its many length scales, determine its strength and stiffness and also how it interacts with moisture in the environment, causing dimensional instability both during drying and its lifetime as a construction material. Of particular importance is how the cell wall polymers interact with moisture in the environment and how this effects the properties, due to their strong dependence on intra-molecular hydrogen bonds.

To model the dimensional behaviour of a wood cell under varying moisture conditions, the cell wall polymer matrix is modelled using a formulation of coupled deformation and moisture transport. These governing equations of mass and linear momentum conservation are strongly coupled and nonlinear, and solved using the Finite Element Method. The associated constitutive equations are complex. The free energy is described through the deformation of the polymer matrix and the mixing with solvent (in this case, water). It is assumed that the polymer chains and water molecules are incompressible so that a change in volume of the polymer matrix corresponds to a change in the number of solvent molecules.

The viscoelastic behaviour is resolved using a Zener spring-dashpot model, capturing both creep and relaxation phenomena, and the moisture transport is resolved using Fick's 2nd Law. The effects of wetting on the stiffness and relaxation characteristics of the polymer matrix is taken into account through the chemical kinetics of hydrogen bond dissociation. The implementation using the finite element method is discussed in detail and comprehensively verified using a series of numerical tests. Finally, the model is applied to wood cells and the behaviour of the polymers is compared to experimental findings.

The resulting model is capable of predicting the interaction between viscoelastic material effects and diffusion and has the ability to predict viscoelastically limited diffusion within wood cell polymers. The model can also predict sorption hysteresis in wood cell wall polymers and therefore could be a valuable tool in future research into wood-water interactions.

List of Figures

List of Tables

Motivation

Timber is one of the oldest known construction materials. However its complex internal structure and unpredictable dimensional stability has implications for both the safety and long term serviceability of timber structures. Large scale structures, are not only difficult to construct, but moisture within the environment can cause, for example, swelling, twisting and bowing of structural elements. However, as a naturally growing material, timber has many ecological advantages in an era of climate change. It has the potential to provide a low carbon, effective construction material for both small scale and larger scale structures.

In order to maximize the benefits of timber, there is a need to understand and predict the structural behaviour, allowing for more accurate dimensioning, thereby improving its potential as a construction material in the future. The aim of this thesis is to present a new approach to modelling timber as a multi-scale material, starting with the polymer level. Hopefully then it can provide a basis for further research leading to increased knowledge of timber as a structural design material.

Acknowledgement

I would like to thank my PhD supervisors. My original supervisors, Doctor Karin de Borst and Professor Michael Jarvis, for giving me the opportunity to pursue a PhD at Glasgow. I would also like to thank Professor Chris Pearce and Doctor Lukasz Kaczmarczyk for allowing me to continue my studies under their supervision. Chris's insight into problems and how to present my work has been valuable, as have his comments on my thesis and I would like to thank him for his patience and help during my final years of study.

I would especially like to thank Lukasz. His help and patience since becoming my supervisor has been invaluable and I am very grateful to for being allowed the opportunity to pursue my research using MoFEM. The help I received from him whilst learning how to use MoFEM and implementing my model has been invaluable and without this help I would have struggled a great deal. His insight into the physics of the problems and numerical techniques have really changed the way I think about problems and I have greatly enjoyed our many discussions about the work. I would also like to thank Zahur for all his help during my PhD and guidance in using MoFEM.

I should also like to thank my family for their continued support, both during my PhD studies and previous education, and now in my engineering career. They have always encouraged me and have supported me at times when I was struggling.

I would also like to thank my friends. Firstly to my friends in the office who have helped make studying that little bit easier and more enjoyable.

Finally, I would like to thank Kate for her help and support whilst finishing the PhD. Her encouragement and support during the final stages of the PhD has been amazing, without which I would have struggled a lot more over the last few months. Hopefully now there will be time for more adventures.

Nomenclature

List of Symbols

a_w	Activity of water vapour
C	Concentration
C_0	Initial concentration
$\overline{\mathrm{C.I.}}$	Cooperative index
D	Diffusion coefficient
E	Young's modulus
E_0	Young's modulus in the dry state
G	Shear modulus
G_0	Shear modulus in the dry state
G^α	Shear modulus of spring α
G^β	Shear modulus of spring β
$\hat{G}^\beta$	Dashpot viscosity $\hat{\beta}$
$\overline{\mathrm{G}}$	Gibb's free energy per mole
$\overline{\mathrm{G}}_0$	Initial Gibb's free energy per mole
$\mathcal{H}^1$	Piecewise continuous approximation
J	Energy in joules
J	Solvent flux
$\mathbf{K}$	Stiffness contribution to global matrix
K	Bulk modulus
k	Proportionality coefficient

L	Avogadro's Constant
L^2	Piecewise discontinuous approximation
N	Number of effective hydrogen bonds
N_0	Initial number of effective hydrogen bonds
n	Number of moles
p	Pressure
p_0	Saturation vapour pressure
$q^{\mathbf{u}}$	Vector of degrees of freedom for displacement
q^{μ}	Vector of degrees of freedom for chemical potential
$q^{\hat{\varepsilon}}$	Vector of degrees of freedom for dashpot strain
$\mathbf{r}_{\hat{\varepsilon}}$	Residual for the Conservation of the Dashpot Strain
$\mathbf{r}_{\mu}$	Residual for the Conservation of Mass
$\mathbf{r}_{\sigma}$	Residual for the Conservation of Momentum
R	Gas constant
RH	Relative humidity
S	Surface
S_{σ}^{h}	Discretised body surface where tractions are applied
t	time
$\mathbf{t}$	tractions
T	Temperature in degrees Kelvin
T_E	Temperature below which a pure polymer acts as an elastic solid
T_g	Glass transition temperature
T_v	Temperature above which a pure polymer acts as a viscous fluid
$\mathbf{u}^h$	Displacement vector
V	Volume
V_0	Volume in the dry state

V^h	Discretised body volume
w	Water content
W	Helmholtz free energy
W	Water content at which all hydroxyl groups carry one water molecule

Greek Letters

δ_{ij}	Kronecker delta
Δt	time step
ε	Strain
$\hat{\varepsilon}$	Dashpot strain
$\hat{\varepsilon}^h$	Dashpot strain vector
ε_{kk}	Volumetric strain
η	Viscosity of polymer network
η_w	Viscosity of solvent
κ	Permeability of polymer network
μ	Chemical potential
μ_e	Chemical potential of the Environment
μ_s	Chemical potential of the Solvent
μ_0	Initial chemical potential
$\overline{\mu}$	Chemical potential per mole
$\overline{\mu}_0$	Initial chemical potential per mole
μ^h	Chemical Potential vector
ν	Poisson's ratio
ν^α	Poisson's ratio of spring α
ν^β	Poisson's ratio of spring β
$\hat{\nu}^\beta$	Poisson's ratio of the dashpot $\hat{\beta}$
σ	Stress

σ^{α}	Stress in spring α
σ^{β}	Stress in spring β
$\hat{\sigma}^{\beta}$	Stress in dashpot β
τ_v	Viscoelastic relaxation time
$\boldsymbol{\Phi}$	Piecewise continuous polynomial
χ	Molar fraction
$\boldsymbol{\Psi}$	Piecewise discontinuous polynomial
Ω	Volume per solvent molecule
$\overline{\Omega}$	Volume per mole of solvent

Declaration

I declare that this thesis is a record of the original work carried out by myself under the supervision of Doctor Lukasz Kaczmarczyk, Professor Chris Pearce, Doctor Karin deBorst and Professor Michael Jarvis in the Infrastructure and Environment Division of the School of Engineering at the University of Glasgow, United Kingdom. This research was undertaken during the period of October 2012 to June 2017. The copyright of this thesis belongs to the author under the terms of the United Kingdom Copyright acts. Due acknowledgment must always be made of the use of any material contained in, or derived from this thesis. The thesis has not been presented elsewhere in consideration for a higher degree.

Euan Richardson

Contents

Introduction

Timber is a naturally occurring material which is widely used in construction, with good structural properties, including a strength to density ratio close to that of steel for some species. As such, it has the potential to be used in a wide variety of complex structural design applications. Furthermore, as a naturally occurring material, timber provides a more sustainable option for construction design, which could be of increased importance due to climate change and the increased need to reduce carbon footprints in industry. However, the fact that the material grows naturally, and interacts with the environment as a living organism, means the properties of the material are adapted to its environment of growth in a very complex manner. This combined with the many length scales within timber, including the different types of cell, composition of cell wall layers and proportion of primary polymer constituents, means predictions of structural performance can be difficult. This problem becomes particularly prevalent when interactions with water vapour occur.

The interactions with water vapour distinguishes timber from other construction materials and gives rise to the unique problem of humidity induced distortion. The constituent polymers on the cell wall level (cellulose, hemicellulose and lignin), contain an abundance of hydroxyl groups. These hydroxyl groups are interconnected throughout the wood cell wall, resulting in a strong network of intramolecular hydrogen bonds between hydroxyl groups of the constituent polymers. Unlike porous media on the micro or meso scales, wood does not require pore water pressure to cause significant changes in volume, due to water ingress. Instead the adsorption of water is caused by the chemical interaction of the hydroxyl groups within the polymers, interacting with the water vapour molecules within the surrounding air. The amount of swelling and the amount of clustering of the water molecules is dependent upon the environmental humidity and therefore the chemical potential of the water vapour mixture entering the wood cell that forces the chemical interactions with the hydroxyl groups. As such, it is the ability of the constituent polymers to incorporate the water itself that is the key factor in moisture induced swelling, and therefore the reason for its unique behaviour compared to other porous media. Under pore water pressure, wood behaves in a manner similar to other porous media, transporting moisture through the cells on the micro-scale, but this is out with the scope and aim of this work.

The swelling process, on the cell wall polymer scale, can lead to dimensional changes that are observed on the macro-scale. This phenomenon which has been observed experimentally [56, 75, 87], is referred to as mechano-sorptive creep, in which the mechanical effects combine with moisture sorption to produce a response that cannot be predicted by modelling each field separately [47]. Therefore, to model timber under mechanical load and in changing environmental conditions, the hygro-mechanical behaviour of the cell wall constituent polymers is necessary, within a multi-scale framework. As such, this thesis presents the formulation of a hygro-mechanical model for a ligno-cellulosic polymer mixture, as is found within the wood cell wall, capturing both deformation and moisture content within a fully coupled framework.

Another question that arises when considering wood-water interactions is, what is the rate-limiting process within the adsorption and desorption processes? Is it diffusion or substrate swelling? Furthermore, is there a link between viscoelastic processes and sorption hysteresis? Recent studies have found that using Fick's law alone to describe the moisture adsorption process in wood using a diffusion model does not accurately describe the process [94]. Theories for viscoelastically limited diffusion within polymers by Vrentas and others [106,108,111–113] suggest that there is the possibility of a link between the two processes. Experimental work carried out extensively by Hill and Xie [50–54,115,116] suggests there is a link, using Parallel Exponential Kinetics to confirm the link by interpreting material properties for the amorphous properties; properties that are in line with results expected from mechanical testing and molecular dynamics modelling. This provides the best evidence yet of a link between viscoelastic processes and sorption hysteresis. The use of a fully coupled stress-diffusion model, incorporating viscoelastic response could go further and reproduce experimental work using well known and defined material properties for the cell wall polymers that interact with water. The material properties are obtained from the literature within the field. Due to the complex nature of the wood microstructure, and the difficulty in isolating the behaviour of each individual phase and constituent experimentally, material properties obtained from multi-scale modelling [31] will be used in order to clearly distinguish the viscoelastic behaviour of the cell wall polymers. By isolating the various phases of the material, using Finite Element modelling, it is hoped that further understanding of the behaviour of each phase can be gained, complementing experimental work in the field that has not yet managed to totally elucidate the material behaviour of the complex microstructure within the cell wall.

In this work the viscoelastic material behaviour is captured using springs and dashpots, an approach that has been widely used to describe the behaviour of timber and other cellulosic polymers [26, 28, 29, 42, 52, 89, 116]. The limitations of this Hookean description have been discussed in [82]. These limitations exist within the highly nonlinear behaviour of the intramolecular hydrogen bonding network, which interacts readily with water vapour to create bound water, increasing the mass of the material and causing the stress induced deformations. This bonding between water and the polymers reduces the internal rigidity of the amorphous polymers (mainly hemicellulose and lignin and limited amorphous celluloses), reducing the stiffness of the material and changing the material behaviour from relatively stiff glassy material to a free-flowing rubber like material, in turn leading to large deformations and rearrangement of internal molecular structure.

In this thesis, the water within the wood cell wall polymer network has been modelled, within a multi-scale framework, using poroelasticity to describe its mechanical role and capture the coupling between the two physical processes [7]. However, extension to viscoelastic theory is required to capture the time dependent processes that lead to such behaviour as mechano-sorptive creep and even more complex processes such as sorption hysteresis, to be discussed further on. In this case the polymers within the cell wall are treated as a polymeric gel, within a fully coupled poroelastic and viscoelastic framework to model the interaction between environmental changes and mechanical loading. In this case a Zener rheological model is specified for the constitutive equations to account for both time-dependent creep and relaxation behaviour. The deformation and environmental changes are formulated together within a Helmholtz free energy function, alongside internal relaxation of the polymer network, to create a three way fully coupled description of the stress diffusion behaviour of polymer networks.

To implement the model across as wide a range of environmental conditions as possible, an approach is needed to capture the softening of the cell wall polymers due to water uptake. This phenomenon has been observed experimentally and is particularly significant for high relative humidity within the environment. The adsorption of the water molecules occurs between the hydroxyl groups of the cellulosic polymers, and therefore needs to be predicted on the molecular scale. Experimental observations of stiffness related to moisture content within wood fibres are insufficient as it is the concentration of water molecules at each individual sorption site (i.e. hydroxyl group) that is of importance, as opposed to the overall macroscopic concentration. Furthermore, the stiffness and relaxation properties take part in a complex interaction, transitioning between different phases of material behaviour, with the degree of degradation in the material stiffness of the polymers and the ability to withstand relaxation occurring to both different degrees and at different rates. Molecular mechanics can provide a suitable approach for determining the polymer properties at a given point in time, accounting for both the external environmental conditions and any internal or external loading.

To simulate both complex loading scenarios and geometries, the framework is implemented in 3D using the finite element method. The modelling is carried out using MoFEM (Mesh Oriented Finite Element Method) [1,67]. The advantage of using MoFEM is that it provides a flexible finite element development framework for solving multi-physics problems. It overcomes the limitations of many commercial packages, allowing the user to create their own user modules, within which unique multi-physics problems can be solved to an arbitrary complexity of mesh refinement, orders of approximation and degrees of freedom. This gives a high level of flexibility for carrying out research using finite elements. Furthermore, MoFEM is optimised for high performance computing, allowing the user to make use of mesh partition and parallel processing, leading to the ability to solve problems with a high number of degrees of freedom.

Thesis Outline

The first Chapter of this thesis reviews the literature within the fields of wood science and chemistry and the field of polymeric gel modelling. To begin, a brief overview of the microstructure of wood is presented. This establishes the complexity of the material and the current understanding of the chemical behaviour and composition of the cell wall and each of its many layers. The contribution and primary purpose of each individual constituent polymer is also detailed, focusing in particular on the internal hydrogen bonding structure.

The moisture transport properties of the cell wall are also examined. The different states in which water can exist within the wood cell are established and the different moisture transport processes are described, with particular focus on diffusion across the cell wall. Early literature on the diffusion of water within wood is examined, particularly within the context of more modern and complex theories such as viscoelastically limited solvent migration as proposed by Vrentas and Hill [51, 52, 111, 112]. This discussion is then extended into sorption theory, where the water vapour held within the surrounding air acts as the solvent. This is particularly relevant to the problems that face wood as a construction material where changes in environmental humidity can lead to dimensional changes, as discussed earlier.

The final section of Chapter 1 examines various numerical modelling approaches that have been used previously within Wood science and engineering. Multi-scale modelling and viscoelastic constitutive models are summarised and critically evaluated and assessed against the moisture transport criteria outlined in the previous sections. Approaches that fully capture the coupled processes of viscoelastic deformation and solvent migration are presented from the literature. Several theories from the field of polymeric gel modelling are examined and compared for use within the model.

In Chapter 2 the approach to the model is defined. The environmental conditions to which the polymer is exposed are established within a thermodynamic framework and the governing equations of mass and linear momentum conservation are set out in a thermodynamically consistent manner, based upon the approach by Hu et al [60]. The associated complex constitutive model is described. The Helmholtz free energy of the system under isothermal conditions is described through the deformation of the polymer matrix and the exchange of solvent with the environment. The discretisation of the model over space using the finite element method is described. The integration through time using a backwards Euler scheme is described as well as the solving of the nonlinear system of algebraic equations using the Newton Raphson method.

In Chapter 3 a sensitivity analysis is carried out to demonstrate the behaviour of the model, using four numerical examples. To begin with, a creep test is described, demonstrating the ability of the model to resolve viscoelastic effects due to the application of an external force. Within this test the convergence of the model using both mesh refinement and increased orders of approximation is demonstrated. The influence of the input parameters of the model behaviour is examined to fully understand the complex behaviour.

To assess the suitability of the model to capture viscoelastic effects due to changes in the environmental conditions, a sorption test is carried out. This test, under no external loading and a change in the free energy of the environment, demonstrates the appearance of viscoelastically limited diffusion of water through the sample under certain conditions. The results also show a degree of sorption hysteresis, establishing the potential of the model to carry out analysis on sorption with polymers, according to the criteria set out in Chapter 1.

The final two tests within Chapter 3 demonstrate the capabilities of the model implemented within MoFEM to capture complex problems using multi-layer materials and complex geometries. Again the sensitivity of parameter changes within these conditions is demonstrated to fully understand the results and behaviour of the model.

In Chapter 4 the model is applied to wood polymers in several distinct steps. First the multi-physics approach to this problem is outlined, in which a further review of the literature is carried out. Specifically, the hydrogen bond behaviour of the polymers, already briefly described in Chapter 1, is described. In this, the importance of the hydrogen bonding to describe sorption in wood and other cellulosic polymers is established. Using Nissan's theory of hydrogen bond dissociation [80], the nonlinear behaviour of the hydrogen bond network is incorporated within the constitutive model.

Suitable material parameters for the model are then selected from the literature and the behaviour of the model is assessed and compared to experimental sorption results obtained from the literature. Different conditions are described for the sorption process. Gradually, additional complexities are added, such as different initial moisture equilibrium conditions, the importance of which are described in detail.

These gradually increasing complexities culminate in the description of an isotropic wood cell. The diffusion of the water vapour from the environment is taken into account, with the application of the boundary conditions on the edge of the wood cell simulating different positions within a wood specimen exposed to the environment (i.e. different depths from the exposed surface). The stresses within the cell and the deformation under both adsorption and desorption is demonstrated, demonstrating the ability of the model to carry out analysis on wood cells and other complex cellulosic fibres.

Chapter 5 brings conclusions to the work carried out and also highlights areas for future research using the model and areas for improvement of the current model.

Chapter 1

Literature Review

The aim of this thesis is to present new theories and processes for modelling the coupled hygro-mechanical behaviour of wood cell wall and its constituent polymers, particularly with respect to changes in climatic conditions and the amount of water vapour held within the environment. Changes in climatic conditions lead to large changes in the moisture content within the cell wall, causing the build up of stress in the cell wall and consequent deformations that are observable on the macro-scale. Due to the complex nature of the problem, the literature review is split into three sections covering experimental observations, current theories and current progress on modelling both timber and cellulosic polymers.

First, the hierarchical structure of softwoods and the behaviour and properties of its constituent polymers are briefly introduced. The focus is on softwoods as this is generally the most abundant type of wood available in Scotland and accounts for a very large portion of the timber industry, especially Sitka Spruce and Scots Pine.

Second, a review of wood-water interactions is presented, including sorption theory. The main focus is on the theory of viscoelastically limited solvent migration, which is a widely accepted theory within the area of research and as such presents a good area on which to focus the modelling in order to bring something new to field. Third, a review of modelling within the field of wood and associated cellulosic polymers is presented, including both multi-scale modelling of wood and the field of coupled stress and diffusion.

1.1 The Hierarchical Structure of Softwoods

Timber is a hierarchical multi-scale material, with properties varying across its many length scales, the properties of which are adapted to its local environment during growth. The main components, and the point at which interaction with moisture in the environment occurs, are the cell wall polymers: cellulose, hemicelluloses and lignin. These polymers are organised into a complex multi-layer laminate composite structure of different cell types, with different composition and structural layout. Small changes to the organisation and composition of these layers on the microstructural level can cause very large and noticeable changes on the macroscopic level. To accurately model the microscopic, and ultimately the macroscopic, behaviour of softwoods, it is important to gain an understanding of the properties of each level of the multi-layer hierarchy within the wood cells. The following section highlights the behaviour of each individual length scale within the wood hierarchy as a brief summary to the multi-scale nature of timber and the complexity of the overall structure.

1.1.1 Wood Cells

There are two main types of wood cell, earlywood and latewood, also referred to as tracheids, and these contribute significantly to the volume of softwoods. They provide mechanical strength and manage the transport of water with dissolved minerals in an upward direction. They are usually 1-4mm long and 15-40 μm wide [17, 19, 35, 107]. The different characteristics of earlywood and latewood cells are behind the formation of growth rings within trees.

The early wood cells are laid down in the spring months, when due to the favourable climatic conditions, there is a high rate of growth. To sustain this growth rate a greater amount of water is required to be transported through the cellular structure. The cells constructed at this time of year are characterised by a thin cell wall, 3 - 4 μm thick [37,43], with a large open pore space within with which to transport moisture.

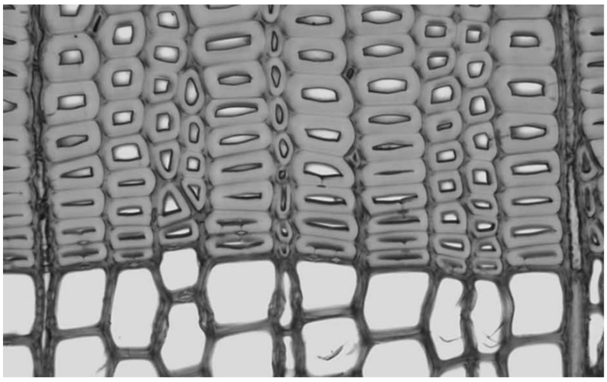

Figure 1.1: Images taken using light microscopy of a transverse section of Norway Spruce showing a transition between the earlywood (bottom layer) and latewood (top layer) cells. Taken from [76].

The latewood cells are produced in the late summer - autumn months, when the rate of growth decreases, requiring less transportation of water. As such these cells are characterised by a thick cell wall, 4.5 - 6 μm [37, 43], and a smaller pore space contained within. Adjacent cells are bound together by the middle lamina, which when aged, can form the compound middle lamina with the secondary cell wall when lignified [43].

1.1.2 Cell Wall Structure

The cell wall is a multilayer composite structure, consisting of a primary cell wall, secondary cell wall (consisting of 3 layers denoted S1, S2 and S3), the middle lamina and a lumen contained within [76]. The function of the middle lamella, which is mostly composed of lignin [73], is to surround the cell and hold neighbouring cells together [2]. Of the three secondary cell wall layers, the S2 layer is the most abundant, making up about 80 percent of the mass of a fibre [36] and varies between 1 and 10μm thick [86]. Since the S2 layer is the dominant layer, being by far the thickest, containing the majority of the cellulose within the wood cell [49], it is common for the properties, such as the microfibril angle, of this layer to be applied across the cell wall [32]. The primary cell wall is around 0.12μm thick in earlywood cells and 0.38μm thick in latewood cells of softwoods [20].

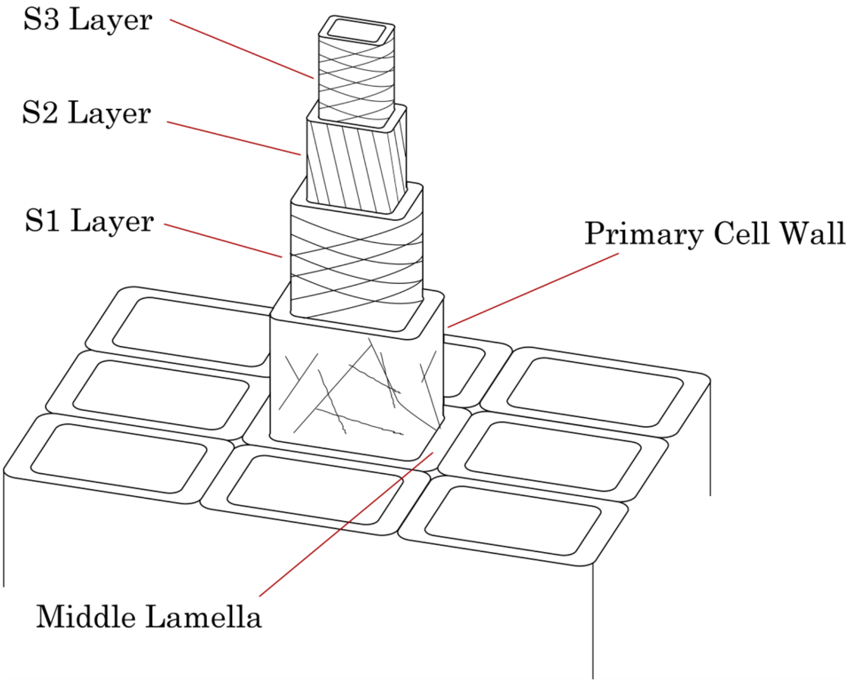

Figure 1.2: The multi-layer structure within an individual wood cell. The secondary cell wall is split into 3 layers (S1, S2 and S3) and the Primary cell wall and the Middle Lamella are towards the outside of the cell.

Both the primary and secondary cell walls are made up of a mixture of cellulose, hemicellulose and lignin polymers. The cellulose chains are the discrete component embedded in a non-cellulosic polymer matrix, consisting mainly of hemicelluloses and lignin, as well as extractives. This matrix can be described as a homogeneous blend of the amorphous polymers [90]. Lignin is not bound directly to cellulose but is covalently bound to hemicelluloses [57], therefore the hemicelluloses play a key role in binding the cell walls together.

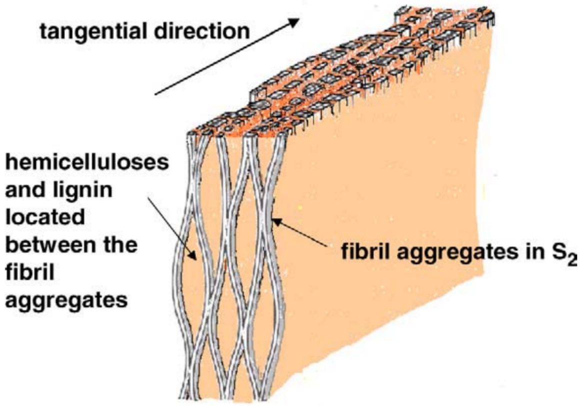

Figure 1.3: Schematic diagram of the aggregate structure of cellulose in the S2 layers, based on the ideas of Boyd [18]. Taken from [90].

Within the secondary cell wall the crystalline cellulose fibrils are arranged in a helical pattern, with the angle denoted as the microfibril angle (abbreviated as MFA). This microfibril angle varies between each layer of the secondary cell wall, with a higher angle to the vertical in the S1 and S3 layers [20] than that in the S2 layer. The microfibrils in the S2 layer have a slight spiral angle of between 10-30 degrees to the vertical axis [43]. The microfibril angle is important as it sets the orientation of the crystalline cellulose fibrils, which offer up a far higher stiffness in the longitudinal direction than the transverse direction, and also a far higher stiffness than the amorphous polymers, more of which will be discussed further on. As such the MFA is the parameter that defines the anisotropic material properties of each layer of the cell wall within each individual wood cell.

Layer	**Cellulose**	**Hemicellulose**	**Lignin**
Primary	15	15	70
S1	28	27	45
S2	45	35	20
S3	47	38	15

Table 1.1: Composition, in terms of approximate dry mass of each, as a percentage of the three main polymers in each individual cell wall layer [63]

Table 1.1 gives a summary of the percentage of each constituent polymer that can be found within each layer of the cell wall. The primary cell wall is highly lignified, with more or less equal proportions of cellulose and hemicellulose. The three secondary cell wall layers contain a far higher percentage of cellulose, with the highest proportions being found in the S2 and S3 layers. The contributions of lignin within these layers are relatively small, i.e. 20% or less.

Microfibril Angle Variation

The variations in microfibril angle between different sections of a tree have an influence on the overall macroscopic behaviour when under stress or during moisture uptake and are a key defining property in the dimensional stability of timber. The microfibril angle varies throughout the width of a tree with the highest values being in the inner most growth rings (the juvenile wood from the trees early life) and the lowest value being towards the outer growth rings [10]. However the MFA generally remains constant throughout the length of each different wood fibre [11]. The MFA also decreases as the height of the tree increases [11]. As the MFA increases the longitudinal modulus of elasticity decreases and the wood becomes less rigid (and therefore more flexible) [86]. The higher MFA in juvenile wood is regarded as being a result of the need for increased flexibility of a tree in its early life. In short, the wide variation of MFA between sections of timber needs to be taken into account when creating multi-scale models designed for predicting behaviour on the macro-scale.

1.1.3 Cell Wall Polymers

To fully understand the behaviour of the wood cell wall, both during wood-water interactions and when under mechanical stress, it is important to understand the role and behaviour of each of the main constituent polymers within. As such this section provides a brief introduction and overview of the chemistry of each of the constituents, cellulose, hemicellulose and lignin.

Cellulose

Cellulose is the most abundant material in the earths biosphere and is the most highly ordered and stable of the polymers in the cellular structure of softwoods. It is a glucan polymer consisting of linear chains of 1,4-β-bonded anhydroglucose units [85] and it is the main contributor to the stiffness properties of the wood fibres [90]. The cellulose acts as the main structure within the cell wall polymer mixture and has been found to exhibit anisotropic behaviour [105]. However it is common for it to be treated as isotropic for use in modelling [76]. This makes sense, particularly when dealing with wood-water interactions where the interactions happen within the highly disordered amorphous regions of the polymers.

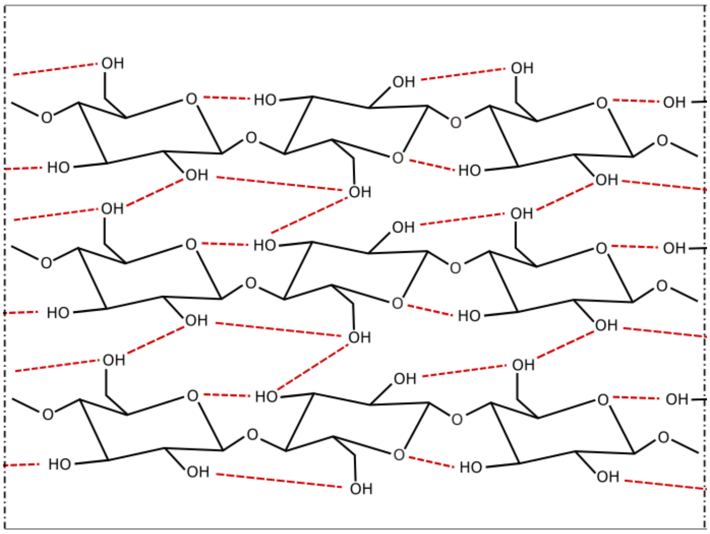

Figure 1.4: The structure of cellulose as a repeatable unit switching along it's glycosidic bond (C-O-C). It consists of three polymer chains (top to bottom) linked by hydrogen bonds in between (red dotted lines)

The structure and internal hydrogen bonding of the cellulose structure is shown in Figure 1.4. It is organised into cellulosic microfibrils within the wood cell wall, consisting of many linked cellulose chains. The chains are largely crystalline in the middle but amorphous on the more exposed surface chains. It is on the exposed surface chains that the majority of the celluloses interaction with water will likely occur.

Recently, research into cellulose microfibril dimensions using wide angle x-ray scattering (WAXS) has proposed a 24 chain model for the structure of cellulose with two possible packing arrangements [38]. The possibility of 18 chains with tightly bound glucomannan contributions is also considered. Previously a 36 chain structure had been suggested. The cellulose chains are tightly packed together in cellulose microfibrils in a highly crystalline structure, linked together by intermolecular hydrogen bonds between surface chains. These bonds are molecule to molecule bonds and as such are, in the main, not exposed to the surface of the microfibril; as such they do not readily interact with water [57]. However, as the lattice is not infinite, there are regions of disorder within cellulose crystals, generally located towards the surface of a chain. FT-IR (Fourier Transform Infrared Spectroscopy) experiments [57, 91] have also observed that water accessible regions of cellulose are located towards the surface of a crystal. These regions of disorder, on the outer surface of crystals, have been found to interact with water [12, 70]. More recently molecular dynamics has been used to determine the weakening effect of water on both the cellulose and hemicelluloses and the role of hydrogen bonding within this context [65], more of which will be discussed in Chapter 4.

The longitudinal stiffness of a wood fibre is mainly a product of the strength of the cellulose chains which themselves have a Youngs modulus largely governed by the strength of the intermolecular hydrogen bonding between cellulose molecules, including the 3-OHO-5 bond [105]. It is proposed that a softening of this bond due to the adsorption of water affects the stiffness of the cellulose chain as this bind is important to the stress transfer along the cellulose chains [83]. Youngs modulus values for cellulose vary greatly, however a range of between 120-167.5 GPa has been suggested [61,64,88]. Furthermore the elastic properties of cellulose are generally regarded as not being dependent on moisture changes, with the exception of the small amorphous regions [76].

Hemicellulose

Hemicelluloses are polysaccharides associated with cellulose and lignin in the cell wall wood cells. They are composed of several polysaccharides and have a random amorphous structure within the wood cell wall and contribute relatively little stiffness. Due to their amorphous structure they can adsorb a larger proportion of water than cellulose [83]. They combine with pectin to bind with cellulose in order to create a cross-linked polymer network. The most common type of hemicellulose in wood is Xylans which represent up 30 percent of the dry weight of wood [71]. Other hemicelluloses contained within wood include *xyloglucans, glucomannans* and *galacto-glucomannans.* However, in softwoods it is the *glucomannans* that are predominant. The *galactoglucomannans* in softwoods are mainly composed of a backbone with $(1 \rightarrow 4) linked - \beta - D{-}mannopyranosyl$ units substituted with $(1 \rightarrow 6)$ *linked -α-D-glactopyranosyl* and *acetyl* groups [34]. The main difference between cellulose and hemicellulose is that the hemicellulose chains are shorter and contain different sugars. The hemicelluloses provide mechanical linkage of the polymers by linking cellulose fibres into microfibrils and bonding with the lignins [92]. The cellulose and hemicelluloses are linked together by hydrogen bonding between cellulose and hemicellulose chains. Due to the similarity of cellulose and hemicellulose, it can be very hard to distinguish between the two in micro-spectroscopy experiments where the cellulose and hemicellulose bands overlap. This makes it difficult also to predict the behaviour and stiffness contribution of the hemicellulose when in-situ.

The Young's modulus of hemicellulose has a much lower value than that of the crystalline cellulose fibres. At 10 percent moisture content the stiffness is as high as 8 GPa but at higher moisture contents this reduces dramatically, to 0.01 GPa at around 70 percent moisture content. Therefore, at higher moisture contents the hemicellulose will offer little in the way of stiffness and appears to decouple itself from the cellulose fibrils [25]. The transverse loads in the cell wall will therefore be carried mainly by the lignin at higher moisture contents as well as higher angle cellulose microfibrils. The obtained values for stiffness of hemicellulose can also be considered as unrepresentative as they were not obtained in-situ and therefore the behaviour within wood may be different. It is also known that isolated hemicelluloses can crystallize which could further affect the results with regards to the high values of the elastic modulus when in the dry state [90]. Polarised vibrational spectroscopy has been used to investigate the cell wall polymer orientation of all the major wood polymers [5]. It has been found that the hemicelluloses are orientated in the direction of the cellulose microfibrils [92] and thus when insitu the hemicellulose could also be regarded as exhibiting transverse isotropy.

Lignin

Lignin is interspersed between the cellulose fibrils and is covalently bonded to the hemicelluloses within a three-dimensional matrix, and can be assumed to be an isotopic material. It consists of many hydroxyl and methoxyl substituted phenyl propane units [3]. They fill any openings on the cell wall after the cellulose and hemicelluloses have been deposited and can be considered to be the cellular glue in which the cellulosic fibres are embedded. It is covalently bound to hemicellulose within the cell wall. Lignin provides structural support to the cellulose chains and its hydrophobic surface allows transport of water [86]. It also aids in resistance against microbial attack and aids in tree recovery after wounding. While Lignin is often modelled as isotropic, it has been found that there are preferential directions within the matrix. For instance Akerholm and Salmen found that the phenylpropane units within lignin are orientated in the direction of the cellulose microfibrils [5]. This could be due to the fact that lignin formation takes place after the formation of the cellulose/hemicellulose structure which provides a template for the lignin deposition [93]. The Youngs modulus of lignin (like cellulose and hemicellulose) is moisture dependent [24]; however it is not as extreme a reduction in stiffness as occurs within hemicelluloses. Lignin generally retains a high stiffness when in high moisture contents at room temperature [92]. The minimum value for lignin stiffness is around 2.8GPa whereas at low moisture contents (3 percent as opposed to 12 percent) it is as high as 6.7GPa [24]. It is worth noting that experiments to isolate lignin for testing do affect the structure chemically; this probably changes the measured stiffness and may not properly represent the in situ behaviour [49]. Thus, the resulting values should only be considered as indicative.

Molecular Deformation

When external strains are applied to the cell wall, deformations within the cell wall polymer networks occur. This is an important factor in predicting moisture induced warping, since establishing a relationship between external strains and molecular deformations could provide valuable information on cell wall behaviour.

The behaviour of cellulose chains, particularly the inter-molecular hydrogen bonding between the chains, has been investigated to determine the deformation behaviour of cellulose and the related molecular straining. Dynamic FT-IR has been used [55] to investigate the molecular deformations when under external strain. The results indicate that the load bearing structure within the cellulose is mainly the C-O-C *glycosidic* bond and the 3-OHO-5 hydrogen bond, with the 2-OHO-6 hydrogen bond contributing very little stiffness. Raman testing [44] under tensile deformation also supported the C-O-C linkage contribution, further adding that there appears to be a widening of the torsion angle of the *glycosidic* bond, indicating that the bond is in fact straightening under strain. The tests also gave evidence that the lignin within the sample was acting as a low-modulus, non-load-bearing amorphous polymer. Tests using Tensile FT-IR spectroscopy established that is was not possible to verify the behaviour of lignin using this technique [4]. FT-IR tensile tests with humidity control [91] indicate a decrease in wavenumbers of the vibrating covalent bonds, signalling a stretching (and therefore progressive weakening) of the covalent bonds within the sample. This wavenumber shift is found to happen at a faster rate with regard to the applied stress at higher moisture contents (90 percent relative humidity) with the process still happening in a linear manner. Therefore, increased moisture content leads to an increase in the rate at which the covalent bond strength decreases with respect to an applied stress. In the same experiment on the 3OH.O5 hydrogen bond it was found that the wavenumber increased with an increase in stress, again in a linear manner. This is due to a reduction in length of the OH bond, caused by a weakening of the hydrogen bonding under straining. Again, moisture has a significant effect, with the hydrogen bond strength decreasing with respect to stress and the rate at which this happens increases at higher moisture contents [91].

Altaner et al [6] proposed a mechanism of molecular velcro type interactions between hemicelluloses, in which the hemicelluloses are the bridging polymer between crystalline chains of cellulose. Under mechanical stress, these hydrogen bond interactions undergo a slip mechanism, whereby they shift locally and reattach further along a cellulose microfibril. The sum of these local arrangements will lead to a rearrangement of the internal structure between microfibrils within the wood cell wall when under mechanical stress. Kulansinski et al [65] have also observed similar effects within molecular dynamics studies on the interface between crystalline cellulose and hemicellulose and have found a de-bonding effect between the two under wetting, due to the high number of sorption sites available on the surface of crystalline cellulose microfibrils [65].

1.2 Wood-Water interactions

1.2.1 States of Water in Wood

In this thesis water content is frequently referred to. To ensure clarity it is defined at this point as the mass of water, m_w, over the dry mass of the polymer, m_p. The percentage water content is defined in Equation 1.1 below:

$$\mathrm{WC\%} = \frac{m_w}{m_p} \times 100 \tag{1.1}$$

Water in wood has been found in three different states using differential scanning calorimetry and thermogravimetric analysis; free water, freezing bound water and non-freezing bound water [14, 74]. However, more recent evidence suggests there may only be two states in which water can exist in wood: free-water and non freezing bound water [117]. However, this will not impact the work contained within this thesis, as it will focus only on bound water transport well above freezing conditions, close to room temperature.

Free water is contained within the cell lumens and undegoes capilliary effects and is not directly bound to the wood polymers. Non-freezing bound water directly interacts with the hydrophilic wood polymers within the wood cell wall. This hygroscopic water is bound to the cell wall chemically by forming hydrogen bonds with the hydroxyl groups of the amorphous cellulose and hemicelluloses and some hydroxyl groups within the lignin matrix [33,95,98]. Of these, its the hemicelluloses that interact the most freely with water. In cellulose, only the outer surfaces of the microfibrils are available for sorption [57], with these areas being termed as amorphous cellulose.

The natural fibres and mixture of ligno-cellulosic polymers within wood are hygroscopic materials and as such they can swell to adsorb water from the environment. Interactions between the polymer and the water happens at the hydroxyl groups within the polymer network. The hydroxyl groups that are available for interaction with water within the polymer matrix are referred to as sorption sites [32, 97]. The amount of hygroscopic water within the cell wall is limited both by the number of sorption sites and the number of water molecules that can be held per sorption site [95, 98], normally just one water molecule per sorption site [13]. These hydroxyl groups are locations at which intramolecular hydrogen bonding can occur, increasing the stiffness and torsional rigidity of the polymer network. Other chemical groups may also attract and interact with water but their contribution is negligible in the overall system [13, 32]. Incoming water molecules can disrupt the hydrogen bonding network, forming hydrogen bonds with the hydroxyl groups themselves, leading to a drop in the stiffness properties of the network and a subsequent increase in the swelling.

When dealing with wood-water interactions below the fibre saturation point (often denoted as the FSP), the amount of water within wood depends upon the amount of water within the air in the surrounding environment as well as the temperature of the surroundings. The fibre saturation point is the maximum amount of water that can be held within the cell wall without any water being held within the lumens [95]. Any additional water content beyond this point will be held within the lumens. When in equilibrium within an environment of a given relative humidity and temperature, the moisture content corresponding to these conditions is known as the equilibrium moisture content (EMC), often referred to as a percentage of the original dry mass (i.e. EMC%). Factors that determine the EMC include mechanical stress (i.e. either external loading or internal stress build up within the wood micro-structure), the drying history, the specific gravity of the wood and the extractive content [95].

1.2.2 Moisture Transport in Wood Cells

Moisture can move through wood in two different processes: vapour diffusion and liquid transport. The former is specifically relevant to this thesis, while the latter is not. A short description of both processes and the relevance to the modelling of wood cell wall interactions with moisture follows.

Liquid Transport in Softwoods

Liquid transport can be described in terms of the bulk flow of water through the interconnected system of voids within the wood (i.e. the lumen held within each individual cell). These individual wood cells are interconnected through pits held within the lumens [95]. Therefore the wood material can be described as permeable. However, this type of moisture transport only happens above the saturation point, beyond the point of where the wood cell polymers are saturated and/or during immersion in a body of water. In this thesis the main focus is on the wetting and drying behaviour when exposed to air of different moisture contents and as such diffusion is the dominant moisture transport process, with capillary effects not needing to be considered. Thus capillary processes are not considered from this point on. Some results have been obtained for the determination of the permeability of water through the cell wall in spruce heartwood [84]. Due to the high permeability, a gradient of osmotic pressure was used to pass solution of far higher molecular weight than water, preventing uptake of the solution by the cell wall polymers. It was found that the permeability is 6.8×10^{-14} mm^3/mm in the longitudinal direction of the fibre and 7×10^{-15} mm^3/mm in the tangential direction [84, 95].

Diffusion in Softwoods

Diffusion is the primary transport process for water when dealing with wood-water interactions below the fibre saturation point. It can be described as the molecular mass flow under the influence of a concentration gradient [95] and it can be described in terms of Fick's 1st law for steady state problems and in terms of Fick's 2nd law when dealing with unsteady moisture transport. These relationships are regularly applied to describe moisture transport through the wood cell wall [95, 98]. However several different suggestions have been made as to the primary driver for moisture diffusion through the cell wall [98]. Suggestions for this include the chemical potential, the concentration, the internal pressure and the vapour pressure. In fact we may think of these as all interconnected in a fully coupled system of different physical effects. For instance the chemical potential and the water vapour pressure are intrinsically linked, as will be demonstrated in Chapter 2. In this thesis an attempt is made at linking these processes together to fully resolve the moisture transport mechanisms within the cell wall. More of which is described in later sections and chapters.

There are two different diffusion processes which concern the work in this thesis: water vapour diffusion and the bound water diffusion. The water vapour diffusion coefficient, shown in Figure 1.5 alongside the bound water coefficient, is the proportionality constant which links the bound water diffusion flux to the gradient of the concentration (or chemical potential as will be discussed in Chapter 2).

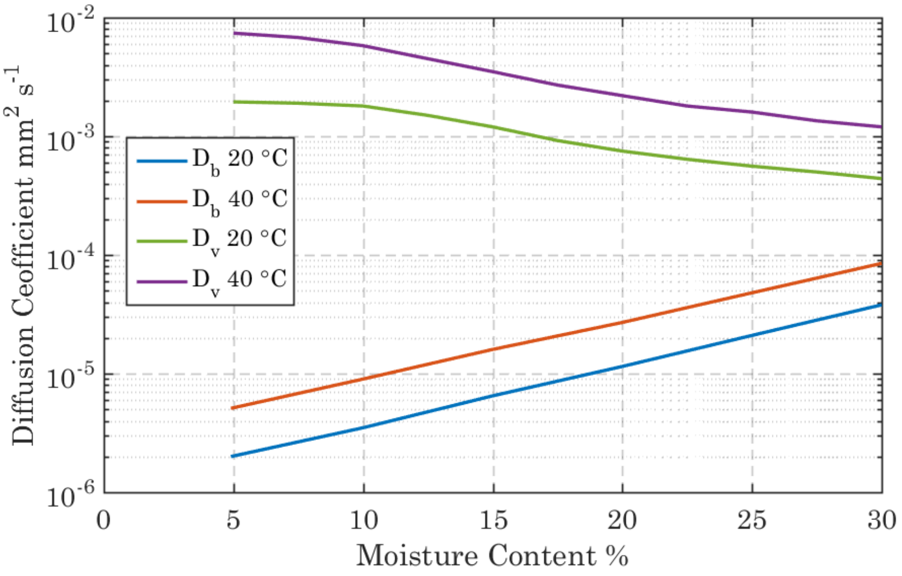

Figure 1.5: Diffusion Coefficient for bound-water diffusion and water vapour diffusion in the longitudinal direction of wood cells at different temperatures, as a function of moisture content. Data from Stamm 1959 and Siau 2012 [95, 100].

The rate at which the water migrates through the cell wall polymers is partly defined by its bound water diffusion coefficient. This is typically smaller than the diffusion coefficient determined for larger samples of wood, where diffusion through the lumens greatly speeds up the process when observed on the macro-scale [95]. This rate has been found to be between 1×10^{-07} and 4×10^{-06} $mm^2\ s^{-1}$ for wood and other cellulosic polymers [22, 78, 95, 96, 98, 100, 101]. It has also been found that the diffusion coefficient in the longitudinal direction of a wood cell is 2.5 times larger than the coefficient in the tangential or radial direction [102]. This could be due to the fact that the bound-water has to pass across the dense crystalline cellulose microfibrils in the radial and tangential directions and therefore blocking the path of diffusion in that direction.

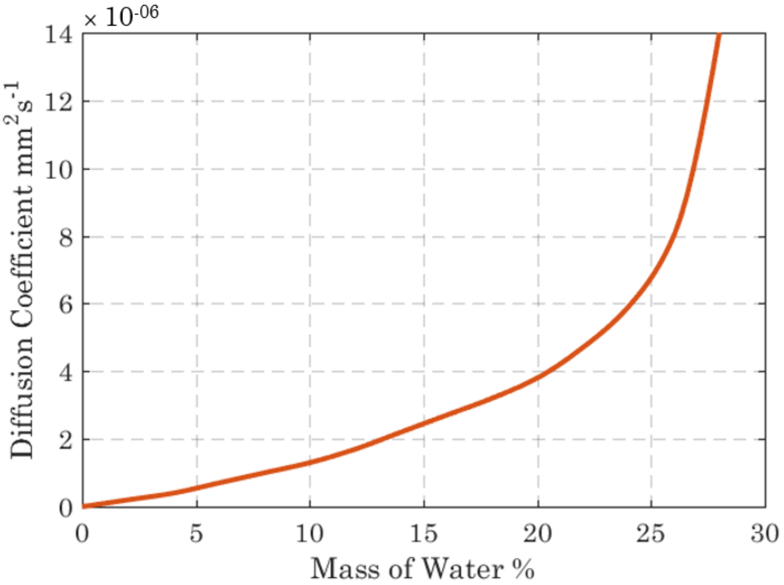

Figure 1.6: Diffusion Coefficient for bound-water diffusion in the longitudinal direction of wood cells at a temperature of 20°C, as a function of moisture content. Data from Stamm 1959 and Siau 2012 [95, 100]

The diffusion coefficient has been found to increase as the moisture content increases within wood cells [100]. The relationship between diffusion and moisture content is given in Figure 1.6, based upon the work of Stamm. Siau predicted that the increase in diffusion coefficient may be due to lower bonding energy between the sorption sites and the bound-water molecules at higher moisture contents [95]. The idea behind this is that lower bonding energy would allow fast transport of the bound-water molecules through the dense structure of hemicelluloses and lignins and their corresponding hydroxyl groups.

Furthermore it was anticipated that bonding energy should approach zero at the fibre saturation point, where any additional moisture after this point is to be regarded as free-water, governed by relatively weak capillary forces [95]. However, the idea that bound-water diffusion through the polymers can be explained by Fickian processes alone has been questioned. It has been proposed more recently by Vrentas [111–113] and subsequently Hill and Xie [50, 52–54, 115], that viscoelastic processes play a part in determining the rate of bound water diffusion through polymer networks.

The view taken in this thesis is that the observation by Stamm [100] of the rate of diffusion increasing with moisture content is down to a combination of several factors. These include the coupled stress-diffusion process causing substrate swelling, the time dependent viscoelastic processes and the nonlinear hydrogen bonding behaviour within the polymers changing both the stiffness and relaxation properties of the polymer upon interaction with water. These theories will be explained in more depth, in Chapters 1 and 4. As such, the coefficient is taken to be a constant, when the material is dry, on the understanding that other factors determine the rate of sorption.

1.2.3 Sorption in Wood Cells

When discussing the wood-water interactions within the wood cell wall layers, sorption theory is referred to, which is the chemical process by which one substance becomes chemically attached to the other. In this case, the adsorption of water within the wood cell wall is the incorporation of water into the network of cell wall polymers. Desorption is the reverse process, where the water leaves the wood cell wall. Explanations for the sorption process in wood tend to fall into two categories.

First, there are the clustering theories, based upon clustering of water molecules on internal sorption sites within the polymer mixture. For instance the Langmuir theory that assumes a single layer of water vapour molecules condensing upon polymer sorption sites [68] and the BET (Brunaeuer-Emmett-Teller) theory based upon several layers of adsorbed water [21]. These theories, especially extensions such as the Dent model [27], can reasonably predict the sorption isotherms of wood materials, including the adsorption and desorption cycles and the hysteresis effect (explained further on in this section). However, experimental work is required to determine adsorbed water vapour at various levels of relative humidity as a basis for isotherm prediction. As such they are of little practical use in terms of predictive modelling in a multi-physics framework. However, certain points can be noted from the research, such as the effect of substrate swelling within the wood cell increasing the activity of the bound-water, where the pressure is caused by the cell wall polymers resisting the deformation of the incoming bound-water [98]. This essentially links energy of the mechanical behaviour to the chemical potential field, implying a coupled relationship between the two.

The second theory explaining sorption behaviour is the mechanical response and the changing behaviour of the polymers within the network. A lot of work has been carried out on these theories, based upon the assumption that the polymers behave in two different manners, glassy or rubbery, and that it is the switch between these states that defines the behaviour. As such this work attempts to explain sorption theory through the mechanical, viscoelastic response of the polymer network due to external environmental loading, in a fully coupled framework. This is explained in the following section, where the mechanical sorption behaviour is discussed in the context of sorption isotherms.

Sorption Behaviour and the Sorption Isotherm

A common test of the behaviour of wood and other cellulosic materials is the sorption isotherm. In this experiment the sample is held within an environment of gradually increasing, and then decreasing water content. Commonly this takes the form of incremental increases of the relative humidity percentage (RH%) from dry (0%) to close to saturation vapour pressure (100%) and then back down to zero. Equilibrium moisture content is achieved for each given increment by ensuring the change in mass is sufficiently small. For instance Hill et al [51, 53, 54] ensure that the mass changes no more than 0.002% per minute over a ten minute period to ensure the EMC has been attained. Figure 1.7 shows a typical sorption experiment as carried out by Hill et al [53] on sitka spruce.

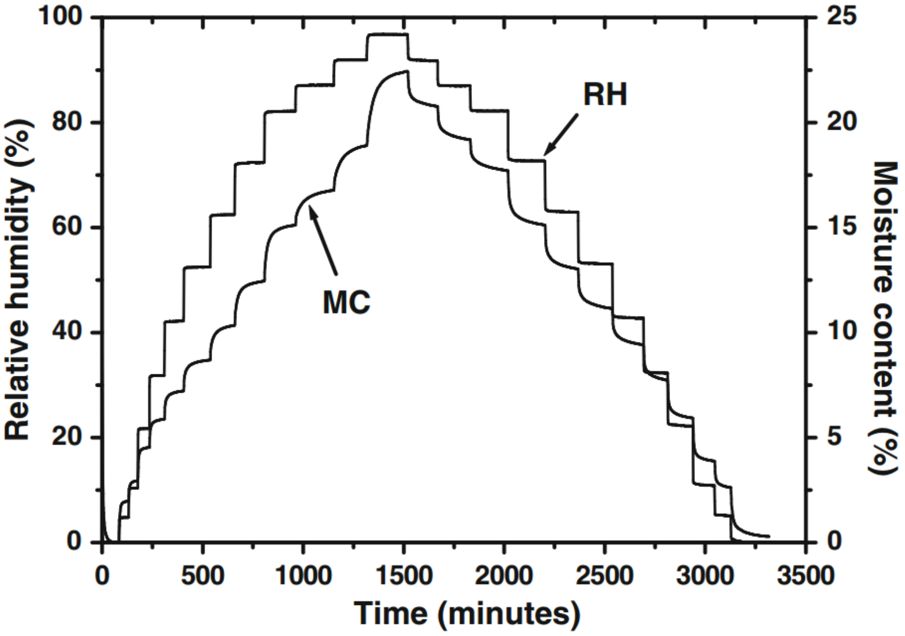

Figure 1.7: The sorption behaviour of sitka spruce at a temperature of 24.1 degrees Celsius, showing the adsorption and desorption run of a typical sorption experiment. The line labelled RH refers to the relative humidity of the environment and MC refers to the moisture content within the sample. Taken from [53]

Typically the sorption isotherms of wood and other polymeric materials have a sigmoidal shape [112]. Dual mode sorption theories [9, 109, 110, 112, 113] assume that the material behaviour has two stages above and below a critical temperature, referred to as the glass transition temperature, T_g.

Vrentas et al [111] theorised that a Deborah (DEB) number can describe the rate limiting behaviour when describing the polymer as a viscoelastic fluid, where the molecules within the polymer reorientate themselves over time noting that this description is weaker below the glass transition where the reorientation of the molecules within the polymer material is extremely slow. The theory defines the relaxation time as related to the relaxation shear modulus and refers to both characteristic diffusion time and relaxation time as related to mass transfer. The Deborah number can be defined as the ratio of the viscoelastic relaxation time, τ_v, to the timescale of the observation, t. Referring to the time of observation, t, as the time taken for Fickian diffusion to take place, the Deborah number for the diffusion is formulated as:

$$(\text{DEB})_D = \frac{\tau_v}{t} \tag{1.2}$$

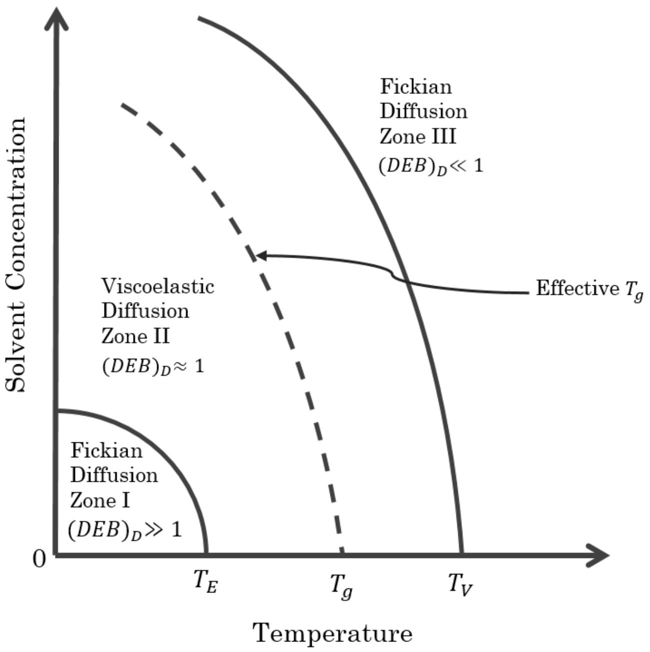

Figure 1.8: Solvent concentration (vertical axis) and the associated material temperatures (horizontal axis). Taken from the idea of Vrentas et al. [111]

Figure 1.8 shows the different transitions of material behaviour and the dependence on concentration. At the extremes of the proposed Deborah number, i.e. $1 << (\text{DEB})_D << 1$, Fickian diffusion is observed. When the Deborah number is close to being equal to 1 the viscoelastic processes happen on a similar time scale to diffusion, hence the rate of diffusion is controlled by the viscoelastic processes. This phenomena is known as viscoelastically limited diffusion.

The different material temperatures, T_v, T_g and T_E, are the concentration and temperature dependent transition temperatures of material behaviour. This refers to the relaxation behaviour and whether or not the material behaves as a glassy or rubbery polymer. T_v refers to the temperature above which the pure polymer acts as a viscous fluid and T_E is the temperature below which the pure polymer acts as an elastic solid. T_g is the glass transition temperature, where the material transitions between its glassy and rubbery states. Experimental work has also suggested that, at high RH, wood behaves as a free flowing material [77], similar to the rubbery description given by Vrentras for polymers. The transition between the glassy and rubbery material behaviour is shown in Figure 1.9, where the sorption isotherms are plotted for three different temperatures and the dashed line represents the rubbery material phase. It can be seen that there is a sharp upturn in mass gain due to solvent uptake after the glass transition as the material offers less mechanical resistance to moisture uptake. From Figure 1.8, it can be established that increasing the moisture concentration, from an initially dry state, within the polymer, whilst keeping the temperature constant, will mean all three stages of this material behaviour will be observed. The temperature governs the concentration of solvent needed to effect these changes, especially when referring to normal climatic changes where exposure to extreme changes temperature is unlikely. Therefore material temperatures can be described as concentration dependent.

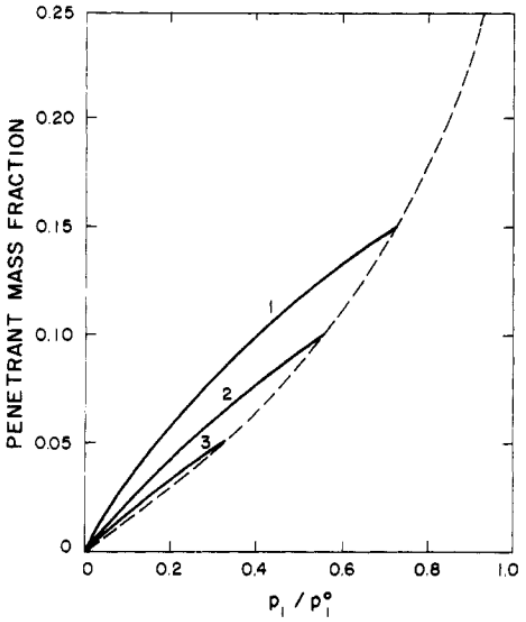

Figure 1.9: Penetrant mass fraction (vertical axis) and the water vapour pressure ratio (horizontal axis), showing the sorption isotherms for curves of three different temperature, 1,2 and 3 (25, 50 and 75 $°C$). The dashed line represents the rubbery material behaviour. Taken from Vrentas et al. [112]

Reflecting on the relationship of the diffusion coefficient as a function of moisture content, Figure 1.6, it is possible to observe an important behaviour pattern: there is an increase in the diffusion coefficient where there is an exponential increase in the water uptake beyond 20% moisture content. This suggests that the viscoelastic process is taking part in the exponential increase. If the diffusion of the bound-water below 20% moisture content is regarded as Fickian transport, then there is a clear change from this behaviour upon further wetting.

This can then explain the behaviour after the glass transition. At this point the polymer is in its rubbery state and viscoelastic processes happen on the same time-scale as the time for diffusion, i.e. the Deborah number is close to unity $(\mathrm{DEB})_D \approx 1.0$. The internal rearrangement of polymer molecules allows an extra volume of solvent to enter the polymer material, thus increasing the rate of uptake. By not considering the internal viscoelastic processes, one could arrive at the conclusion that the increase in diffusion coefficient is due to internal bonding energy, as concluded by Siau and others [95]. In fact, it is important to include viscoelastic effects in the same manner as Vrentas and others, with regards to the rate of diffusion [50, 52–54, 106, 108, 111–113, 115].

1.2.4 Sorption Hysteresis

The sorption behaviour of wood is dependent upon the moisture content, and as mentioned previously, the concentration within the wood polymers cause the material to undergo different phase changes, i.e. switch between Fickian and non-Fickian diffusion processes. It has also been observed that the sorption behaviour of wood is dependent on its moisture history. This phenomenon is known as sorption hysteresis. In most cases of observed hysteresis, the EMC during an adsorption for a given humidity is lower than the EMC for the corresponding humidity during desorption. Hysteresis in both cellulosic polymer materials and wood fibres have been observed widely in experimental conditions [51–54, 115, 116], and it has been observed that the EMC when the wood is in its green state (before any industrial drying has occurred since the initial felling of the tree) is higher than in any subsequent state thereafter [98], highlighting the importance of the initial drying process. Fleming and Koros observed hysteresis for amorphous polymers in their glassy state [39], noting that the volume due to the solvent is higher in desorption than in adsorption. Vrentas et al also noted that a higher relative humidity is needed to achieve the same moisture content in adsorption than in desorption [113]. Furthermore, above the glass transition, it has been noticed that the hysteresis dissapears as the amorphous polymers can swell more freely [112].

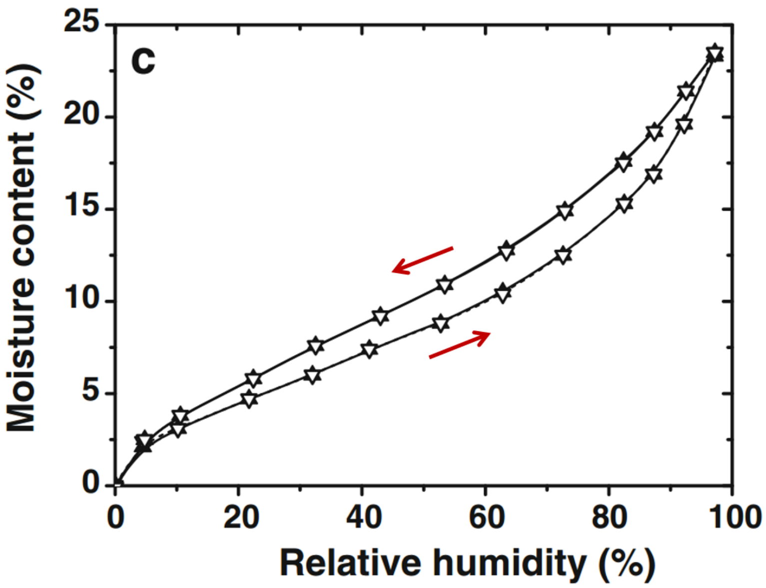

Figure 1.10: Water sorption isotherm of sitka spruce where the bottom line represents the adsorption isotherm and the top line is the desorption isotherm. Taken from Hill et al. [53]

Hill et al have attributed the hysteresis phenomenon, in both cellulosic and lignocellulosic materials, to a response lag in the collapse of nanopores in the interfibrillar matrix as water molecules exit and a lag in the structural expansion of the pores during the adsorption process [116]. There are thought to be sorption sites (i.e. hydroxyl groups within the nanopores) that are initially not accessible to incoming water due to the packing arrangement of the polymer chains. However, some time after wetting, due to internal deformations of the polymer chains, these hydroxyl groups become accessible to incoming water.

It is proposed that this lag in nano-structural behaviour is due to the adsorption and desorption processes taking place in a polymer that is in different states. This occurs below the glass transition where the structural response time, i.e. the re-orientation of polymer molecules under stress, happens at a very slow rate. This is similar to the theory of Vrentas et al [111] whereby the material, when below the glass transition, behaves like an elastic solid. However, the polymer is also thought to behave as a non-equilibrium liquid in this state, with long term reorientation of molecules within the polymer happening at such a slow rate it is very difficult to observe experimentally within a reasonable time frame. Hence, any changes in orientation above the glass transition will effectively be locked in place when the material returns to its glassy state, as re-orientation of molecules changes from a free-flowing process, happening within a similar time frame to the diffusion of solvent, to a highly viscous liquid that re-orientates on a time frame assumed to be beyond what is observable.

Within wood, sorption hysteresis remains above the glass transition of the constituent amorphous polymers [32, 52], unlike in amorphous polymers where hysteresis dissapears as the material behaves in a rubbery manner [112]. This could be due to the high degree of crystallinity within wood, due to the cellulose microfibrils within. As the moisture content increases the different constituents within the cell wall will be undergoing different phases of behaviour. For instance, the semi-crystalline cellulose may be constrained by the crystalline chains and may not yet be beyond the glass transition even when the cell wall is at saturation. The constraint of the cellulose microfibrils could also raise the glass transition temperature of the amorphous polymers within the network [104].

1.2.5 Sorption Conclusions

The sorption behaviour of wood is a complex interplay of different polymers at different stages of material behaviour. At some stages of sorption, diffusion is controlled by Fickian processes alone and poro mechanics can provide an adequate material description. However, as the cell wall material approaches the concentration dependent glass transition temperature, the relaxation behaviour starts to interplay with the diffusion behaviour to open nanopores at a rate similar to that of diffusion, hence relaxation becomes the controlling process within the polymers. Therefore, to accurately describe the physics of these wood-water interactions, any model created will need to describe the behaviour at these stages:

1. Fickian diffusion below the glass transtition. Relaxation happens on a time scale far longer than the length of observation, hence the polymer behaves in a linear elastic

manner. However, as relaxation is happening at a very slow rate, the polymer is regarded as a non-equilibrium liquid.

2. Viscoelastically limited diffusion, where the time of relaxation is similar to the time of diffusion and observation, hence the material undergoes a complex interplay of void creation and collapse, increasing solvent uptake and increasing the length of time the progress takes until equilibrium is reached. This happens in the region of the glass transition.

3. Fickian diffusion above the glass transition. At this point the material is undergoing entirely rubbery behaviour and behaves as a free flowing liquid where equilibrium is reached quickly. Relaxation happens far quicker than the time of diffusion and/or observation.

If the proposed constitutive model can describe these scenarios it could provide a good basis from which to create a multi-scale model for use in sorption theory, to both ascertain regions of viscoelastically limited material behaviour numerically, thereby confirming experimental theories. It could also be used in more complex problems, whereby timber, under external load, is exposed to environmental changes, or previously dried timber undergoes moisture induced deformation when used within a multi-scale framework. As such the aim is to capture these behaviours for the individual polymers for use in future multi-scale environments. Additional theories could provide a path for the model to automatically switch between these different material behaviours due to the environmental conditions and internal moisture content. Further discussion of this addressed in Chapter 4.

1.3 Numerical Modelling Review

The aim of this thesis is to provide a path towards predictive multi-physics modelling of wood-water interactions and the associated stresses within. To do this, models for both wood and polymeric gels are examined.

Wood modelling is complex due to the multi-scale nature of the material, as outlined earlier. However, as any interactions with moisture happen on the cell level we focus in particular on multi-scale modelling and how this resolves wood-moisture interactions.

Theories for polymeric gels have existed for many years using coupled-stress diffusion models, however realising them within finite elements is a relatively new field, with most developments happening within the last decade. It is thought that this area of modelling could provide a path to resolving wood-water interactions in a complete thermodynamic framework, including both poroelastic and viscoelastic swelling of the polymers upon interaction with the environment. As such it would make a good addition to future multi-scale modelling.

1.3.1 Wood Modelling Review

As a complex multi-scale, viscoelastic material, timber requires a complex multi-physics approach to modelling. In naturally occurring environmental conditions the material is exposed to stresses from changing moisture content and from external mechanical loading. These two effects are coupled processes which, along with viscoelastic deformation of the molecular chains of the cell wall polymers, leads to a three way coupled system. Harrington suggested that the coupling between the stress and concentration fields would make a good addition within a multi-scale modelling context [48].

In addition to the viscoelastic processes, the breakdown of internal hydrogen bonds in response to internal moisture content, leading to a change of internal stiffness and time dependent relaxation behaviour, brings an additional variable that needs to be taken into account. Creating a model to satisfy these physical processes will allow future development of life cycle analysis of timber structures, potentially increasing the usability of timber as an environmentally friendly construction material.

Dubois et al [28] present a model of linearly viscoelastic, mechano-sorptive behaviour and effects during moisture changes within timber, simulating a hygro-lock effect using Kelvin-Voigt cells in series and taking into account external loading and moisture content history. The process takes into account both softening and hardening of the material with changing moisture content. Fortino et al [42] describe a 3D couple moisture-stress analysis model, implemented using Abaqus, for timber structures at the macroscopic level, taking into account viscoelastic and mechanosorptive creep behaviour with the corresponding coefficients calculated from fitting experimental results. However, the model does not take into account different cell properties, rather it distinguishes between the tangential and radial directions of growth and assigns orthotropic properties dependent on whether the earlywood and latewood cells are either aligned in series or parallel. This orthotropic macroscale behaviour does not model the complex cell wall behaviour and interactions with the environment and the coupling between the stress and diffusion on the length scale of the constituent polymer mixture. Similar to the work presented in this thesis, the model is formulated in terms of Helmholtz free energy, at constant climatic temperature.

Bader et al [7] formulated a poromechanical model of a RVE (representative volume element) using a four stage homogenization scheme, taking into account the properties of several scales of observation. A periodic honeycomb structure is represented using the unit cell method. Eitelberger et al [30] developed a model for the prediction of linear viscoelastic properties of softwood using multi-scale homogenization, theorising that the orthotropic creep behaviour at the macroscale can be derived from the molecular behaviour of the isotropic network of polymers (lignin and hemicelluloses) at the cell wall level. Several multi-scale approaches have described the cell wall material as an isotropic matrix within which crystalline fibres are embedded, containing lignin, hemicellulose, mixing with a mixture of water and extractives, where the water increases the ability to take compression loads but contributes minimally to tensile loading [7,7,26,30,31,40]. The limitation of poromechanical description of the cell wall polymers is that the viscoelastic processes are not described. These contribute to both limiting the diffusion and leading to internal re-arrangement of the cell structure, leading to deformation changes on the macro-scale. As such a multi-scale model is required that also incorporates viscoelastic processes within the polymers in a coupled system.

Flores et al [40] formulated a large strain, multi-scale model to investigate the irreversible non-linear response of the wood cell wall using Finite Elements and homogenization to create an RVE through which investigations are carried out for the viscous relaxation process. The amorphous polymers within the wood cell wall polymer matrix, hemicelluloses and lignin, are modelled with a viscoelastic/viscoplastic material description, where the viscoelastic behaviour is captured using a Maxwell model. Numerical studies were carried out to obtain stress-strain relationships to look at viscous relaxation and recovery mechanisms whilst under loading. The model does not account for changes in moisture content however, and as such is of limited use when describing wood-water interactions and the stress created within due to sorption processes. Joffre et al [62] use the finite element method, along with x-ray micro-computed tomography, to determine the hygroexpansion properties of a single wood cell, accounting for large deformations due to large changes in humidity.

To fully understand and predict the mechanics of wood under varying climatic conditions, an approach is needed to model the coupled relationship between stress, diffusion and viscoelastic relaxation within the isotropic matrix of cell wall polymers and their molecular behaviour when in contact with water. This will allow the capture of each process and the complex interaction between each as the polymers soften and undergo the glass transition. Ideally the model will interact with the environment and have the capability to numerically simulate complex problems and geometries.

1.3.2 Polymeric Gel Modelling

When considering mechano-sorptive phenomena in wood cell wall polymers, the problem can be separated into two physical processes: the conformational change of the polymer network under stress and the migration of water vapour through the polymer network. In wood cell wall polymers these processes have both an elastic and a viscoelastic contribution and thus combined theories of viscoelasticity and poroelasticity are required to capture phenomena. Within the polymer network, the term poroelasticity can be thought of as processes in which viscoelastic processes have either not yet started, or have happened almost immediately. In both these cases the rate of the solvent migration is determined by the coefficient of diffusion for the network. The viscoelastic processes occur when the network undergoes viscoelastic deformation at a similar rate to the time of diffusion, thus viscoelasticity of the network controls the rate of adsorption or desorption.

An approach is required for modelling these coupled processes within the cell wall polymer network. As such we can treat the polymer matrix as a simple isotropic polymeric gel as a starting point to more complex multi-scale models of wood cell wall polymers within a fully coupled, multi-physics framework of modelling. An elastomeric gel is defined as a cross-linked network of polymers which undergoes swelling response when interacting with a solvent, exhibiting the same behaviour as the polymers within the wood cell wall. Biot developed a generalised theory of poroviscoelasticity that could be applied to both heat and diffusion problems [15,16] and it has been further developed to apply specifically to the case of elastomeric gels [23,58–60]. Some of these theories have extended to the use of a free energy function to incorporate the changes to the free energy function during the mixing process between the polymer and solvent.

Hu et al [60] present a theory of coupled viscoelasticity and poroelasticity in elastomeric gels. The theory accounts for both diffusion-limited and viscoelasticity-limited fluid migration through gels. Dealing with engineering strains, the theory presents both homogeneous and inhomogeneous states of swelling and describes a theory of different stages of material behaviour, i.e. glassy or rubbery, as will be discussed further on. The description is taken further with a full constitutive model within a standard linear elastic solid rheological model set-up. Coupling between the stress and the diffusion is achieved by assuming incompressibility of the molecular chains within the network, assuming that any change in volume can be accounted for by changes in the solvent content within the network as well as configuration changes between the polymer chains. The incoming solvent is also assumed to be incompressible. This is a fair assumption, as when dealing with small deformations and correspondingly small changes in environmental conditions at a stable temperature, the forces involved are small enough to be of no concern to the polymer and solvent compounds on the molecular level.

Several theories apply to large deformation problems [23, 46, 58, 59]. Hong et al [58] implemented a coupled swelling and diffusion model within the finite element package ABAQUS for a hyperelastic solid for inhomogeneous states of swelling. In this case the deformation and concentration were treated as two separate fields of material behaviour. The coupling was achieved by assuming an incompressibility condition within the heat of mixing term. This is accounted for in the free energy function by Flory and Rehner [41], allowing for the associated changes in configurational entropy in the mixture and the polymer network, presenting a thorough thermodynamic framework. However, this finite element model does not include viscoelastic processes related to solvent migration and thus cannot describe viscoelastic deformation and/or viscoelastically controlled solvent migration within polymeric gel networks. Chester et al [23] formulated a large strain coupled theory for isotropic elastomeric materials, in which they provide some numerical examples solved using a finite difference scheme for both a 3 dimensional free-swelling problem and several one-dimensional transient problems.

The theory of molecular diffusion-deformation has been theorised for case II diffusion [46] in which a polymer undergoes a phase transition from the glassy to the rubbery state and exhibiting sigmoidal sorption isotherms, as is the case with wood cell wall polymers. The constitutive model is based upon a standard linear solid rheological model. The switch between the glassy and rubbery states within the polymer are presented as a drop in the viscosity of the dashpot within the rheological model. The viscosity is therefore given as a function of the concentration field within the polymer network.

To build on these theories, the intention is to create a fully coupled viscoelastic coupled stress and diffusion model as a basis on which further multi-scale modelling of wood can be carried out. Currently there are no finite element models describing both the poroelastic and viscoelastic behaviour within one fully coupled framework for elastomeric gels. Thus the proposed model will have wider applications than just the theory of wood-water interactions. The model will also be set up for future development into hyperelastic material problems and extension to include heat of mixing terms, accounting for the entropy changes within the solvent mixture and polymer network. As such, the problem is solved for wood cells first, looking in detail at the small strain theory [60] and formulate this as a model for predicting the mechano-sorptive behaviour of the wood polymer network.

1.3.3 Conclusions of Modelling Review

The model proposed in this thesis fills a gap that exists in both the field of multi-scale modelling of wood and the field of polymeric gel modelling. A polymeric gel is modelled within a fully coupled finite element framework, for concurrent processes of poroelasticity and viscoelasticity and as such represents a step forward in this relatively new field of modelling. This should provide the framework from which the three key stages of material behaviour can be described within cell wall polymers, as outlined in the previous section. Previous models within this field have so far been limited to poroelastic phenomena, either in a finite element or finite difference framework [23, 58].

In terms of wood modelling, the model serves as a potential tool within multi-scale modelling of the wood cell wall. Currently, multi-scale models for wood are limited to the poroelastic processes when dealing with the length scales on the cell wall level i.e. the amorphous polymer network. Viscoelasticity has been implemented at higher length scales for wood [28,42]. However, this implementation of a fully coupled model describing the behaviour of the constituent polymers will enable the solution to more complex problems on the cell wall level. By incorporating the behaviour from the basic constituent polymers and their interactions with the surrounding environment, processes such as viscoelastically-limited diffusion, as described in the previous section, can be implemented within a multi-scale framework. This could lead to predictions of moisture induced warping based upon the cell wall properties of a particular specimen, the arrangement of the wood cells (i.e. earlywood and latewood) and the environmental conditions the specimen is exposed to.

Chapter 2

Gel Model Theory

In this Chapter, the formulation and subsequent implementation of a polymeric gel model is discussed. In a similar manner to Hu et al [60], concurrent processes of poroelasticity and viscoelasticity are resolved. This formulation allows a link to be made between moisture transport, poroelastic deformation and viscoelastic deformation to create a model which can describe both poroelastically limited diffusion (i.e. Fickian processes) and viscoelastically limited diffusion.

2.1 The Chemical Potential of the Environment

Before discussing the implementation of the model, it is important to examine the chemistry of the interaction between the environment and the wood polymers. This is important to the understanding of the model description, where the driving force behind the moisture transport is the gradient of the chemical potential. Thus the derivation of the environmental chemical potential is described in detail.

Initially a closed system is considered, containing solid cellulose, bound water, dry air and water vapour. The amount of each substance can be accounted for by its number of moles, with n_a, n_v, n_b and n_c as the number of moles of dry air, water vapour, bound water and cellulose respectively, with total number of moles, n_t, defined as:

$$n_t = n_a + n_v + n_b + n_c \tag{2.1}$$

The number of moles of each substance can then be separated into their respective molar fractions, χ, as follows:

$$\chi_a = \frac{n_a}{n_t}\ ; \quad \chi_v = \frac{n_v}{n_t}\ ; \quad \chi_b = \frac{n_b}{n_t}\ ; \quad \chi_c = \frac{n_c}{n_t}, \tag{2.2}$$

where the total of the molar fractions is equal to unity (Eq. (2.3)).

$$\chi_t = \chi_a + \chi_v + \chi_b + \chi_c = 1 \tag{2.3}$$

Assuming the number of moles of cellulose, n_c, remains constant, exchange of the solvent is induced by altering the water vapour mixture; increasing/decreasing the number of water vapour moles, n_v, in the system, whilst also keeping the number of moles of dry air, n_a, constant. This change in the number of moles of water vapour will cause adsorption/desorption where the solid cellulose will adsorb or desorb some water vapour, in the form of bound water, until equilibrium is reached within the system.

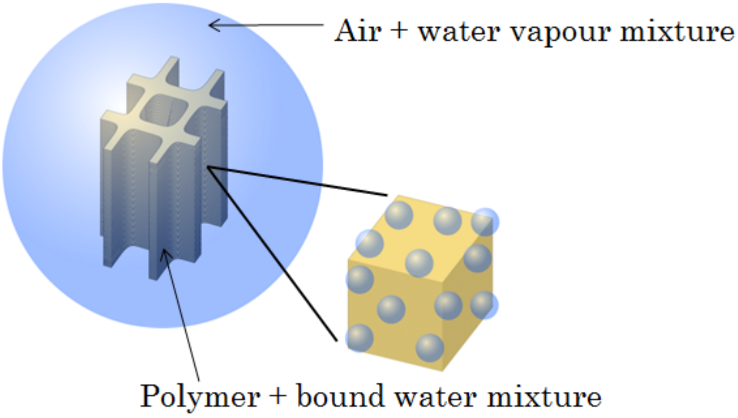

Figure 2.1: Left: Wood cell in a small environment of water vapour and air mixture (transparent blue). Right: A small cube of the cell wall with water molecules that are now bound to the polymer matrix.

In this case the environment is assumed infinitely larger than the solid cellulose sample, i.e. $\chi_a + \chi_v >> \chi_b + \chi_c$. In this infinitely bigger environment, any exchange of water vapour molecules with the cellulose, will not effect any change upon the molar fraction between dry air, χ_a, and the water vapour, χ_v. Thus chemical equilibrium will be reached when the conditions within the sample are the same as the conditions within the environment, without any need to take into account the entropy of mixing. Again the number of moles of cellulose is constant.

The dry air and water vapour mixture in the environment can be assumed to be an ideal gas and Raoult's law can be applied, where the partial vapour pressure of each component in an ideal mixture is equal to the vapour pressure of the pure component multiplied by it's mole fraction in the mixture.

The environment can be formulated in terms of partial pressure, p_p, where the partial pressure is the hypothetical pressure of a gas (in this case water vapour) if it alone occupies the volume of the mixture at the same temperature. The partial pressure of the water vapour can be related to both quantity, n number of moles, and volume, V, of the gas as follows:

$$p_p = \frac{p_v}{p_t} = \frac{n_v}{n_t} = \frac{V_v}{V_t} \tag{2.4}$$

where p_t, according to Dalton's Law, is the total pressure of all gases within the mixture, in this case dry air, p_a, and water vapour, p_v.

$$p_t = p_a + p_v \tag{2.5}$$

The environment can then be formulated in terms of Gibb's free energy per mole, $\overline{G}$, as a function of both temperature and pressure, using the pressure ratio, p/p_0, where p_0 is the saturation vapour pressure at a given temperature. The gas constant, R, is given as 8.314 J $K^{-1}mol^{-1}$ and the temperature, T, is given in Kelvin.

$$\overline{G}(T,p) = \overline{G}_0(T) + RTln\left(\frac{p}{p_0}\right) \tag{2.6}$$

In the case of wood polymer sorption, the Gibb's free energy can be formulated as a function of only pressure, assuming that the sample is undergoing adsorption in isothermal conditions. This is necessary as the gel model if formulated in terms of Helmholtz free energy for isothermal conditions. However Gibb's free energy has been regularly used to describe the conditions for wood moisture transport, even under isothermal conditions [50, 95, 98]

$$\overline{G}(p) = \overline{G}_0 + RTln\left(\frac{p}{p_0}\right) \tag{2.7}$$

The Gibb's free energy per mole is normally written as the chemical potential [98], which is the partial molar Gibbs free energy:

$$\mu_e = \mu_0 + RTln\left(\frac{p}{p_0}\right) \tag{2.8}$$

where μ_e is the chemical potential of the the environment. In order for the environment to be in equilibrium, the chemical potential of the water vapour, μ_v, and the inert gases that constitute air, μ_a, must be equal.

This can be related to sorption experiments, which describe the boundary in terms of the relative humidity (i.e. water vapour content) of the air, in a range from 0% to 100%. The relative humidity, RH, is defined as the ratio of the partial vapour pressure in the air to the saturated vapour pressure of the air, expressed as a percentage, RH% [95]. It can also be expressed as a ratio of the absolute humidity in the air to the absolute humidity at saturation [95].

$$RH\% = \left(\frac{p}{p_0}\right) \times 100 \tag{2.9}$$

Alternatively the chemical potential can be simply described as the ratio of the current relative humidity percentage (RH%) to the relative humidity at saturation vapour pressure (100% RH) [95]:

$$\mu_e = \mu_0 + RTln\left(\frac{RH\%}{100}\right), \tag{2.10}$$

where μ_0 is the chemical potential per mole of liquid water at 1 atm. It is this final equation that is used to formulate the chemical potential conditions on the boundary of the sample. This is done for simplicity of comparison to experimental work on sorption behaviour of wood and other lignocellulosic material, where the equilibrium moisture contents obtained are often attributed to a particular relative humidity as opposed a water vapour pressure [45, 51–54, 115, 116].

2.2 Gel Model Description

Taking the same approach as Hu et al [60], the mixture of wood cell wall polymers (amorphous cellulose, hemicelluloses and lignins) is formulated in a poroelastic and viscoelastic framework. The poroelastic behaviour is caused by the migration of the solvent into the polymer network, in this case water vapour entering the amorphous polymer matrix. The viscoelastic behaviour is caused by the conformational change of the polymer network, i.e. relaxation of a hydrogen bond dominated network through bond stretching and/or molecular slippage between polymer chains through the breakage and reformulation of an intricate and complex network of intramolecular hydrogen bonds between molecular chains.

The chosen rheological model is a Zener model, shown in Figure 2.2. The advantage of the Zener model is that it can capture both creep and relaxation behaviour. The elastic spring α captures the elastic deformation whilst the spring-dashpot in series β captures the viscoelastic deformation. The full constitutive implementation of the model is described further on in this Chapter.

Describing the poroelastic and viscoelastic behaviour as two parallel processes allows the model to resolve poroelasticity and viscoelasticity as concurrent processes. This is vitally important to the ability of the model to capture viscoelastic rate limited diffusion as discussed in Chapter 1 and to switch freely between poroelastic or viscoelastically limited diffusion depending upon the material properties assigned to each spring.

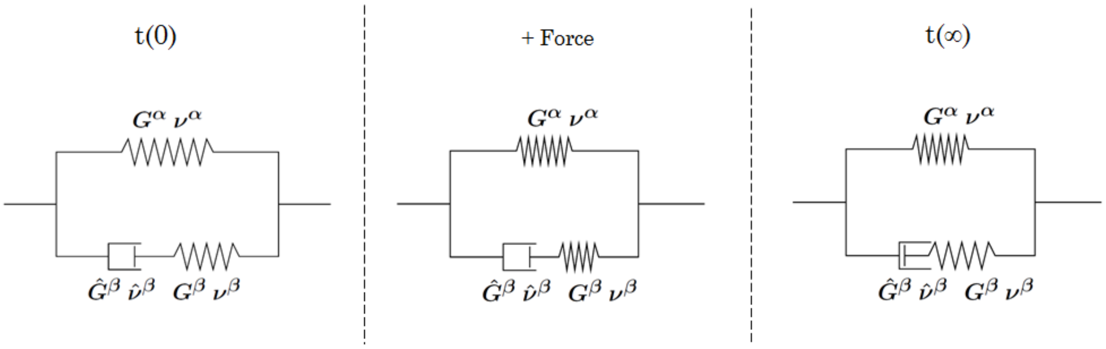

Figure 2.2: The rheological model represented as a spring, α, in parallel with a spring/dashpot, $\beta/\hat{\beta}$, in series. Initially the load is taken up by both springs, and then over time the load in spring β is relaxed as the dashpot, $\hat{\beta}$, is compressed. This happens until the spring is completely relaxed and the load is taken up entirely by spring α. At this point the system is in equilibrium with the environment.

It is also important to remember that Fickian diffusion occurs when the poroelastic behaviour dominates. Viscoelastic rate limited diffusion occurs when the time taken for viscoelastic diffusion is similar to the time taken for Fickian diffusion, as discussed in Chapter 1, where the Deborah number, Eq. (1.2), gives a guide to which process is likely to dominate.

In a reference equilibrium state, the polymer network is under no stress, with concentration of water molecules within the cell wall, C_0, and a corresponding chemical potential of the solvent within the gel, μ_s. The system is then subjected to a mechanical force and submerged in an environment of chemical potential, μ_e, representing the chemical potential of the surrounding environment.

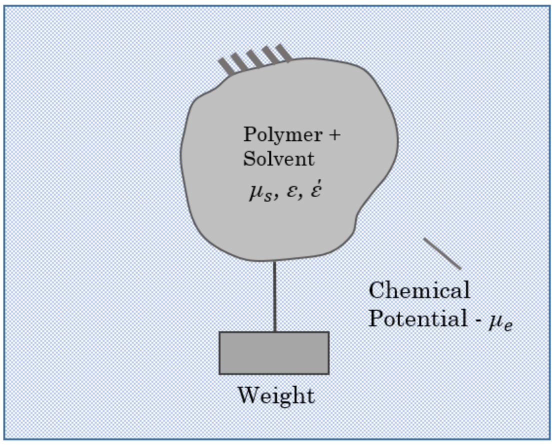

Figure 2.3: A volume of polymer subjected to a mechanical force within an environment of free energy μ_e. The polymer has an internal chemical potential of μ_s which is influenced by the mechanical forces subjected to the volume by the weight. The weight represents the potential energy of any forces acting upon the volume. Adapted from [60].

The problem can be described as a thermodynamic system, where W is the Helmholtz free energy of the polymer network. It has state variables strain ε_{ij} and chemical potential μ and a time dependent internal variable $\hat{\varepsilon}_{ij}$. The potential energy of the deformation is given as $\sigma_{ij}\delta\varepsilon_{ij}$ and describes the mechanical component. The free energy of the solvent flux within the gel is given by subtracting the free energy of the environment from the free energy of the solvent within the gel $(\mu_e - \mu_s)\delta C$. Following arguments from [46], starting from the balance of entropy and considering isothermal conditions with a homogeneous temperature distribution, and considering inhomogeneous concentration of solvent, then the change of Helmholtz free energy of the mixture results in the reduced entropy inequality

$$\delta W \; - \; \sigma_{ij}\delta\varepsilon_{ij} \; - \; (\mu_e - \mu_s)\delta C \; + \; \frac{\partial \mu_s}{\partial x_i}\delta J_i \; \leq \; 0. \tag{2.11}$$

The Helmholtz free energy of the polymer network, W, is a function of the strain, ε_{ij}, the relative concentration of solvent molecules $(C - C_0)$, and the internal variable, $\hat{\varepsilon}_{ij}$,

$$W(\varepsilon_{ij}, \hat{\varepsilon}_{ij}, C). \tag{2.12}$$

In the last term of Eq. (2.11), J_i expresses solvent flux, and allows a size dependent and time dependent overall mixture response to be considered. Note that the solvent flux J_i is relative to the matrix. This last term expresses the tendency of a solvent to increase mixing entropy when material points are in close proximity to each other. It is important to note that, in the absence of any external loading, when $\mu_e = \mu_s$ and the incremental change in the flux, δJ_i is equal to zero, the gel will be homogeneous and in equilibrium with the environment. The constitutive equation for flux will be discussed in Section 2.2.3.

The individual constituent polymer chains and water molecules (once in their liquid bound form) are assumed to be incompressible [58–60]. This is not to be confused with assuming an incompressible material, rather the individual molecular chains will not compress and any change in volume can be accounted for as a change in the concentration of solvent within the sample. Given that the mass of the polymer network will remain constant, any change in strain can be attributed to a change in the concentration of solvent molecules within the gel, where Ω is the volume per water molecule in it's liquid state ($18\text{cm}^3\text{mol}^{-1}$).

$$\varepsilon_{kk} = (C - C_0)\Omega. \tag{2.13}$$

By inserting Eq. (2.13) into Eq. (2.11), the change in Helmholtz free energy of the polymer network can now be described as follows,

$$\delta W \; - \; \sigma_{ij}\delta\varepsilon_{ij} \; - \; (\mu_e - \mu_s)\frac{\delta\varepsilon_{kk}}{\Omega} + \frac{\partial \mu_s}{\partial x_i}\delta J_i \; \leq \; 0. \tag{2.14}$$

Thus the Helmholtz free energy of the polymer network is a function of only two field variables, the strain, ε_{ij}, and the time dependent internal variable representing viscoelastic strain, $\hat{\varepsilon}_{ij}$,

$$W(\varepsilon_{ij}, \hat{\varepsilon}_{ij}). \tag{2.15}$$

2.2.1 Viscoelastic Response

Rearranging Eq. (2.14), the change of free energy is expressed as:

$$\left(\frac{\partial W}{\partial \varepsilon_{ij}} - \frac{\mu_e - \mu_s}{\Omega}\delta_{ij} - \sigma_{ij}\right)\delta\varepsilon_{ij} + \frac{\partial W}{\partial \hat{\varepsilon}_{ij}}\delta\hat{\varepsilon}_{ij} + \frac{\partial \mu_s}{\partial x_i}\delta J_i \leq 0, \tag{2.16}$$

where δ_{ij} is the Kronecker delta. The second term $\left(\frac{\partial W}{\partial \hat{\varepsilon}_{ij}}\delta\hat{\varepsilon}_{ij}\right)$ enables the size-independent viscous response due to the rate of the chemical reactions to be taken into account. The chemical reactions referred to are the internal rearrangement of the hydrogen bonds within the polymer networks typically found within wood and other ligno-cellulosic materials (as discussed in Chapter 1). The rate of the chemical reactions is the rate at which the internal network of intra-molecular hydrogen bonds re-configure to reduce the stress within the material (i.e. relaxation).

This can now be applied to a standard linear solid rheological model (also known as a Zener spring-dashpot model), shown in Figure 2.2. For changes of the field variable $\delta\varepsilon_{ij}$ and the internal variable $\delta\hat{\varepsilon}_{ij}$ the resulting relationship is shown in Eq. (2.16).

If the dashpot is assumed to be rigid (i.e. the dashpot cannot compress and relax the strain due to an infinitely high dashpot shear modulus/viscosity, $\hat{G}^{\beta}$), and the gel is in a homogeneous state, the elastic springs control the process, and Eq. (2.16) can be simplified to,

$$\frac{\partial W}{\partial \varepsilon_{ij}} = \frac{\mu_e - \mu_s}{\Omega}\delta_{ij} + \sigma_{ij}, \tag{2.17}$$

representing an elastic and fully reversible deformation. However, if the dashpot is assumed rigid and the gel is allowed to evolve through an inhomogeneous state, the gel will behave poroelastically and Eq. (2.16) can be modified to account for the change in the solvent flux as follows:

$$\frac{\partial W}{\partial \varepsilon_{ij}} - \frac{\mu_e - \mu_s}{\Omega}\delta_{ij} - \sigma_{ij} + \frac{\partial \mu_s}{\partial x_i}\delta J_i \leq 0, \tag{2.18}$$

When spring α is held constant, and spring β and the dashpot are free to move, Eq. (2.16) can be simplified to,

$$\left(\frac{\partial W}{\partial \hat{\varepsilon}_{ij}}\delta\hat{\varepsilon}_{ij} + \frac{\partial \mu_s}{\partial x_i}\delta J_i\right) \leq 0. \tag{2.19}$$

At this point a stronger argument can be made, noting that the characteristic length of the polymer chains (i.e. the length of the micro structure) is much smaller than the flux gradient and therefore the rate of chemical reaction depends only on the concentration, thus

$$\frac{\partial W}{\partial \hat{\varepsilon}_{i,j}}\delta\hat{\varepsilon}_{ij} \leq 0, \tag{2.20}$$

and

$$\frac{\partial \mu_s}{\partial x_i}\delta J_i \leq 0. \tag{2.21}$$

Therefore the elastic deformation and time dependent viscoelastic deformation can be treated separately. Moreover, note that Eq. (2.21) express the well-known fact, that solvent flux is from higher to lower concentration.

2.2.2 Physical Model for Matrix Chemo-Mechanical Response

The stresses in the two springs, from the rheological model, are defined using a hookean description, where springs α and β deform under elastic loading and the stress in spring β is dependent on the current strain in the dashpot, $\hat{\varepsilon}$. The hookean description of each spring is given as follows:

$$\sigma = K\, \varepsilon_{kk}\delta_{ij}\; + 2G\varepsilon_{ij} \tag{2.22}$$

where the bulk modulus is $K = 2G(1+\nu)/3(1-\nu)$ and G is the shear modulus of the springs. Formulating in terms of the energy within each spring, (W^{α} and W^{β}), the energy within the two springs of the rheological model yields:

$$W^{\alpha} = G^{\alpha}\left[{\varepsilon_{ij}}^2 + \frac{\nu^{\alpha}}{1-2\nu^{\alpha}}{\varepsilon_{kk}}^2\right] \tag{2.23}$$

and

$$W^{\beta} = G^{\beta}\left[(\varepsilon_{ij} - \hat{\varepsilon}_{ij})^2 + \frac{\nu^{\beta}}{1-2\nu^{\beta}}(\varepsilon_{kk} - \hat{\varepsilon}_{kk})^2\right]. \tag{2.24}$$

Combining Eqns. (2.23) and (2.24) and differentiating with respect to the strain yields the following:

$$\frac{\partial W}{\partial \varepsilon_{ij}} = 2G^{\alpha}\left[\varepsilon_{ij} + \frac{\nu^{\alpha}}{1-2\nu^{\alpha}}\,\varepsilon_{kk}\right] + 2G^{\beta}\left[(\varepsilon_{ij} - \hat{\varepsilon}_{ij}) + \frac{\nu^{\beta}}{1-2\nu^{\beta}}(\varepsilon_{kk} - \hat{\varepsilon}_{kk})\right]. \tag{2.25}$$

The rheological model requires the two springs to equilibriate with the applied loads. Inserting Eq. 2.25 into Eq. 2.17 gives a relationship for the stress within the system, with contributions from the springs on the right hand side.

$$\sigma_{ij} + \frac{\mu_e - \mu_s}{\Omega}\delta_{ij} = 2G^{\alpha}\left[\varepsilon_{ij} + \frac{\nu^{\alpha}}{1-2\nu^{\alpha}}\,\varepsilon_{kk}\right] + 2G^{\beta}\left[(\varepsilon_{ij} - \hat{\varepsilon}_{ij}) + \frac{\nu^{\beta}}{1-2\nu^{\beta}}(\varepsilon_{kk} - \hat{\varepsilon}_{kk})\right] \tag{2.26}$$

In this case we simplify Eq. (2.26), taking the total stress of the system, as defined within the Zener rheological model, as follows:

$$\sigma_{ij} = \sigma^{\alpha}_{ij} + \sigma^{\beta}_{ij} + \hat{\sigma}^{\beta}_{ij}, \tag{2.27}$$

where σ^{α}_{ij} is the stress given in the elastic contribution, i.e. spring α. The viscoelastic stress contribution is given by σ^{β}_{ij}, which includes the behaviour of the dashpot and the spring β. Finally the stress due to the environmental conditions (i.e. the change in the chemical potential, μ) is given as $\hat{\sigma}^{\beta}_{ij}$. All three relationships are defined as follows:

$$\sigma_{ij}^{\alpha} = 2G^{\alpha}\left[\varepsilon_{ij} + \frac{\nu^{\alpha}}{1-2\nu^{\alpha}}\,\varepsilon_{kk}\right], \tag{2.28}$$

$$\sigma_{ij}^{\beta} = 2G^{\beta}\left[(\varepsilon_{ij} - \hat{\varepsilon}_{ij}) + \frac{\nu^{\beta}}{1-2\nu^{\beta}}(\varepsilon_{kk} - \hat{\varepsilon}_{kk})\right], \tag{2.29}$$

$$\hat{\sigma}_{ij}^{\beta} = \frac{\mu_e - \mu_s}{\Omega}\delta_{ij}. \tag{2.30}$$

The dashpot is modelled as an isotropic linearly viscous material, and the evolution of the dashpot strain, $\hat{\varepsilon}$ with respect to time is defined as follows:

$$\frac{\partial \hat{\varepsilon}_{ij}}{\partial t} = \frac{1}{2\hat{G}^{\beta}}\left[{\sigma_{ij}}^{\beta} - \frac{\hat{\nu}^{\beta}}{1+\hat{\nu}^{\beta}}\,{\sigma_{kk}}^{\beta}\right], \tag{2.31}$$

where the time of viscoelastic relaxation, τ_v, is determined by the ratio of the shear modulus in the spring, G^{β}, and the dashpot, $\hat{G}^{\beta}$, respectively.

$$\tau_v = \frac{\hat{G}^{\beta}}{G^{\beta}}. \tag{2.32}$$

2.2.3 Physical Model for the Solvent Flux

The diffusion of solvent molecules through the gel is kinetically described through non-Fickian law, as result of present viscous terms, where the driving force behind the concentration is the chemical potential field. The chemical potential field has been commonly used as the driving force behind diffusion in wood-water interactions [95,98], and provides the best thermodynamic basis with which to resolve the flux.

$$J_i = -\left(\frac{\kappa}{\eta\Omega^2}\right)\frac{\partial \mu_s}{\partial x_i}, \tag{2.33}$$

where κ is the permeability of the polymer network and η is the viscosity of the solvent.

2.2.4 Conservation laws

In the following approach, a Lagrangian description for the mixture deformation, and as a result the conservation of linear momentum is given as follows,

$$\frac{\partial \sigma_{ij}}{\partial x_i} = 0, \tag{2.34}$$

where the body and inertial forces are neglected. Note that stress $\sigma_{ij} \equiv \sigma_{ji}$ is symmetric and the conservation of angular momentum is automatically satisfied.

The rate of change of the conservation of the solvent is defined as:

$$\frac{\partial C}{\partial t} = -\left(\frac{\kappa}{\eta\Omega^2}\right)\frac{\partial^2\mu_s}{\partial x_i\partial x_i}, \tag{2.35}$$

where it is assumed that the pores are dilute and non-connected and that the gravity terms are neglected, thus no pressure driven terms are present. Combining Eq. (2.35) with the incompressibility condition (Eq. (2.13)), yields a relationship for the evolution of the volumetric strain over time due to the influx of solvent molecules,

$$\frac{\partial \varepsilon_{kk}}{\partial t} = -\left(\frac{\kappa}{\eta\Omega}\right)\frac{\partial^2\mu_s}{\partial x_i\partial x_i}. \tag{2.36}$$

2.2.5 Fickian and non-Fickian Diffusion

The rate of diffusion of the solvent, which is assumed to be incompressible, through the gel is controlled by the permeability of the polymeric gel, viscosity of the solvent and the properties of the two springs (κ, η_w and G, ν respectively). The effective diffusivity is given as follows [60]:

$$D = \frac{2\kappa}{\eta_w}\left(\frac{1-\nu^\alpha}{1-2\nu^\alpha}G^\alpha + \frac{1-\nu^\beta}{1-2\nu^\beta}G^\beta\right). \tag{2.37}$$

When combined with the softening of the polymers in both springs, discussed further on in the thesis, this will allow a changing effective diffusivity due to the softening of the polymers as this in reality is not a constant across all moisture contents. Thus the rate of the solvent uptake will be regarded as a function of the material stiffness from the elastic contributions of the spring and also the viscoelastic relaxation processes of the internal variable in Eq. (2.31). The permeability of the polymer will remain a constant for now as discussed in Section (1.2.2).

The two time scales, diffusivity and the viscoelastic relaxation time (Eqns. (2.37) and (2.32) respectively), describe the time over which the poroelastic and viscoelastic relaxation times occur. The time of poroelastic diffusion is given as $t = \mathrm{L}^2/D$ and is length dependent. If a sample of very small length, L, is considered where the time of relaxation, τ_v, is far longer than the time of poroelastic diffusion, the observed behaviour will be poroelastic. Over the short length the viscoelastic relaxation process has not yet started and as such does not take effect. However, if the small length is considered again, but in this case the relaxation time is very small, for instance wood polymers in their rubbery state where relaxation happens extremely fast, the time of viscoelastic relaxation may not be observed.

Condition	**Observed Behaviour**
$t <<< \tau_v$	The sample undergoes poroelastic relaxation, with the deformation controlled by both springs, α and β. The viscoelastic process has not yet started to take effect.
$t >>> \tau_v$	The sample undergoes viscoelastic deformation extemely quickly and behaves poroelastically with the deformation controlled by spring α only. The dashpot is depressed throughout
$t \approx \tau_v$	The sample undergoes viscoelastically limited solvent migration

Table 2.1: Summary of the conditions within which the gel model operates, where τ_v is the time of viscoelastic deformation and t is the time taken for diffusion in poromechanical conditions.

Where the time of viscoelastic relaxation is similar to the time of diffusion, viscoelastically limited solvent migration occurs. In this case there are two process at play. Firstly the diffusion of solvent through the sample and secondly the slow process rearrangement of molecules within the polymer network. This rearrangement of the molecular structure when under stress allows the polymer to slowly adsorb more solvent. The final mass of adsorbed water may be the same as the case where $t >>> \tau_v$, however the slower rate of molecular rearrangement limits the rate at which the solvent can be adsorbed by the network.

Furthermore, the observed behaviour is also dependent upon the length of the sample. If for instance the sample is very long, the same rate of relaxation and diffusion may interact differently. However, the focus of this thesis is on the cell wall level or smaller, and as such the focus will be on length scales between nanometres and micrometres.

2.3 3D Finite Element Model

The theory of poroelasticity in hydrogels has been applied using finite elements [69], although without the addition of viscoelasticity. The chemical potential and displacement field are treated as two independent field variables. In this model, a similar approach is taken to define the two field variables, although with the addition of an internal field variable to account for viscoelastic deformation, similar to [60].

The model is discretised in space using the finite element method. The three fields that are independently approximated are the displacements $\mathbf{u}^h$, the chemical potential μ^h and the dashpot strain $\hat{\varepsilon}^h$. The displacement and chemical potential are the two primary fields, with an additional internal variable of the dashpot strain, which can be considered on the element level, although in this case is independently approximated. The reasons for this are outlined further on in this section, when describing the approximation of the dashpot strains.

2.3.1 Approximation Base

The model presented up till this point in Chapter 2 achieves a coupling through the strain terms, where the chemical potential field and the displacement field are fully coupled through the strains as defined by the incompressiblity condition, Eq. (2.13). Implementing this condition allows the flux field and the displacement field to be approximated using the strains.

This has significance when approximating the problem in a finite element model. For instance, if the problem is dealt with using linear elements, then the displacement field would yield constant strains across each element, due to the strains being the derivative of the displacements. However, the chemical potential flux field would yield linear strains across each element, leading to stability issues.

The use of hierarchical base functions allows higher order polynomials of different orders to be applied to each field. For instance, using a 2nd degree polynomial for the displacement field, obtaining quadratic approximation of the displacements across each element, would yield a linear approximation of the strain across each element. If at the same time, there remains a linear approximation for the chemical potential flux, a linear strain would also be obtained across each element. This ensures stability between the two primary fields.

Approximation Using Hierarchical Basis Functions

In 3D, the hierarchical basis functions are applied to the nodes, edges, faces and volumes, demonstrated in Figure 2.4. $\mathcal{H}^1(V)$ approximation consists of piecewise continuous polynomials of arbitrary order (2nd order or higher). $L^2(V)$ approximation consists of piecewise discontinuous polynomials. For $\mathcal{H}^1(V)$ space, the approximation functions are constructed on the nodes, edges, faces and volumes. However, it is only the degrees of freedom on the edges that have physical meaning. $L^2(V)$ space approximation functions are constructed in the domain of the element (i.e. internally).

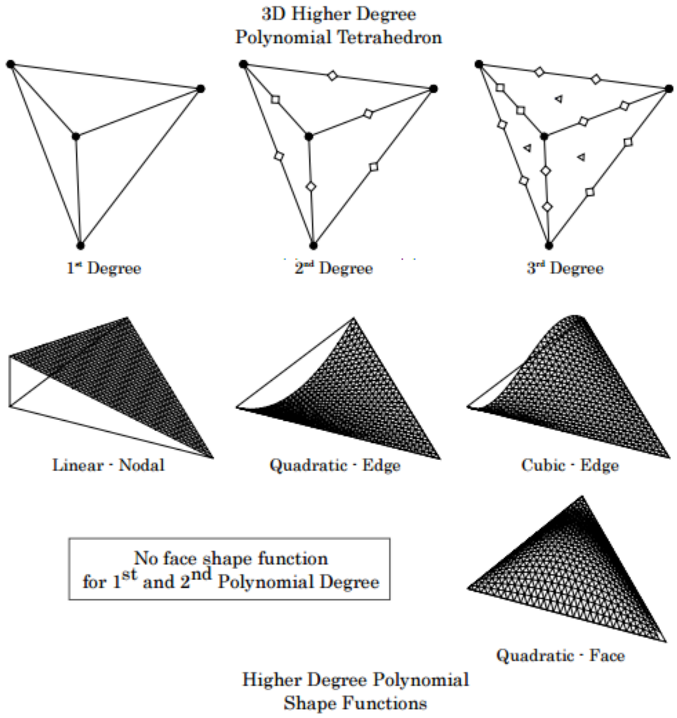

Figure 2.4: A linear tetrahedral element with 4 nodes (shown as black dots). The empty squares and triangles represent the higher order polynomial degrees of freedom, demonstrating the shape functions on the nodes, edges and shapes [99].

2.3.2 Conservation of Linear Momentum

The conservation of the linear momentum is given, in its strong form, as follows,

$$\sigma_{ij,j} = 0, \tag{2.38}$$

where body forces are neglected in this case, when dealing with small bodies.

The residual for conservation of linear momentum (Eq. (2.38)) has the following discrete weak form,

$$\mathbf{r}_\sigma = \int_{V^h} \frac{\partial \mathbf{\Phi}_i^n}{\partial x_j} \sigma_{ij}(\mathbf{u}^h, \mu^h, \hat{\varepsilon}^h)\mathrm{d}V - \int_{S_\sigma^h} \mathbf{\Phi}_i^n t_i \mathrm{d}S, \tag{2.39}$$

where $\mathbf{\Phi}^n$ are piecewise continuous polynomial base functions, that span the space of admissible variations, applied on finite elements of order $n \geq 2$, i.e. on a tetrahedron mesh $\mathcal{T}$ the base function is given as $\Phi^n \in \mathcal{P}_{\mathcal{T}}^n \subset \mathcal{H}^1(V)$. The function is piecewise continuous, i.e. $\mathcal{H}^1$ approximation, due to the presence of the gradient of deformation and as such continuity across element boundaries is enforced. V^h and S^h_σ are discretised body volume by tetrahedral and discretised body surface where tractions $\mathbf{t}$ are applied respectively. In addition, on the boundary S^h_σ, kinematic conditions, i.e. essential boundary conditions, are applied, where the displacement field is known. In this implementation essential boundary conditions are enforced in a standard procedure by eliminating rows and columns in the stiffness matrix and setting values equal to the right hand side vector.

The displacement vector is approximated as:

$$u_i^h = \sum_{j=1}^{\dim(\mathbf{\Phi}^n)} \Phi^n_{ij} q^u_{ij}, \tag{2.40}$$

where $\mathbf{q}^u$ is a vector of degrees of freedom $i = 1 \ldots 3$, the elements of the displacement vector, and $j = 1 \ldots \dim(\mathbf{\Phi})$, the number of degrees of freedom.

2.3.3 Conservation of Mass

The residual for the conservation of mass, $\mathbf{r}_\mu$, is given a semi-discrete form. The strong form of the conservation of mass is given in Eq. (2.36), recalling that the concentration, C, has been replaced by the volumetric strain, ε_{kk}, in accordance with the incompressibility condition, Eq. (2.13). The semi-discrete weak form of Eq. (2.36) is given as follows:

$$\mathbf{r}_\mu = \int_{V^h} \left(\mathbf{\Phi}^{n-1} \frac{\partial \varepsilon^h_{kk}(\mathbf{u^h})}{\partial t} - \frac{\partial \Phi^{n-1}}{\partial x_i} \Omega J_i(\mu^h) \right) \mathrm{d}V - \int_{S^h_{\nabla\mu}} \mathbf{\Phi}^{(n-1)} f \mathrm{d}S \tag{2.41}$$

where $\mathbf{\Phi}^{n-1}$ are piecewise continuous polynomial base functions, that span the space of admissible variations, applied on finite elements of order $n-1$, i.e. one order of approximation lower than the displacement field. $S^h_{\nabla\mu}$ is the discretised body surface where chemical potential, f, is applied. In addition, part of the boundary, S^h_μ, is distinguished where the chemical potential is known. Note that displacement vector, $\mathbf{u}^h$, is approximated with polynomial order n over the elements, whereas chemical potential μ^h is approximated to the order $n-1$.

The polynomial base functions on the displacement field must be set one order higher than the chemical potential flux field in an attempt to ensure stability in the solution. This is due to the volumetric strain appearing within the flux term and the derivative of the volumetric strain appearing in the mechanical deformation term within the coupled Eq. (2.14). This can cause problems during the approximation, as outlined earlier within this Section. To ensure stability between the fields, and the same approximation of the strain across the fields, the displacement field is approximated one order higher than the chemical potential field,. In this case the displacement field is approximated at order n, where $n \geq 2$.

The functions are piecewise continuous to ensure continuity across element boundaries for the chemical potential flux. The chemical potential is approximated by the same base functions, i.e.

$$\mu^h = \sum_{j=1}^{\dim(\mathbf{\Phi}^{n-1})} \Phi_j^{(n-1)} q_j^{\mu}, \tag{2.42}$$

where $\mathbf{q}^{\mu}$ is a vector of degrees of freedom.

2.3.4 Residual for the Conservation of the Dashpot Strain

The strong form of the conservation of the dashpot strain, which controls the uptake of the relaxation strain, is given in Eq. (2.31). The residual of the dashpot strain, $\mathbf{r}_{\hat{\varepsilon}}$ can be defined, in its semi-discrete form, as follows:

$$\mathbf{r}_{\hat{\varepsilon}} = \int_{V^h} \mathbf{\Psi}_{ij} \left(\frac{\partial \hat{\varepsilon}^h_{ij}}{\partial t} - 2G^{\beta} \left[\left(\varepsilon_{ij}(\mathbf{u}^h) - \hat{\varepsilon}^h_{ij} \right) + \frac{\nu^{\beta}}{1 - 2\nu^{\beta}} \left(\varepsilon_{kk}(\mathbf{u}^h) - \hat{\varepsilon}^h_{kk} \right) \delta_{ij} \right] \right) \mathrm{d}V \tag{2.43}$$

where $\mathbf{\Psi}_{ij}$ are piecewise discontinuous polynomials, i.e. on $\Psi^{n-1}_{ij,k} \in \mathcal{P}^{n-1}_{\mathcal{T}} \subset L^2(V)$. The approximation can be piecewise discontinuous, L^2, for the dashpot residual as there is no gradient requiring continuous approximation across the boundaries. The dashpot strain is approximated by:

$$\hat{\varepsilon}^h_{ij} = \sum_{k=1}^{\dim(\mathbf{\Psi}^{n-1})} \Psi_{ij,k} q^{\hat{\varepsilon}}_{ij,k}. \tag{2.44}$$

Note that approximation for the dashpot strain, $\hat{\varepsilon}^h$, is defined on each element independently, thus could be considered statically condensed on the element level, however for convenience and clarity of derivation it is shown explicitly. In the same manner as Eq. (2.41), order of approximation applied of the dashpot strain, $\hat{\varepsilon}^h$, is one lower order than is used for displacements, i.e. $n - 1$, in order to obtain a stable system of discretised equations where the displacement field is approximated at order $n \geq 2$.

As mentioned earlier, the dashpot strain is approximated explicitly. This allows potential for future h and p refinement as the Gauss points are assigned to each element individually, which could be particularly useful in terms of modelling dense fibre networks within polymers, where changes in spiral angle and changing distances between fibres require complex meshing. It also allows the option of future multi-grid simulations. Furthermore it simplifies the post processing and allows the user to look directly at the viscoelastic strains, an important factor in modelling and understanding systems with rate limiting viscoelastic processes within diffusion problems.

2.3.5 Newton-Raphson Method

The nonlinear system of equations (Eq. (2.39), (2.41) and (2.43)) are solved using the Newton-Raphson method. At iteration k of the Newton-Raphson method, the out of balance residual vector is formed as follows:

$$\mathbf{r}(\mathbf{u}^h, \mu^h, \hat{\varepsilon}^h) = \begin{bmatrix} \mathbf{r}_\sigma(\mathbf{u}^h, \mu^h, \hat{\varepsilon}^h) \\ \mathbf{r}_\mu(\mathbf{u}^h, \mu^h) \\ \mathbf{r}_{\hat{\varepsilon}}(\mathbf{u}^h, \mu^h, \hat{\varepsilon}^h) \end{bmatrix} = \begin{bmatrix} \mathbf{0} \\ \mathbf{0} \\ \mathbf{0} \end{bmatrix} \tag{2.45}$$

where $\mathbf{r}_\sigma$, $\mathbf{r}_\mu$ and $\mathbf{r}_{\hat{\varepsilon}}$ are the residuals for the conservation of momentum, conservation of mass and the dashpot (viscoelastic) strain residual respectively (Eq. (2.39), (2.41) and (2.43)).

2.3.6 Discretisation in Time

At this point there is a fully coupled system of ordinary differential equations. By discretising in time, a discrete set of algebraic equations can be obtained. In this thesis, a backwards euler time integration scheme has been utilised. The rate of change of the chemical potential is given as follows:

$$\begin{aligned} \Omega \frac{\partial \mu^h}{\partial t} = \frac{\partial \varepsilon^h_{kk}}{\partial t} &= \frac{\partial u^h_k}{\partial x_k \partial t} \\ &= \frac{1}{\Delta t} \left[\left(\left.\frac{\partial u^h_k}{\partial x_k}\right|_t + \Delta \left.\frac{\partial u^h_k}{\partial x_k}\right|_{t+\Delta t} \right) - \left.\frac{\partial u^h_k}{\partial x_k}\right|_t \right] \\ &= \frac{1}{\Delta t} \sum_{k=1}^{3} \frac{\partial \mathbf{\Phi}^n_i}{\partial x_k} \Delta \mathbf{q}^u_{i,t+\Delta t}. \end{aligned} \tag{2.47}$$

In a similar manner, the rate of the dashpot strain is calculated as follows:

$$\frac{\partial \hat{\varepsilon}^h_{ij}}{\partial t} = \frac{1}{\Delta t} \left[\left(\left.\hat{\varepsilon}^h_{ij}\right|_t + \Delta \left.\hat{\varepsilon}^h_{ij}\right|_{t+\Delta t} \right) - \left.\hat{\varepsilon}^h_{ij}\right|_t \right] = \frac{1}{\Delta t} \mathbf{\Psi} \left(\Delta \mathbf{q}^{\hat{\varepsilon}}_{t+\Delta t} \right). \tag{2.48}$$

where t is current time and Δt is the size of the time step. The quantities $\mathbf{q}_t$ and $\mathbf{q}_{t+\Delta t}$ are the vectors of degrees of freedom at the previous time step and the current time step respectively.

2.3.7 Linearised System of Equations

At this point the system of equations have been discretised in both space and time. Now the residual can be expanded using the Taylor series, with the series truncated after the first order term as follows:

$$\left.\frac{\partial \mathbf{r}(\mathbf{u}^h, \mu^h, \hat{\varepsilon}^h)}{\partial \mathbf{q}^{u,\mu,\hat{\varepsilon}}_{t+\Delta t}}\right|_{\mathbf{q}^{u,\mu,\hat{\varepsilon}}_{t+\Delta t,J}} \delta \mathbf{q}^{u,\mu,\hat{\varepsilon}}_{t+\Delta t,J+1} + \left.\mathbf{r}(\mathbf{u}^h, \mu^h, \hat{\varepsilon}^h)\right|_{\mathbf{q}^{u,\mu,\hat{\varepsilon}}_{t+\Delta t,J}} = \mathbf{0} \tag{2.49}$$

where J is the iteration number and the equation is solved to find $\delta\mathbf{q}^{u,\mu,\hat{\varepsilon}}_{t+\Delta t,J+1}$. Note that vector is of unknown degrees of freedom here and is additively decomposed as follows:

$$\mathbf{q}^{u,\mu,\hat{\varepsilon}}_{t+\Delta t,J+1} = \mathbf{q}^{u,\mu,\hat{\varepsilon}}_{t} + \Delta\mathbf{q}^{u,\mu,\hat{\varepsilon}}_{t+\Delta t,J} + \delta\mathbf{q}^{u,\mu,\hat{\varepsilon}}_{t+\Delta t,J}, \tag{2.50}$$

with the following initial conditions applied:

$$\Delta\mathbf{q}^{u,\mu,\hat{\varepsilon}}_{t+\Delta t,0} = \mathbf{0},\ \delta\mathbf{q}^{u,\mu,\hat{\varepsilon}}_{t+\Delta t,0} = \mathbf{0} \tag{2.51}$$

where $\mathbf{q}^{u,\mu,\hat{\varepsilon}}_{t}$ is the equilibrium state, when converged, at time t. $\Delta\mathbf{q}^{u,\mu,\hat{\varepsilon}}_{t+\Delta t,J}$ is the increment at time step $t+\Delta t$ and iteration J while $\delta\mathbf{q}^{u,\mu,\hat{\varepsilon}}_{t+\Delta t,J}$ is the iterative sub-increment at iteration $J+1$. This results in the following linearised system of algebraic equations:

$$\begin{bmatrix} \mathbf{K}_{uu} & \mathbf{K}_{u\mu} & \mathbf{K}_{u\hat{\varepsilon}} \\ \mathbf{K}_{\mu u} & \mathbf{K}_{\mu\mu} & \mathbf{K}_{\mu\hat{\varepsilon}} \\ \mathbf{K}_{\hat{\varepsilon}x} & \mathbf{K}_{\hat{\varepsilon}\mu} & \mathbf{K}_{\hat{\varepsilon}\hat{\varepsilon}} \end{bmatrix} \begin{bmatrix} \delta\mathbf{q}^{u} \\ \delta\mathbf{q}^{\mu} \\ \delta\mathbf{q}^{\hat{\varepsilon}} \end{bmatrix} = \begin{bmatrix} \mathbf{r}_{u} \\ \mathbf{r}_{\mu} \\ \mathbf{r}_{\hat{\varepsilon}} \end{bmatrix} \tag{2.52}$$

where for convenience subindices t and J, related to time stepping at Newton iterations, are dropped. The matrices in the left hand side matrix are defined as follows:

$$\mathbf{K}_{mn} = \left.\frac{\partial \mathbf{r}_m}{\partial \mathbf{q}^{n}_{t+\Delta t}}\right|_{\mathbf{q}^{u,\mu,\hat{\varepsilon}}_{t+\Delta t,J}}, \quad m,n \in \{u,\mu,\hat{\varepsilon}\} \tag{2.53}$$

2.3.8 Implementation Aspects

The time integration scheme and the solution to the system of equations is implemented using PETSc [8], with the library integrated within MoFEM code [1, 67]. The tangent matrix is calculated using automatic differentiation with ADOL-C [114], integrated within the MoFEM code, removing need for analytical derivations of formulae for the stiffness matrix yet guaranteeing efficiency and robustness. This allows the user flexibility when changing the constitutive relations due to the automatic computation of the tangent stiffness matrix. As such this allows different relationships to be added to the constitutive assumptions in the future, by the inclusion of new automatic doubles (i.e. adouble) variables. For instance polymer softening can be added with relative ease, once the appropriate variables have been defined. The calculation of the tangent stiffness matrix is carried out by ADOL-C on the first time step, and is remembered thereafter, guaranteeing computational efficient but yet removing the potential for user error when defining new tangent stiffness matrices.

Chapter 3

Sensitivity Tests

To assess the performance of the model some benchmark tests are carried out to ensure the behaviour is captured as expected. Each test is carried out on a generalised isotropic polymer network, with a relatively low stiffness. The importance in this chapter is not the particular material properties but the sensitivity of the model to changes in parameters and thus the ability to pick up complex interconnected processes. It is important to note that the time scales used in this chapter are extremely small and ordinarily dynamic effects would be expected. This is a result of often unrealistic boundary conditions, with changes in the environment and loading being applied very quickly. However, the purpose of this Chapter is to assess the sensitivity and behaviour of the model and any potential dynamic effects are ignored.

First a creep test is studied to assess the viscoelastic behaviour of the polymer network, in a test that simulates real world issues that often arise when using wood polymers under long term loading. The conditions in the external environment were held constant outside the sample, meaning all changes of chemical potential within the sample were a result of the external loading applied. Second, a test was carried out to assess the response to a change in the external environment, i.e. changes to the concentration of water vapour within the surrounding air. In this case, the sample was under no external loading and thus all stresses and changes in dimension were a result of solvent migration.

A third test was carried out on a material that contained two different layers of polymers. The behaviour and interactions of this composite was assessed as a result of changing the material properties. This allowed assessment of the dimensional stability in complex multi-layer arrangements of the polymers, as is found in wood cell walls. This demonstrates potential future performance in predicting both load induced and moisture induced, long term deformations.

Finally a compression test of a cylindrical shaped gel was carried out. This test demonstrates that the model can perform well when estimating complex geometrical shapes, as is encountered within the cell wall - for instance fibre reinforced networks or cylindrically shaped compression wood cells within the network of wood cells, and a combination of both.

Test	**Description**	**Aim**
Test 1	Creep Test	Assess the behaviour within the polymer network due to external loading
Test 2	Response to environmental change	Assess the adsorption and desorption behaviour of the polymer network due to a change in humidity
Test 3	Multilayer response to environmental change	Investigate the interaction between layers of material
Test 4	Cylinder compression	Apply the model to a complex geometrical shape

Table 3.1: Summary and corresponding aim of each verification test

For each test the full range of material behaviour is considered, capturing pre-viscoelastic diffusion, viscoelastically limited diffusion and post viscoelastic diffusion, as well as assessing the sensitivity of the parameters within the model.

It is important to note that the solvent migration is linked to the displacements and not the chemical potential. The rate of the chemical potential through the sample represents the passing of an air/water vapour mixture through the polymer network. However, recalling Eq. (2.13), the actual water uptake is given by the displacement of the sample due to the environmental conditions. When including external loading this can be confused, as displacements can be applied almost instantaneously, however the amount of solvent within the sample does not change. It is at this point that the evolution of the chemical potential becomes the significant factor in determining whether or not solvent uptake has been completed and the sample is at equilibrium with the given load and the given solvent content.

3.1 Test 1: Creep Test

Description of Test

To test the viscoelastic and poroelastic behaviour of the polymeric gel modelled, and view the interaction between the two processes, a small sample was subjected to a uniaxial tensile traction. Three different material behaviours were observed:

In Case 1, the time of viscoelastic relaxation, τ_v, is far longer than the time of diffusion, t_D, for a problem of this size; thus the material behaves poroelastically. The material properties are the properties defined before relaxation (i.e. both springs are taking the load).

In the second creep test (Case 2), the uptake of the dashpot strain happens very quickly. In this case the time of viscoelastic relaxation is far smaller than the time of diffusion over the length of material. Therefore, in the rheological model, the spring β relaxes almost instantaneously and the load is only taken in spring α.

In the third creep test (Case 3), the time of viscoelastic relaxation and the time of diffusion are similar. In this case the sample is undergoing a complex interplay between these two processes. In this case the rate of solvent migration is considered viscoelastically limited rather than diffusion limited.

Modelling Approach

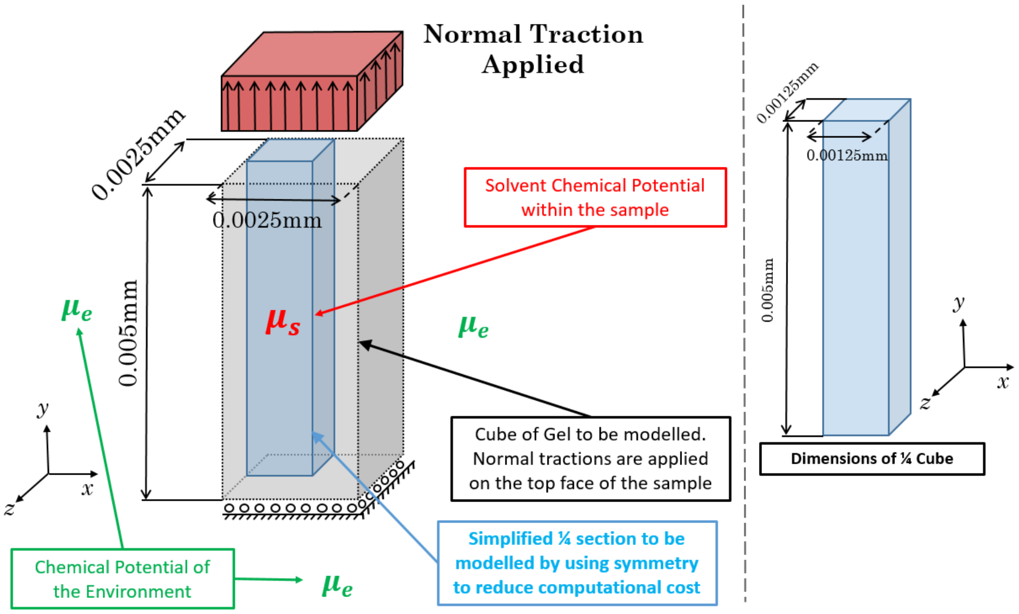

Figure 3.1: Creep test of a cube of a polymeric gel subjected to a tensile pressure. The pressure is applied in the y-direction, normal to the top surface. The bottom face is fixed in the y-direction. To reduce the computational cost only a 1/4 section of the cube is modelled, with appropriate boundary conditions applied according to Table 3.2, taking advantage of symmetry.

Figure 3.1 shows the setup for the test, where the bottom of a sample of length 50 μm and width 25 μm is subjected to a tensile traction of 50 N/mm^2 in the y direction.

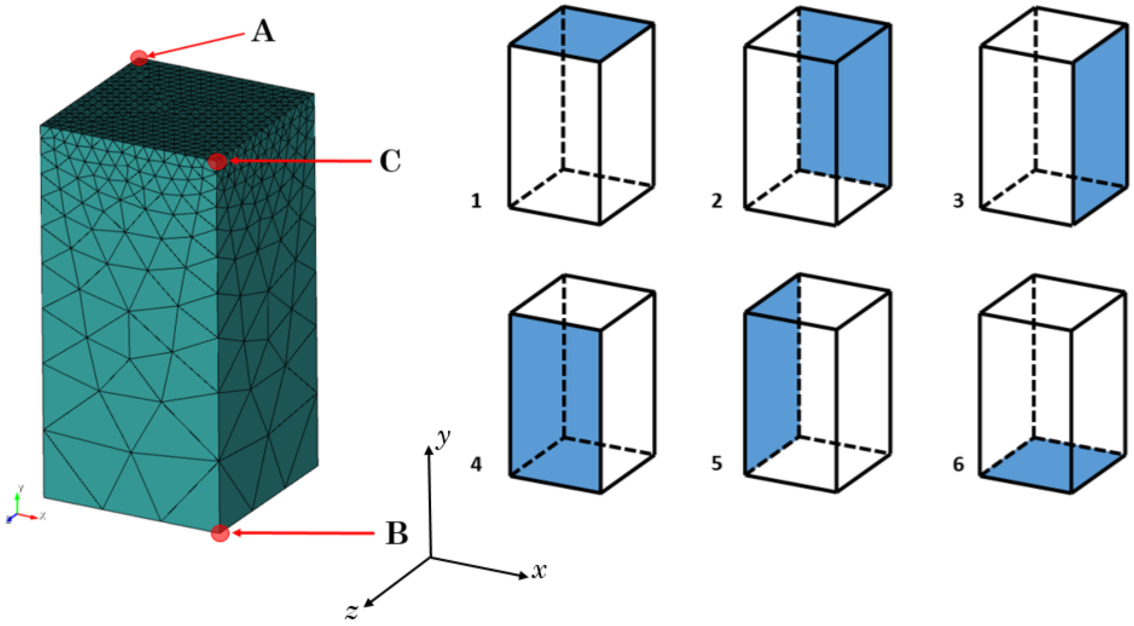

Figure 3.2: 1/4 Cube of cellulose polymers with a fine mesh on the surface, where the load is applied, transitioning to a coarse mesh at the middle of the sample. Points A - C represent the position of nodes from which time series data are obtained. The faces where mechanical and chemical boundary conditions are applied are numbered and highlighted in blue.

Numerical Approach

A prescribed chemical potential, μ_e, was applied to the external vertical sides to represent the free energy of the surrounding environment. The sample was split into a quarter section, enforcing symmetry to increase computational efficiency. The symmetry condition was enforced on the inner faces (3,4 and 6 of Figure 3.2) through constrained displacements in the perpendicular direction of each face and by enforcing zero flux of the solvent chemical potential ($\frac{\partial \mu_s}{\partial x} = 0$) across the boundaries, see Table 3.2.

Face	Mechanical Conditions	Chemical Conditions
1	-	μ_e
2	-	μ_e
3	$u_x = 0$	$\frac{\partial \mu_s}{\partial x} = 0$
4	$u_z = 0$	$\frac{\partial \mu_s}{\partial z} = 0$
5	-	μ_e
6	$u_y = 0$	$\frac{\partial \mu_s}{\partial y} = 0$

Table 3.2: Boundary conditions for the creep test. The boundaries (Faces 1-6) where mechanical and chemical boundary conditions are applied are visualised in Figure 3.2.

Chemical Condition	Value	Units	Time
μ_e	8.430953×10^{06}	$\mathrm{J\,mol^{-1}}$	0.00s - 0.000400s
μ_s	8.430953×10^{06}	$\mathrm{J\,mol^{-1}}$	0.00s

Table 3.3: Chemical potential conditions for the creep test. The environmental chemical potential, μ_e is held constant throughout the test and the chemical potential of the solvent μ_s is allowed to evolve within the gel after the first time step. The boundaries on which μ_e is applied are visualised in Figure 3.2.

Traction Magnitude	Units	Time
0	$\mathrm{N/mm^2}$	0.00s
50	$\mathrm{N/mm^2}$	0.000004s - 0.000200s
0	$\mathrm{N/mm^2}$	0.000204s - 0.000400s

Table 3.4: Applied tensile traction conditions, applied to Face 1 (refer to Figure 3.2, for the creep test.

Figure 3.2 shows the finite element mesh used for the creep test, with an increase in mesh refinement towards face 1, where the tensile load is applied and the gradient of the chemical potential is at its highest. Please note that the chemical potential gradient is also high towards both face 2 and 5, however due to the computational cost the refinement was carried out in the y direction only. Points A-C refer to points of interest for plotting, as will be discussed shortly. All simulations in Case 1-3 are carried out using approximation functions of order 3.

3.1.1 Case 1 - Poroelastic Behaviour Before Relaxation

Material Properties

In this example the ratio of G^β and $\hat{G}^\beta$ is given for an amorphous wood polymer in its glassy state, i.e. dry at room temperature. As such a value of 9×10^{06} MPa.s for the shear viscosity of the dashpot $\hat{G}^\beta$ is assigned. The polymer is assumed isotropic and equal stiffness was assigned to both the elastic and viscoelastic regimes (i.e. $G^\alpha = G^\beta$). The viscosity of the solvent (in this case water) was given as 1×10^{-10}MPa.s and the permeability as $6 \times 10^{-12}\mathrm{mm}^2$. The chemical potential of the solvent within the sample and the chemical potential of the environment was $8.430953 \times 10^{06}\mathrm{J\,mol^{-1}}$ ($\mu_e = \mu_s = 8.430953 \times 10^{06}\mathrm{J\,mol^{-1}}$) at $t = 0$. At $t > 0$, the chemical potential of the environment is held at $\mu = 8.430953 \times 10^{06}\mathrm{J\,mol^{-1}}$ and the chemical potential of the solvent within the sample is allowed to evolve freely.

Material Parameter	**Symbol**	**Value**	**Units**
Shear Modulus Spring α	G^{α}	3×10^{03}	MPa
Shear Modulus Spring β	G^{β}	3×10^{03}	MPa
Viscosity Dashpot β	$\hat{G}^{\beta}$	9×10^{06}	MPa.s
Poisson's Ratio Spring α	ν^{α}	0.232	-
Poisson's Ratio Spring β	ν^{β}	0.232	-
Poisson's Ratio Dashpot β	$\hat{\nu}^{\beta}$	0.232	-
Volume per Mole of Water	Ω	18000	$\text{mm}^3\ \text{mol}^{-1}$
Permeability	κ	6×10^{-12}	mm^2

Table 3.5: Material Input data for the creep test case 1 where the time of viscoelastic relaxation, $\tau_v = 3000\text{s}$.

The traction of 50 N/mm^2 is applied to face 1 in the y direction on the first time step and this is held for 0.0002s. The force is then released and the sample is given the same amount of time again with which to reach equilibrium with the surrounding environment.

Physical Behaviour

Figure 3.3 shows the evolution of the chemical potential through the sample after the tensile load has been applied to the sample. Initially there is a drop in μ_s towards the middle of the sample, due to the increased volume in the sample, ε_{kk}, and a lack of time for diffusion to occur, i.e. voids have been created within the network, exposing new sorption sites but initially there is a lack of solvent available to occupy the new sites. Over time the number of solvent molecules within the sample increases to fill the volume, until the chemical potential within the sample is at equilibrium with the outside environment.

In Figure 3.4, the evolution of the chemical potential is shown after the load has been released. Intially the chemical potential within the sample increases towards the middle as the number of solvent molecules remains the same but the space in which they occupies reduces. The solvent then leaves the sample, as poroelastic relaxation occurs, until the chemical potential is in equilibrium with the external environment.

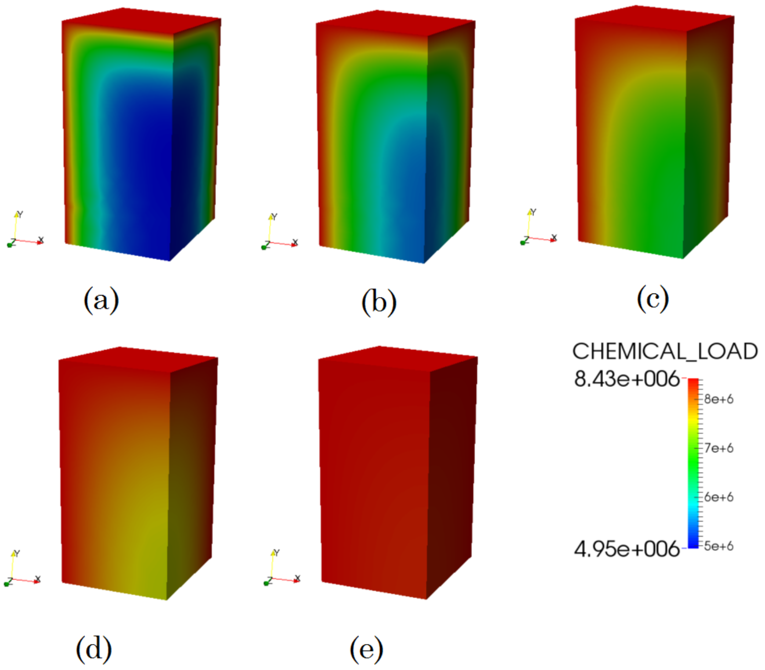

Figure 3.3: Evolution of the chemical potential for the creep test during the applied tensile loading phase (a) First time step (0.000004s) immediately after the tensile load is applied. (b) 0.000012s. (c) 0.000024s (d) 0.000040s (e) 0.000080s

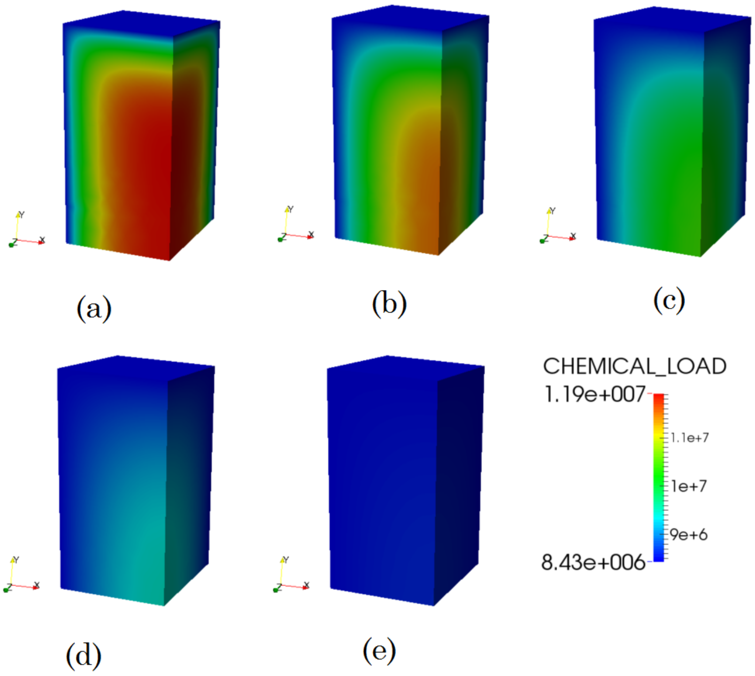

Figure 3.4: Evolution of the chemical potential after the tensile load is released (a) First time step (0.000204s) immediately after the tensile load is applied. (b) 0.000212s. (c) 0.000224s (d) 0.000240s (e) 0.000280s

The displacements for the top corner (point A), are plotted in Figure 3.5. At this point, the relaxation behaviour within the dashpot has only just started (i.e. the rate of change of the dashpot strain is very slow), thus it has a negligible effect upon the diffusion or the displacements. As such in this test the sample behaves poroelastically, with an initial elastic deformation and then diffusion of water from the environment into the sample in the new configuration. The sample then recovers elastically after the load is released and the water is then driven out of the sample until it returns to its original configuration.

In Figure 3.5, the x displacements are negative after the load is removed. This is due to the elastic extension of the sample (in the y direction) leading to a proportional decrease in the lateral length of the sample (x and z directions), before the poroelastic recovery is completed.

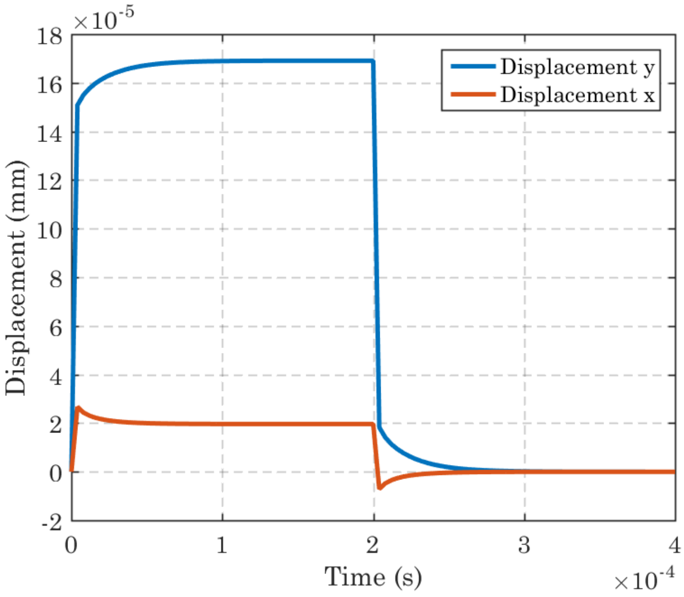

Figure 3.5: Displacement in the x and y directions vs time for point A. The displacements in the z direction are equal to those in the x direction.

In this case the polymer network is in a very glassy state and rearrangement of the molecular network happens as an extremely slow process. Thus the sample reaches equilibrium with the external load and the environment long before any viscoelastic processes have the opportunity to take effect.

Figure 3.6 shows the evolution of the dashpot strain, showing virtually no relaxation of the dashpot within the time frame. There appears to be no movement of the dashpot strain; this is due to the dashpot strain axis being calibrated to incorporate the maximum dashpot strain for this polymer for the given environmental conditions.

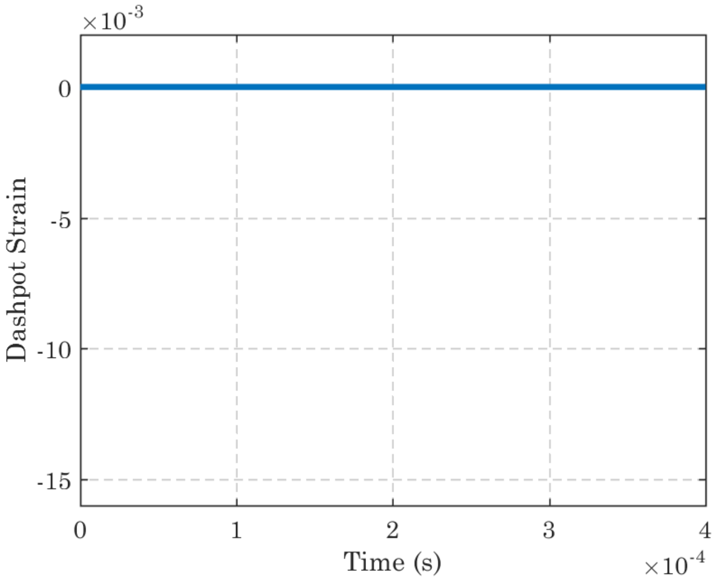

Figure 3.6: Dashpot strain, $\hat{\varepsilon}_{yy}$, vs time within the sample for a material behaving as a glassy polymer.

Whilst there is some dashpot strain evolution in this case, it is very low and essentially a product of this being a numerical model, with the consequent accuracy of measurement, this dashpot strain would be not be picked up experimentally. Furthermore, the degree to which the dashpot strain is compressed is dependent upon the dashpot viscosity as will be demonstrated in Case 2-3.

Numerical Convergence

To check convergence, the chemical load is plotted along the y-axis from point C to B and the results for several levels of mesh refinement are demonstrated in Figure 3.7. As shown, towards point C the highest gradient of chemical load is found; this is due to it being located on the boundary with the external environment where the external chemical potential is applied.

To obtain convergence, the mesh discretisation on this boundary is increased in order to capture the high gradient of chemical potential on the edge of the sample, where it is exposed to the environment and where the load it applied. This is done initially by discretising the entire mesh. However, to improve the accuracy and reduce the computational effort, a graded mesh was introduced, where the mesh is discretised more towards Point A and C and less towards point B (i.e. the point furthest from the external environment) where the chemical potential gradient is lower. Convergence was attained using this graded mesh, shown in Figure 3.7.

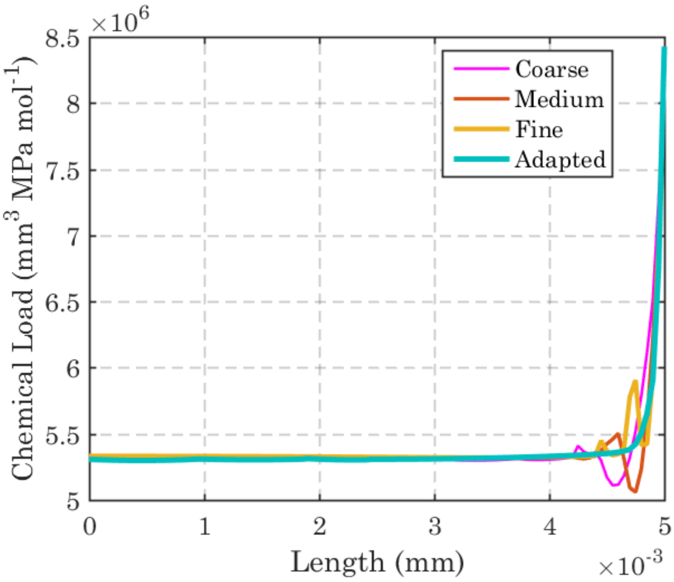

Figure 3.7: Mesh convergence along the y-axis (from point C to B) of the chemical load, after the first time step, for different meshes. All four results are calculated for approximation order 3.

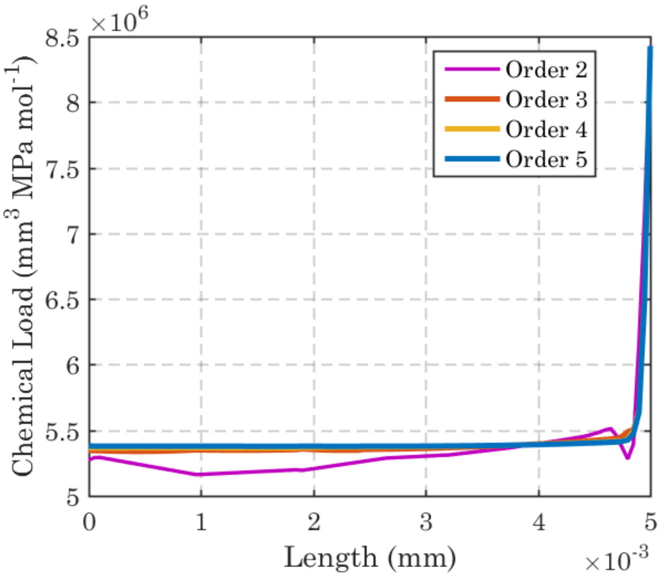

Figure 3.8: Approximation order convergence along the y-axis (from point C to B) of the chemical load after the first time step. The mesh is a refined 5039 element graded mesh.

The effect of the order of approximation convergence of the chemical load is shown in Figure 3.8. As discussed in Section 2.3 (3D Finite Element Model), a polynomial base function of order $n \geq 2$ is applied to the displacement field. Furthermore, to ensure a stable solution, a lower order of polynomial base function is applied to the flux field (i.e. order $n-1$). The consequence of this is demonstrated in Figure 3.8, where the solution for order 2 is noticeably less refined than the rest. This is due to the flux being approximated as a first order approximation. Approximation orders 4-5 produce very similar results to order 3, demonstrating good convergence.

3.1.2 Case 2 - Poroelastic Behaviour Post Creep/Relaxation

In Case 2, the time of viscoelastic relaxation was very small, far smaller than the time over which diffusion occurs within the sample. In this case $\hat{G}^{\beta}$ is given as 1×10^{-6}MPa.s. All other properties and conditions to which the sample are subjected to remain unchanged.

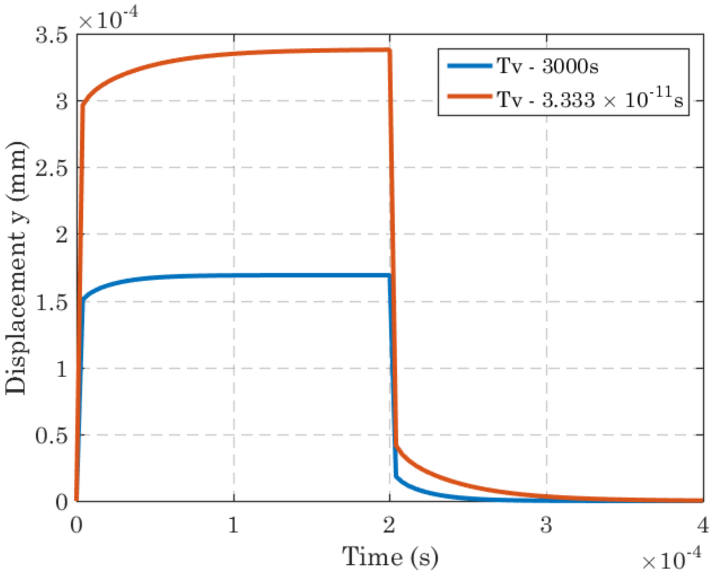

Figure 3.9: Displacement time series in the y for two different relaxation times (τ_v), demonstrating both pre-relaxation and post relaxation behaviour. Displacements taken at point A.

Plots of the displacements vs time are shown in Figures 3.9 and 3.10. Comparisons are made with the previous example, where the time of viscoelastic relaxation, τ_v, is far longer. In both cases the material exhibits the same poromechanical diffusion behaviour, however the displacements in case 2 are exactly double of those in case 1. This is expected as the stiffness is identical in both springs, thus when spring β is relaxed, the stiffness of the material is exactly half of what it was before it undergoes relaxation.

The dashpot strain in the y direction is shown in Figure 3.11, and a comparison is made with case 1. In case 2, where $\tau_v = 3.333 \times 10^{-11}$, the dashpot strain reaches a maximum almost instantly, allowing the instantaneous relaxation of spring β, as observed in Figures 3.9 and 3.10. The dashpot strain returns to zero instantly when the load is released, as the negative stress within the sample causes the reverse process to occur.

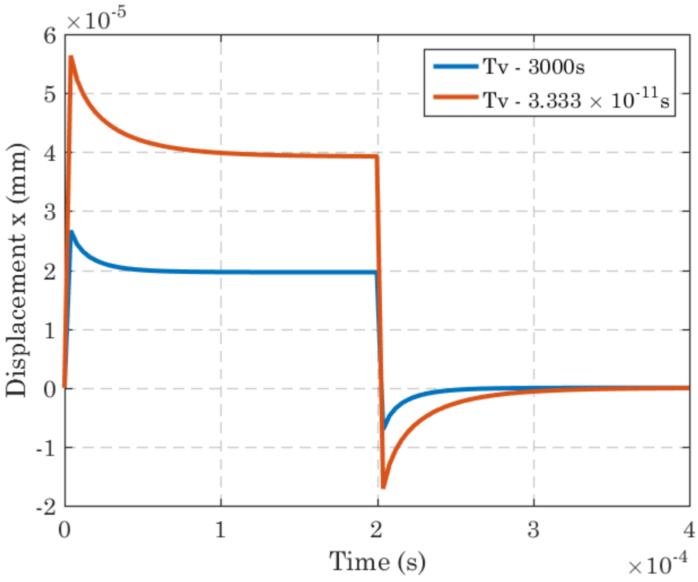

Figure 3.10: Displacement time series in the y for two different relaxation times (τ_v), demonstrating both pre-relaxation and post relaxation behaviour. Displacements taken at point A.

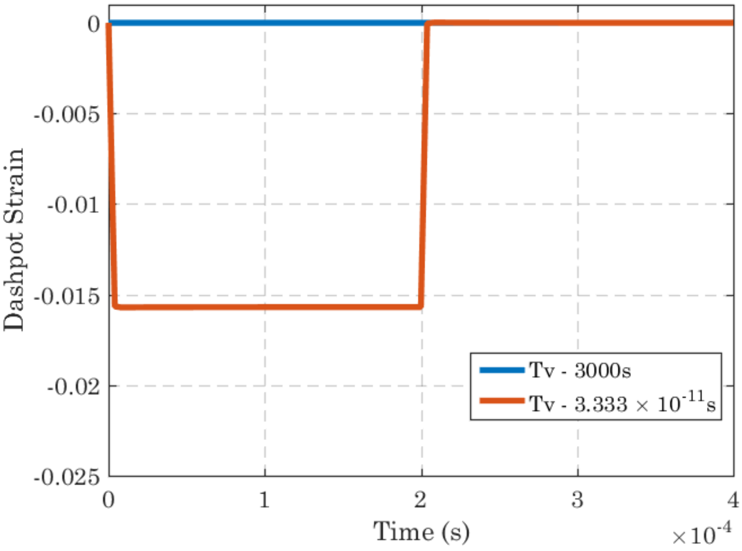

Figure 3.11: Dashpot strain, $\hat{\varepsilon}_{xx}$, for two different relaxation times (τ_v), showing the uptake of the dashpot strain, providing evidence of both no relaxation, $\tau_v = 3000$s, and almost instant relaxation, $\tau_v = 3.333 \times 10^{-11}$. Taken at point A.

From Figure 3.11, it can be concluded that there is an area between these two extreme cases in which concurrent poroelasticity and viscoelasticity can occur, which will be shown in case 3.

Influence of G^α and G^β

The ratio of G^α and G^β defines how much of the polymer stiffness can be associated with the relaxation process. For instance if G^α and G^β are equal, then after viscoelastic relaxation the amount of swelling is defined by G^{α} only, and the system has only half the stiffness of pre-relaxation. If G^{α} is far stiffer than G^{β} then the increase in swelling during the viscoelastic regime will be smaller. Conversely, if G^{α} is far less stiff than G^{β}, then the increase in swelling, as a proportion of the total swelling, during the viscoelastic process will be far higher.

To examine the influence of the ratio of the shear modulus of each spring, a combination of properties was selected to demonstrate the corresponding displacements. This was examined for both pre relaxation and post relaxation conditions, with the behaviour change determined by changing the dashpot viscosity $\hat{G}^{\beta}$.

Combination	G^{α} (MPa)	G^{β} (MPa)	$\hat{G}^{\beta}$ (MPa.s)
Combination 1	3×10^{03}	0.5×10^{03}	9×10^{06}
Combination 2	3×10^{03}	0.5×10^{03}	0.0333
Combination 3	3×10^{03}	0.5×10^{03}	0.0000001
Combination 4	0.5×10^{03}	3×10^{03}	9×10^{06}
Combination 5	0.5×10^{03}	3×10^{03}	0.1
Combination 6	0.5×10^{03}	3×10^{03}	0.0000001

Table 3.6: Material data for different combinations. In each combination the shear modulus of the spring, G^{β}, remains the same and the value of the dashpot shear viscosity $\hat{G}^{\beta}$ determines τ_v

Input Parameter	**Symbol**	**Value**	**Units**
Poisson's Ratio Spring α	ν^{α}	0.232	-
Poisson's Ratio Spring β	ν^{β}	0.232	-
Poisson's Ratio Dashpot β	$\hat{\nu^{\beta}}$	0.232	-
Volume per Mole of Water	Ω	18000	$\text{mm}^3\ \text{mol}^{-1}$
Permeability	κ	6×10^{-12}	mm^2
Viscosity of Water	η	1×10^{-06}	MPa.s

Table 3.7: Material data for the Creep Test. Data for the shear moduli are given in Table 3.6.

The selected material properties, shown in table 3.6, cover six scenarios to demonstrate the physical importance of the ratio of the spring shear moduli. Table 3.7 shows the material parameters which remain constant through all six scenarios.

The behaviour is examined for both pre-relaxation and post relaxation behaviour, as defined and demonstrated for case 1 and case 2 in the creep test respectively. A set of parameters was selected which allowed viscoelastic deformation to be captured. Further discussion of the viscoelastic deformation is carried out in the next section (case 3).

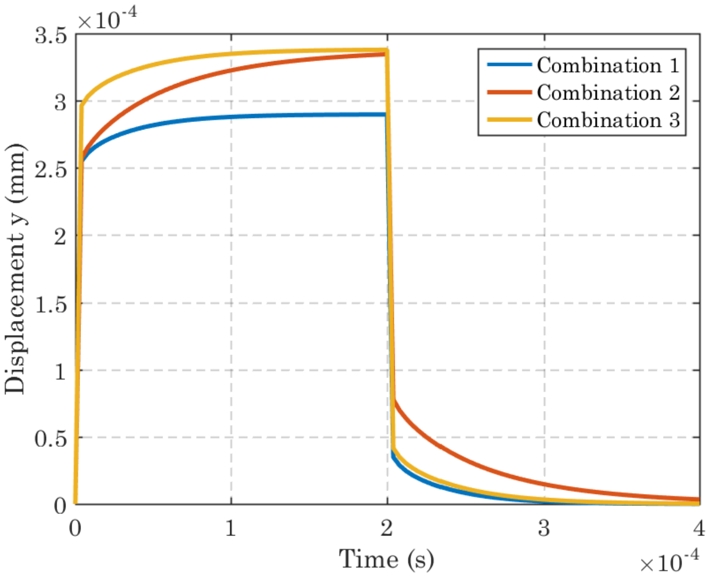

Figure 3.12: Displacement in the y direction vs time for combinations 1-3 as defined in Table 3.6.

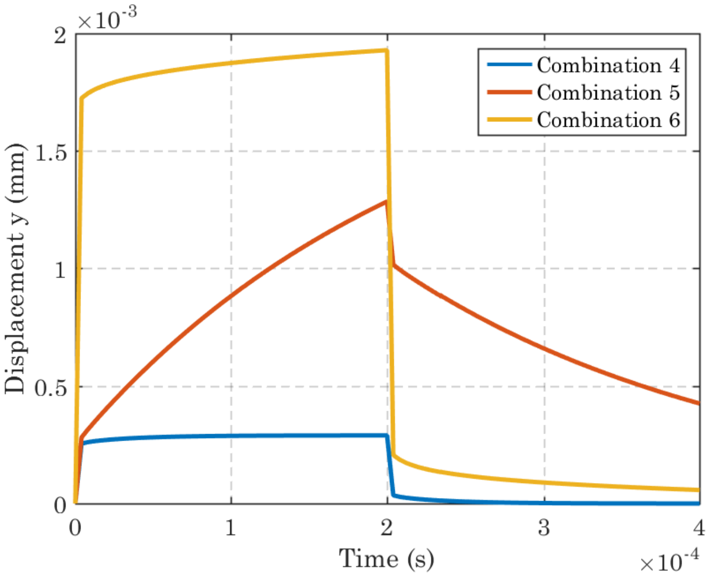

Figure 3.13: Displacement in the y direction vs time for combinations 4-6 as defined in Table 3.6.

Combinations 1-3 are plotted in Figure 3.12. This shows, due to the relatively small increase in displacements with each reduction in $\hat{G}^{\beta}$, that the influence of the viscoelastic regime is very small. By contrast, Figure 3.13 shows a very large influence of the viscoelastic regime. The difference between the displacements when the polymer is in its glassy state (Combination 4) and when its in a rubbery state (Combination 6) are very large. Therefore, the selection of these parameters is very important when determining the degree to which the material can undergo viscoelastic deformation.

3.1.3 Case 3 - Concurrent Viscoelastic and Poroelastic Processes

In Case 3 the rate of solvent migration is limited by the rate of viscoelastic deformation. In this case the rate at which the mechanical load causes viscoelastic deformation controls the rate of solvent uptake. This happens when the time for diffusion to occur through the samples length is close to that of the time of viscoelastic relaxation τ_v.

Combination	$\hat{G}^\beta$ (MPa.s)	G^β (MPa)	τ_v (s)
Combination 1	9×10^6	3×10^3	3000
Combination 2	0.0000001	3×10^3	3.333×10^{-11}
Combination 3	0.05	3×10^3	0.0000167
Combination 4	0.3	3×10^3	0.0001
Combination 5	1.2	3×10^3	0.0004
Combination 6	2.4	3×10^3	0.0008
Combination 7	3.0	3×10^3	0.001
Combination 8	6.0	3×10^3	0.002

Table 3.8: Material data for a variety of different relaxation times. In all cases the shear modulus of the spring, G^β, remains the same and the value of the dashpot viscosity $\hat{G}^\beta$ determines τ_v

Table 3.8 shows a number of different combinations of G^β and $\hat{G}^\beta$ that were used to determine τ_v. For each of these sets of parameters, the test shown in Figure 3.1 was used to look at the region where the rate of solvent migration is viscoelastically controlled by the rearrangement of molecules within the polymer network. Figure 3.14 shows the displacements in the direction of the loading taken at point A. The upper and lower bound values ($\tau_v = 3000$s and $\tau_v = 3.333 \times 10^{-11} s$) are shown along with the intermediate values.

Physically this test shows different stages of the material behaviour, i.e. at both extremes, glassy or rubbery, and a state between the two. The aim was to demonstrate the ability of the model to capture the different complex material behaviours by simply changing the viscosity of the dashpot, as suggested by Govindjee et al [46].

In Figure 3.14, fully reversible creep was observed in Combination 3 ($\tau_v = 0.0000167$s). This was shown as dashpot was relaxed (Figure 3.16) by the time equilibrium was reached, after the initial loading, and the sample returns to the reference configuration by the time an equilibrium condition was obtained after the load was released. It also demonstrated the phenomena of viscoelastically limited solvent migration, as the final displacement in the y direction was the same as the results obtained poroelastically on spring α only, combination 2 ($\tau_v = 3.333 \times 10^{-11}$), although it did take a longer time to obtain this displacement as the rearrangement of the molecules within the polymer network occurred as a slower process. For Combination 4 ($\tau_v = 0.0001$s) it was observed that the dashpot was close to being compressed, and that the rate of relaxation was close to that of the rate of diffusion. The rate of deformation at the end of the test (t = 0.0004s) suggested that, given time, this may have reached an equilibrium state similar to the configuration in the reference state.

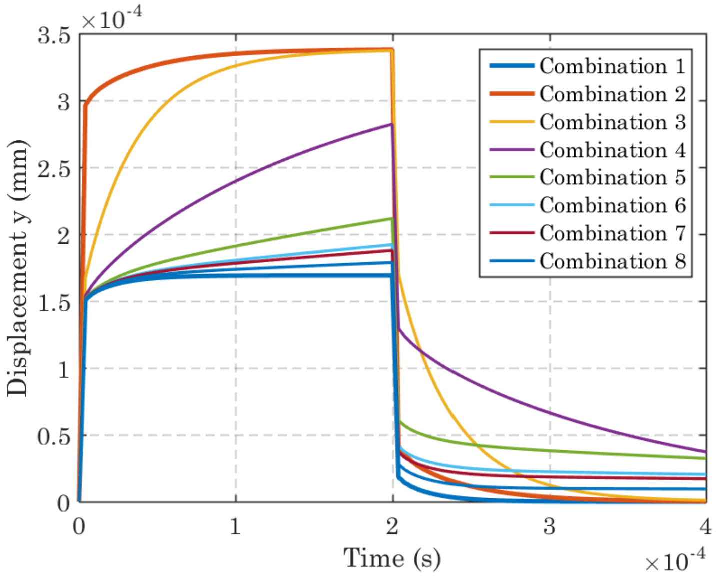

Figure 3.14: Displacement in the y direction vs time at point A for various times of viscoelastic relaxation τ_v.

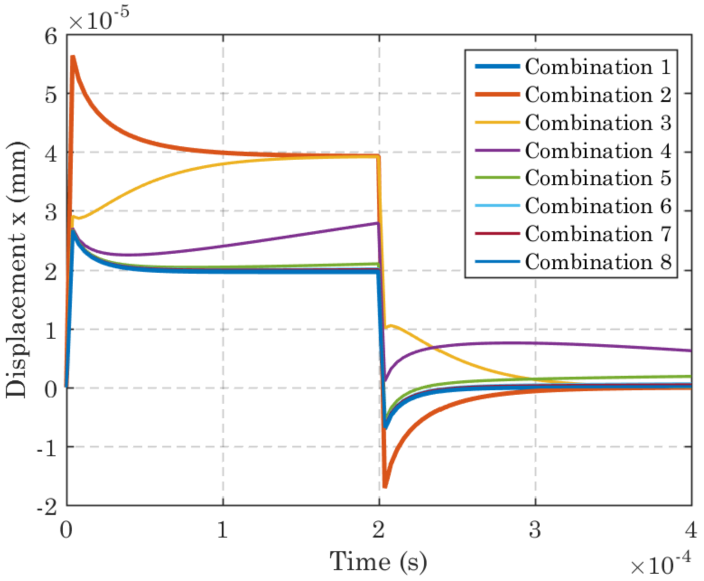

Figure 3.15: Displacement in the x direction vs time at point A for various times of viscoelastic relaxation τ_v.

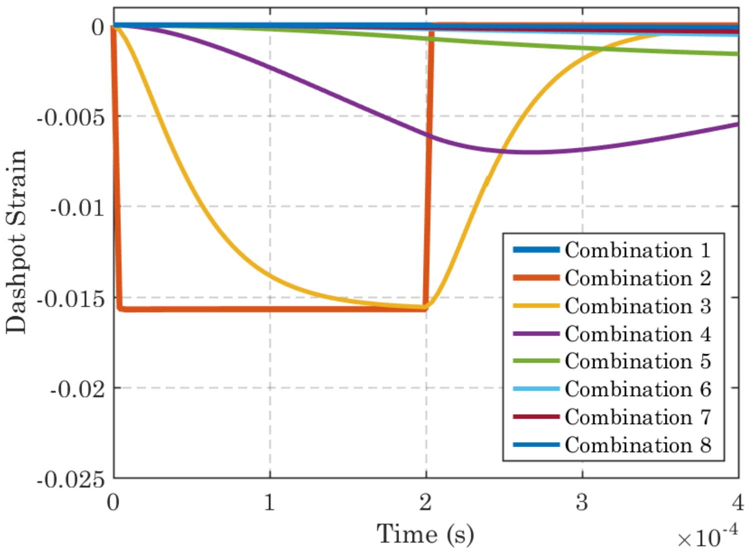

Figure 3.16: Dashpot strain, $\hat{\varepsilon}_{yy}$, vs time at point A for various times of viscoelastic relaxation τ_v.

For the rest of the viscoelastic time frames, the rate of deformation at the end of the test (t = 0.0004s) was very slow. For Combination 8, the sample had returned to a state of equilibrium with the environment before it had returned to the reference configuration. This clearly demonstrated the ability of the model to capture creep deformation. As can be seen in Figure 3.16, the dashpot strain was very small for Combinations 5-8 ($\tau_v =$ 0.0004s - 0.002s), when compared to both Combination 3 and 4 ($\tau_v = 0.00000167$s and $\tau_v = 0.0001$s). This demonstrated a relatively small window of material properties within which the viscoelastic process dominates the rate of moisture uptake and therefore the rate at which the sample deforms. Therefore it can be concluded that the model is very sensitive to τ_v.

Spring β Behaviour

To fully understand the viscoelastic behaviour of the model, it was necessary to look closely at the stress behaviour of spring β, as it is expected that the stress in spring β should reduce as the dashpot strain, $\hat{\varepsilon}_{ij}$, increases. This was done to check the creep behaviour, by examining the relationship between the stress and the strain. If the sample did not return to the reference configuration (i.e. zero displacement) when it returned to a zero stress state, after the load was released, then it was demonstrating clear creep deformations. To check the relaxation behaviour of spring β, a stress/displacement graph was plotted. Figure 3.17 shows the stress path (stress vs spatial position) taken at point A. The tensile stresses are positive and compressive stresses are negative; this convention remains throughout the thesis.

Initially, when the load was applied, the stress increased linearly until relaxation of the stress occurred, as the sample adsorbed solvent from the environment in order to reach equilibrium. The opposite held true after the load was released. The stress and the displacements were both fully reversible for Combination 3, as was expected from the Dashpot Strain given in Figure 3.17.

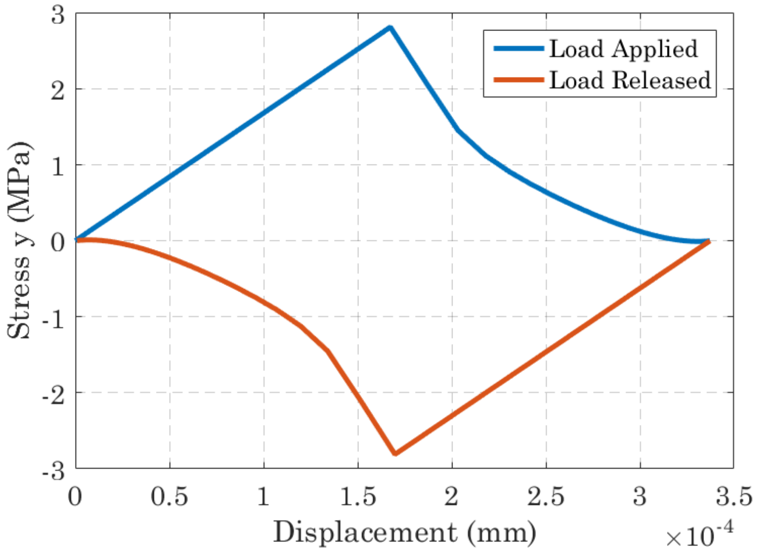

Figure 3.17: Hysteresis Loop showing the relaxation of σ_{yy} in spring β, initially with the traction load applied and then the reverse process after the traction load is removed. Combination 3 ($\tau_v = 0.0000167s$).

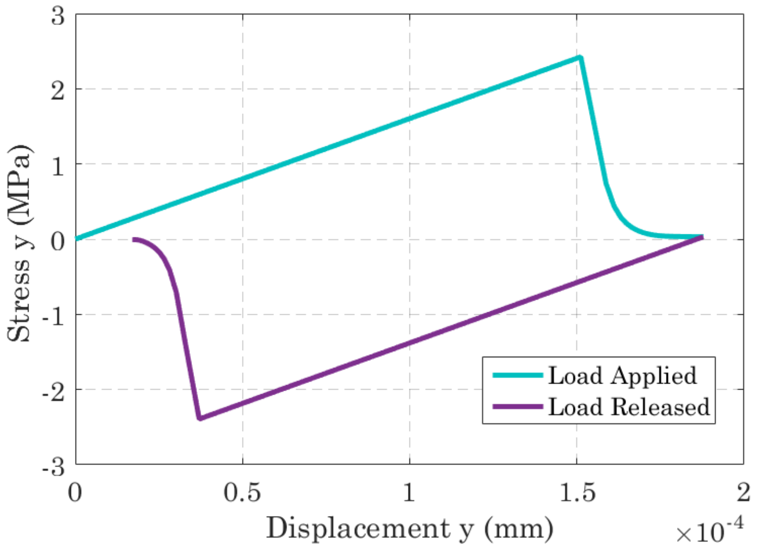

Figure 3.18: Hysteresis Loop showing the relaxation of σ_{yy} in spring β, initially with the traction load applied and then the reverse process after the traction load is removed. Combination 7 ($\tau_v = 0.001s$).

The same test was carried out and the results observed for Combination 7 ($\tau_v = 0.001s$). For this Combination, the stress returned to zero after the load has been released. However, by the time this equilibrium with the environment had been reached, the sample had not yet returned to the reference configuration (zero displacement). Therefore it was concluded that, for Combination 7, there was clear evidence of viscoelastic creep (Figure 3.18).

3.2 Test 2: Deformations Caused by Changes in the Moisture Content of the Surrounding Environment

Description of the Test

The second test applied to the model was a test of the material response to an environmental change, i.e. the moisture content of the surrounding environment, with no external loading applied. To do this a small cube of polymeric gel was exposed to an environment of increased chemical potential. The higher chemical potential in the environment penetrated the sample, causing deformations due to the chemical uptake of solvent from the environment, i.e. water from the surrounding environment forming hydrogen bonds within the hydroxyl groups of the polymeric gel.

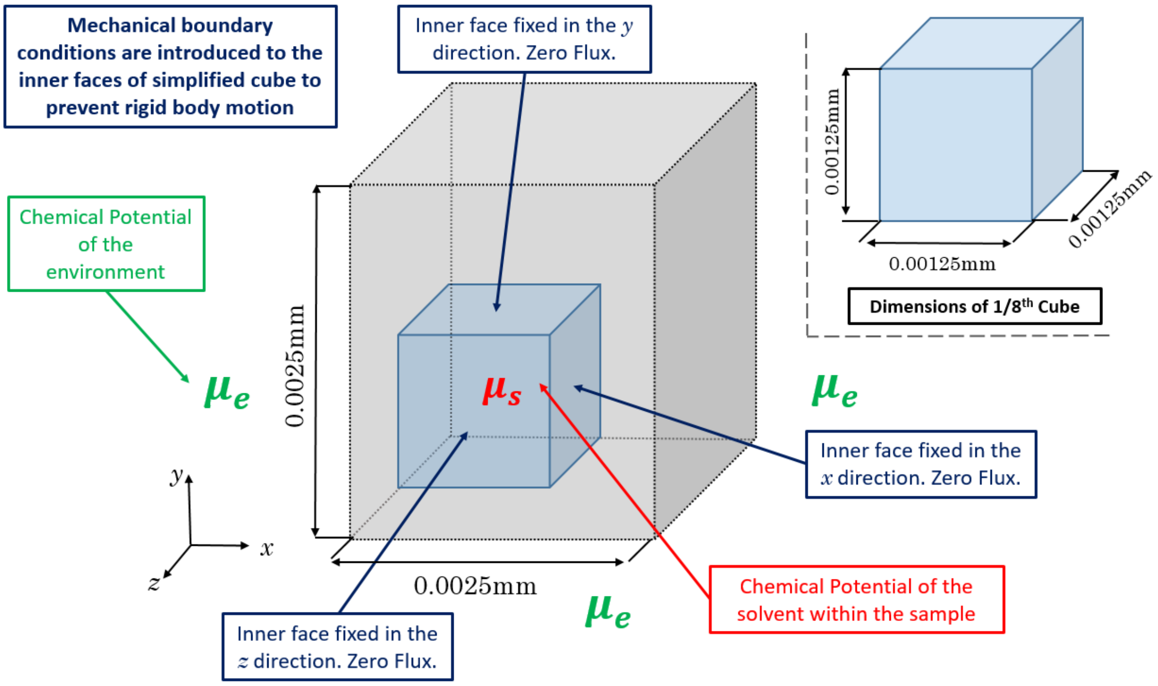

Figure 3.19: A simple cube split into a 1/8th section with symmetry enforced on the internal faces (zero flux and displacement perpendicular to the face) and a Dirichlet boundary condition specified on the external faces representing climatic changes.

The test was carried out for three different scenarios. The first scenario (Case 1) is a simple free-swelling test was carried out. This test demonstrates the ability of the model to capture deformations due to changes in the moisture content of the surrounding environment.

In the second scenario (Case 2) the dashpot was changed from having a relatively high viscosity, and therefore a slow relaxation of the intramolecular bonds within the network of the gel, to having a lower viscosity, and a faster relaxation of the intramolecular bonds within the network of the gel. This is the same approach that was suggested by Govindjee et al [46] as a method of capturing the polymer in different material states.

In the third scenario (Case 3), the sensitivity of the model to changes in the permeability of the material is assessed. The permeability of the material is one of several material parameters that determine the diffusivity of the material, given in Eq. (2.37). These also include the stiffness of the two springs and their corresponding Poisson's ratio. The viscosity of the fluid, in this case water, remains as a constant at a given temperature. Therefore Eq. (2.37) can be thought of as a function of the permeability and the stiffness of the material. In this case the stiffness of each spring remains constant and only the permeability of the material is changed. However it is important to keep in mind that the changes in the stiffness will have a similar effect. This will become of more importance further on (Chapter 4).

Numerical Approach

A 1/8th section of the cube was modelled due to symmetry. As such, the internal faces had symmetrical boundary conditions applied, i.e. zero flux and zero displacements in the direction normal to the face. The chemical potential of the surrounding environment was applied on the external faces (i.e. the faces exposed to the environment) and the external faces had no constraints upon the displacements. The increased environmental chemical potential on the boundary, μ_e was applied for 0.0004 seconds before being instantaneously returned to the reference chemical potential of the solvent within the gel, μ_s.

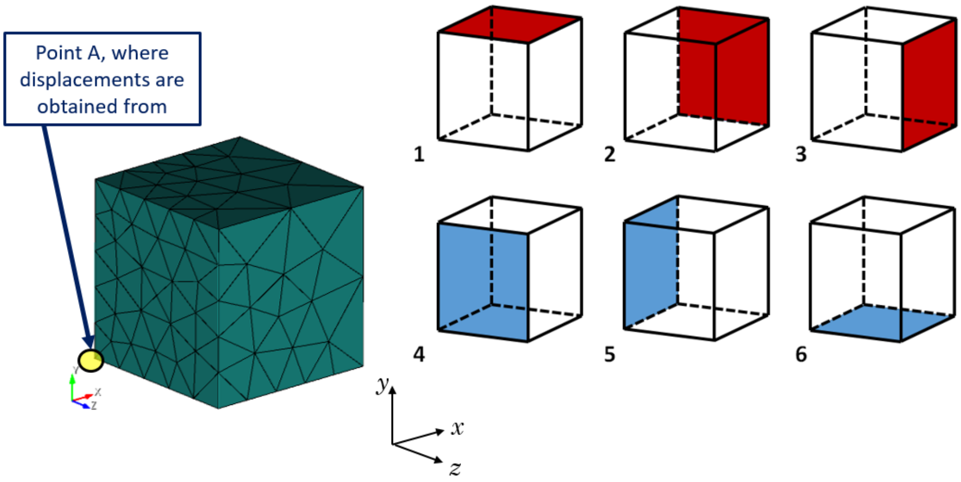

Figure 3.20: 1/4 Cube of cellulose polymers with a fine mesh on the surfaces where the μ_e is applied, transitioning to a coarse mesh at the middle of the sample. The mesh consists of 375 10 node tetrahedral elements. Points A represents the position of the node from which time series data are obtained for displacements. The faces where mechanical and chemical boundary conditions are applied are numbered and highlighted in blue (for outer surfaces exposed to the environment) and red (for inner surfaces where mechanical boundary conditions are applied).

Face	Mechanical Conditions	Chemical Conditions
1	$u_y = 0$	$\frac{\partial \mu_s}{\partial y} = 0$
2	$u_x = 0$	$\frac{\partial \mu_s}{\partial x} = 0$
3	$u_z = 0$	$\frac{\partial \mu_s}{\partial z} = 0$
4	-	μ_e
5	-	μ_e
6	-	μ_e

Table 3.9: Boundary conditions for the sorption test. The boundaries (Faces 1-6) where mechanical and chemical boundary conditions are applied are visualised in Figure 3.20.

Parameter	Value	Units	Time
μ_e	1.5×10^{06}	$\mathrm{J\,mol^{-1}}$	0.00s - 0.000004s
μ_e	3.0×10^{06}	$\mathrm{J\,mol^{-1}}$	0.000004s - 0.000080s
μ_e	1.5×10^{06}	$\mathrm{J\,mol^{-1}}$	0.000080s - 0.000160s
μ_s	1.5×10^{06}	$\mathrm{J\,mol^{-1}}$	0.00s

Table 3.10: Chemical potential conditions, applied to faces 4,5 and 6, for the sorption test. The environmental chemical potential, μ_e is applied on boundaries according to Table 3.9. μ_s is the initial chemical potential within the sample and is allowed to evolve within the gel after the first time step.

3.2.1 Case 1 - A Simple Free-Swelling Test

In Case 1 the behaviour of the model is examined for a single combination of material parameters, given in Table 3.11. The relatively high dashpot viscosity $\hat{G}^{\beta}$ is representative of a polymeric material in a glassy state, where the relaxation of the intramolecular hydrogen bonds within the gel occurs slowly. The increased external chemical potential of 3.0×10^{06} $\mathrm{J\,mol^{-1}}$ was applied instantly on the boundary at time zero for 0.00004s until it was reduced to 1.5×10^{06} $\mathrm{J\,mol^{-1}}$, i.e. equal to the internal chemical potential, μ_s, of the gel at time zero (see Figure 3.21).

Figure 3.22 demonstrates the behaviour of the dashpot alongside the displacement of the polymer. At this stage the polymer was behaving like an elastic solid, exhibiting Fickian diffusion behaviour. This was characterised by a very slow evolution of the Dashpot Strain. When observing the displacement time series it was clear that the material seemed to have reached equilibrium, where the rate of change of the displacements is zero. However, it can be seen from the Dashpot Strain that the displacement must have been increasing at a very slow rate as the relaxation of the intramolecular bonding was occuring at a very slow rate. As the relocation of polymer molecules was still ongoing, the system had not yet attained equillibrium. Vrentas et al [111] defined material behaviour below the glass transition as a non-equilibrium liquid structure, and regarded the glass transition temperature as the temperature below which it is not possible to obtain an experimental time for equilibrium. Therefore, in this case, the observed behaviour could be defined as Fickian diffusion in a non-equilibrium liquid structure.

Input Parameter	**Symbol**	**Value**	**Units**
Shear Modulus Spring α	G^{α}	3×10^{03}	MPa
Shear Modulus Spring β	G^{β}	3×10^{03}	MPa
Viscosity of Dashpot β	$\hat{G^{\beta}}$	9×10^{04}	MPa.s
Poisson's Ratio Spring α	ν^{α}	0.232	-
Poisson's Ratio Spring β	ν^{β}	0.232	-
Poisson's Ratio Dashpot β	$\hat{\nu^{\beta}}$	0.232	-
Volume per Mole of Water	Ω	18000	$\mathrm{mm}^3\,\mathrm{mol}^{-1}$
Permeability	κ	1×10^{-12}	mm^2

Table 3.11: Material Input data for the sorption verification test.

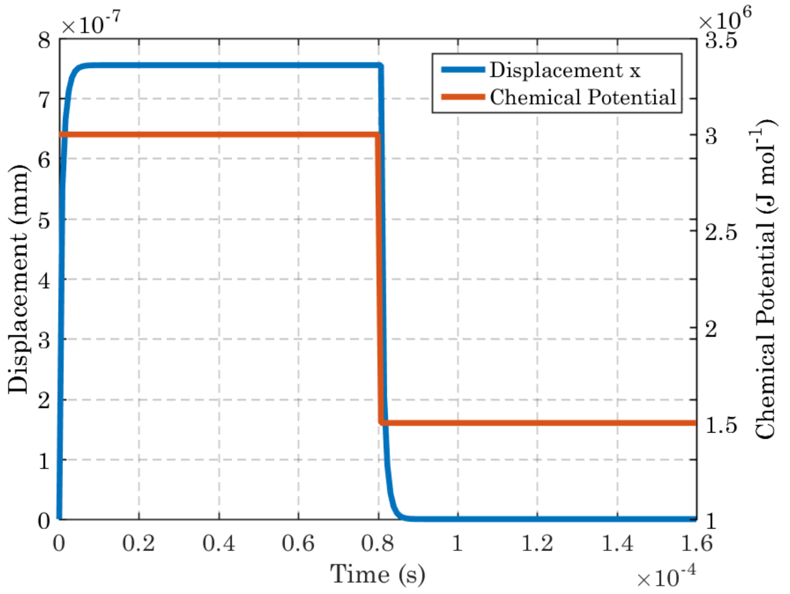

Figure 3.21: Displacement in the x direction, taken at point A, (left vertical axis) and the chemical potential of the environment μ_e (right vertical axis) as a function of time.

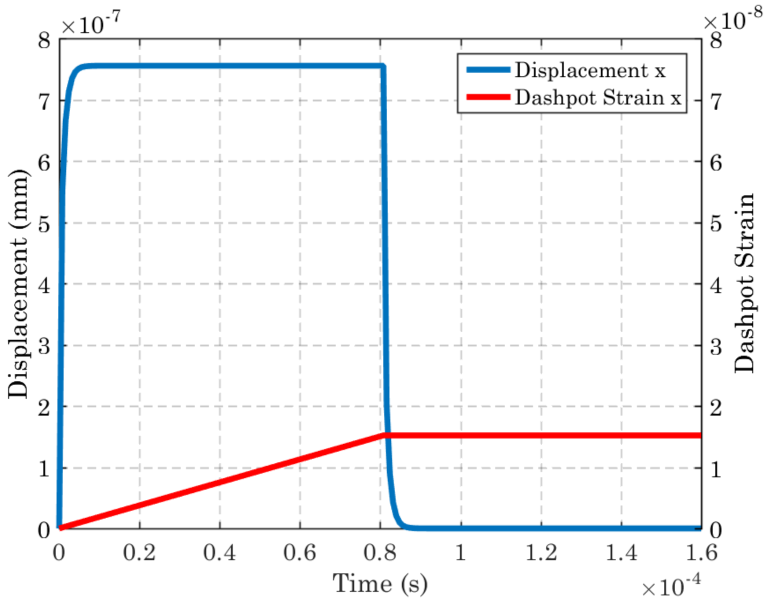

Figure 3.22: Displacement time series in the x direction (left vertical axis) and the dashpot strain, $\hat{\varepsilon}_{xx}$, (right vertical axis). Both time series are taken at Point A.

3.2.2 Case 2 - Influence of the Dashpot Shear Modulus

In this example, the ratio of $\hat{G}^{\beta}$ and G^{β} was changed, in a similar manner to the Creep Test Case 3. The shear modulus of the spring β, G^{β}, was kept constant and the value of $\hat{G}^{\beta}$ was changed in order to capture a wide range of viscoelastic relaxation times, shown in Table 3.13. All other material parameters were kept constant and are given in Table 3.12. Both springs, α and β, were assigned equal shear moduli, therefore giving an equal contribution of elastic and viscoelastic deformations by the time the dashpot was fully relaxed.

Input Parameter	**Symbol**	**Value**	**Units**
Shear Modulus Spring α	G^{α}	3×10^{03}	MPa
Shear Modulus Spring β	G^{β}	Table 3.13	MPa
Viscosity of Dashpot β	$\hat{G}^{\beta}$	Table 3.13	MPa.s
Poisson's Ratio Spring α	ν^{α}	0.232	-
Poisson's Ratio Spring β	ν^{β}	0.232	-
Poisson's Ratio Dashpot β	$\hat{\nu^{\beta}}$	0.232	-
Volume per Mole of Water	Ω	18000	$\mathrm{mm}^3\ \mathrm{mol}^{-1}$
Permeability	κ	1×10^{-12}	mm^2
Viscosity of Water	η	1×10^{-06}	MPa.s

Table 3.12: Material data for the viscoelastically limited diffusion test. The combinations of shear modulus in spring β, G^{β}, and the dashpot viscosity, $\hat{G}^{\beta}$ is given in Table 3.13.

Combination	$\hat{G}^\beta$ (MPa.s)	G^β (MPa)	τ_v (s)
Combination 1	0.0000001	3×10^3	3.333×10^{-11}
Combination 2	9×10^4	3×10^3	30
Combination 3	0.01	3×10^3	0.00000333
Combination 4	0.05	3×10^3	0.0000167
Combination 5	0.1	3×10^3	0.0000333
Combination 6	0.25	3×10^3	0.0000833
Combination 7	0.5	3×10^3	0.000167

Table 3.13: Material data for a variety of different relaxation times. In each case the shear modulus of the spring, G^β, remains the same and the value of the dashpot shear modulus $\hat{G}^\beta$ determines τ_v.

Similar to Creep Test 3, the material behaviour either side of the viscoelastic time frame was captured, i.e. pre relaxation poroelasticity and post relaxation poroelasticity, as well as more complex behaviour between the two extremes.

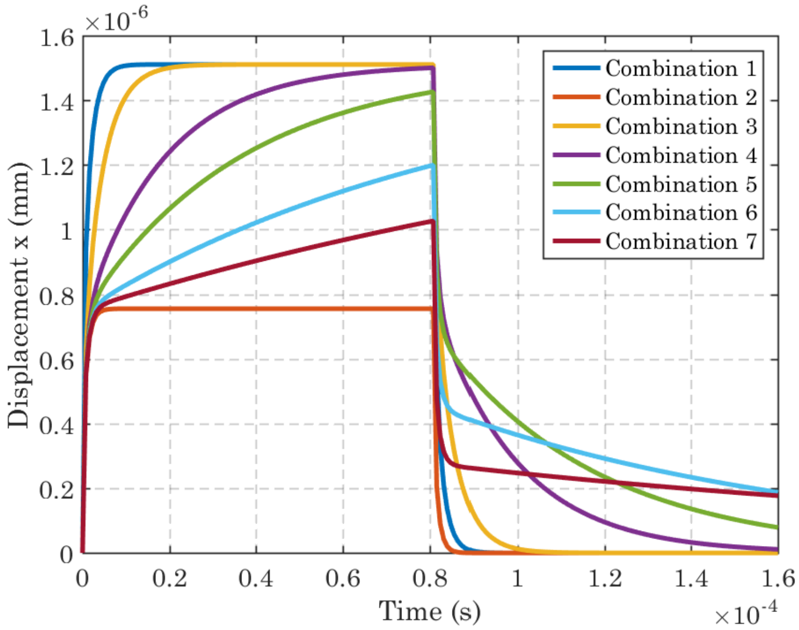

Figure 3.23: Sensitivity of the model to the dashpot viscosity, $\hat{G}^\beta$, whilst keeping the shear modulus of spring β, G^β, constant. The vertical axis shows the displacement in the x direction.

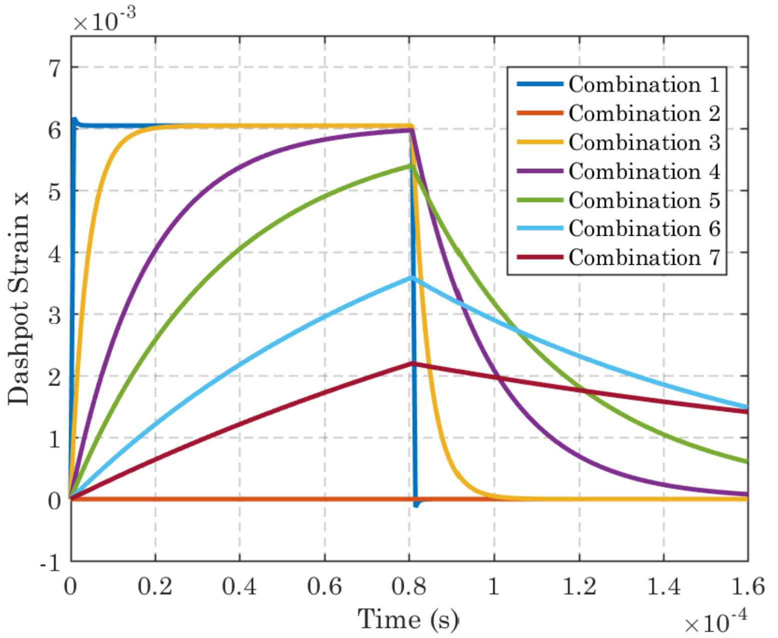

Figure 3.24: Sensitivity of the model to the dashpot viscosity, $\hat{G}^{\beta}$, whilst keeping the shear modulus of spring β, G^{β}, constant. The vertical axis shows the dashpot strain, $\hat{\varepsilon}_{xx}$.

Figure 3.23 shows the displacement, taken at point A, for various different states of relaxation. Test 1 and test 2 give the upper bound and lower bound material behaviour, where the rate of solvent migration is governed by the diffusivity and the viscoelastic properties have no effect, where Combination 1 demonstrates post instantaneous relaxation and Combination 2 demonstrates pre-relaxation behaviour (i.e. rubbery and glassy material behaviours respectively).

Combinations 3 and 4 demonstrated fully reversible deformation within the time frame, however the flow of solvent through the polymer was limited by the viscoelastic process, i.e. the internal realignment of polymer chains to accommodate an increased volume of solvent. Combinations 5-7 all exhibited viscoelastic deformations, not reversible within the observed time frame. All three are slowly returning to their reference configuration at different rates.

3.2.3 Case 3 - Influence of the Diffusivity

To verify whether or not viscoelastically limited solvent migration was being observed, the diffusivity was both increased and decreased and the effects observed. Table 3.14 gives the material parameters applied to each spring and the dashpot, which were kept constant in this case. Table 3.12 gives the other material parameters, including the permeability, κ.

Input Parameter	**Symbol**	**Value**	**Units**
Shear Modulus Spring α	G^{α}	3×10^{03}	MPa
Shear Modulus Spring β	G^{β}	3×10^{03}	MPa
Viscosity of Dashpot β	$\hat{G}^{\beta}$	0.1	MPa.s
Poisson's Ratio Spring α	ν^{α}	0.232	-
Poisson's Ratio Spring β	ν^{β}	0.232	-
Poisson's Ratio Dashpot β	$\widehat{\nu^{\beta}}$	0.232	-
Volume per Mole of Water	Ω	18000	$\mathrm{mm}^3\ \mathrm{mol}^{-1}$
Permeability	κ	Table 3.15	mm^2
Viscosity of Water	η	1×10^{-06}	MPa.s

Table 3.14: Material data assigned to the springs and dashpot within the rheological model (Figure 2.2) for Test 2. The value of permeability, κ, used for each combination within Case 3 is given in Table 3.15.

Several different values of the permeability are given in Table 3.15, that were used to carry out a study into the influence of the diffusivity on the displacements and interplay between poroelastic and viscoelastic processes.

Combination	κ (mm^2)
Combination 8	1×10^{-10}
Combination 9	1×10^{-11}
Combination 10	1×10^{-12}
Combination 11	1×10^{-13}
Combination 12	1×10^{-14}

Table 3.15: Material data for different combinations. In each combination the shear modulus of the spring, G^{β}, remains the same and the value of the dashpot viscosity $\hat{G}^{\beta}$ determines τ_v

Figure 3.25 shows the displacements obtained at point A, plotted against time. For Combinations 8-10 ($\kappa = 1 \times 10^{-10}$ - $\kappa = 1 \times 10^{-12}$) there was virtually no difference in the rate of solvent uptake (i.e. rate of volume change), despite the corresponding increase in the diffusivity (Eq. (2.37)), clearly indicating that the rate of swelling was viscoelastically limited. However, the rate of solvent uptake did undergo a noticeable drop when the permeability was reduced in Combinations 11-12 ($\kappa = 1 \times 10^{-13}$ and $\kappa =$

1×10^{-14}). The significance of this being the solvent migration was not viscoelastically limited for these given parameters in the conditions presented but instead was a complex interplay between both diffusion and relaxation.

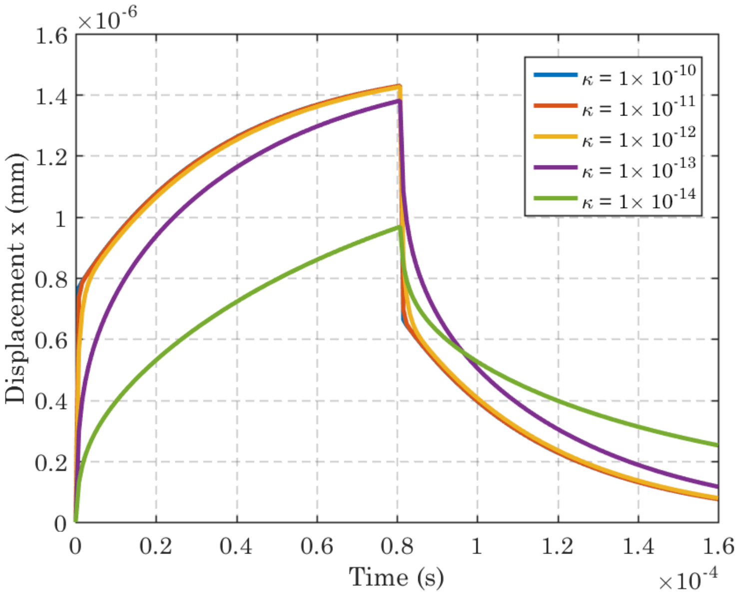

Figure 3.25: Displacement time series for the sorption experiment, demonstrating the effect of different values of permeability of the polymer.

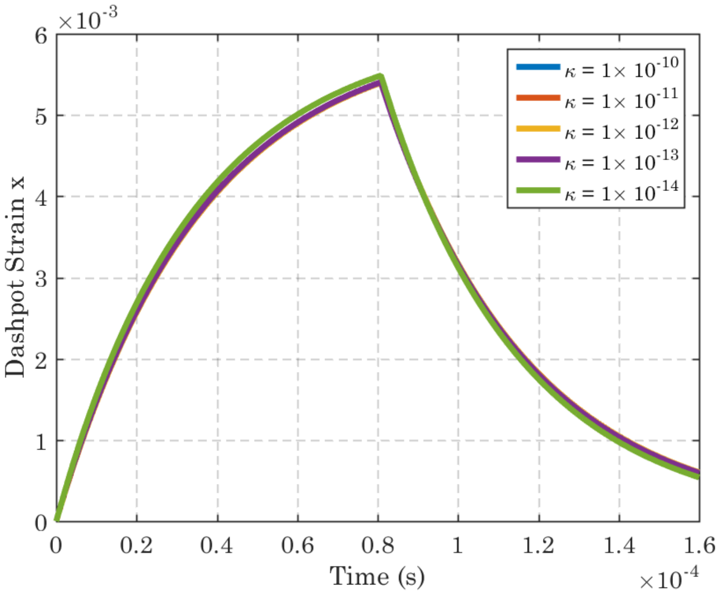

Figure 3.26: Dashpot strain, $\hat{\varepsilon}_{xx}$, time series for the sorption experiment, demonstrating the effect of different values of permeability of the polymer.

The dashpot strain time series is presented in Figure 3.26, showing very little change between each value of permeability presented. This result was expected as the ratio of the dashpot shear modulus to the spring modulus of spring β ($\hat{G}^{\beta}/G^{\beta}$), i.e. the time of viscoelastic relaxation, is the same for each Combination (8-12). Furthermore, there was little change in the overall magnitude of swelling (Figure 3.25), with the exceptions being

Combination 12 and to a lesser extent Combination 11 which still results in a similar overall magnitude of swelling to Combinations 8 -10 (Table 3.15).

The approaches demonstrated in Case 2 and 3 are relevant to wood sorption theory, as discussed in Chapter 1, where sorption hysteresis is linked with changes around the glass transition in the polymer (i.e. the change between glassy and rubbery material behaviour) [52, 54, 116]. If viscoelastic deformations can be captured due to changes in the moisture content of the external environment, under no external loading or constraints, it can provide an indication that the model may be able to capture moisture hysteresis in the future. This would provide a good basis for applying to wood cells where capturing sorption hysteresis is an important factor in life cycle design and/or moisture induced warping.

3.3 Test 3: The Response of a Complex Multi-Layered Composite to a Change in the Moisture Content of the Surrounding Environment

Description of the Test

Many natural composites, such as wood, that are polymeric gels at the polymer level, contain cells which are complex multi-layer structures with interactions occurring between layers, each with different material properties. The different types and arrangement of cells give a similar effect, i.e. concentric rings of latewood and earlywood cells leading to a very complex composite structure. These complex arrangements may play a role in moisture induced deformations.

To assess the capability of the model to capture the interactions between layers, a simple two layer polymeric gel with different properties assigned to each layer is introduced. The aim was to capture complex viscoelastic creep behaviour between the layers. It was anticipated that this would lead to small changes in the geometry of the problem as the process of molecular realignment takes place during the viscoelastic phase.

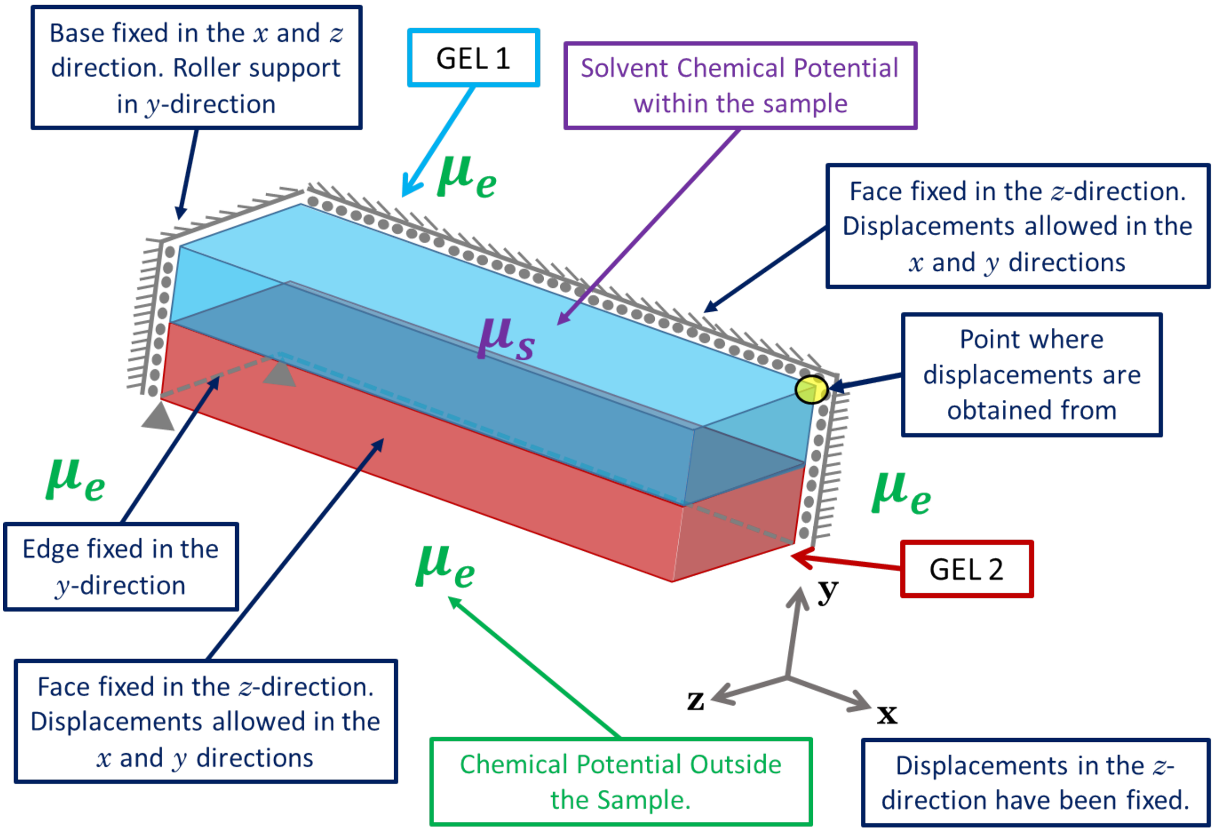

Figure 3.27: Set up for a multi-layered composite test to assess the response to a change in the moisture content of the surrounding environment. GEL 1 and GEL 2 were assigned different material properties in order to view the sensitivity and behaviour of composite gels. Displacements are only considered in the x and y directions.

In this example two Cases were examined. First, when each layer in the gel composite was assigned a different stiffness, allowing for different magnitudes of swelling to occur in each layer, as the sample with the lower shear modulus adsorbed more solvent than its stiffer counterpart. Second, the problem when the stiffness in both layers is identical, but a different permeability is assigned to each was examined. In this case it was the different sorption kinetics of each layer that caused warping of the gel composite.

Numerical Approach

Figure 3.27, shows the set up used for the multi-layer problem, with the point where displacements are obtained from marked in yellow. Different combinations of material properties were assigned to each block, denoted GEL 1 and GEL 2. The gel was fixed at one end and the displacements in the z direction are constrained throughout the sample. Thus the swelling was accounted for by an increase in length in the x direction and/or deflection towards the y direction. The two layers of gel share a common surface as it is assumed that the polymers are chemically bonded.

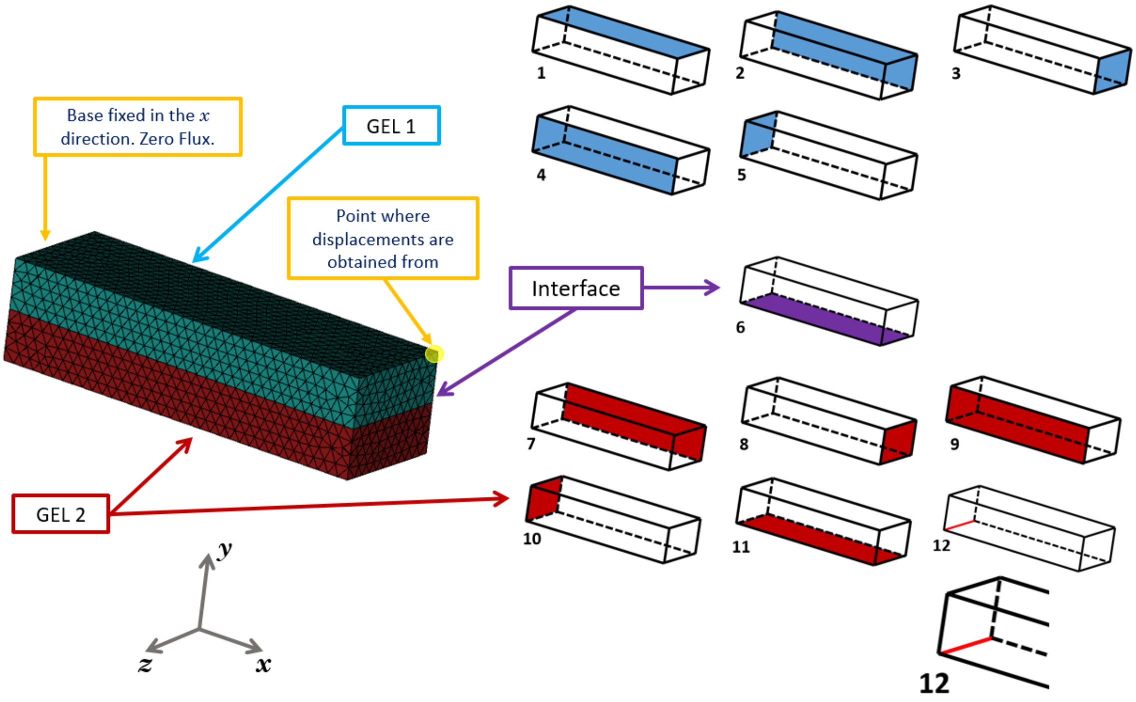

Figure 3.28: Mesh used for the multi-layered composite test. The composite gel has had symmetry enforced along the x-y plane. The yellow dot corresponds to the position of the yellow dot in Figure 3.27, where the displacements are obtained from for Case 1 and 2. The faces/edges where mechanical and chemical boundary conditions are applied are numbered and highlighted for both GEL 1 (blue) and GEL 2 (red). The interface between the two Gels is shown in purple.

Parameter	**Value**	**Units**	**Time**
μ_e	1.5×10^{06}	J mol^{-1}	0.00s
μ_e	3.0×10^{06}	J mol^{-1}	0.000004s - 0.000040s
μ_e	1.5×10^{06}	J mol^{-1}	0.000044s - 0.000080s
μ_s	1.5×10^{06}	J mol^{-1}	0.00s

Table 3.16: Chemical potential conditions, applied to faces 1,3,4,8,9 and 11 for the Complex Multi-Layered Composite test. The environmental chemical potential, μ_e is applied on boundaries according to Table 3.17. The chemical potential of the solvent, μ_s, within the sample is given for $t = 0$ and is allowed to evolve freely at $t > 0$.

Number	**Feature**	**Mechanical Conditions**	**Chemical Conditions**
1	Face	-	μ_e
2	Face	$u_z = 0$	$\frac{\partial \mu_s}{\partial z} = 0$
3	Face	-	μ_e
4	Face	$u_z = 0$	μ_e
5	Face	$u_x = 0$	$\frac{\partial \mu_s}{\partial x} = 0$
6	Face	-	-
7	Face	$u_z = 0$	$\frac{\partial \mu_s}{\partial z} = 0$
8	Face	-	μ_e
9	Face	$u_z = 0$	μ_e
10	Face	$u_x = 0$	$\frac{\partial \mu_s}{\partial x} = 0$
11	Face	-	μ_e
12	Edge	$u_y = 0$	-

Table 3.17: The boundary conditions for the Complex Multi-Layered Composite test. The boundaries (Faces 1-11 and Edge 12) where mechanical and chemical boundary conditions are applied are visualised in Figure 3.28. The magnitude of the chemical boundary conditions are given in Table 3.16.

The mesh used for the multi-layered composite test is given in Figure 3.28, where the faces and edges where boundary conditions are highlighted in blue (for GEL 1) and red (for GEL 2). The chemical potential conditions are given in Table 3.16, where the chemical potential for the surrounding environment, μ_e, is varied according to the time column. The initial chemical potential of the solvent within the sample at time zero is given as μ_s, and it is allowed to evolve freely after the first time step.

3.3.1 Case 1 - Influence of Shear Modulus

In Case 1, the two layers of gel have different shear moduli and were exposed to a change in the environmental conditions. The different shear moduli assigned to each gel resulted in a different magnitude of swelling in each gel, and therefore a warping of the composite (shown in Figure 3.29 - 3.31) and a high concentration of shear on the interface between the layers.

Input Parameter	**Symbol**	**GEL 1**	**GEL 2**	**Units**
Shear Modulus Spring α	G^{α}	3×10^{03}	6×10^{03}	MPa
Shear Modulus Spring β	G^{β}	3×10^{03}	6×10^{03}	MPa
Viscosity of Dashpot β	$\hat{G}^{\beta}$	3	3	MPa.s
Poisson's Ratio Spring α	ν^{α}	0.232	0.232	-
Poisson's Ratio Spring β	ν^{β}	0.232	0.232	-
Poisson's Ratio Dashpot β	$\hat{\nu}^{\beta}$	0.232	0.232	-
Volume per Mole of Water	Ω	18000	18000	mm^3 mol^{-1}
Permeability	κ	1×10^{-12}	1×10^{-12}	mm^3/s
Viscosity of Water	η	1×10^{-06}	1×10^{-06}	MPa.s

Table 3.18: Material data for the test with two layers of polymeric gel. The shear modulus in GEL 1 is half that of GEL 2 for both springs α and β.

Table 3.18 shows the material properties for Case 1, where the assigned shear modulus of GEL 1 was lower than that of GEL 2. However the shear modulus of the Dashpot, G^{β}, is the same for both samples, leading to a different time of viscoelastic relaxation τ_v in each layer of the composite.

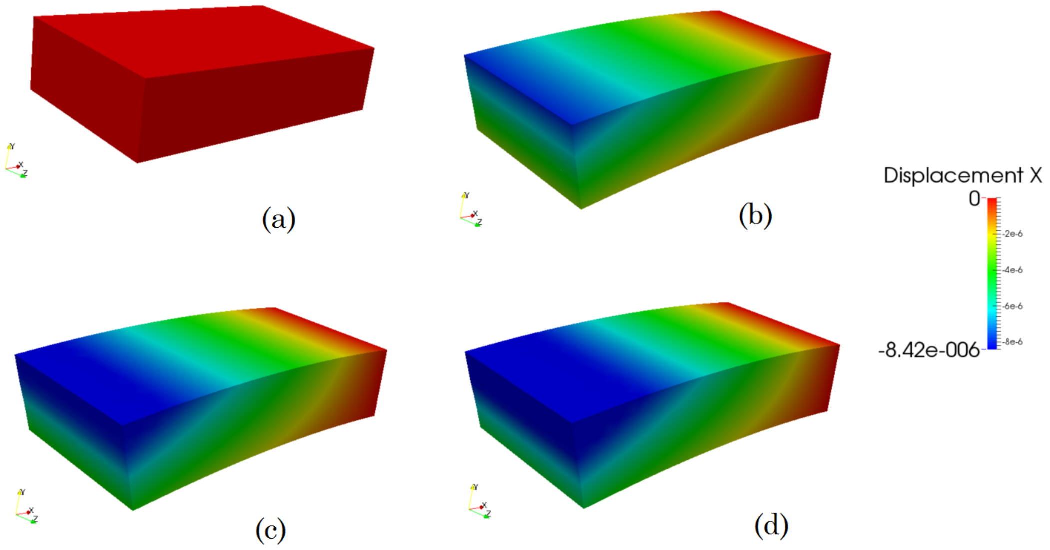

Figure 3.29: Displacement in the x direction for the two layer gel test. (a) 0.000008s (b) 0.000080s (c) 0.000160s (d) 0.000400s. A scale factor of 20 is applied to the displacements to exaggerate the deformations.

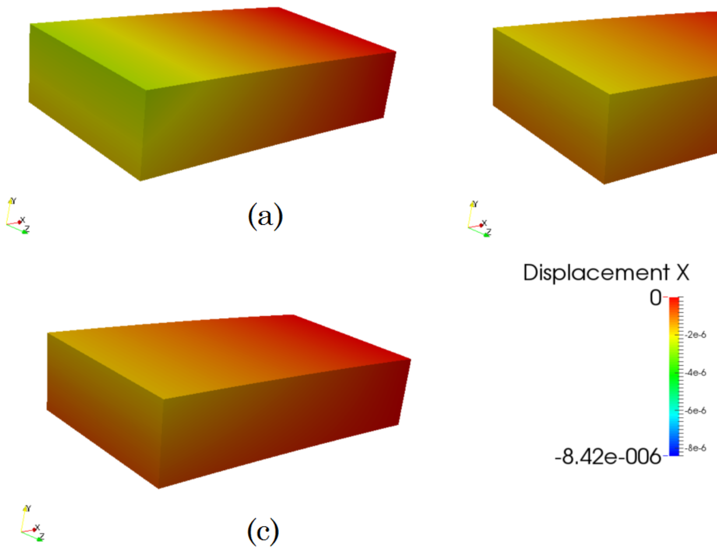

Figure 3.30: Recovery of the displacement in the x direction for the two layer gel test after the external chemical potential is returned back to μ_0. (a) 0.000408s (b) 0.000480s (c) 0.000560s (d) 0.000800s. A scale factor of 20 is applied to the displacements to exaggerate the deformations.

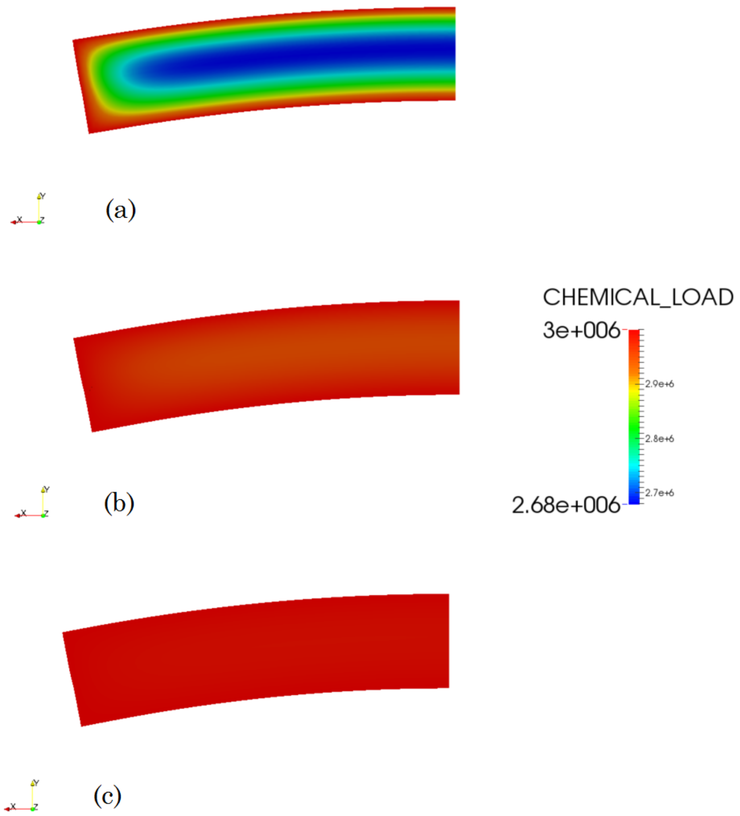

Figure 3.31: Chemical potential evolution through the two layers of polymer network for the first three timesteps. (a) 0.000008s (b) 0.0000160s (c) 0.0000240s. A scale factor of 20 is applied to the displacements to exaggerate the deformations.

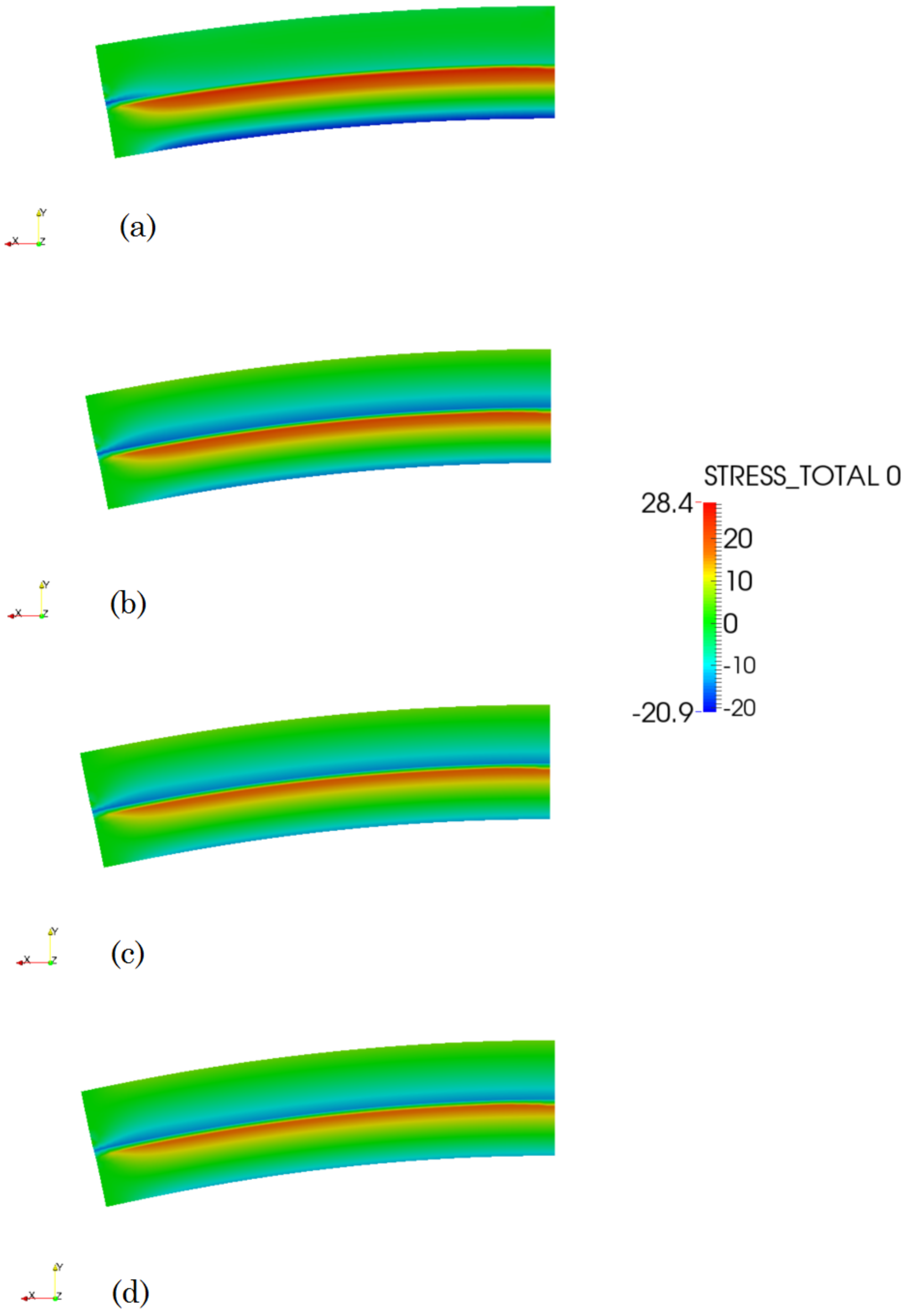

Figure 3.32: Stress, σ_{xx}, along the boundary between the two layers of polymer network. (a) 0.000008s (b) 0.000080s (c) 0.000160s (d) 0.000400s. A scale factor of 20 is applied to the displacements to exaggerate the deformations.

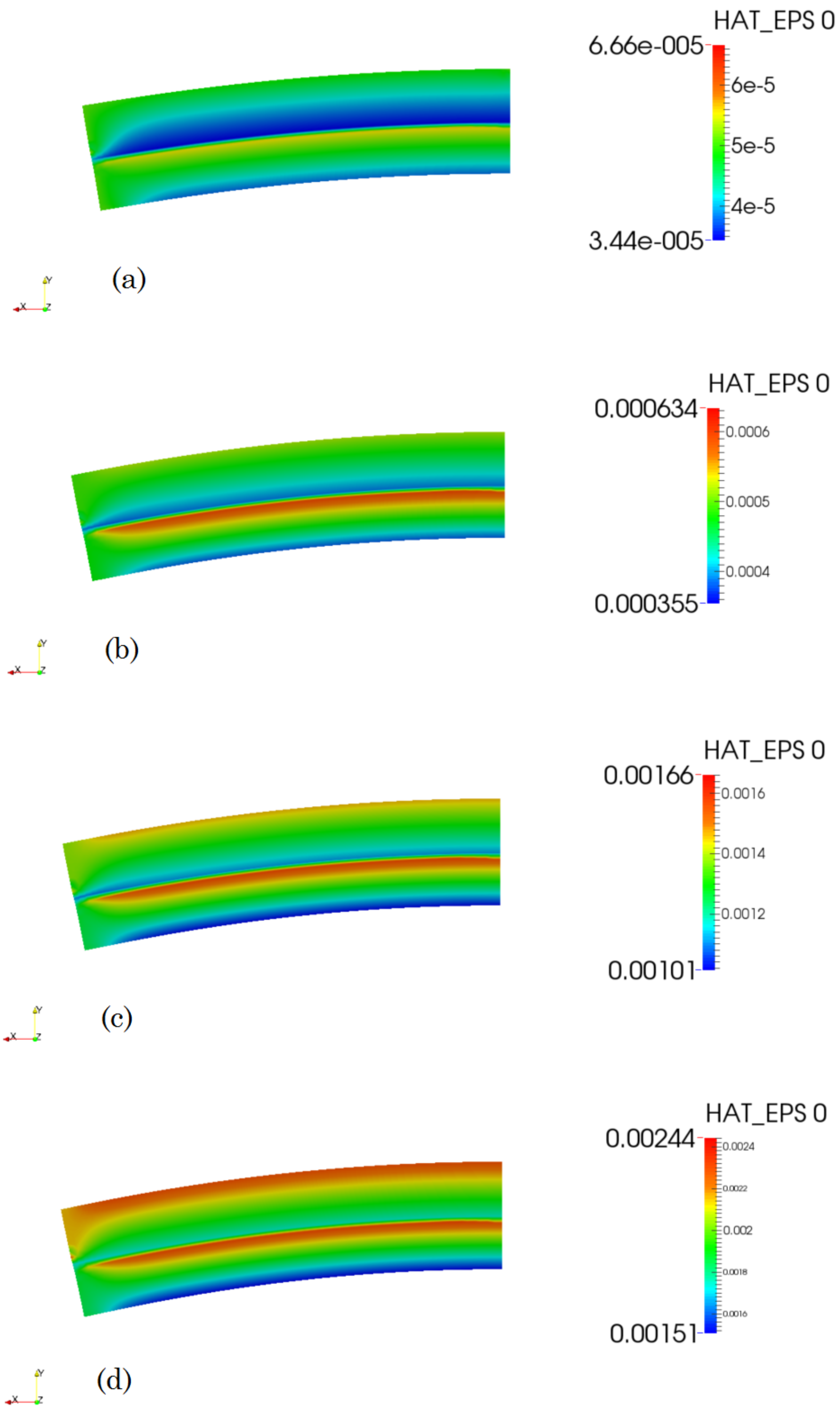

Figure 3.33: Dashpot Strain, ε_{xx}, along the boundary between the two layers of polymer network. ((a) 0.000008s (b) 0.000080s (c) 0.000160s (d) 0.000400s. A scale factor of 20 is applied to the displacements to exaggerate the deformations.

Figures 3.29 and 3.30 show the displacements in adsorption and desorption respectively. The displacements increase all the way until the chemical potential on the boundary changes. By examining the chemical potential flow through both layers of gel (Figure 3.31) it can be seen that the flow through the sample was achieved within the first three time steps, thus the further displacements can be accounted for as viscoelastic deformations caused by the stresses within the sample. Figure 3.31 (a) also shows a small difference in the evolution of the chemical potential through the sample, between the two layers of gel. The bottom layer of gel (i.e. below the neutral axis of bending), has a generally higher chemical potential that the top layer of gel, despite each having the same permeability. This result is due to two reasons. First, according to Eq. (2.37), a higher stiffness will yield a higher rate of diffusion. Second, due to the hogging motion, the high area below the neutral axis will be undergoing compressive stresses.

As can be seen in Figure 3.30, there was a change in configuration at the end of the test due to the viscoelastic deformations. This demonstrates a viscoelastic deformation not reversible within the observed time frame.

Further Variation in the Shear Modulus

To further analyse the displacements due to variation in the shear modulus, the shear modulus in spring β was varied and the effects observed. Three Combinations were studied where the shear modulus in spring β was assigned lower than spring α (Combinations 1-3) as well as a further three Combinations where spring β has a greater shear modulus than spring α (Combinations 4-6). In each Combination the rate of the viscoelastic process changed due to the variation G^β while $\hat{G}^\beta$ remained constant. Hence the time of viscoelastic relaxation τ_v was be different for each Combination.

Input Parameter	**Symbol**	**GEL 1**	**GEL 2**	**Units**
Shear Modulus Spring α	G^α	Table 3.20	6×10^{03}	MPa
Shear Modulus Spring β	G^β	Table 3.20	6×10^{03}	MPa
Viscosity of Dashpot β	$\hat{G}^\beta$	3	3	MPa.s
Poisson's Ratio Spring α	ν^α	0.232	0.232	-
Poisson's Ratio Spring β	ν^β	0.232	0.232	-
Poisson's Ratio Dashpot β	$\hat{\nu^\beta}$	0.232	0.232	-
Volume per Mole of Water	Ω	18000	18000	$\mathrm{mm}^3\ \mathrm{mol}^{-1}$
Permeability	κ	1×10^{-12}	1×10^{-12}	mm^3/s
Viscosity of Water	η	1×10^{-06}	1×10^{-06}	MPa.s

Table 3.19: Material data for the test with two layers of polymeric gel. The shear modulus of GEL 1 can be found in Table 3.20.

The evolution of the dashpot strain is plotted in Figure 3.36, showing large variation in the viscoelastic response within the polymer. Furthermore, as the shear modulus was increased, the overall system became stiffer, resulting in a smaller displacement along the polymer in the x-direction. This is plotted in Figure 3.35, where each displacement was positive in the direction of the x axis, with a small decrease each time the overall stiffness of the system was increased. Figure 3.34 shows the variation in y displacements. For Combinations 1-3 (G^β = 3-5 GPa) there is a negative displacement, as more swelling occurred in the top layer of the composite than in the stiffer layer below. Conversely in Combinations 4-6 a displacement in the positive in the direction of the y-axis was observed.

Combination	G^{α}	G^{β}	Units
Combination 1	6×10^{03}	3×10^{03}	MPa
Combination 2	6×10^{03}	4×10^{03}	MPa
Combination 3	6×10^{03}	5×10^{03}	MPa
Combination 4	6×10^{03}	7×10^{03}	MPa
Combination 5	6×10^{03}	8×10^{03}	MPa
Combination 6	6×10^{03}	9×10^{03}	MPa

Table 3.20: Material data for GEL 1 for different combinations. In each combination the shear modulus of the spring, G^{α}, remains the same and the values of the spring, G^{β}, relative to the dashpot shear viscosity, $\hat{G}^{\beta}$, determines the viscoelastic relaxation time, τ_v.

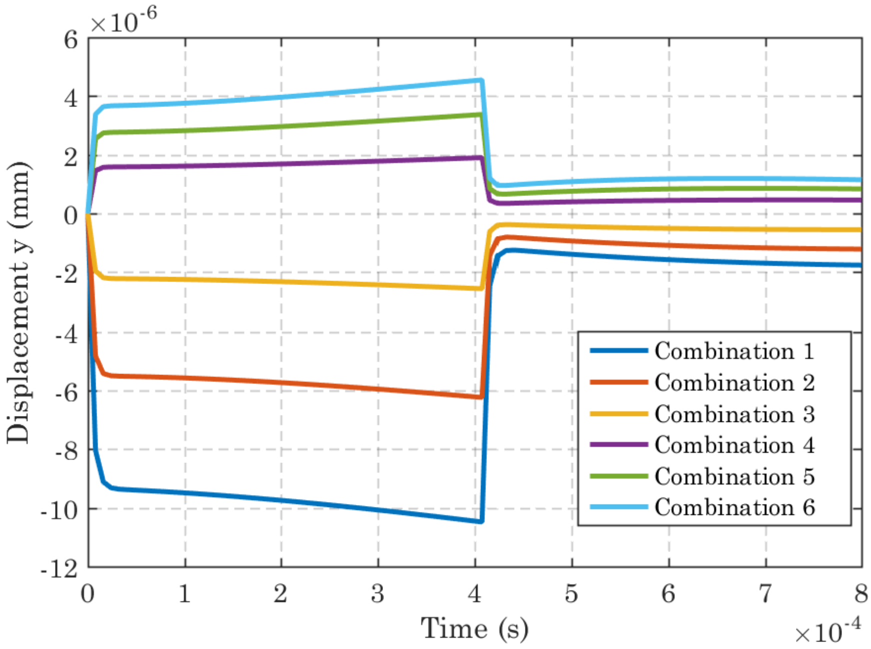

Figure 3.34: Displacement histories in the y direction due to the change in climatic conditions surrounding the polymeric gel. The legend within the graph gives the shear modulus of spring beta, G^{β}, for each corresponding line in the graph.

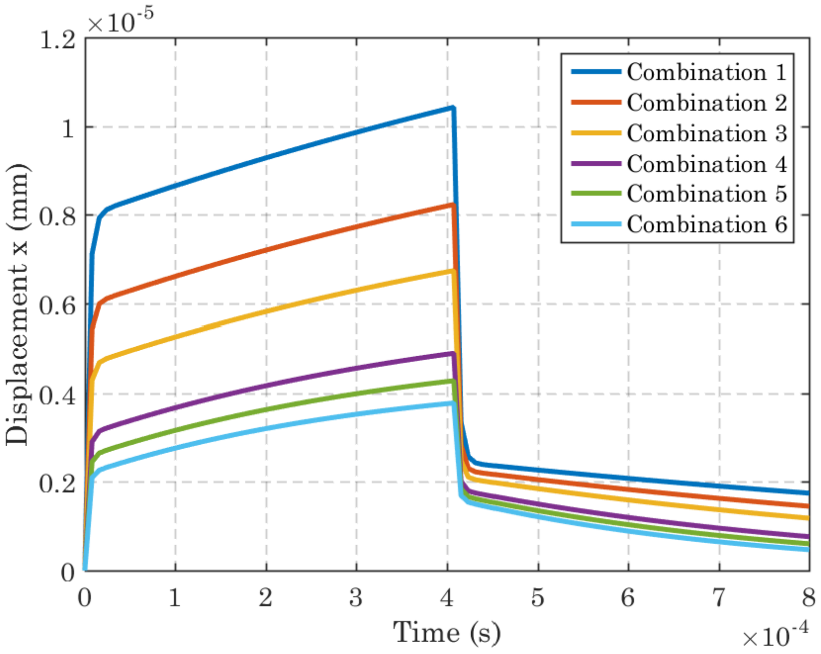

Figure 3.35: Displacement histories in the x direction due to the change in climatic conditions surrounding the polymeric gel. The legend within the graph gives the shear modulus of spring beta, G^{β}, for each corresponding line in the graph.

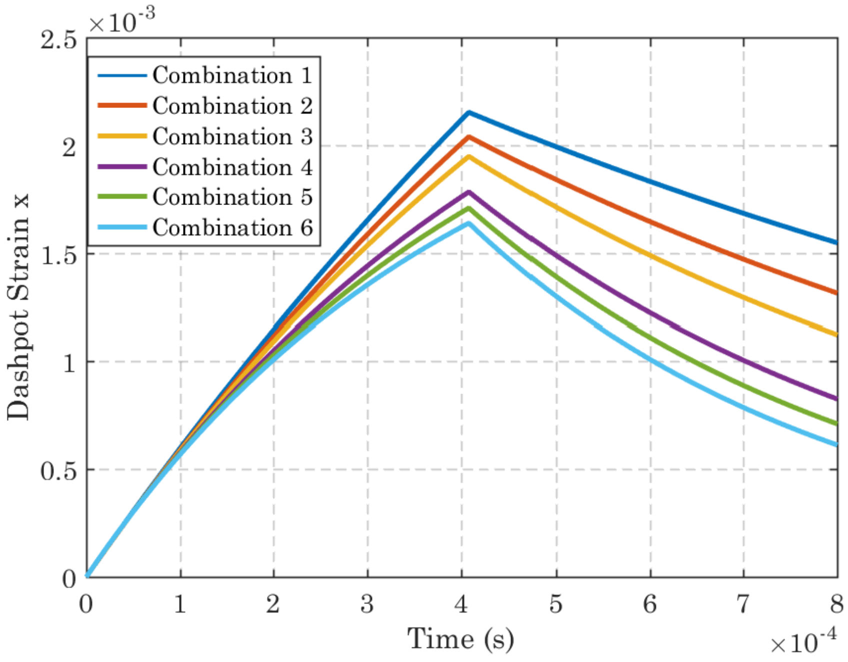

Figure 3.36: Dashpot strain, $\hat{\varepsilon}_{xx}$, histories due to the change in climatic conditions surrounding the polymeric gel. The legend within the graph gives the shear modulus of spring beta, G^{β}, for each corresponding line in the graph.

3.3.2 Case 2 - Influence of the Permeability of the Gel

In Case 2, each layer of the composite is assigned identical stiffness properties. However different values of permeability are assigned. This showed the effect of the sorption kinetics upon the overall deformations of the composite and demonstrated how the model could be applied to more complex kinetic problems, such as a multi-layered wood cell.

For each Combination the time of viscoelastic relaxation (τ_v) was constant. Hence the amount of viscoelastic deformation at the end of the cycle was determined by how long the stress in the sample took to relax, and therefore how much time the molecular chains within the polymer have had to conform to a new arrangement.

Input Parameter	**Symbol**	**GEL 1**	**GEL 2**	**Units**
Shear Modulus Spring α	G^{α}	6×10^{03}	6×10^{03}	MPa
Shear Modulus Spring β	G^{β}	6×10^{03}	6×10^{03}	MPa
Viscosity of Dashpot β	$\hat{G^{\beta}}$	3	3	MPa.s
Poisson's Ratio Spring α	ν^{α}	0.232	0.232	-
Poisson's Ratio Spring β	ν^{β}	0.232	0.232	-
Poisson's Ratio Dashpot β	$\hat{\nu^{\beta}}$	0.232	0.232	-
Volume per Mole of Water	Ω	18000	18000	mm^3 mol^{-1}
Permeability	κ	Table 3.22	Table 3.22	mm^3/mm
Viscosity of Water	η	1×10^{-06}	1×10^{-06}	MPa.s

Table 3.21: Material data for the test with two layers of polymeric gel. The combinations of permeability are given in Table 3.22.

Combination	κ - **GEL 1**	κ - **GEL 2**	Units
Combination 7	1×10^{-12}	1×10^{-13}	mm^3/mm
Combination 8	1×10^{-12}	1×10^{-14}	mm^3/mm
Combination 9	1×10^{-12}	1×10^{-15}	mm^3/mm

Table 3.22: Material data for different combinations. In each combination the permeability of GEL 2 is changed by a factor of 10.

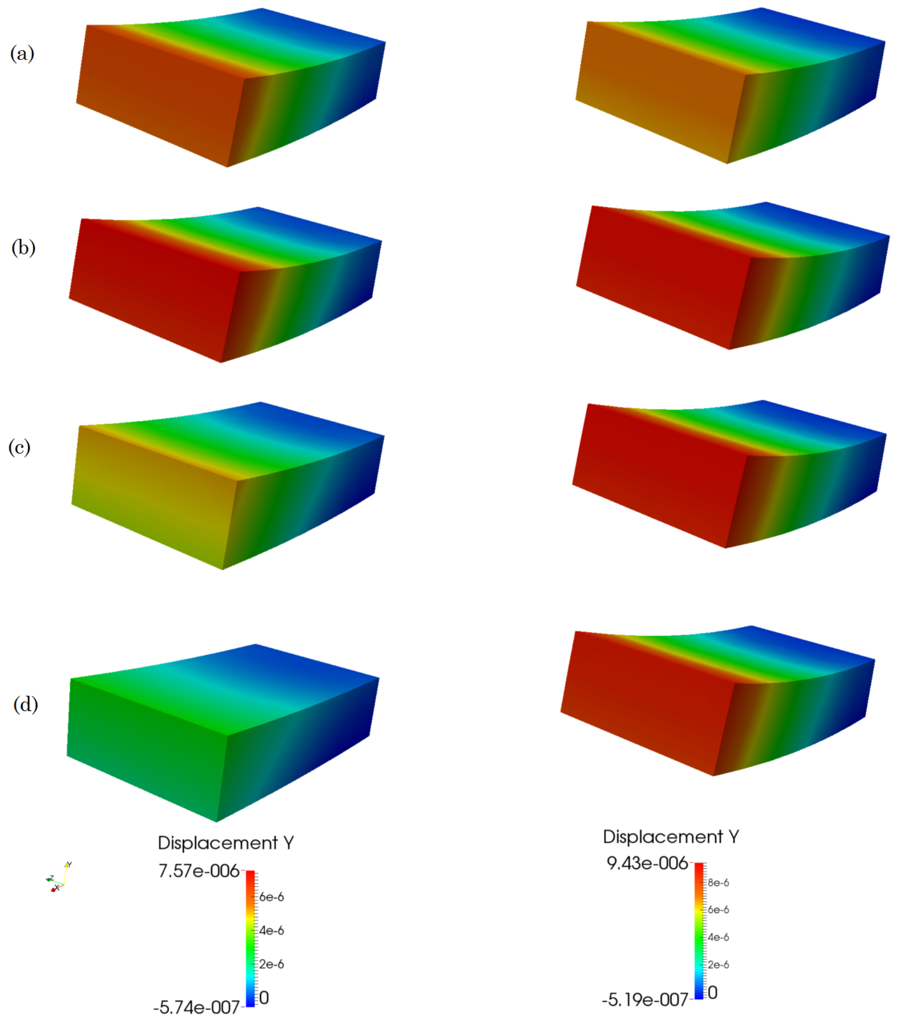

Figure 3.37: Comparison between $\kappa = 1 \times 10^{-14}$ (left) and $\kappa = 1 \times 10^{-15}$ (right) in the case 2 test for the multi-layer problem. Taken at time (a) 0.0000016s (b) 0.0000036s (c) 0.0000160s (d) 0.0000320s.

Figure 3.37 demonstrates the deformations induced by the different rates of swelling within the two layers of the composite. The deformation in the y direction (the sagging motion) was induced and then recovered far quicker in the left hand side composite (Combination 8) than the right hand side composite (Combination 9), shown in Figure 3.37.

Figures 3.38 and 3.39 show the displacements in the x and y directions respectively, taken from point A. They again demonstrated similar behaviour between $\kappa = 1 \times 10^{-13}$ to $\kappa = 1 \times 10^{-14}$, where there is a very small difference in the rate of solvent uptake caused by the reduction in polymer permeability. However, $\kappa = 1 \times 10^{-15}$ caused a more significant difference as the rate of diffusion becomes noticeably slower than the rate of relaxation. Hence the sample spends more time deformed and the displacements at the end of the cycle are far higher in the y-direction as the polymer molecules have conformed to a new arrangement.

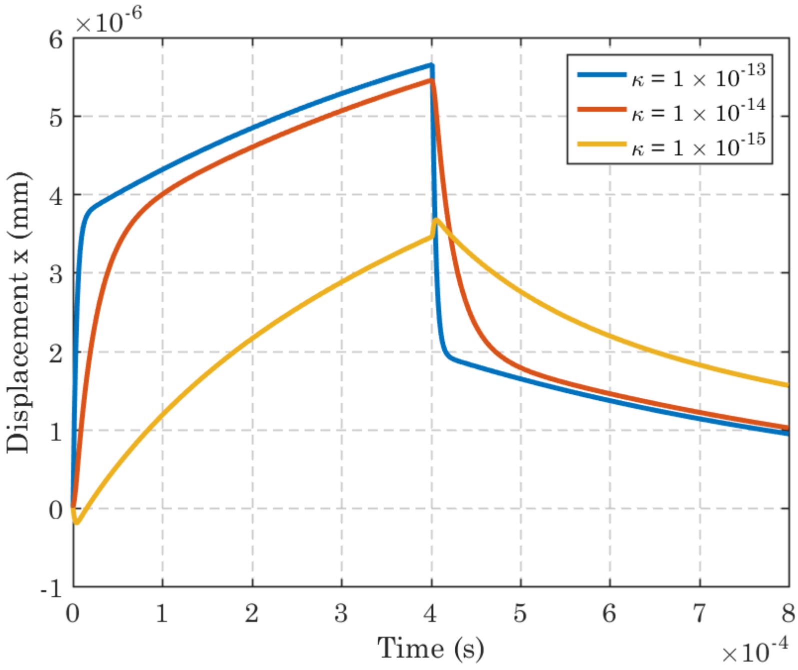

Figure 3.38: Displacement history in the x direction due to the change in climatic conditions surrounding the polymeric gel. The legend within the graph gives the permeability, κ, for each corresponding line in the graph (Combinations 7-9).

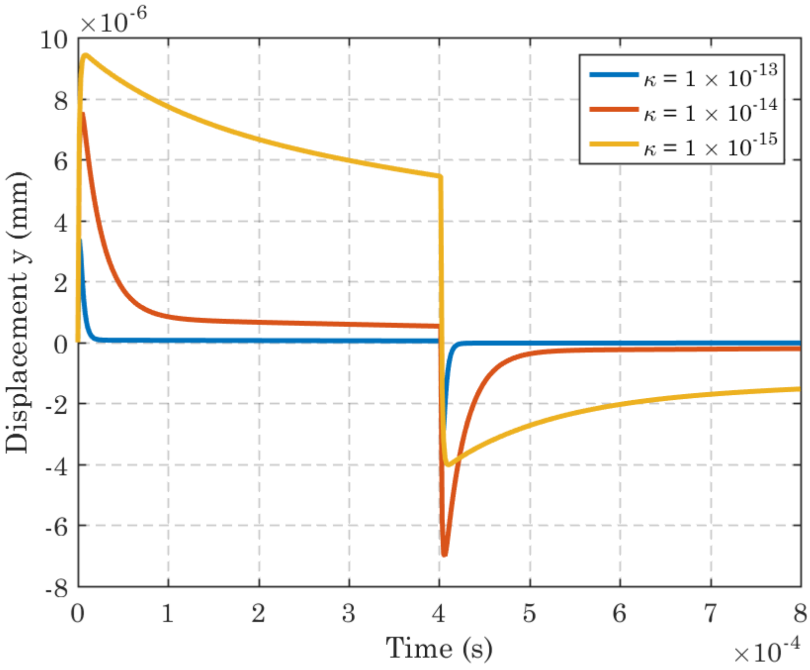

Figure 3.39: Displacement history showing deflection in the y direction due to the change in climatic conditions surrounding the polymeric gel. The legend within the graph gives the permeability, κ, for each corresponding line in the graph (Combinations 7-9).

3.4 Test 4: Viscoelastic Deformation of a Hollow Cylinder of Polymeric Gel

Description of the Test

Many polymeric gels are part of a complex multi-scale structure, such as wood cells and the cells of other cellulosic polymers like cotton. As such, they are embedded as the discrete component within more complex structures. To test the model in a more complex shape, a hollow cylinder of polymeric gel, similar in shape to a compression wood cell or cellulose cell, is modelled. A pressure of 50 N/mm^2 is applied normal to the outer surface whilst both ends were held in place. A series of cyclic tests were carried out to assess the behaviour of viscoelastic deformations in such cases.

In this Test the observation time is referred to. This is equivalent to an experiment where values are selected at certain points in time, for instance in a sorption test a value of mass may be taken every minute. However, within this observation time, processes could be in effect that happen quickly enough that they are not observable in the time frame, as the test will demonstrate. For Test 4, the size of time step is the observation time, as processes that occur exclusively between time steps can remain hidden unless further investigation is carried out. This is an important point to note and this section will highlight the role this model can play in predicting all the physics that is occurring within the polymers and therefore the ability to give a better understanding to the behaviour.

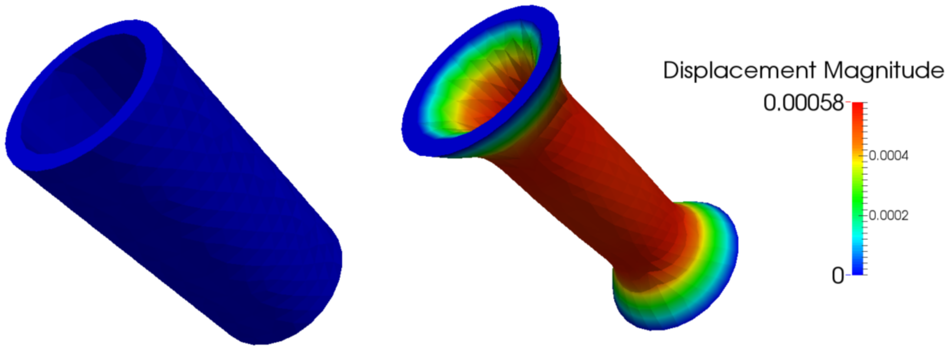

Figure 3.40: Deformation of the hollow polymeric gel cylinder under the compressive normal pressure applied to the outer surface surface. The pressure causes the cylinder to narrow in the middle. The displacements are held constant at the top and the bottom of the cylinder and the chemical potential of the surrounding environment, μ_e, is held constant. The chemical potential of the solvent, μ_s within the wall of the cylinder is allowed to evolve freely throughout the test, and is initially set equal to μ_e at time zero.

Numerical Approach

The cylinder was split into a 1/8th section due to symmetry. Both the internal and external face were exposed to the external environment, with a Dirichlet boundary, of chemical potential μ applied. The faces where symmetry was enforced had zero flux applied and constrained displacements in the axis perpendicular to the corresponding face. The mechanical and chemical boundary conditions are given in Table 3.23 and the initial chemical conditions are given in Table 3.24.

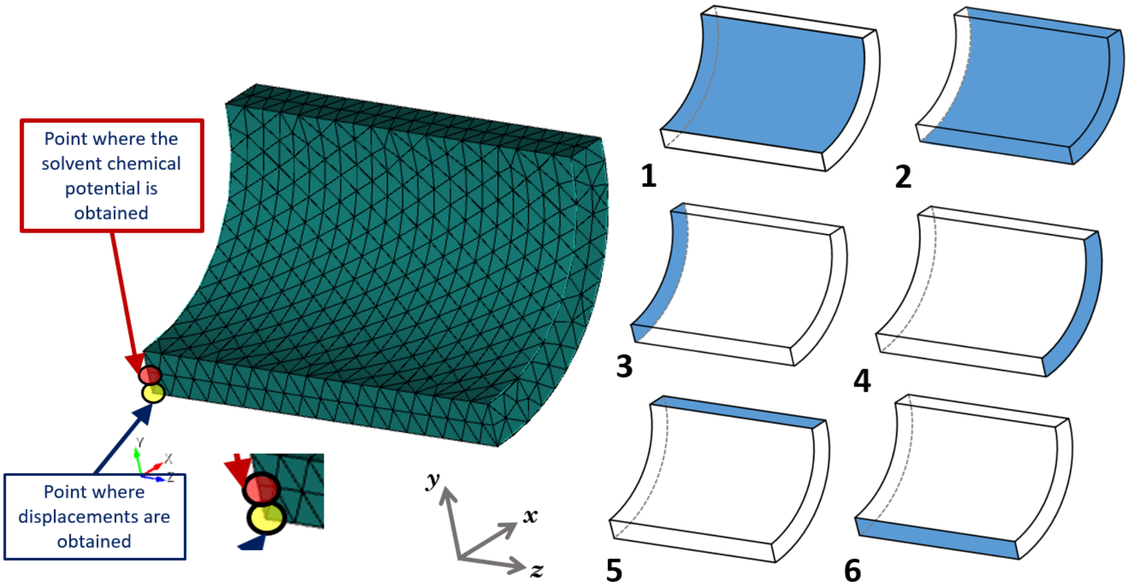

Figure 3.41: Mesh used for the cylinder test after simplifications have been made to account for symmetry. Each face of the cylinder is numbered to allow a full description of the applied mechanical and chemical boundary conditions, initial conditions and applied forces, outlined in Tables 3.23 - 3.25 below. The red and yellow circles refer to points where time series data is taken for the chemical potential of the solvent μ_s and the displacements respectively.

Face	Mechanical Conditions	Chemical Conditions
1	-	μ_e
2	-	μ_e
3	$u_z = 0$	$\frac{\partial \mu_s}{\partial z} = 0$
4	$u_x = 0, u_y = 0, u_z = 0$	μ_e
5	$u_y = 0$	$\frac{\partial \mu_s}{\partial y} = 0$
6	$u_x = 0$	$\frac{\partial \mu_s}{\partial x} = 0$

Table 3.23: Boundary conditions for the hollow cylinder test. The faces to which the boundary conditions are applied are shown in Figure 3.41.

Chemical Condition	**Magnitude**	**Units**	**Time**
μ_e	1.5×10^{06}	J mol^{-1}	0.00s - 0.005s
μ_s	1.5×10^{06}	J mol^{-1}	0.00s

Table 3.24: Chemical potential conditions for the cylinder test. The environmental chemical potential, μ_e is held constant throughout the test and the chemical potential of the solvent μ_s is allowed to evolve within the gel after the first time step.

Pressure Magnitude	**Units**	**Time**
0	N/mm^2	0.00s
50	N/mm^2	0.000005s - 0.0005s
0	N/mm^2	0.0005005s - 0.0010s
50	N/mm^2	0.0010005s - 0.0015s
0	N/mm^2	0.0015005s - 0.0020s
50	N/mm^2	0.0020005s - 0.0025s
0	N/mm^2	0.0025005s - 0.0030s
50	N/mm^2	0.0030005s - 0.0035s
0	N/mm^2	0.0035005s - 0.0040s
50	N/mm^2	0.0040005s - 0.0045s
0	N/mm^2	0.0045005s - 0.0050s

Table 3.25: Load history for the pressure of 50 N/mm^2 , applied as a compressive pressure normal to Face 2, shown in Figure 3.41, for the cylinder test.

3.4.1 Case 1 - Short Time Scale

In Case 1 the cylinder was subjected to the loads on a very short time scale. The load was applied instantly and released instantly. The dashpot shear modulus was set very low, and therefore the viscoelastic behaviour occurred within the time of diffusion. The displacement time series are obtained from a node on the edge of the cylinder, highlighted in yellow in Figure 3.41. The corresponding time series for the chemical potential of the solvent within the gel, μ_s. is obtained from a point within the wall of the cylinder, highlighted in red in Figure 3.41.

Input Parameter	**Symbol**	**Value**	**Units**
Shear Modulus Spring α	G^{α}	3×10^{03}	MPa
Shear Modulus Spring β	G^{β}	3×10^{03}	MPa
Viscosity of Dashpot β	$\hat{G^{\beta}}$	1	MPa.s
Poisson's Ratio Spring α	ν^{α}	0.232	-
Poisson's Ratio Spring β	ν^{β}	0.232	-
Poisson's Ratio Dashpot β	$\hat{\nu^{\beta}}$	0.232	-
Volume per Mole of Water	Ω	18000	$\mathrm{mm}^3\ \mathrm{mol}^{-1}$
Permeability	κ	1×10^{-12}	mm^2
Viscosity of Water	η	1×10^{-06}	MPa.s

Table 3.26: Material data for the hollow cylinder test case 1 where the time of viscoelastic relaxation, $\tau = 3.333 \times 10^{-04} s$.

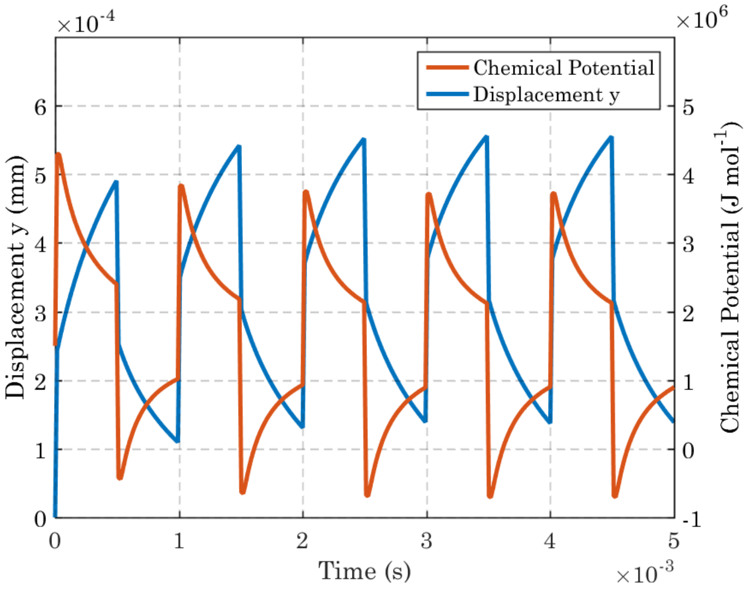

Figure 3.42: Displacement history in the y direction due to external pressure applied on the cylinder (left axis) and the chemical potential within the wall of the cylinder (right axis)

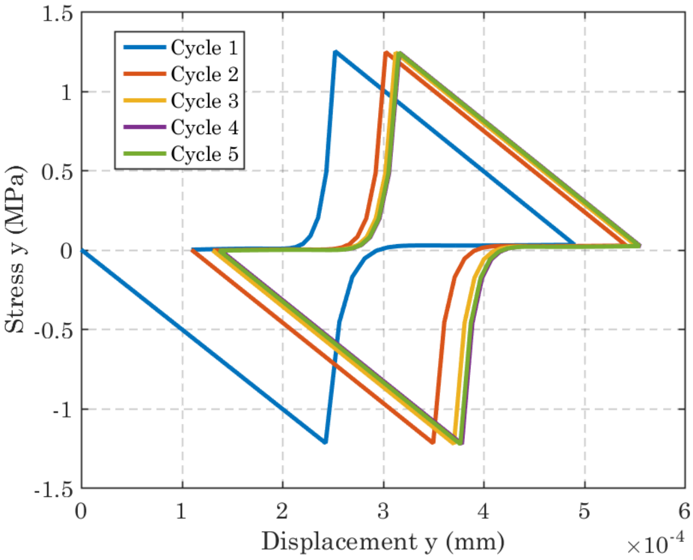

Figure 3.43: Viscoelastic shakedown effect caused by repeated exposure to changing environmental conditions. Each colour represents an identical cycle of exposure but at a different point in time. The stress returns to zero yet the cylinder does not return to its reference shape.

Figure 3.40 shows the deformation of the cylinder due to the external loading. The load cycles are plotted in Figure 3.42 where the displacements and chemical potential are taken at a point within the wall of the sample. The loading caused a cycle of viscoelastic displacements along with corresponding changes to the chemical potential. The chemical potential evolved at a similar rate to the rate of diffusion, therefore under these loading conditions the change in the chemical potential caused by the loading was observed within the time of observation. Figure 3.43 shows the stress loop obtained when plotting the stress in the y direction vs the displacements in the y direction from a point near the middle of the cylinder. Each cycle of loading caused the displacement to increase until it converged on a loop during cycle four.

Influence of Dashpot Shear Modulus

To further explore the loading cycles, the shear modulus of the Dashpot was changed in accordance with table 3.27. This allowed further analysis of viscoelastic shakedown effects and it carried out in accordance with cylinder Test Case 1.

Combination	G^{α} (MPa)	G^{β} (MPa)	$\hat{G}^{\beta}$ (MPa.s)
Combination 1	3×10^{03}	3×10^{03}	1
Combination 2	3×10^{03}	3×10^{03}	2
Combination 3	3×10^{03}	3×10^{03}	5
Combination 4	3×10^{03}	3×10^{03}	10

Table 3.27: Spring and dashpot shear moduli for the cylinder test.

The displacements are shown in Figure 3.44 for each Combination. There is less viscoelastic deformation for each Combination, 1-4, as was expected due to a reduction in the dashpot modulus. These displacements corresponded to changes in the chemical potential within the cylinder, plotted in Figure 3.45.

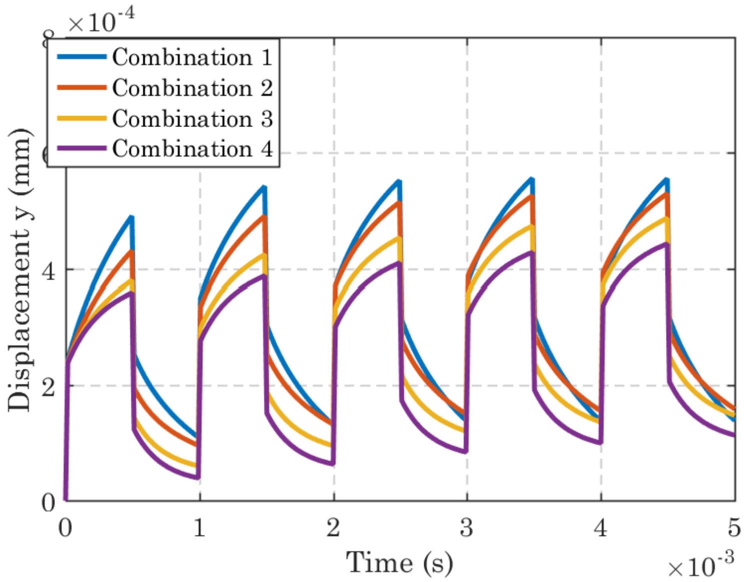

Figure 3.44: The effect of the dashpot viscosity, $\hat{G}^{\beta}$, on the observed shakedown effect. Combination 1 reaches the maximum displacement, in a fully relaxed state, much sooner than Combinations 2-4, shown by the lack of increase in displacement beyond the 2nd cycle..

An important point to note is that there was a negative chemical potential generated by the model during these cycles, when the load was released and the sample returned towards its original configuration. This was a side effect of assuming that the volume change was accounted for by the same change in the volume of the solvent, which is a violation of the primary field variables [46]. The negative value of chemical potential implies that there is a negative water content within the sample, which is of course impossible. This is due to the model incorrectly assuming that the material remains compressible when $\mu \leq 0$. In reality, as the chemical potential, μ, approaches zero, the incompressibility condition should be imposed, ensuring that negative values of chemical potential do not arise.

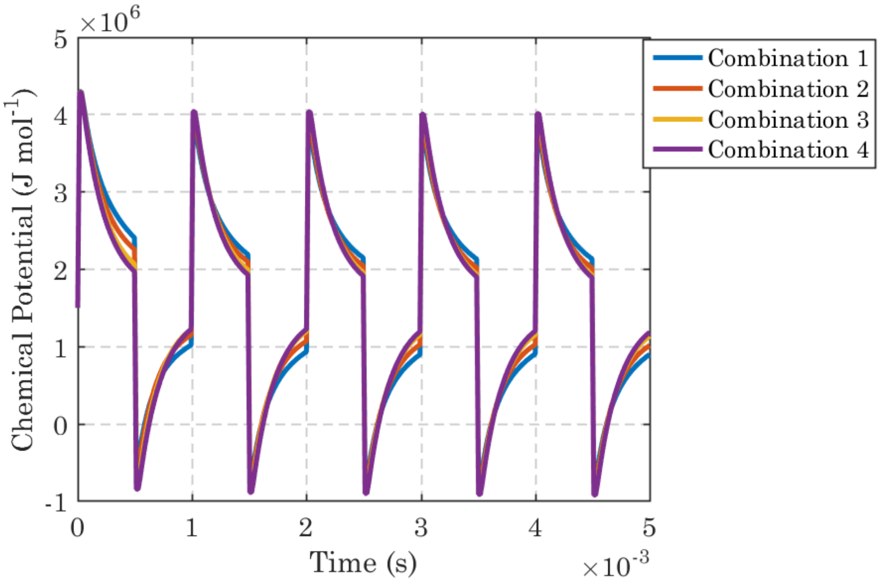

Figure 3.45: Chemical potential within the wall of the cylinder, changing due to the external pressure. In each case the chemical potential evolves differently, due to the different rates of viscoelastic deformation, dictated by the dashpot viscosity $\hat{G}^{\beta}$.

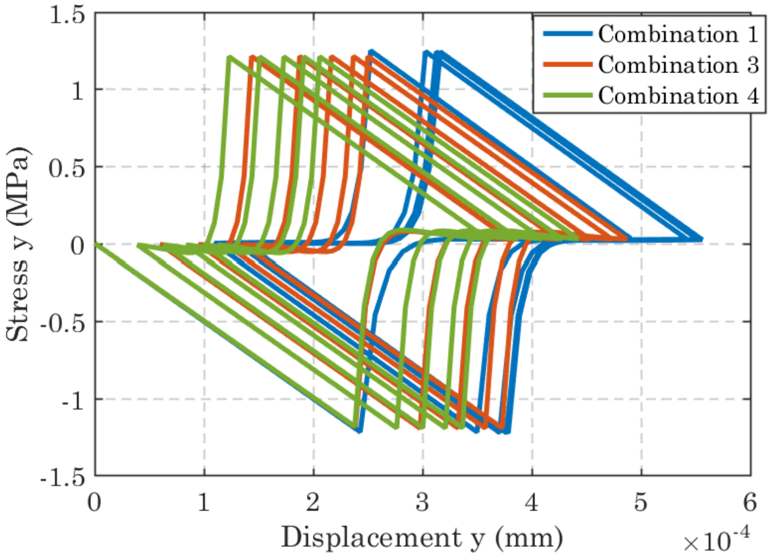

Figure 3.46: Viscoelastic shakedown effect caused by repeated exposure to changing environmental conditions. Each colour represents an identical cycle of exposure for a different value of dashpot viscosity, $\hat{G}^{\beta}$. The stress returns to zero yet the cylinder does not return to its reference shape.

Several authors have suggested that the two primary fields be allowed to evolve separately and that the coupling be introduced through a free-energy term [46,58,59], accounting for configurational changes within the polymer and the associated impact this has on the chemical potential field. This will be discussed in more depth in further Chapters.

3.4.2 Case 2 - Long Time Scale

For Case 2, viscoelastic behaviour within the glassy material behaviour was observed. For this it is assumed that the dashpot viscosity $\hat{G}^\beta$ is relatively high, leading to a long relaxation time. Taking values from Xie et al [116] it was assumed that the relaxation modulus of the polymer was between 4-10 TPa.s. All other material properties remained the same as Case 1. For Case 2, the observation time is now far larger, with each loading cycle taking 50 minutes (1500s/25min loaded then 1500s/25min unloaded), in order to capture the viscoelastic deformations.

Combination	G^α (MPa)	G^β (MPa)	$\hat{G}^\beta$ (MPa.s)
Combination 1	3×10^{03}	3×10^{03}	4×10^{06}
Combination 2	3×10^{03}	3×10^{03}	6×10^{06}
Combination 3	3×10^{03}	3×10^{03}	8×10^{06}
Combination 4	3×10^{03}	3×10^{03}	10×10^{06}

Table 3.28: Spring shear moduli and dashpot viscosity combinations for the cylinder test.

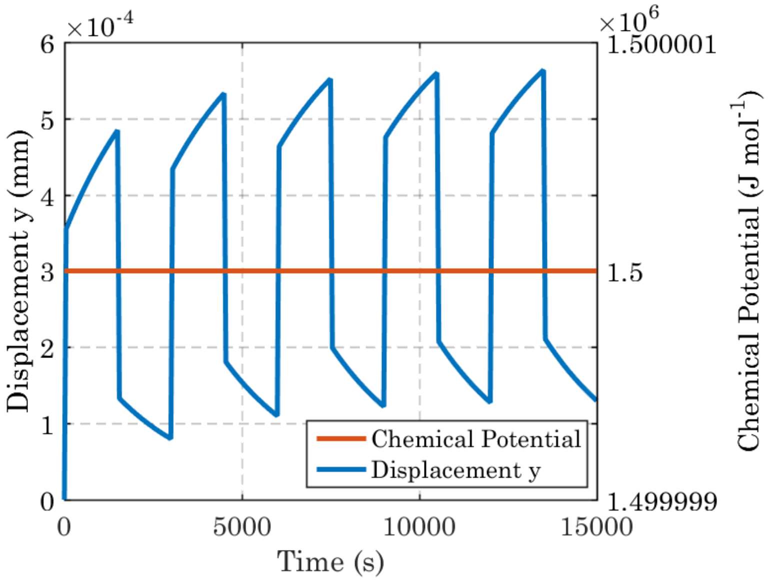

Figure 3.47: Displacement and chemical potential histories within the cylinder wall for Combination 1. The lack of visible change to the chemical potential is due to the far longer time of viscoelastic evolution, and as such the far faster time for diffusion to occur is not captured within the length of time step.

Figure 3.47 shows the comparison of the displacement in the y direction and the chemical load within the cylinder wall for Combination 2. The difference between Case 1 (Figure3.42) and Case 2 (Figure 3.47) is that the chemical potential appeared not to change in Case 2. This was due to the diffusion process happening on a different time scale to the observation scale. Viscoelastic deformation still took place however, due to the external loading, but on a far longer time frame as the polymer was in a glassy state (as determined by the material properties).

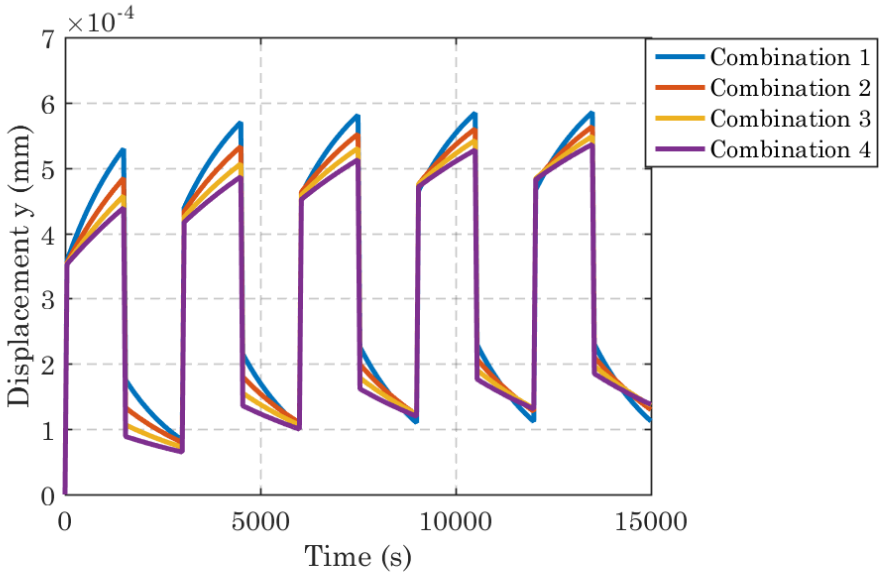

Figure 3.48: The effect of the dashpot viscosity, $\hat{G}^{\beta}$, on the shakedown effect. Combination 1 reaches the maximum displacement, in a fully relaxed state, much sooner than Combinations 2-4, shown by the lack of increase in displacement the 3rd cycle.

3.5 Conclusions of Sensitivity Tests

The aim of the verification tests in this chapter was to establish if the model described in Chapter 2 is behaving as expected. Using the creep test, it is shown that the model could exhibit both poroelastic and viscoelastic material behaviour due to external load, dependent upon the characteristic time for relaxation τ_v.

The free-swelling test demonstrated the swelling response of the polymer to environmental changes alone, including viscoelastically limited solvent migration. Hence the model provides a good framework for modelling wood cell walls and water interactions.

The multi-layer test demonstrated the ability of the model to deal with more complex multi-layer structures, where different polymer stiffness and moisture transport properties will lead to stress build up and configurational changes. This demonstrates good potential for use in the wood cell wall, which consists of several different layers of material.

The cylinder test showed the capability of the model to deal with more complex problems. In this final example, the geometry was more complex and the series of loading patterns showed the viscoelastic shakedown effect. It also demonstrated the ability of the model to predict viscoelastic behaviour on a different time-scale to the diffusive behaviour. As such can potentially predict configurational changes within the wood polymers at low moisture contents due to external loading whilst in the glassy phase of material behaviour.

Chapter 4

Application to Wood Cells

Until this point, the gel model has been formulated as a generic polymeric gel. This allows maximum flexibility for other users when applying to other polymers which may exhibit different internal physics whilst also displaying viscoelastic material behaviour. For instance, some polymers may be dominated by the influence of Van der Waal's interactions. Therefore, the results of the model in Chapter 3 allow for a more general look at the capabilities for any user looking to implement the model for other problems and materials. Within this chapter the more specific case of wood is considered and other similar cellulosic materials such as cotton, flax etc. To achieve this the complex physical processes necessary to describe such materials are studied, without being too specific on the material arrangement. The primary focus is the amorphous network of polymers, in this case either amorphous cellulose or a mixture of amorphous cellulose, hemicelluloses and lignin, and as such consideration is limited to isotropic materials.

Many multi-scale approaches have been presented already for describing the hierarchical properties of wood cells with good effect [7, 29–31], and as such the focus here is the physical processes of the cell wall polymers. The key interest here is the interactions between the incoming moisture and the evolving mechanical properties of the polymer, and how the complex physics apply to sorption theory and the influence this has on the viscoelastic behaviour. This is particularly important when applying the model to the glass transition as well as the transition between Fickian solvent transport and viscoelastically limited solvent transport, as discussed in Chapter 1 and demonstrated within the existing model framework in Chapter 3. It is therefore within this approach that there is the most to gain, rather than trying to build upon already well established and refined multi-scale models [7, 29–31].

4.1 Multi-Physics Modelling Approach

Within wood cells, complex interactions occur between the incoming water and the constituent polymers that will impact upon the mechanical results. The three main polymers, cellulose, hemicellulose and lignin all interact strongly with water, particularly the amorphous regions of cellulose and the hemicelluloses. The mechanical behaviour of these polymers is dominated by the behaviour of their hydrogen bonds. Nissan and Sternstein state that the cellulosic materials cannot be be considered as composed of linear springs and Newtonian dashpots [82]. They elaborate, explaining that there are nonlinear effects, impacting on the stiffness of the polymers and the relaxation rate as moisture content and stress changes occur. However, there is a significant amount of literature where Newtonian springs and dashpots have been used to describe the behaviour of wood and cellulosic polymers [26, 28, 29, 42, 52, 53, 89, 116]. As such, the best approach to the modelling of wood polymers will incorporate both a phenomenological approach, using Newtonian springs and dashpots, alongside a nonlinear approach implemented upon the material to incorporate the complex hydrogen bonding behaviour.

Nissan and Sternstein suggest that the primary elastic elements within the polymer system are hydrogen bonds in the amorphous regions [82], which cannot be considered Hookean in nature. This is addressed in this thesis by incorporating the evolution of material stiffness with water content, thus combining the Hookean material description alongside the complex hydrogen bonding behaviour to yield a result combining both processes. Nissan and Sternstien also suggest there is no need to postulate the existence of separate viscous elements to account for time dependent phenomena, instead they consider that the changing number of elastic elements can occur over time [82]. Other approaches to modelling have included several elements, in complex arrangements, to describe the behaviour using a solely rheological approach [42, 89]. However, the aim here is to present a combined theory for describing the behaviour of wood polymers using both the phenomenological approach and the approach taken by the hydrogen bond theory. The hope is that a combined approach, where the properties of the standard linear solid polymeric gel model shown in the previous section are constantly evolving due to stress and moisture content, will simplify the rheological description. As such it will then provide a good basis from which to add more complexity, where each individual phase within the complex hierarchical structure of the cell wall can be described through this multi-physics approach, therefore leading to future predictive models for wood-water interactions, without a need for experimental data fitting.

A two part approach is adopted to describe the non-linear hydrogen bonding behaviour of the polymers. First we examine the elastic stiffness, i.e. the contribution of the springs within the phenomenological description. Secondly we examine the non-linear relaxation behaviour and how this could be applied to the dashpot within the material description. As such, each element within the model can be defined as either hydrogen bond dependent due to the moisture, i.e. the springs, or hydrogen bond dependent due to both the stress and the moisture content.

4.1.1 Polymer Elastic Stiffness

As discussed in Chapter 1, it has been theorised that the sharp increase in the amount of water adsorption towards the higher relative humidities in the sorption isotherm in cellulosic materials occurs as the material transitions though its glass transition, taking the material from a more rigid glassy state to a more rubbery state [112] and that this transition temperature is moisture dependent.

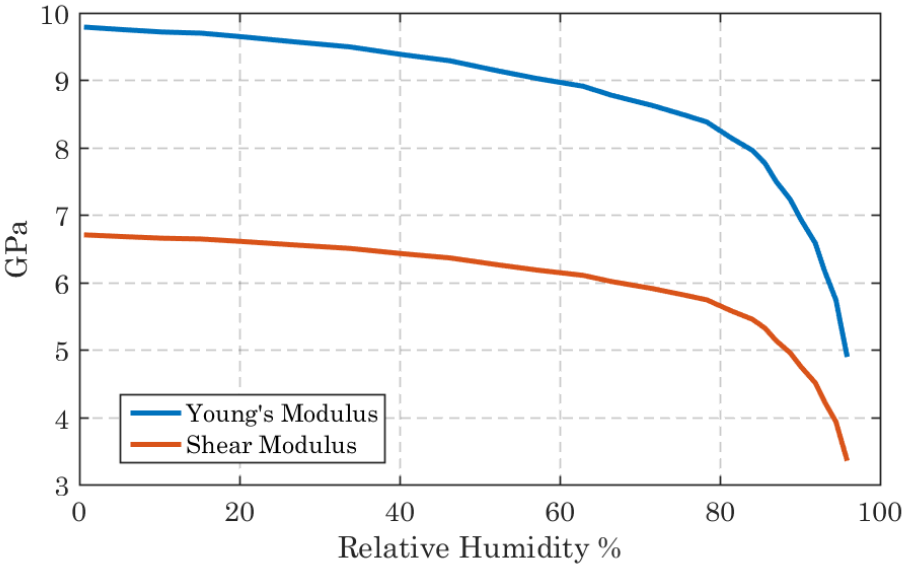

Figure 4.1: Young's modulus of Hemicellulose compared to relative humidity as determined by Cousins [24]. The shear modulus is also included, determined from the Young's modulus.

It is widely known that the stiffness of amorphous celluloses and hemicelloses are also strongly dependent on their moisture content. However, the elastic properties of the crystalline regions are not a function of the moisture content, instead it is just the amorphous regions on the outer edge of the cellulose microfibrils which undergo softening and water interactions [12, 65, 70, 76]. It has been suggested that this softening is a consequence of the dominant influence of hydrogen bonds on the mechanical behaviour and the breakage and re-organization of hydrogen bonds upon moisture uptake [66,77,82]. Through molecular dynamics it has been shown there is a linear relation between the stiffness of the material and the hydrogen bond density at higher water contents, where the bond density is lower [66]. Experimental tests carried out by Cousins has highlighted the degree of softening of the individual polymers [24, 25], particularly for hemicelluloses which produce a very sharp and extreme softening curve beyond the glass transition [33]. The relationship between Young's modulus and the relative humidity obtained by Cousin's is plotted in Figure 4.1, as well as a corresponding Shear modulus for comparison. Please note that the shear modulus has been derived using a constant value of Poisson's ratio from the glassy to rubbery material phase, which may be incorrect. It is also important to note that as the tests were not carried out with the polymer insitu within the network this may behave differently within the network than out. For instance, it is known that hemicelluloses crystallize when exposed outwith the polymer network and that the covalent bonds within are far stronger than the hydrogen bonds [66], thus such a large drop in stiffness seems unusual.

Experiments on wood cells and various other cellulosic polymers have also been carried out to obtain sorption isotherms for both the case of adsorption and desorption [45, 52, 54, 115, 116] and from this values for the stiffness have been back calculated using the PEK method [116] (Parallel Exponential Kinetics). As this is also a spring-dashpot style model (two Kelvin-Voigt models in series), it is particularly relevant to the approach taken using the linear standard model and a clear indication that the physics of polymer softening is a worthwhile approach to compute a physically realistic solution. It also backs the theory of Nissan [82], that Hookean elements alone cannot describe the behaviour of the wood polymers and that more complex physics is in process that need to be accounted for in order to make predictive modelling a reality. It has been theorised that, as a hydrogen bond dominated solid, the stiffness of cellulosic polymers are dependent on the number of intramolecular hydrogen bonds between the chains. This has been formulated in terms of the kinetics of hydrogen bond dissociation [80, 82], linking the stiffness of the polymer to the number of water molecules attached to the clustering of water, solvent, molecules. The theory has also been presented for lignin [81], which exhibits different softening behaviour [92]. However it has been noted that the stiffness of lignin can be assumed constant beyond 12% moisture content [90], contradicting Cousins results for the softening of isolated Lignin, i.e. not insitu [24]. Through this approach, the 3D polymeric gel model will interact with the environment to change the properties, for hemicelluloses and/or lignins, at each gauss point, as a time dependent process, thereby incorporating the changing stiffness of the polymers due to varying environmental conditions.

4.1.2 Relaxation Behaviour

In order to fully describe the behaviour of wood cell polymers across all ranges of the relative humidity (RH%), the shear modulus of the dashpot has to be predicted and the effects of the water content and stress taken into account. It has already been shown in Chapter 3 that a drop in the viscosity of the dashpot will lead to viscoelastic process becoming dominant within the solvent transport within the polymeric gel model. However, in order to formulate a multi-physics approach to this problem, an approach is needed to describe this transition using the physics of the problem, in particular hydrogen bond theory, thus providing a route to predictive modelling of wood cell behaviour.

Nissan and Sternstein view the viscoelastic relaxation behaviour of cellulose as being a product of hydrogen bond breakdown within the cellulose [82]. While other factors may be at play, such as stretching of cellulose molecules along the glycosidic bond (C - O - C) and the twisting and subsequent configurational changes of microfibrils, it is clear that the hydrogen bonds are the dominant process, especially when taking into account moisture changes within the polymer. The rate of relaxation can be described in terms of the decay in the number of effective hydrogen bonds within the polymer, which itself is a product of both the stress and the moisture content. The number of these bonds and the rate at which they breakdown can be related to the flow of the polymer, assuming that movement of units of cellulose can be attributed to the destruction of several intra-molecular hydrogen bonds around that unit.

Kulansinski et al have recently used molecular dynamics simultations to determine the behaviour of the cellulose and hemicellulose on the interface between the microfibrils and the isotropic amorphous matrix. In this they found that due to the densely packed and well ordered nature of the cellulose cyrstals, that there are a very high number of potential hydrogen bond sites to the surface of the microfibrils. As such a very high degree of bonding can happen with water on this interface with the hemicelluloses [65]. As such it seems to be that the interface between the crystalline and amorphous parts is a major factor in the relaxation of the polymers. This theory is also supported by Altaner and Jarvis [6] with their theory of a Velcro type molecular on the interface between the polymers. More work needs to be done understanding the interface effects and from there the relaxation behaviour can be incorporated. The molecular dynamics simulations by Kulansinski et al certainly provide promising work in this area. The advantage of molecular dynamics is that the behaviour of the polymers within their insitu environment can be simulated, whereas experimental techniques need to isolate the individual polymers to distinguish behaviour. However, by isolating the polymers the behaviour of each may be changed from the behaviour insitu.

For now the changing relaxation properties are considered by simply changing the viscosity, as suggested by Govindjee and Simo [46]. With this different stages of relaxation behaviour can be observed. However, this approach limits the use of the model to small changes in moisture content or loading. In the future a firm relationship between the relaxation in the wood and the hydrogen bond behaviour of the individual polymers could provide a method of establishing the different phases of the material behaviour within a predictive framework.

4.1.3 Theory of Hydrogen Bond Dissociation

Using an approach presented by Nissan [80], the change of the Young's modulus on wetting can be related to the change of the number of hydrogen bonds, and this, in turn, to the change of moisture content of cellulose. At low moisture contents, each water molecule is assumed to break approximately one hydrogen bond when it attaches to a hydroxyl group. Considering the molecular weights of cellulose and water, Nissan suggests the following equation [80]:

$$\ln(\mathrm{N}/\mathrm{N}_0) = -(w/\mathrm{W}) \tag{4.1}$$

where N denotes the number of effective hydrogen bonds at moisture content, w, N_0 is the initial number of effective hydrogen bonds in the dry state, and W is the moisture content at which all hydroxyl groups carry one water molecule, which is close to 1/3 for cellulose. The number of hydrogen bonds can be related to the Young's modulus, E, as follows:

$$\mathrm{N} = (\mathrm{E}/k)^{1/3} \tag{4.2}$$

where the proportionality coefficient, k, describes the average force constant between the hydrogen bonds and has been identified as 8×10^3 [80]. This assumes that the force constant does not change with respect to water and also that any possible lengthening of the intramolecular hydrogen bonds not yet broken down has no effect. This assumption can be made on the basis that the variation in force constant would be very small for wood. The force constant will however change as a function of the temperature.

By combining Eqns. (4.1) and (4.2) and considering $W = 1/3$ [80], the change in Young's modulus, E/E_0, for low moisture contents can be formulated,

$$\ln(\mathrm{E}/\mathrm{E}_0)_1 = -w, \tag{4.3}$$

where E_0 is the initial Young's modulus in the dry state and the subscript, 1, refers to regime 1, i.e. the slow breakdown of hydrogen bonds where 1 water molecule breaks 1 hydrogen bond when attaching to a hydroxyl group. The ratio of E/E_0 is plotted in Figure 4.2.

Above a critical moisture content w_c (regime 2), there is an abundance of water and, thus, the breakdown of intramolecular hydrogen bonding happens cooperatively, i.e. one bond breaking down will trigger others in the vicinity. The degree to which this happens is described by the cooperative index ($\overline{\mathrm{C.I.}}$). The ($\overline{\mathrm{C.I.}}$) is the number of H_2O molecules per cluster as they bond onto a hydrogen bond dominated solid. Thus the change in Young's Modulus above w_c can then be described by [80]:

$$\ln(\mathrm{E}/\mathrm{E}_0)_2 = (w_c)[(\overline{\mathrm{C.I.}}) - 1] - (\overline{\mathrm{C.I.}})(w) \tag{4.4}$$

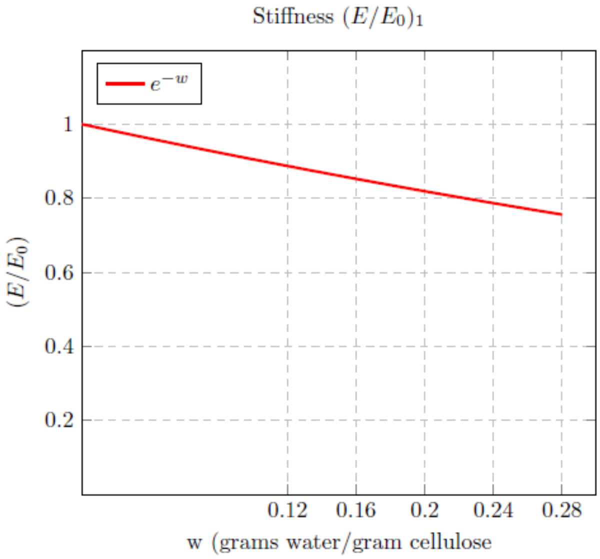

Figure 4.2: Relationship between moisture content, given in grams of water per gram of cellulose, and the stiffness ratio in terms of Young's modulus E and the initial Young's modulus in the dry state, E_0.

The cooperative index, $(\overline{\text{C.I.}})$, from Nissan's work [80], shown in Figure 4.3, was obtained from experimental work and formed the basis of Nissan's formulation of stiffness above the critical moisture content, w_c. To implement this within the gel model, the plot was digitised and a best fit curve was created in order to use the data within the computational framework.

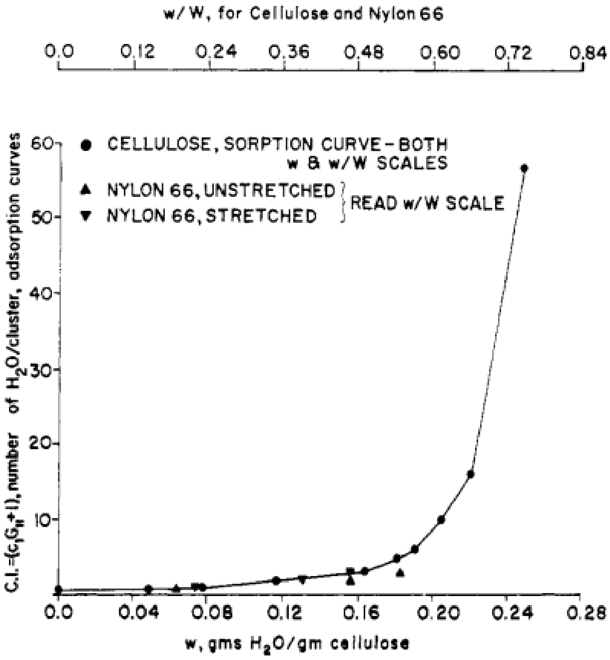

Figure 4.3: The cooperative index, $(\overline{\text{C.I.}})$, curve for cellulose obtained from Nissan's paper on h-bond dissociation [80]. These results were re-plotted by Nissan [80] from experiments by Starkweather [103], for $0 < w < 0.212$, and by Nemethy and Scheraga [79] for $0.212 < w < 0.25$.

The cooperative index from Figure 4.3 is plotted as two seperate best fit curves as shown in Figure 4.4. This was done to ensure a good fitting for the behaviour below the critical moisture content, w_t, and the behaviour above this critical moisture content.

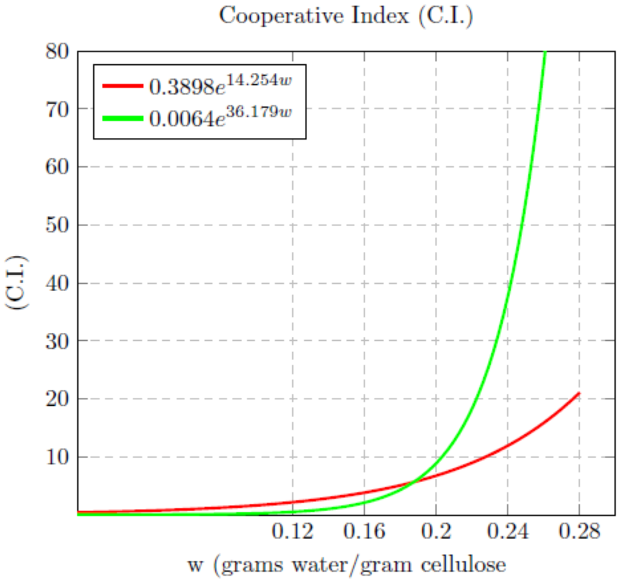

Figure 4.4: The slow cooperative breakdown behaviour (red line) and the fast cooperative breakdown (green line) of hydrogen bonds related to moisture content, w. each line represents a best fit curve of the data presented in Figure 4.3, obtained from [80].

$$(\overline{\text{C.I.}})_{slow} = 0.3898e^{14.254w} \tag{4.5}$$

$$(\overline{\text{C.I.}})_{fast} = 0.0064e^{36.179w} \tag{4.6}$$

The point of intersection, the transition moisture content, between Eqns. (4.5) and (4.6) was calculated ($w_t = 0.1874$) to allow a smooth transition to be enforced between the curves. To implement a numerically stable relationship into the numerical model, Eqns. (4.5) and (4.6) were plotted within a hyperbolic tan function. This ensured a smooth transition between the two curves in Figure 4.4 whilst also ensuring a good close fit.

$$(\overline{\text{C.I.}}) = (\overline{\text{C.I.}})_{slow} + \frac{1 + tanh(K(w - 0.1874))}{2}((\overline{\text{C.I.}})_{fast} - (\overline{\text{C.I.}})_{slow}) \tag{4.7}$$

where K is a fitting parameter in this case that determines the smoothness of the transition between the fast and slow process. Eq. (4.7) represents a new relationship created for use in applying the model outlined in Chapter 2 to hydrogen bond dominated polymers, e.g. cellulose and hemicellulose as found in wood cells.

Several values of K were plotted to view the sensitivity of this fitting parameter, shown in Figure 4.5.

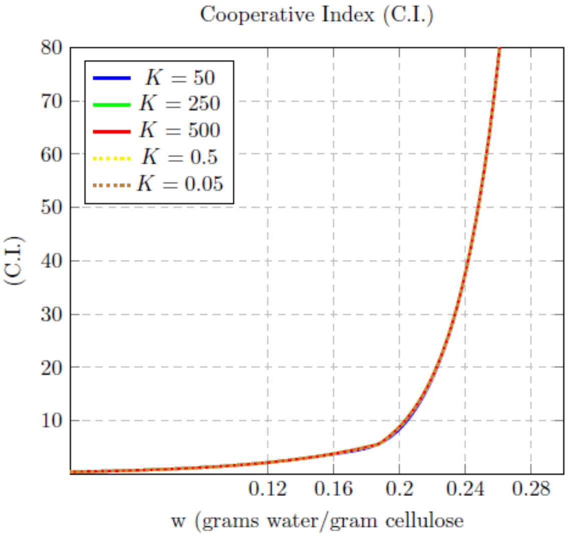

Figure 4.5: The combined equation for the cooperative index $(\overline{\text{C.I.}})$, including both the fast cooperative breakdown process and the slower single bond breakdown process. K is the fitting parameter for the two curves.

Eqns. (4.3) and (4.4), obtained from [80], give the relationship between water content, w, and the Young's modulus of the cellulose, E, for both the glassy and rubbery material behaviours respectively, and were rearranged as follows:

$$\left(\frac{\mathrm{E}}{\mathrm{E}_0}\right)_1 = exp(-w), \tag{4.8}$$

$$\left(\frac{\mathrm{E}}{\mathrm{E}_0}\right)_2 = exp(w_c[(\overline{\text{C.I.}}) - 1] - (\overline{\text{C.I.}})w). \tag{4.9}$$

Taking the same approach as was taken for Eqn. (4.7), Eqns. (4.8) and (4.9) were plotted as a hyperbolic tangent function, ensuring a smooth transition and accurate approximation of the relationship for use within the numerical model.

$$\left(\frac{\mathrm{E}}{\mathrm{E}_0}\right) = \left(\frac{\mathrm{E}}{\mathrm{E}_0}\right)_1 + \frac{1 + tanh(K(w - w_c))}{2}\left(\left(\frac{\mathrm{E}}{\mathrm{E}_0}\right)_2 - \left(\frac{\mathrm{E}}{\mathrm{E}_0}\right)_1\right) \tag{4.10}$$

Although the cooperative index, $(\overline{\text{C.I.}})$, is described in terms of mass of water per unit mass of cellulose, the relationship can be easily adapted for all types of hydrogen bonded solids, including other wood polymers. Assuming that h-bond breakdown can only happen at available sorption sites, and taking into account different degrees of stiffness and crystallinity of cellulosic and wood polymers, the molar concentration of water at each sorption site can be used as it is only available sites that can undergo h-bond dissociation. This molar concentration, at constant temperature, can be described through the Gibb's free energy per mole, $\overline{\mu}$. This is done to avoid scaling issues on the macroscale where the overall moisture content is the cumulative effect of both the mechanical and the chemical behaviour at all length scales, where the overall concentration may be limited by other factors such as the degree of crystallinity and the initial polymer stiffness of the constituent polymers. However, on the polymer level, it is assumed that the clustering at available sorption sites within the material does not change as a function of the overall water concentration but as a function of the internal Gibb's free energy within the polymers. The advantage of using Gibb's free energy is that it is scalable within the system, thus allowing the assumptions on the individual polymer level to be scaled up to the macroscale. Therefore, when μ within the sample, at each available sorption site, is equal to μ outside the sample, chemical equilibrium will occur. However this disregards any energy change of the water from it's vapour state to it's bound state within the cell wall.

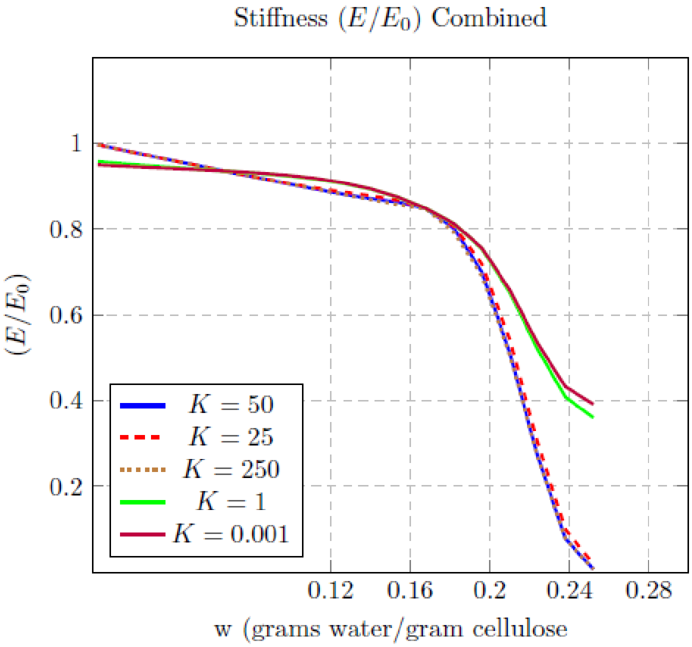

Figure 4.6: The combined regime stiffness curve, (E/E$_0$), obtained from Eq. (4.10) for a range of fitting parameter, K.

Assuming that the range of sorption is from 0% to 100%, the water content per polymer sorption site can be related to the chemical potential per water molecule entering the system. The gradient of the slope relating the water content per cluster, w, to the relative humidity, RH%, was determined as 357.14, by plotting a linear relationship between the two. Therefore the relative humidity at each water content can be described in terms of its chemical potential per molecule entering the cell wall polymer from the environment. In turn this gives a relationship between the water content and the chemical potential as a function of the relative humidity percentage.

$$w = \frac{exp(\frac{\mu L}{\mathrm{RT}})}{357.14} \tag{4.11}$$

where L is Avogadro's constant.

As the shear modulus is also dependent on the number of effective hydrogen bonds, the relationship can be adapted to incorporate shear modulus G where

$$G = \frac{\mathrm{E}}{1 + 2\nu} \tag{4.12}$$

Finally, by inserting Eqns. (4.12) and (4.11) into Eq. (4.10), the relationship between shear modulus at each sorption site and the external environmental conditions was obtained.

$$\left(\frac{G}{G_0}\right) = \left(\frac{G}{G_0}\right)_1 + \frac{1 + tanh(K(\frac{exp(\frac{\mu L}{RT}))}{357.14} - w_c)}{2}\left(\left(\frac{G}{G_0}\right)_2 - \left(\frac{G}{G_0}\right)_1\right) \tag{4.13}$$

Eqn. (4.13) was used to calculate the shear modulus at each gauss point, allowing the evolution of the hydrogen bonds to occur transiently, as a consequence of the flux field and therefore taking into account the mechanical effects associated with the increasing concentration of water vapour molecules. This represents a new approach to including the non linear hydrogen bond effects within the numerical model.

4.2 Application to Sorption Theory

To apply the combination of the gel model and the nonlinear viscoelastic properties of the amorphous polymers within the wood cell, both the properties and contributions of the polymer mixture need to be defined. Much work has gone into determining the time dependent viscoelastic properties of the amorphous polymers [30,116], however determining the properties of each individual polymer is problematic. This is due to the need to study the material in-situ, since extracting the material can be difficult and can change its behaviour. For instance, Cousin's softening curve for hemicellulose suggests a very large drop in the stiffness due to water uptake [25], to the point where the material stiffnes is only 1% of that in the dry state. This is unlikely since the majority of the stiffness of the hemicelluloses comes from the far stronger covalent bonds [65].

The viscoelastic properties are determined using the Parallel Exponential Kinetics model as proposed by Hill et al [52,116]. This method, using two Kelvin-Voigt elements in series, is used to interpret the stiffness and viscosity of different cellulosic polymers for each element. The resulting stiffness values vary greatly from the dry state to the wet state, giving good evidence of a large drop in stiffness values beyond the glass transition. The viscosity of the polymers is in the region 0.1 - 5 TPa.s. This value is relatively high but does include the overall material behaviour, including the crystalline contributions, and as such does not necessarily reflect the behaviour of the two main polymers attributed to relaxation (hemicellulose and lignin) as the crystalline fibres may have a constraining effect. Furthermore, the samples observed were reasonably large when compared to the cell wall polymers (i.e. up to 1.5mm long in the experiments), and as such time dependent properties will be different when applied to much smaller samples. As such, it is not expected that these apply directly to the individual constituent polymers within the much smaller wood cell wall, but they can be used to study the material behaviour by introducing changes in properties.

Eitelberger et al [30], used multi-scale modelling to predict the viscoelastic properties of various components within the wood cell wall (i.e. hemicellulose and lignin matrix, amorphous cellulose, crystalline cellulose etc.). This provides a very useful tool with which some analysis can be carried out on results determined using well known and established multi-scale techniques [7,29,31] which compared well to experimentally obtained material parameters. Several different rheological models were used and parameters were fitted for each. Each set represented a different axis configuration within the wood cell. The fractional zener model used, the same as the gel model, is applied to the longitudinal stiffness and shear contributions. However, the application of this thesis deals with the isotropic matrix, as such it would be better to apply Eitelberger's multi-scale properties [30] for the tangential and/or radial direction, as it is more likely that these reflect the isotropic properties of the polymer matrix. This is known for two reasons. First, the contributions from the crystalline cellulose will have far more influence in the longitudinal direction in which they are orientated (within about 10 degrees). Second, the given values for the shear moduli in the radial and tangential directions match other values found in literature far better for these polymers than the relatively high shear moduli for the longitudinal direction. The contribution of hemicellulose and lignin is given as a combined shear modulus and thus will be of use when isotropically modelling the combined effect of these two polymers.

The behaviour also of amorphous cellulose and crystalline cellulose is predicted, the amorphous cellulose being of more use as there is a tangential and radial contribution from these polymers. The given values for stiffnes and material viscosity line up well with the values of Hill et al [52,116], with a lower viscosity attributed to the amorphous polymers in the dry state (40-90 GPa.s). These values, whilst noticeably lower than those obtained by Hill, probably reflect more accurately the contribution of the individual polymers on the cell wall scale, a case of micrometers vs millimetres. This is due, in part, to the diffusion of water vapour being an important consideration on the higher length scale, and as such the macroscopic observations are for a series of cells, all reacting to the environmental moisture at different times.

4.2.1 Sorption Test

It is possible to assess the suitablility of the model presented in Chapter 2 by numerically undertaking a sorption test on a sample of polymer (lignin + hemicelluloses), similar to experiments carried out by Hill et al [53], shown in Figure 1.7. The relative humidity is increased in increments of 5% from 0% to 40%. The relative humidity is kept low as the model is formulated for small strains and the highly nonlinear behaviour further up the humidity scale causes extremely large strains to occur. By increasing and then subsequently decreasing the humidity, it is possible to examine whether any sorption hysteresis has occurred and to what extent. As discussed in the previous section, there is some uncertainty over which values best represent the viscosity of the polymer network. As such the sorption tests will consider this range of humidity and look for one key phenomena known as sorption hysteresis. If the sample reaches the equivalent of experimental equilibrium moisture content (EMC%), for instance less than 0.002% change in mass per minute, for each time step, yet undergoes a different moisture path in adsorption and desorption, then hysteresis will have occurred. The expectation is that there will be a higher equilibrium moisture content for each relative humidity when in desorption, as has been observed experimentally in many wood and cellulosic fibres [45, 50–54, 115, 116].

It is expected that the hysteresis occurs below the glass transition, as above the glass transition (between 60-80% relative humidity), hysteresis of the amorphous polymers dissapears [112]. As such a much lower material viscosity would be expected approaching and beyond this transition. Therefore, this test will give a good indication of which parameters are most suitable for this length scale of material both by whether or not hysteresis occurs and the degree to which it influences the results.

The values for permeability obtained for the polymers in Chapter 1 were for different solvents passing through under different conditions and as such the values obtained are also up for debate. However, there is significant literature and consensus upon diffusion. Therefore in this case the permeability was determined based upon the liquid water viscosity with a value for the diffusion coefficient adopted from the literature. This approach has the advantage of using material parameters specific to water interactions, within which the range of possible values is well established. The permeability for the corresponding diffusion and assumed material viscosity was determined using Eq. (2.37), for the polymer in the dry state.

Test 1 - Comparison of Material Viscosity

In Test 1 a comparison is drawn between the behaviour resulting from three different values of the dashpot viscosity $\hat{G}^{\beta}$. The values, as discussed previously, are taken from both experimentally obtained data as well as data using multi-scale modelling (for the specific purpose of modelling the polymer behaviour on the length scale of the polymers, i.e. microns). It is expected that the values obtained from multi-scale modelling [31] will best suit the amorphous polymer matrix due to the length scale it is intended for.

Before viewing the results of each different dashpot viscosity, it is necessary to once again state the assertion that hysteresis disappears above the glass transition in amorphous polymers [112]: hence it is expected that a degree of hysteresis occurs below the glass transition, especially when the sample size is considered (in this case a tiny section of the wood cell wall). The cell is exposed to an adsorption then desorption experiment.

It is important to note some differences in Test 1 when compared to experiments carried out on samples on the macroscopic level. The time of exposure to the air humidity is relatively short. In this case it is only 1s per humidity step. The main reason for this is the rate of diffusion through the ligno-cellulosic polymer, whilst slow on the macro-scale, which also includes water vapour diffusion effects, is very fast relatively when dealing with only a micrometre of material. However, the viscoelastic properties of the wood cell polymers will remain constant, and an increase in the relaxation modulus on the macroscale will be due to the summation of the cell effects over the length of the sample.

Input Parameter	**Symbol**	**Value**	**Units**
Shear Modulus Spring α	G^{α}	Table 4.2	MPa
Shear Modulus Spring β	G^{β}	Table 4.2	MPa
Viscosity of Dashpot β	$\hat{G}^{\beta}$	Table 4.2	MPa.s
Poisson's Ratio Spring α	ν^{α}	0.22	-
Poisson's Ratio Spring β	ν^{β}	0.22	-
Poisson's Ratio Dashpot β	$\hat{\nu^{\beta}}$	0.22	-
Volume per Mole of Water	Ω	18000	$\mathrm{mm}^3\ \mathrm{mol}^{-1}$
Permeability	κ	1×10^{-14}	mm^2
Viscosity of Water	η	1×10^{-06}	MPa.s

Table 4.1: Input data for the comparison of material viscosity test (Test 1).

Description	G^{α} (MPa)	G^{β} (MPa)	$\hat{G}^{\beta}$ (MPa.s)	Ref
Hill and Xie Parallel Exponential Kinetics	1.84×10^{03}	1.84×10^{03}	10×10^{06}	[116]
Eitelberger Multi-Scale	1.84×10^{03}	1.84×10^{03}	96×10^{03}	[30]
Eitelberger Multi-Scale	1.84×10^{03}	1.84×10^{03}	42×10^{03}	[30]

Table 4.2: Input data for a variety of different relaxation times. In each case the shear modulus of the spring, G^{β}, remains the same and the value of the dashpot shear viscosity $\hat{G}^{\beta}$ determines τ_v

The results obtained by Hill for cotton and flax sorption experiments were carried out on a sample 1.5mm in length. If the same test was carried out on a timber beam, it would be expected that diffusion and relaxation would be observed over an even longer time frame due to the limitation of water vapour transport. It is therefore expected that the observed viscoelastic relaxation time is much shorter in this case than any experiments carried out. As such, viscoelastic deformation will not be observed to any significant degree over this time scale when using the value for viscosity obtained from the experimental work by Hill [116].

Numerical Approach

The test was carried out as a free-swelling response to a change in the environment, as carried out in Chapter 3. The set up is the same as is given in Figure 3.19, with a 1/8th section of the cube modelled due to symmetry. The length in each of the x,y and z directions was 0.25 micrometers (0.125 micrometers for the simplified cube to be modelled) and it was assumed to be isotropic and consisting only of amorphous polymers, lignin and hemicellulose. The contribution of crystalline cellulose was neglected at this stage. The relative humidity, applied on the boundary, was formulated according to the process outlined in Chapter 2, where the driving force behind the flux is the chemical potential.

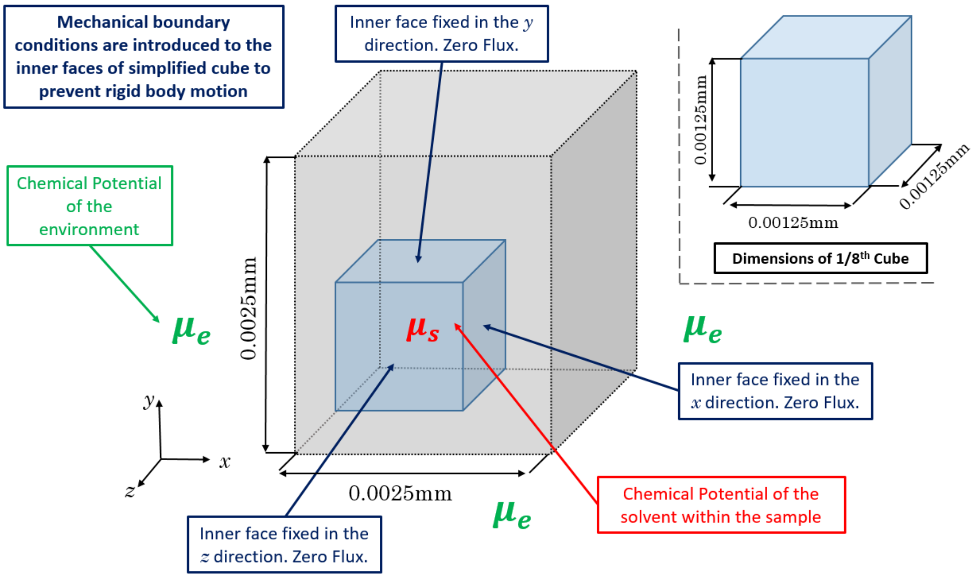

Figure 4.7: A simple cube split into a 1/8th section with symmetry enforced on the internal faces (zero flux of the solvent chemical potential, μ_s, and zero normal displacements for each inner face). The outside environmental chemical potential, μ_e, applies to all external faces and represents the relative humidity of the surrounding environment.

The time dependent chemical potential conditions, applied on boundaries 4-6 in Figure 4.8, are given in Table 4.3. The relative humidity, first column, is increased, from zero, in increments of 5% up to 40% and then back to zero in increments of 5%. The corresponding external chemical potential μ_e is given in the second column. Tables 4.3 to 4.5 initial conditions and chemical and mechanical boundary conditions used in the sorption test.

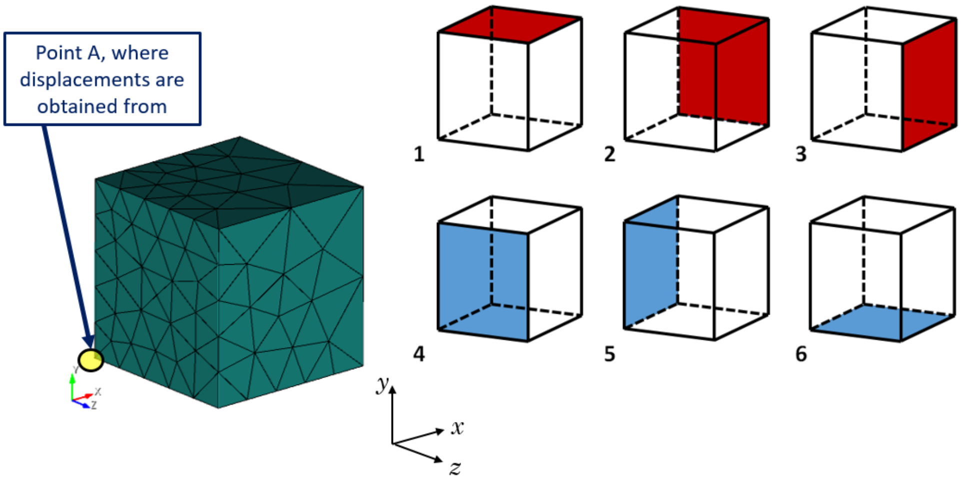

Figure 4.8: Cube of cellulose polymers, simplified to a 1/4 section to take advantage of symmetry, with a fine mesh on the surfaces where the μ_e is applied, transitioning to a coarse mesh at the middle of the sample.The mesh consists of 375 10 node tetrahedral elements. Points A represents the position of nodes from which time series data are obtained. The faces where the mechanical and chemical conditions are applied are numbered 1-6 and referred to in Table 4.5.

RH%	μ_e	**Units**	**Time**
0	0.00	$\mathrm{J\,mol^{-1}}$	0.000s - 0.005s
5	3.989505×10^{06}	$\mathrm{J\,mol^{-1}}$	0.005s - 0.100s
10	5.707692×10^{06}	$\mathrm{J\,mol^{-1}}$	0.105s - 0.200s
15	6.712767×10^{06}	$\mathrm{J\,mol^{-1}}$	0.205s - 0.300s
20	7.425878×10^{06}	$\mathrm{J\,mol^{-1}}$	0.305s - 0.400s
25	7.979011×10^{06}	$\mathrm{J\,mol^{-1}}$	0.405s - 0.500s
30	8.430953×10^{06}	$\mathrm{J\,mol^{-1}}$	0.505s - 0.600s
35	8.813065×10^{06}	$\mathrm{J\,mol^{-1}}$	0.605s - 0.700s
40	9.144065×10^{06}	$\mathrm{J\,mol^{-1}}$	0.705s - 0.800s
35	8.813065×10^{06}	$\mathrm{J\,mol^{-1}}$	0.805s - 0.900s
30	8.430953×10^{06}	$\mathrm{J\,mol^{-1}}$	0.905s - 1.000s
25	7.979011×10^{06}	$\mathrm{J\,mol^{-1}}$	1.005s - 1.100s
20	7.425878×10^{06}	$\mathrm{J\,mol^{-1}}$	1.105s - 1.200s
15	6.712767×10^{06}	$\mathrm{J\,mol^{-1}}$	1.205s - 1.300s
10	5.707692×10^{06}	$\mathrm{J\,mol^{-1}}$	1.305s - 1.400s
5	3.989505×10^{06}	$\mathrm{J\,mol^{-1}}$	1.405s - 1.500s
0	0.00	$\mathrm{J\,mol^{-1}}$	1.505s - 1.800s

Table 4.3: Chemical potential conditions, applied to faces 4,5 and 6, for the sorption test. The environmental chemical potential, μ_e is applied on boundaries according to Table 4.5. The chemical potential of the solvent, μ_s, is allowed to evolve within the gel after the first time step.

Chemical Condition	**Magnitude**	**Units**	**Time**
μ_e	0	J mol^{-1}	0.00s
μ_s	0	J mol^{-1}	0.00s

Table 4.4: Initial chemical potential conditions, applied to faces 2,5 and 6 for the sorption isotherm test. The environmental chemical potential at $t = 0$, μ_e is applied on boundaries according to Table 4.5. At $t > 0$ μ_e is increased in increments according to Table 4.3. The chemical potential of the solvent, μ_s, within the sample is given for $t = 0$ and is allowed to evolve freely at $t > 0$.

Face	**Mechanical Conditions**	**Chemical Conditions**
1	$u_y = 0$	$\frac{\partial \mu_s}{\partial y} = 0$
2	$u_x = 0$	$\frac{\partial \mu_s}{\partial x} = 0$
3	$u_z = 0$	$\frac{\partial \mu_s}{\partial z} = 0$
4	-	μ_e
5	-	μ_e
6	-	μ_e

Table 4.5: Boundary conditions for the sorption test. The boundaries (Faces 1-6) where mechanical and chemical boundary conditions are applied are visualised in Figure 4.8.

Results

The results from the sorption test are shown in Figures 4.9 - 4.11. The results for $\hat{G}^{\beta} = 96$ GPa.s and $\hat{G}^{\beta} = 42$ GPa.s demonstrate a degree of sorption hysteresis, as the desorption path did not return to zero displacement when equilibrium was attained at zero relative humidity. It was determined that the sample was in equilibrium at this point as the change in mass was less the 0.002% per minute mass change over a short time period as stipulated in experimental work [51–53, 115, 116].

The dashpot strain shown in Figure 4.11 demonstrates the viscoelastic behaviour. Firstly, the evolution of the dashpot for $\hat{G}^{\beta} = 10000$ GPa.s [116] shows very little uptake of the dashpot strain over the selected time frame. This is probably due to this dashpot viscosity being derived from experimental work on samples far bigger than have been examined within this thesis (i.e. analysis of a single wood cell).

For $\hat{G}^{\beta} = 42$ and $\hat{G}^{\beta} = 96$ GPa.s [30] there is a greater uptake of the dashpot strain (Figure 4.11) over the selected time frame than for $\hat{G}^{\beta} = 10000$ GPa.s. Furthermore, the sample exhibits moisture sorption hysteresis, (Figure 4.12) demonstrating a complex interplay between the viscoelastic and poroelastic processes.

The value of $\hat{G}^{\beta} = 43$ GPa.s was determined specifically for this phase of the material by Eitelberger [30], therefore for further tests in this thesis it is this value which will be used for the lignin and hemicellulose phase. It is important to note that this value was obtained using experimental data for Douglas fir at 10% moisture content. This is a reasonably high moisture content and as such must apply to the wood polymers in reasonably high relative humidities. It would therefore not be the most suitable for use in modelling the polymers in their glassy (low moisture content) state.

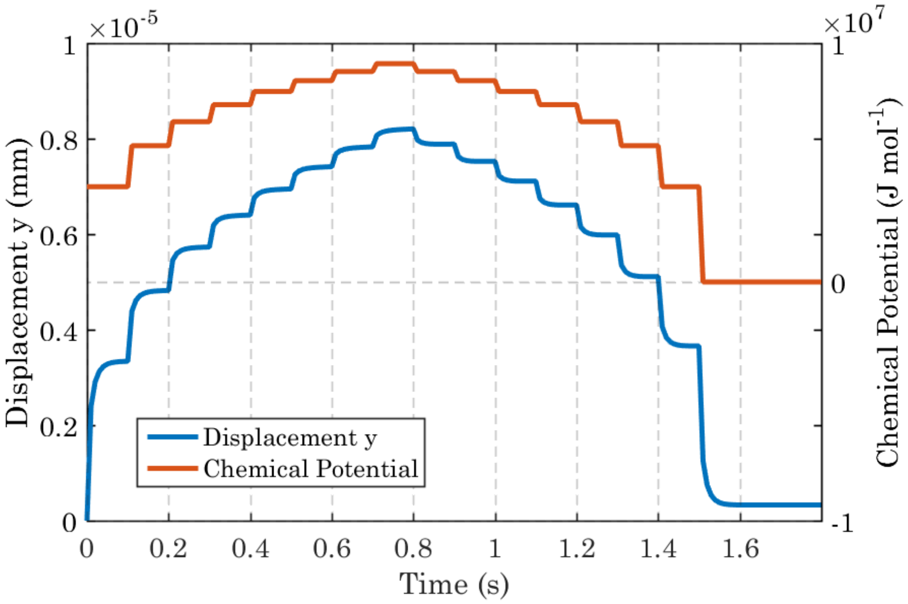

Figure 4.9: Chemical potential changes and displacement change over time for sample with material viscosity $\hat{G}^{\beta} = 42$ GPa.s. The chemical potential and displacements are taken at the edge of the sample where the boundary condition is applied.

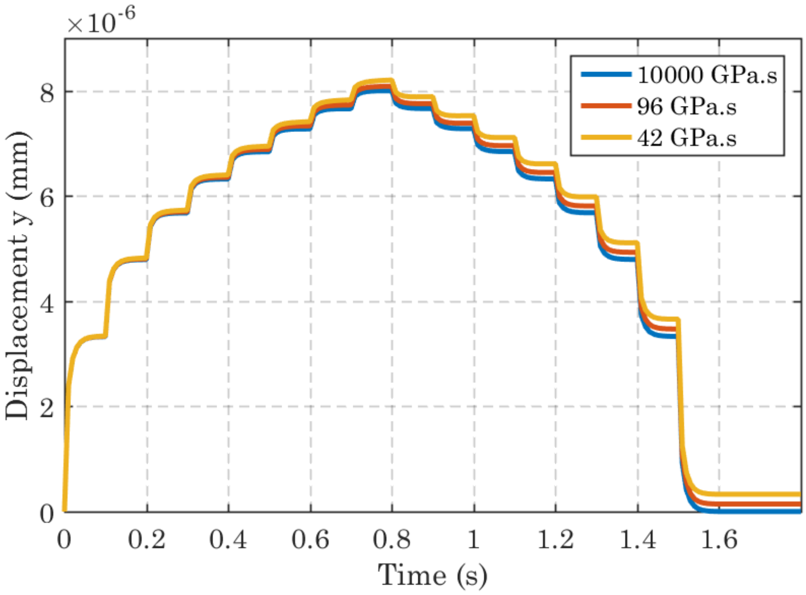

Figure 4.10: Comparison of different displacement histories for 10000 GPa.s, 96 GPa.s and 42 GPa.s. The same boundary conditions are applied to each and all material properties are identical except for the material viscosity $\hat{G}^{\beta}$

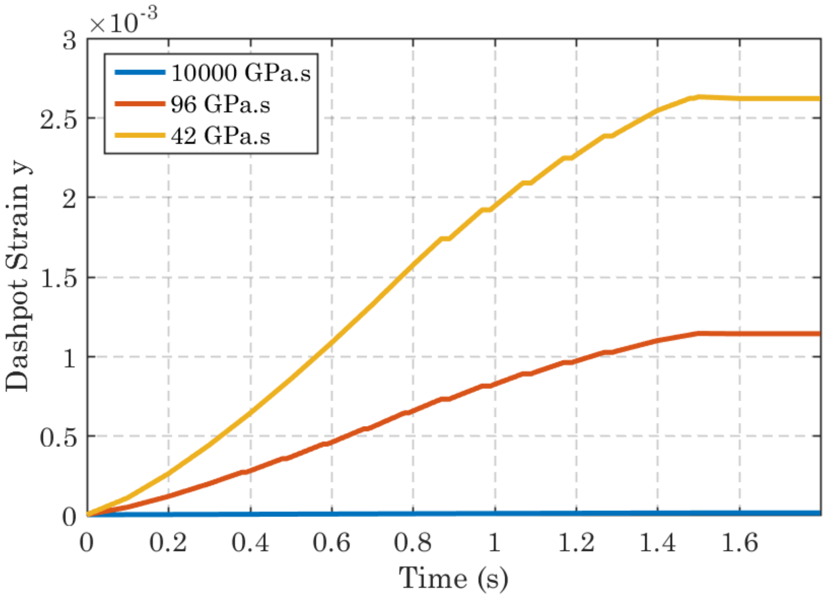

Figure 4.11: Comparison of different dashpot histories for 10000 GPa.s, 96 GPa.s and 42 GPa.s. The same boundary conditions are applied to each and all material properties are identical except for the material viscosity $\hat{G}^{\beta}$

Figure 4.11 also demonstrates that the dashpot continued to increase, even whilst undergoing desorption (after 0.8s). This is due to the stress of the additional water that has been absorbed by the polymers above the initial reference state (which in this example is completely dry). The dashpot strain uptake does not stop until the sample is back to the dry configuration.

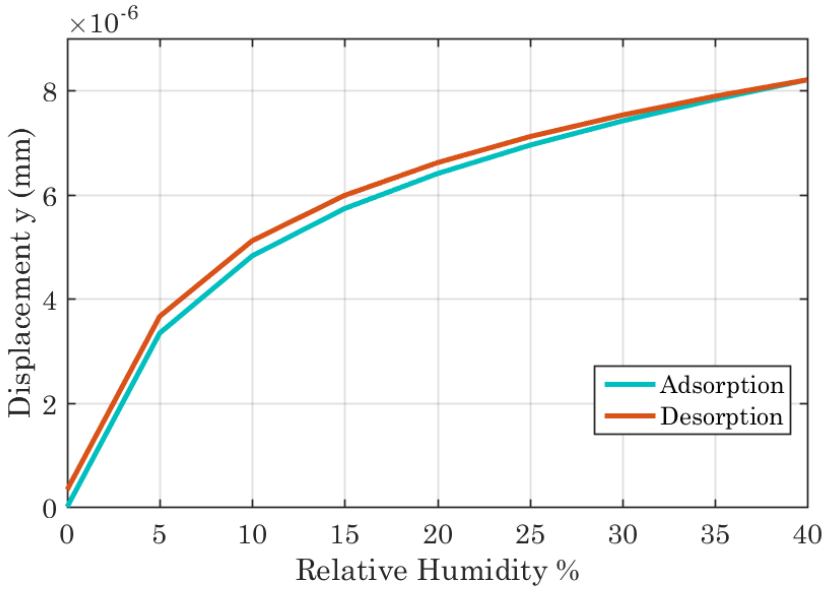

Figure 4.12: Sorption Isotherm plotted using the EMC values for the sample with dashpot shear modulus of 96 GPa.s

Test 2 - Sensitivity to the Initial Relative Humidity and Equilibrium Conditions

It is important when modelling wood cells that the moisture history is taken into account. For instance sometimes samples are kiln dried before use in experimental work. If the material is kiln dried immediately before experimental observations are made it may dry through its glass transition due to the temperature and its new reference state may be close to zero moisture content. Conversely timber that is dried at room temperature (using dried air) may not reconfigure the internal molecular structure in the same way and thus will have slightly different initial conditions before a sorption experiment. The difference between these two methods (kiln or air dried) will have consequences in terms of the initial stress build up or relaxation. This complexity has to be taken into account when using the model presented in this thesis.

Hill et al [53] take moisture history into account within their sorption experiments using previously kiln dried to about 12% moisture content wood chips (although after this they may have been exposed to normal environmental conditions until experiments are carried out). The samples were pre-dried again before experiments using a flow of nitrogen gas to dry the samples at the constant temperature, thus it likely stays well below the materials glass transition temperature. This first drying cycle has been found to be particulary important within experimental work during restrained swelling tests [72], where the material was constrained and cycled from dry (30% RH) to wet (80% RH). In the constrained test the material was found to be stiffer during the initial drying phase than subsequent phases.

In Test 2, the sensitivity of the model to the initial equilibrium conditions is assessed. The initial environmental conditions were represented by an initial internal chemical potential, corresponding to relative humidities. It was expected that the sample with an initial relative humidity of 30% would become smaller during the cycle when exposed to moisture contents less than the initial humidity and increase in size at humidities above 30%. It was also expected that the sample with an initial relative humidity of 10% would increase in size over the cycle due to the time exposed to humidities higher than the initial equilibrium state.

Figure 4.14 demonstrates the dashpot strain vs time for the three different reference states of the polymer. It shows a clear difference in the viscoelastic behaviour, particularly with regard to whether or not the viscoelastic behaviour is leading to a larger or smaller configuration with regards to the volume. The case where $\mathrm{RH}_0 = 30\%$ shows that the dashpot strain is negative throughout, with only a brief period where the sample is under going a viscoelastic strain leading to a larger volume. This occurs between 30 - 40% relative humidity, shown by the positive gradient of the 30% RH_0 dashpot history in Figure 4.14.

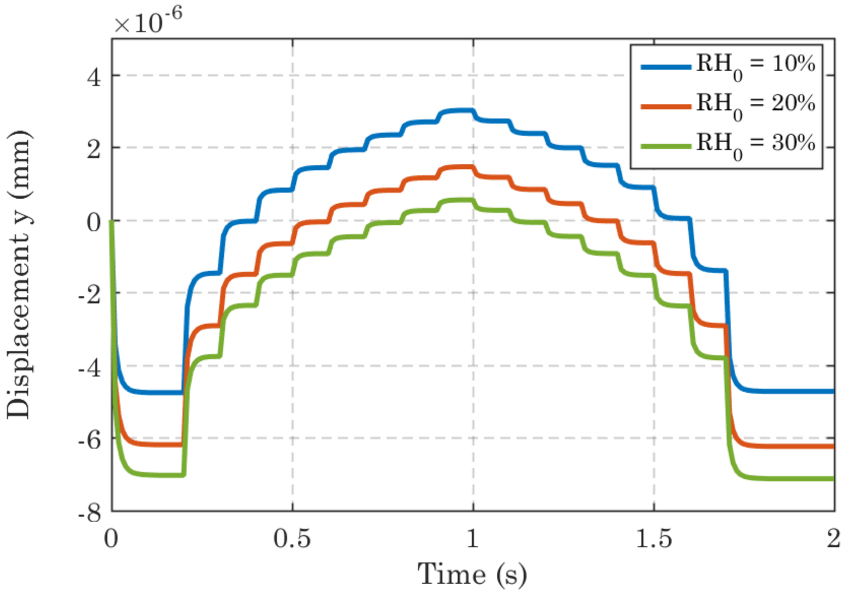

Figure 4.13: Comparison of different displacement histories for different initial relative humidity conditions. The same boundary conditions are applied to each and all material properties are identical.

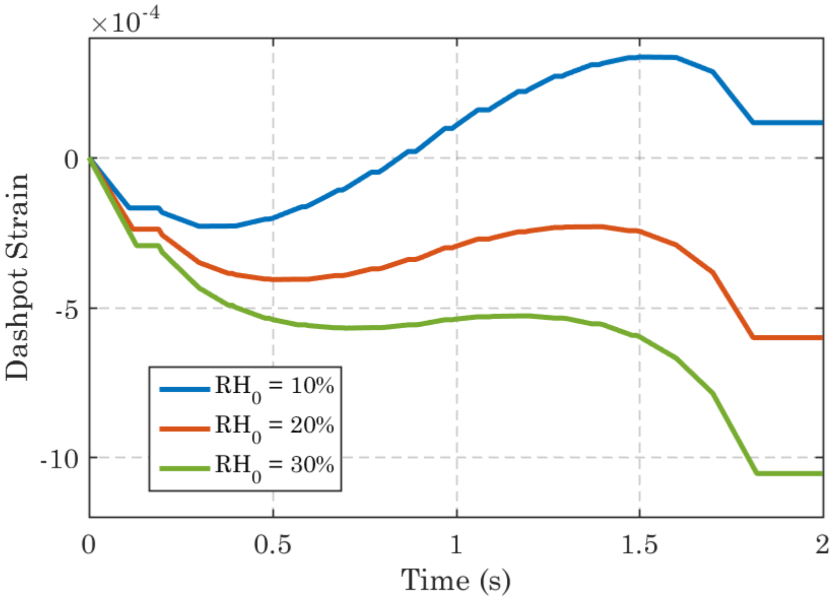

Figure 4.14: Comparison of different dashpot histories for different initial relative humidity conditions. The same boundary conditions are applied to each and all material properties are identical. The plateau near the start and at the end occur when the sample is in equilibrium.

The other two examples, $\mathrm{RH}_0 = 10\%$ and $\mathrm{RH}_0 = 20\%$, exhibit a more positive viscoelastic swelling response, gradually changing the reference configuration, i.e. the configuration at which there is zero stress, to having more volume, shown by the increased time spent at positive dashpot strain gradients in Figure 4.14.

These three examples demonstrate the importance of the moisture history to the sorption behaviour of the polymer mixture. The influence of the initial relative humidity (RH_0) is more pronounced in this range (i.e. only up to 40% relative humidity with

$\mathrm{RH}_0 = 10-30\%$) than it would be over a full sorption cycle, especially for the same range of RH_0. This is due to the fact that even at an initial 30% moisture content, the effects of history will be very small in comparison to a full sorption cycle (up to 90-95% relative humidity) as the non-linear behaviour, due to the breakdown of hydrogen bonds. For these reasons, in a full cycle, the mass gain and viscoelastic behaviour towards and above the glass transition dominate the overall hysteresis effect within the experiment. However, looking at this smaller range (up to 40% RH) does have a purpose as demonstrating the importance of sorption history on the moisture induced deformation processes.

Test 3 - Repeated Sorption Cycles

In Test 3 the sample of ligno-cellulosic polymer mixture was subjected to repeated sorption cycles to observe the viscoelastic shakedown effect and further demonstrate the importance of the moisture history on the sorption behaviour. The sample was subjected to 4 repeated cycles of varying relative humidity, from 0 - 40%, in increments of 5%. The corresponding chemical potential at the constant temperature of 24 degrees Celsius is applied at the boundary for each step.

The initial conditions were determined by first drying the sample to 1-2% moisture content, corresponding to an equilibrium relative humidity of 10% RH_0. The displacements were re-set to zero when the sample reaches equilibrium after the initial drying cycle. This is similar practice to experimental results, where measurements are not expressed relative to the mass of the sample, but relative to the point at which it reaches equilibrium at zero percent relative humidity and the sorption isotherm measurements begin.

The resulting displacements were plotted in Figure 4.15, where the chemical potential cycle applied on the boundary is also plotted on the right hand axis. With each cycle there was a corresponding increase in the total displacement in the y direction due to the hysteresis, with the displacements in the x and z directions being equal to that in the y direction. Therefore, there was a mass increase with each cycle. Figure 4.16 shows the dashpot strain in the y direction over the same period of time. It shows that there was a resulting increase in the dashpot strain over all the cycles due to the stress of the incoming solvent. With each cycle the material was in a new configuration at equilibrium. This again confirms the importance of the moisture history of any ligno-cellulosic material with regards to sorption experiments as with each sorption cycle the material enters a new configuration and thus will behave slightly differently.

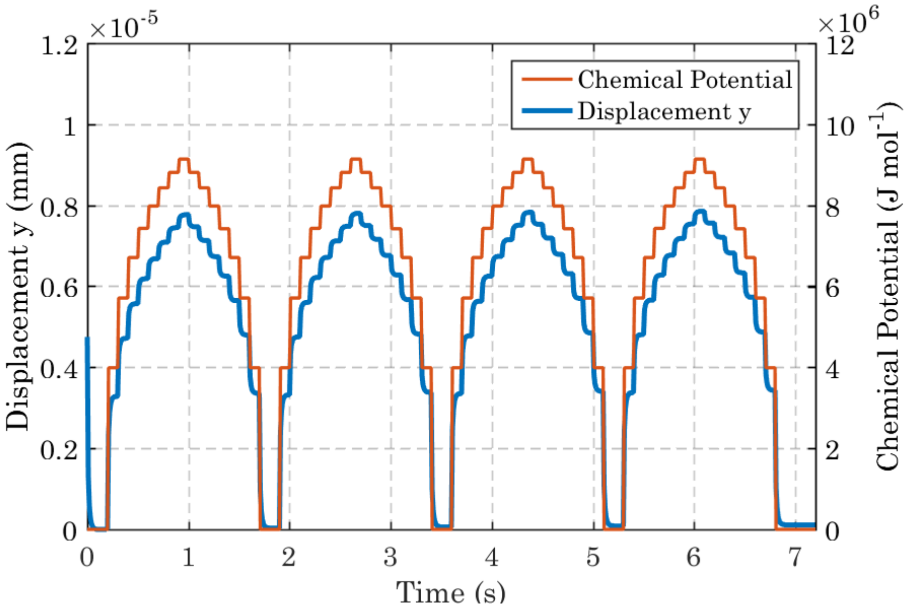

Figure 4.15: Repeated sorption cycles. The y displacements are shown in blue and the chemical potential applied on the boundary is shown in red.

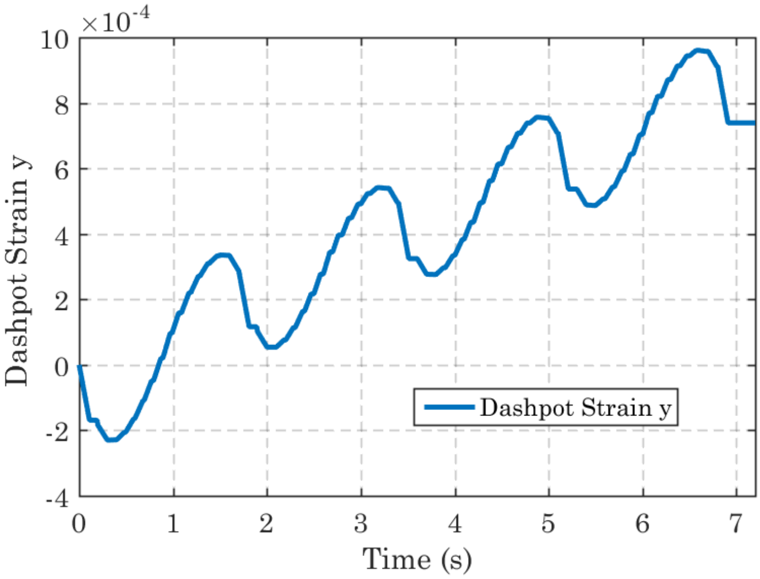

Figure 4.16: The dashpot strain under the sorption cycles shown in Figure 4.15. It shows a gradual increase in the dashpot strain with each sorption cycle. The plateau at the end occurs when the sample is in equilibrium.

The conditions a sample of material is subjected to can be difficult to control before and after testing, particularly when effects such as the weather, storage etc. can have such a large effect on the internal properties of the material. Test 3 was carried out in a entirely controlled manner, in a way that only numerical modelling can realistically achieve. Whilst the numerical modelling in this case is not a substitute for the experimental work, it can in its own way provide knowledge of the physics at work inside the material, in particular this internal rearrangement of the amorphous polymers under moisture induced stress. The implications of which will be discussed in detail further on.

Sorption Isotherm

The sorption results can be plotted in the form of a sorption isotherm, where the equilibrium moisture content (EMC), the moisture content at equilibrium for a given set of environmental conditions, is plotted as a percentage mass increase due to water uptake within the cell wall polymers. The original mass of cellulose remains constant, i.e. the number of moles of dry cellulose does not change, and any increase in mass is assumed to be due to moisture.

To determine whether or not the sample is at the EMC%, the mass gain obtained at the final two time steps for each given relative humidity is used to calculate the change in mass per minute. When this is sufficiently low, for instance less than 0.002%/min, then it can be assumed the equilibrium moisture content has been reached.

To calculate the percentage volume increase of the sample, using the strains in the x,y and z directions:

$$\Delta V\% = \frac{V - V_0}{V_0} \times 100 \tag{4.14}$$

where V is the current volume, and V_0 is the original volume at time zero. The increase in volume can then be converted to a mass increase by applying a factor based upon the relative density of cellulose (ρ^c) and water (ρ^w). The unit-less mass factor, f^m, is determined as follows:

$$f^m = \frac{\rho^w}{\rho^c} = \frac{0.9982 \times 10^{-3} g/mm^3}{1.5 \times 10^{-3} g/mm^3} = 0.665467 \tag{4.15}$$

The equilibrium mositure content, EMC%, can then be calculated:

$$\text{EMC\%} = \Delta V\% \times f^m \tag{4.16}$$

The EMC can then be plotted against the relative humidity and compared to experimental results for cellulose sorption isotherms. The results compare favourably, giving a good qualitative match (Figure 4.17). The model clearly demonstrates similar softening behaviour in the amorphous regions of the polymer network, however results are only qualitative at this stage as it only accounts for the amorphous material behaviour and does not include any crystalline contributions. The addition of which is likely to change the results, especially in regard to the swelling in each direction, with the longitudinal axis exhibiting far greater resistance to moisture induced changes, due to the very stiff longitudinally oriented cellulosic microfibrils.

Furthermore, if the sorption isotherm is to be predicted beyond the glass transition, the relaxation rate of the dashpot would need to evolve as the concentration of water within the polymer mixture does. The results shown in Figure 4.17 are for a mixture of hemicellulose and lignin using the viscoelastic material properties obtained from Eitelberger et al [30].

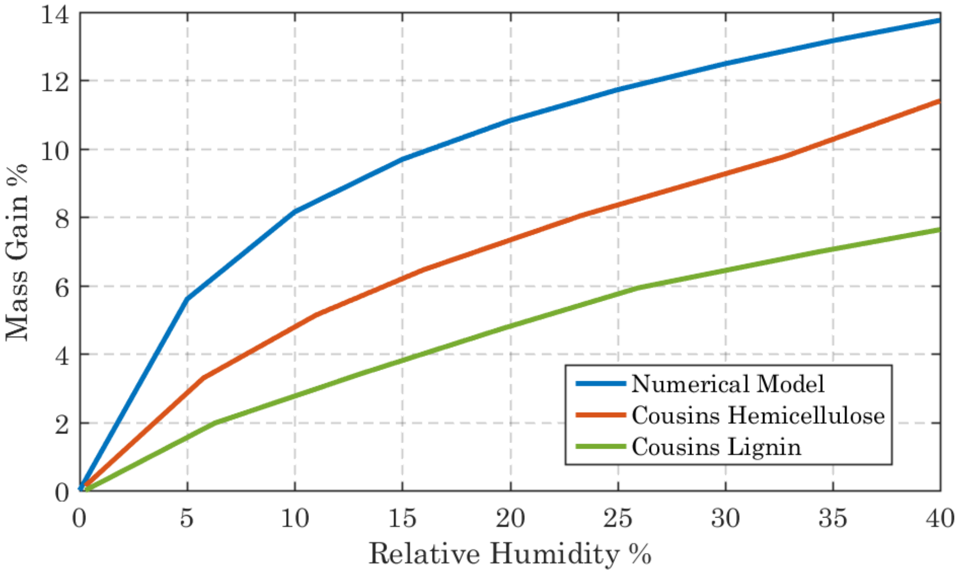

Figure 4.17: Comparison of the numerical model with EMC% results from experiments by Cousins on isolated hemicelluloses and lignin.

The results obtained from the experimental work yield lower equilibrium moisture contents, however this can be explained for several reasons. The numerical result is for a purely amorphous polymer mixture, with an allowance for free-swelling. This means that the constraining effects of being part of a large network of material cells is not accounted for. However, the curves clearly follow a similar gradient as the relative humidity is increased and as such this provides good results. There are also questions of the validity of the hemicellulose and lignin results in isolation as opposed to being insitu. For instance the obtained values for shear modulus of the hemicellulose , Figure 4.1, show a very high obtained value for the shear modulus when compared to those used and determined from other sources [30, 32, 40].

4.2.2 Conclusions of Application to Sorption Theory

The selection of tests carried out on the polymer matrix has provided some useful insight into the behaviour of the matrix of hemicelluloses and lignin, in which the cellulose fibres are embedded within the cell wall. As covered before, the amorphous matrix is thought to be the primary cause of the relaxation behaviour and interactions with the water in the cell wall and as such this phase of the material is of most interest in the context of this model at this time. The model demonstrates clear sorption hysteresis effects when using material properties obtained from multi-scale modelling [30], carried out specifically for use in viscoelastic behaviour models on the length scale of the cell wall. As such this provides a tool from which to understand further the link between sorption kinetics and hysteresis as proposed by Hill [50, 54]. Certainly from the results in the model carried out using the gel model, it seems likely that sorption hysteresis is the result of viscoelastic behaviour within the cell wall of wood and other natural fibres. However, the small section of wood cell polymers used in this case may exhibit different behaviour when observed on the length scale of an entire wood cell, as is demonstrated in the next section. The model also demonstrates a link between the moisture history of a polymer sample and the observed swelling response through the use of the internal viscoelastic variable. This allows moisture history to become a factor in future cell wall calculations, in a numerically controlled environment. As such this provides more control over the environment the sample is exposed to, as in experimental work it is difficult to ensure each sample has the same moisture sorption history before analysis, potentially leading to different results.

4.3 Sorption Test on a Constrained Wood Cell

An individual cell was modelled from within a small slice of wood. It was exposed to different environmental conditions and the effects observed. Until this point the boundary conditions have been applied instantaneously, dealing with one portion of the cell in isolation, where the water vapour change is assumed immediate. However, in the present case the theory is extended to a cell considered to be within a network of cells. Within this, the diffusion of water vapour becomes of importance, as the time taken for water vapour of higher activity to reach cells in the densely packed system of cells may take a while. To investigate this, a simple 1D problem, where the diffusion rate is described using a prescribed value for water vapour transport through wood. The evolution of the chemical potential through this bar can then be used to create the boundary condition for the wood cell within the network.

4.3.1 1D Diffusion Test

Within the wood there are two main considerations with regard to moisture content that must be taken into account. Firstly the diffusivity of the cell wall material itself, and secondly the rate at which water vapour is transported through the network of cells. To determine the boundary conditions for cells within a larger network, a 1D diffusion problem is used, along with the rate of water vapour diffusion, to determine how quickly the chemical potential reaches equilibrium at a point selected within a larger sample. This profile of the chemical potential can then be used to apply to the boundary of a cell within the material, at that distance from the environment.

To do this, first the effective length of diffusion was determined. To keep this similar to experimental conditions, a slice of the wood was modelled. In the present case, for simplicity of modelling, the different wood cells (earlywood and latewood) are neglected and it was assumed to be one consistent cell type.

Figure 4.18 shows a tree disc with a small section cut out from the earlywood and a cell within the earlywood which was represented in the test. The small section cut out represents an experimental test on a small section of timber, taken from an individual earlywood growth ring, that has been removed from a larger disc and is not considered as in-situ. The smallest length of the slice $2l_D$ is the effective length of diffusion in this case and the cell is positioned in the middle, with distance l_D to the exposed surface of the sample. It was assumed that the length in the longitudinal direction of the fibre to this particular cell was much larger than the distance across the fibres (l_D), thus the diffusion in this direction can be disregarded.

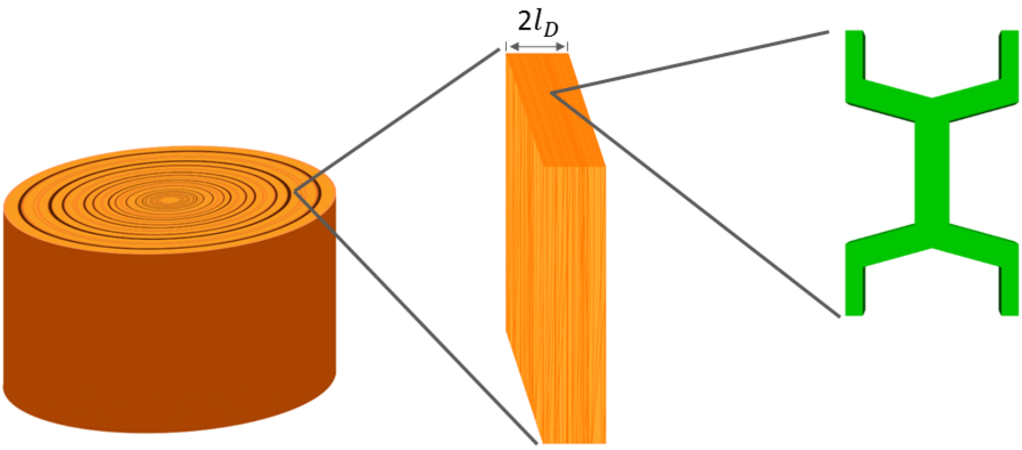

Figure 4.18: Timber disc (left), and a small section cut from the earlywood (middle) in the longitudinal direction of the fibres, which will be used in the sorption test. l_D gives the effective length of diffusion, i.e. the shortest distance to the change of environment to the individual cell that is modelled. Left: Timber disc with growth rings consisting of earlywood (lighter colour) and latewood (darker colour) cells. Centre: Thin section cut from the Timber disc consisting of only earlywood cells. Right: An individual earlywood cell isolated from the thin section of timber.

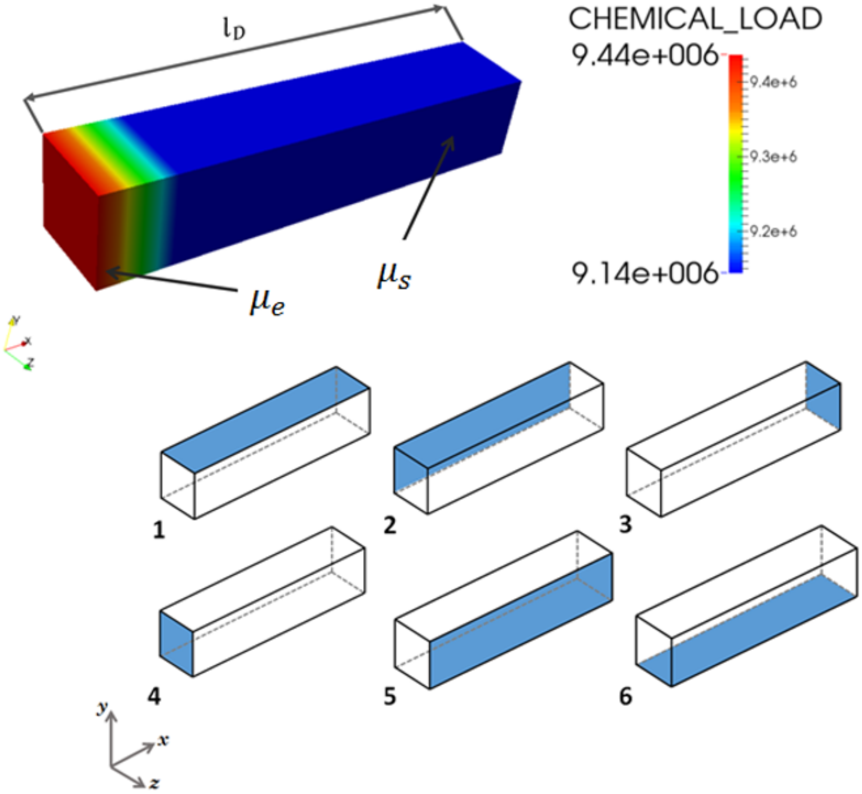

Figure 4.19: Representation of the 1D diffusion problem. l_D gives the effective length of diffusion, i.e. the shortest distance to the change of environment to the individual cell that is modelled. μ_e and μ_s are the external chemical potential and the initial chemical potential of the solvent within the wood sample respectively.

Face	Mechanical Conditions	Chemical Conditions
1	$u_y = 0$	$\frac{\partial \mu_s}{\partial y} = 0$
2	$u_z = 0$	$\frac{\partial \mu_s}{\partial z} = 0$
3	$u_x = 0$	$\frac{\partial \mu_s}{\partial x} = 0$
4	-	μ_e
5	$u_z = 0$	$\frac{\partial \mu_s}{\partial z} = 0$
6	$u_y = 0$	$\frac{\partial \mu_s}{\partial y} = 0$

Table 4.6: Boundary conditions for the sorption test

Chemical Condition	Magnitude	Units	Time
μ_e	9.44×10^{06}	J mol^{-1}	0.00s
μ_s	9.44×10^{06}	J mol^{-1}	0.00s

Table 4.7: Initial chemical potential conditions, at $t = 0$, applied to faces 2,5 and 6, for the bar diffusion test. The environmental chemical potential, μ_e is applied on boundaries according to Table 4.11. The chemical potential of the solvent, μ_s, within the sample is given for $t = 0$ and is allowed to evolve freely at $t > 0$.

RH %	μ_e	Units	Time
40	9.44×10^{06}	J mol^{-1}	0.00s - 1.00
35	8.81×10^{06}	J mol^{-1}	1.00 - 150s
40	9.44×10^{06}	J mol^{-1}	151 - 300s

Table 4.8: Chemical potential conditions, applied to faces 2,5 and 6, for the bar diffusion test. The environmental chemical potential, μ_e is applied on boundaries according to Table 3.9. μ_s is allowed to evolve within the gel after the first time step

As discussed within Test 1 (Chapter 4), the dashpost viscosity, $\hat{G^\beta}$, is an important parameter when determining relaxation behaviour. In this wood cell test, due to the assumption that there is a relatively long distance from the isolated cell to the environment, a dashpot viscosity is selected from experimental results [116]. This will properly account for the relaxation behaviour when determining the rate of diffusion to the isolated wood cell through the network of wood cells.

Input Parameter	**Symbol**	**Value**	**Units**
Shear Modulus Spring α	G^{α}	1.84×10^{03}	MPa
Shear Modulus Spring β	G^{β}	1.84×10^{03}	MPa
Viscosity of Dashpot β	$\hat{G^{\beta}}$	10×10^{06}	MPa.s
Poisson's Ratio Spring α	ν^{α}	0.22	-
Poisson's Ratio Spring β	ν^{β}	0.22	-
Poisson's Ratio Dashpot β	$\hat{\nu^{\beta}}$	0.22	-
Volume per Mole of Water	Ω	18000	$\text{mm}^3\ \text{mol}^{-1}$
Permeability	κ	1×10^{-14}	mm^2
Viscosity of Water	η	1×10^{-06}	MPa.s

Table 4.9: Input data for the 1D diffusion test. The properties take into account the longer length scale through a higher dashpot shear viscosity, $\hat{G^{\beta}}$, and permeability, κ.

The water vapour diffusion coefficient was obtained from Figure 1.5, at an assumed temperature of 25°C. The chemical potential change on the boundary was applied to one face only and all other faces are set to zero flux. The chemical potential was then plotted in Figure 4.20, taken from the end of the sample, in this case 100 micrometers from where the higher chemical potential was applied. This time series can then be used to apply to an individual wood cell within the network.

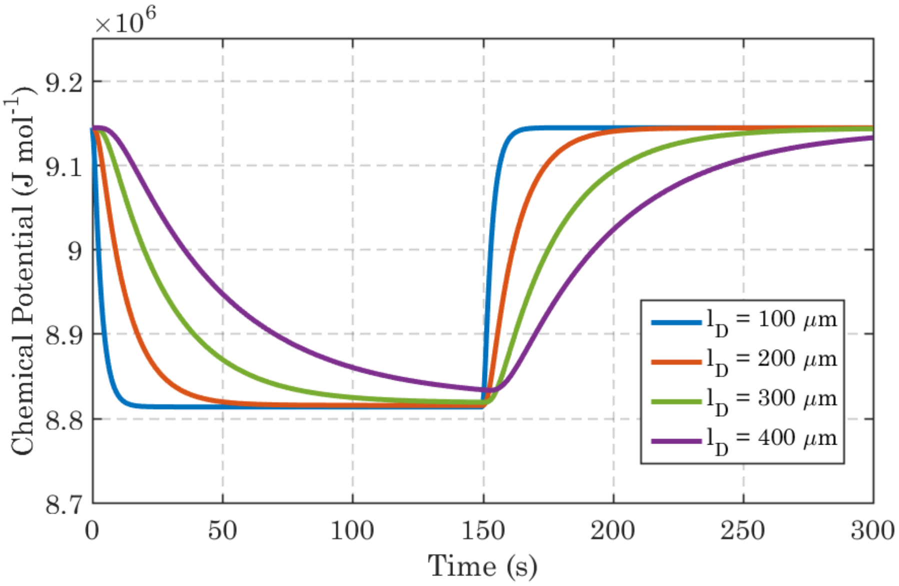

Figure 4.20: Plot of the chemical potential vs time at the end of the bar. Initial RH is 40%, it is then reduced to 35% through the sample and increased back to 40%

4.3.2 Isotropic Wood Cell

To test the applicability to wood cells, a test was carried out on a generalized repeatable cell unit. The complex multi-layer structure was replaced by an isotropic matrix in the general shape of a wood cell, from which assessment of the behaviour of the polymer matrix was carried out in order to establish a basis from which to increase the complexity by including fibres and different layers of materials in a complex arrangement.

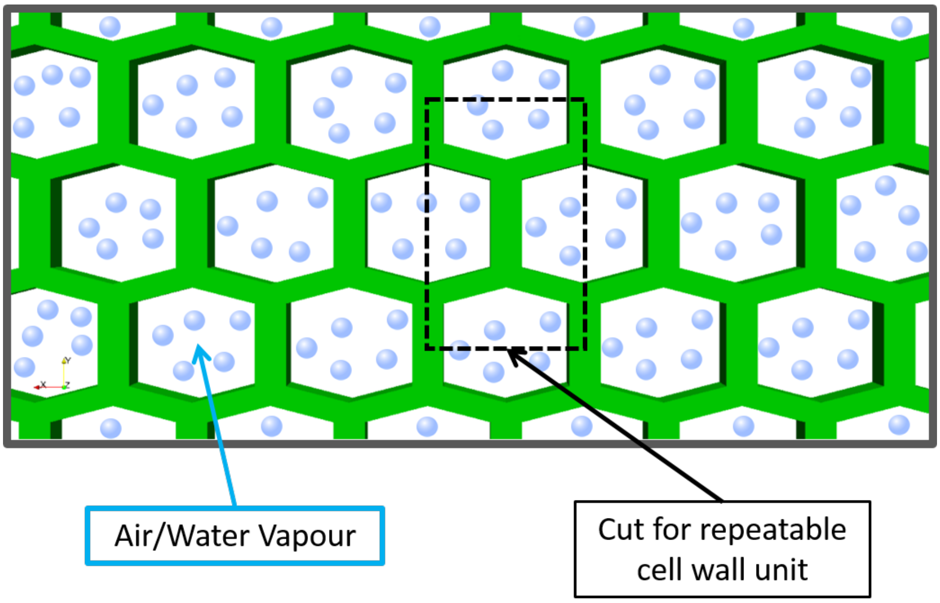

Figure 4.21: Network of wood cell units with expansion allowed within the cells. Within the lumens is the air/water mixture with chemical potential μ_e (represented by droplets). The cell wall has initial chemical potential μ_s.

A tightly packed area of cells was considered, that were exposed to an increase in the air humidity. As the air/water mixture passes through the sample, it is transported through the lumens and thus migrates into the cell wall that surrounds. Figure 4.21 demonstrates this tightly packed arrangement along with an area from which a unit cell was selected.

The unit cell was constrained on its symmetrical boundaries, as shown in Figure 4.22, with expansion allowed into the lumen within the cells. In reality, an individual wood cell would not have full constraint on all boundaries. However, for simplicity it is treated as fully constrained and the focus is on the mechanics of expansion into the lumens and assessing the likelihood of viscoelastically limited solvent migration occuring in the observed range of relative humidity. However, future testing should incorporate a more realistic boundary condition between the cells and anisotropic properties to assess correctly the expansion in the longitudinal direction of the cell. The incoming air/water vapour mixture, with chemical potential given in Joules, was carried through the lumens, and subsequently penetrated into the cell wall polymer mixture which had an initial chemical potential, also given in Joules.

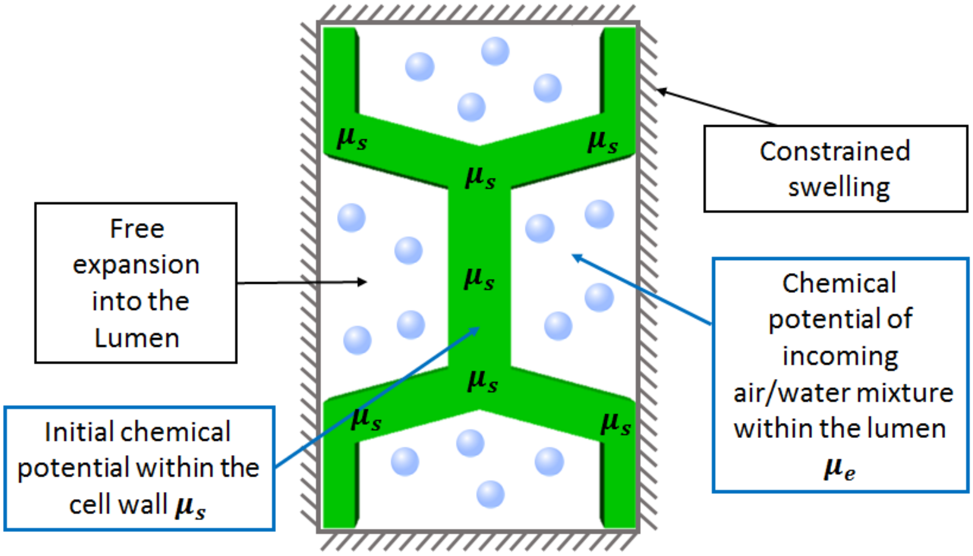

Figure 4.22: Isolated constrained cell unit with expansion allowed within the cells. Within the lumens is the air/water mixture with chemical potential μ_e (represented by droplets). The cell wall has initial chemical potential μ_s.

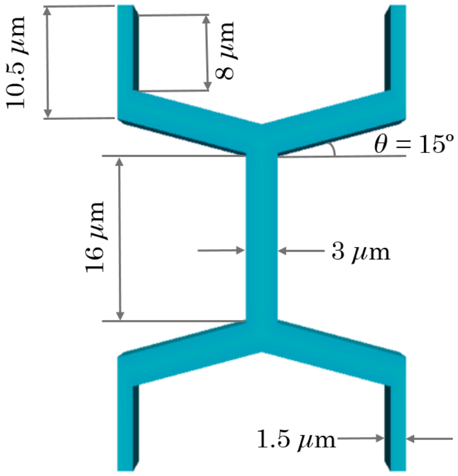

Figure 4.23: Dimensions of the earlywood cell

The cell wall was 3 μm thick with a diameter of 30 μm which was within the range that is expected [37, 43]. It was not an exact replica of any cell in particular as at this stage the focus was to analyse the behaviour of the coupled stress diffusion model, in particular the amorphous matrix within which adsorption tends to occur. Furthermore, without replicating all the cell wall features (exact composition and microfibril angle of fibres within each layer etc) exact comparison would have little meaning at this stage.

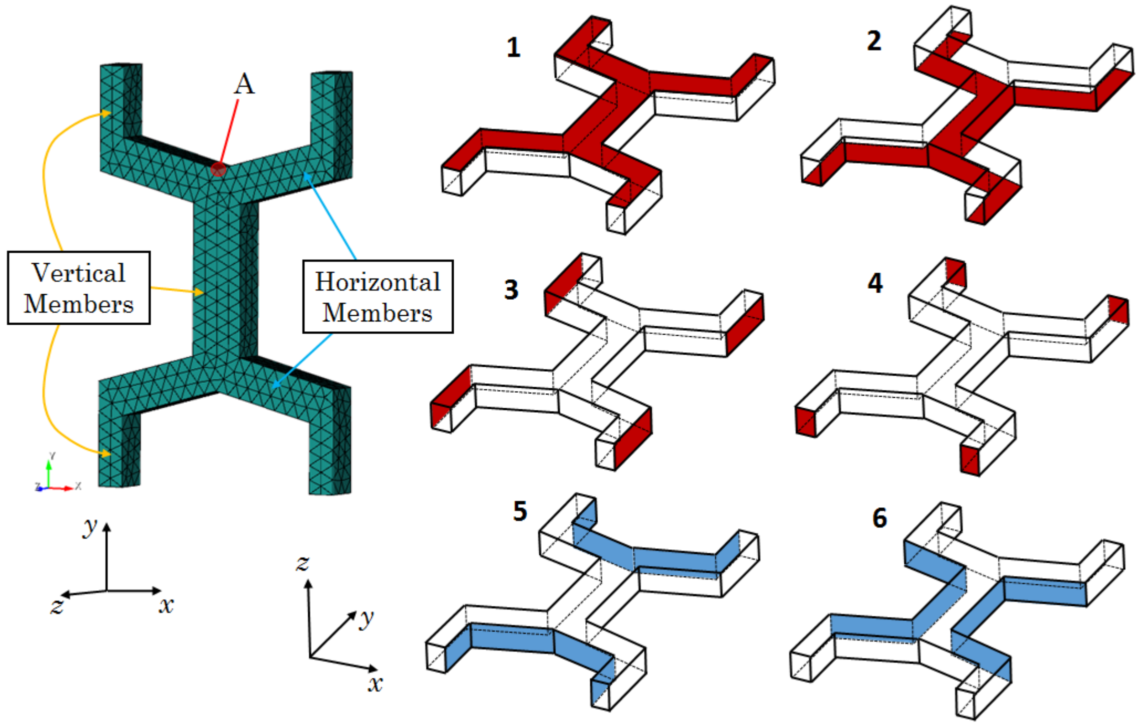

Figure 4.24: The wood cell mesh and groups of faces where mechanical and chemical boundary conditions are applied. The groups of red faces (1-4) are subjected to Neumann conditions for the chemical potential, i.e. $\frac{\partial \mu_s}{\partial x} = 0$, and the displacements normal to the face are constrained. The groups of blue faces (5 and 6) are subjected to the environmental chemical potential, applied as a Dirichlet condition, μ_e.

The material properties were taken from the multi-scale parameters determined by Eitelberger et al [30]. Only the hemicellulose and lignin phase was considered at this point, neglecting the effects of the crystalline fibres within the material properties. However, the effects of the fibres were accounted for by constraining the cell in the z direction, simulating the much stiffer cellulose fibres in a simple manner. The material parameters were determined for a moisture content of 10% in Douglas fir, which was assumed to be in equilibrium with the environment between around 40%-50% relative humidity. The diffusion values were also taken for 10% moisture content.

Chemical Condition	**Magnitude**	**Units**	**Time**
μ_e	9.44×10^{06}	J mol^{-1}	0.00s
μ_s	9.44×10^{06}	J mol^{-1}	0.00s

Table 4.10: Initial chemical potential conditions, applied to groups 5 and 6 for the wood cell test. The environmental chemical potential, μ_e is applied on boundaries according to Table 4.11. The chemical potential of the solvent, μ_s, within the sample is given for $t = 0$ and is allowed to evolve freely at $t > 0$.

Face/Group	**Mechanical Condition**	**Chemical Condition**
1	$u_z = 0$	$\frac{\partial \mu_s}{\partial z} = 0$
2	$u_z = 0$	$\frac{\partial \mu_s}{\partial z} = 0$
3	$u_x = 0$	$\frac{\partial \mu_s}{\partial x} = 0$
4	$u_y = 0$	$\frac{\partial \mu_s}{\partial y} = 0$
5	-	μ_e
6	-	μ_e

Table 4.11: Boundary conditions for the sorption test. The boundaries (Faces 1-6) where mechanical and chemical boundary conditions are applied are visualised in Figure 4.24.

Input Parameter	**Symbol**	**Value**	**Units**
Shear Modulus Spring α	G^{α}	1.84×10^{03}	MPa
Shear Modulus Spring β	G^{β}	1.84×10^{03}	MPa
Viscosity of Dashpot β	$\hat{G^{\beta}}$	96×10^{03}	MPa.s
Poisson's Ratio Spring α	ν^{α}	0.22	-
Poisson's Ratio Spring β	ν^{β}	0.22	-
Poisson's Ratio Dashpot β	$\widehat{\nu^{\beta}}$	0.22	-
Volume per Mole of Water	Ω	18000	$\mathrm{mm}^3\ \mathrm{mol}^{-1}$
Permeability	κ	8.77×10^{-17}	mm^2
Viscosity of Water	η	1×10^{-06}	MPa.s

Table 4.12: Input data for the desorption test for an earlywood cell. The properties are based upon the polymer properties for lignin and hemicellulose, determined through multi-scale modelling by Eitelberger et al [30].

Desorption Test

The first test was carried out on a wood cell in equilibrium with the environment at 40% relative humidity. The humidity was then decreased to 35%, applied using the results from the 1D diffusion test in the previous section (Figure 4.20). The sample was then returned to 40% relative humidity. To fully analyse the effects, the dashpot viscosity was changed several times in order to understand whether the diffusion or viscoelasticity was the rate-limiting material process in the case of a thin walled earlywood cell. From Figures 4.25 and 4.26 it can be concluded that the solvent uptake was viscoelastically limited for this cell with the chosen material properties and environmental conditions.

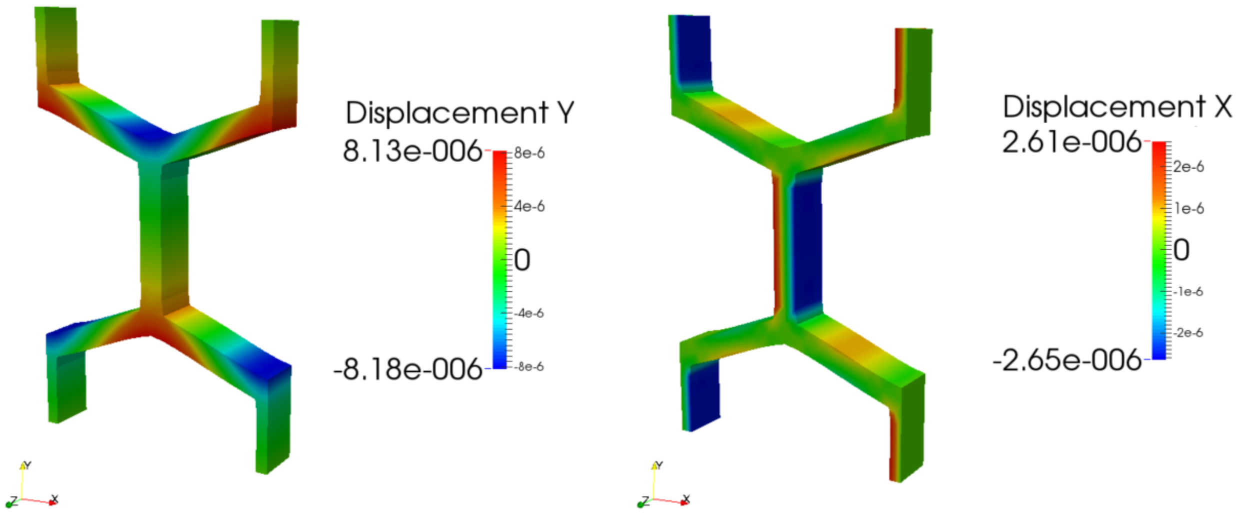

(a) (b)

Figure 4.25: Deformation of a wood cell in desorption (a) Displacements in the y direction (b) Displacements in the x direction

Figure 4.25 shows the displacements in the x and y directions, plotting the movement of the cell wall into/out from the lumen as the moisture content decreased. The displacements into/out of the lumen were plotted and compared for various different values of dashpot viscosity. Figure 4.25 demonstrates both the displacement and dashpot strain in the y-direction and the cell reduces in volume, expanding the size of the lumen.

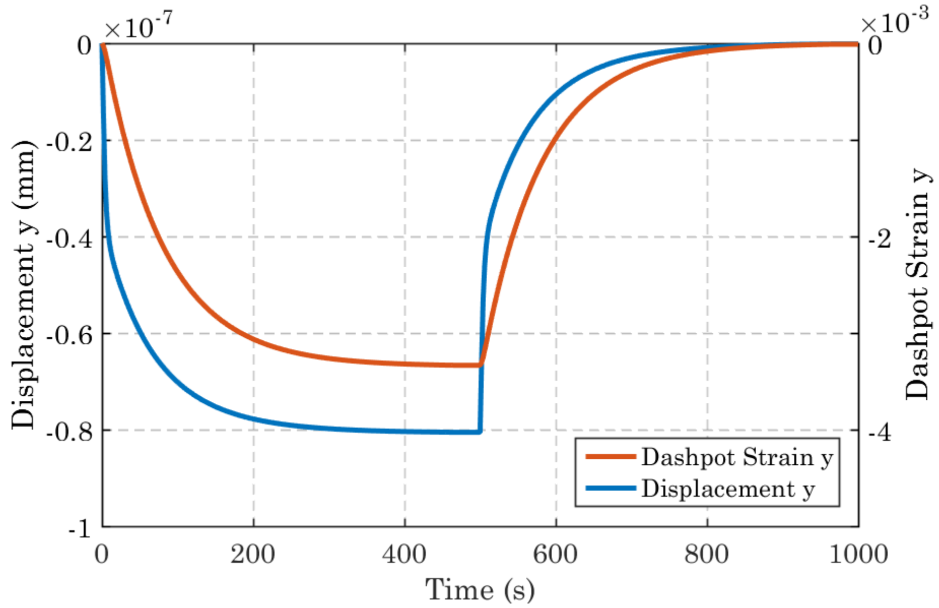

Figure 4.26: Displacement history, taken at point A from Figure 4.24, for the desorption test in the y direction (shown in blue) and dashpot strain history, $\hat{\varepsilon}_{yy}$, in the y direction (shown in red).

Figure 4.26 shows the different values of dashpot viscosity used for comparison. The plot for 96GPa.s, the value given in multiscale modelling studies by Eitelberger et al [30], clearly shows that the solvent uptake was viscoelastically limited, as demonstrated by the much faster time to equilibrium displayed by the sample with a lower dashpot viscosity. The other two values of dashpot viscosity demonstrate glassy behaviour, the kind of behaviour which would be expected closer to zero percent moisture content in a typical sample of wood.

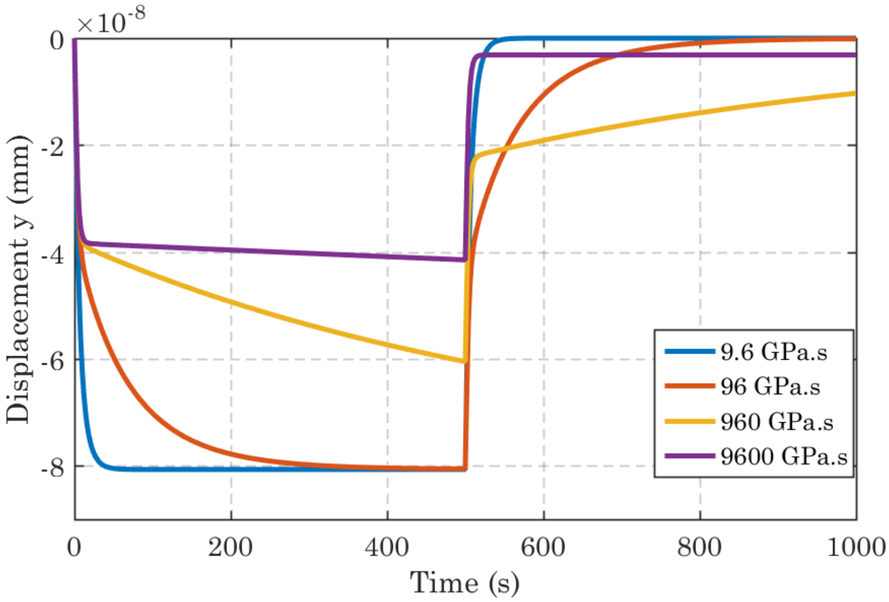

Figure 4.27: Displacement history in the y direction for different values of dashpot viscosity

Influence of Water Vapour Diffusion Length

Figures 4.28 and 4.29 demonstrate the influence of the water vapour diffusion length (l_D) on the uptake of solvent at various points within a sample. This is relevant as the observed macro scale adsorption and desorption behaviour is due to an overall combined response of many different cells acting together and interacting with the environment at different times.

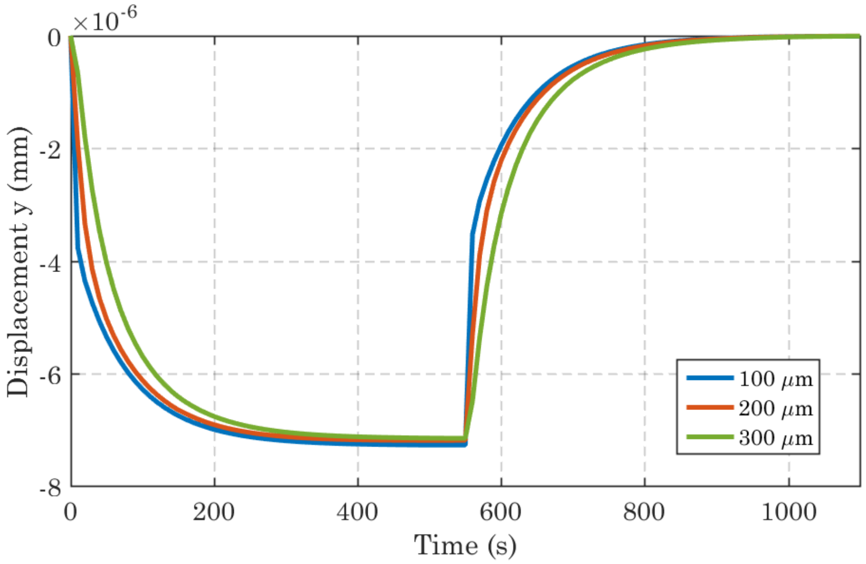

Figure 4.28: Displacement histories in the y direction, taken at point A in Figure 4.24, for samples at different depths to the external environment (100-300 μm).

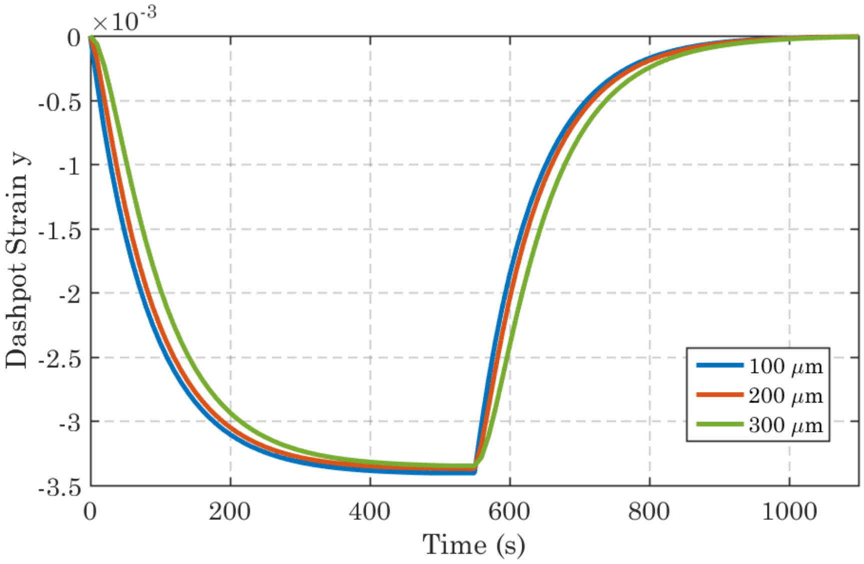

Figure 4.29: Dashpot strain histories in the y direction, $\hat{\varepsilon}_{yy}$, taken at point A in Figure 4.24, for samples at different depths to the external environment (100-300 μm).

Adsorption Test

An adsorption test was also carried out, where the wood cell was initially at equilibrium with the environment at 40% relative humidity and was increased to 45% relative humidity using the results from Figure 4.20. The cell was assumed to be 100 μm within the wood sample.

Input Parameter	**Symbol**	**Value**	**Units**
Shear Modulus Spring α	G^{α}	1.84×10^{03}	MPa
Shear Modulus Spring β	G^{β}	1.84×10^{03}	MPa
Viscosity of Dashpot β	$\hat{G}^{\beta}$	96×10^{03}	MPa.s
Poisson's Ratio Spring α	ν^{α}	0.22	-
Poisson's Ratio Spring β	ν^{β}	0.22	-
Poisson's Ratio Dashpot β	$\hat{\nu^{\beta}}$	0.22	-
Volume per Mole of Water	Ω	18000	$\text{mm}^3\ \text{mol}^{-1}$
Permeability	κ	8.77×10^{-17}	mm^2
Viscosity of Water	η	1×10^{-06}	MPa.s

Table 4.13: Input data for the adsorption test for an earlywood cell. The properties are based upon the polymer properties for lignin and hemicellulose, determined through multi-scale modelling by Eitelberger et al [30].

Chemical Condition	**Magnitude**	**Units**	**Time**
μ_e	9.44×10^{06}	J mol^{-1}	0.00s
μ_s	9.44×10^{06}	J mol^{-1}	0.00s

Table 4.14: Initial chemical potential conditions, applied to groups 5 and 6 for the wood cell adsorption test. The environmental chemical potential, μ_e is applied on boundaries according to Table 4.11. The chemical potential of the solvent, μ_s, within the sample is given for $t = 0$ and is allowed to evolve freely at $t > 0$.

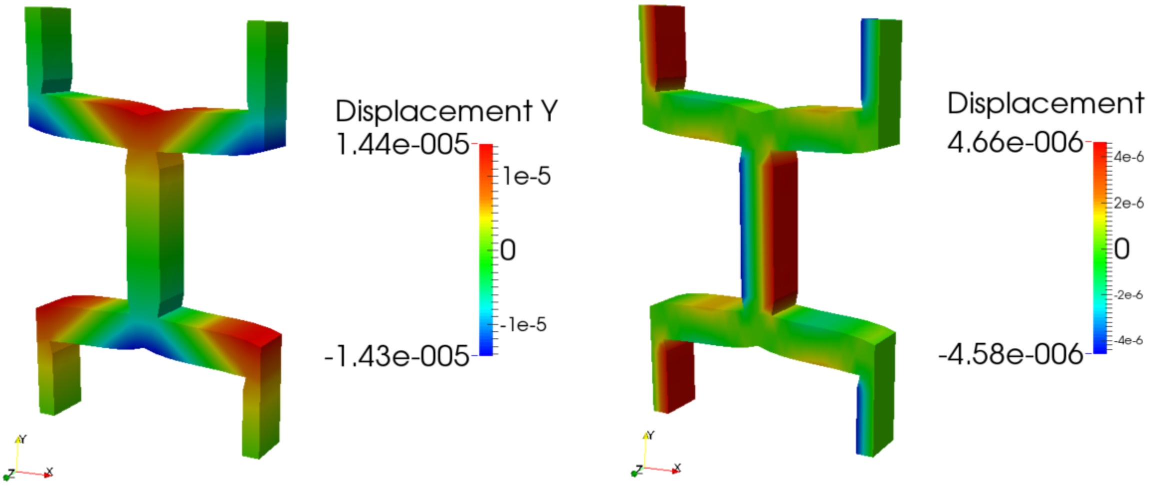

(a)

(b)

Figure 4.30: Deformation of a wood cell in adsorption (a) Displacements in the y direction (b) Shows the Displacements in the x direction

The deformation of the wood cell is shown in Figure 4.30, in which it is clearly shown that the cell expands into the lumens and the initial hexagon shape of the sides of the inner cell flattened out into a more square shape due to the expansion into the lumen.

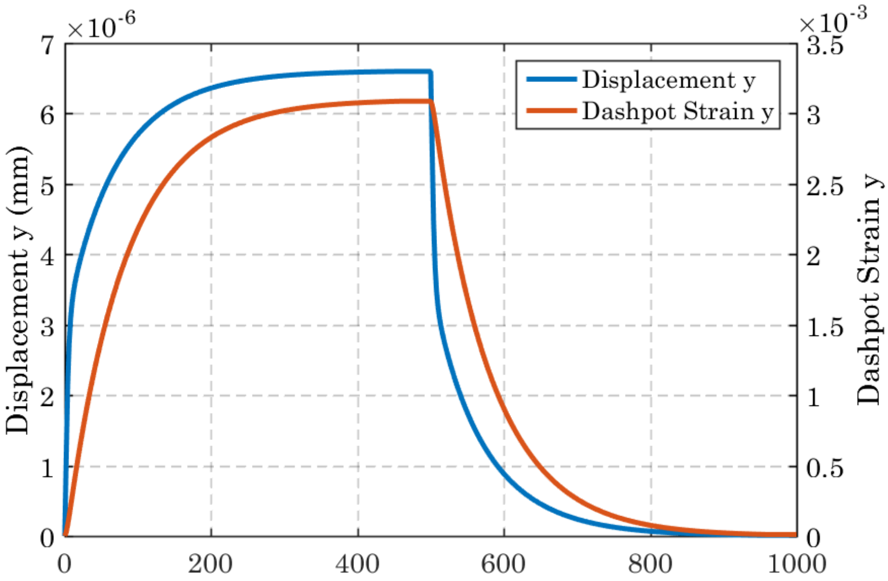

Figure 4.31: Displacement history in the y direction (shown in blue), taken at point A in Figure 4.24, for the adsorption test, and the dashpot strain history, $\hat{\varepsilon}_{yy}$, in the y direction (shown in red).

Again there was a similar uptake of the dashpot strain when compared to the displacement in the y direction (Figure 4.31), indicating viscoelastically limited solvent uptake. The displacements in this case are positive with respect to the y axis due to the expansion into the lumen. This compares well with negative displacement obtained from the same point shown in Figure 4.26 for the desorption case.

Adsorption and Desorption Comparison

In this section a comparison is made between the behaviour the cell in both adsorption and desorption. In particular the stress within and the displacements are compared. The cells are shown alongside each other in order to establish the changing dimensions, where the deformations have been scaled 100 times in order to clearly establish the behaviour. The displacements in the y-direction, shown in Figure 4.32, show the different expansion mechanisms in desorption and adsorption and Figures 4.33 and 4.34 show the build up of stress, σ_{xx} and σ_n respectively, within the individual cell.

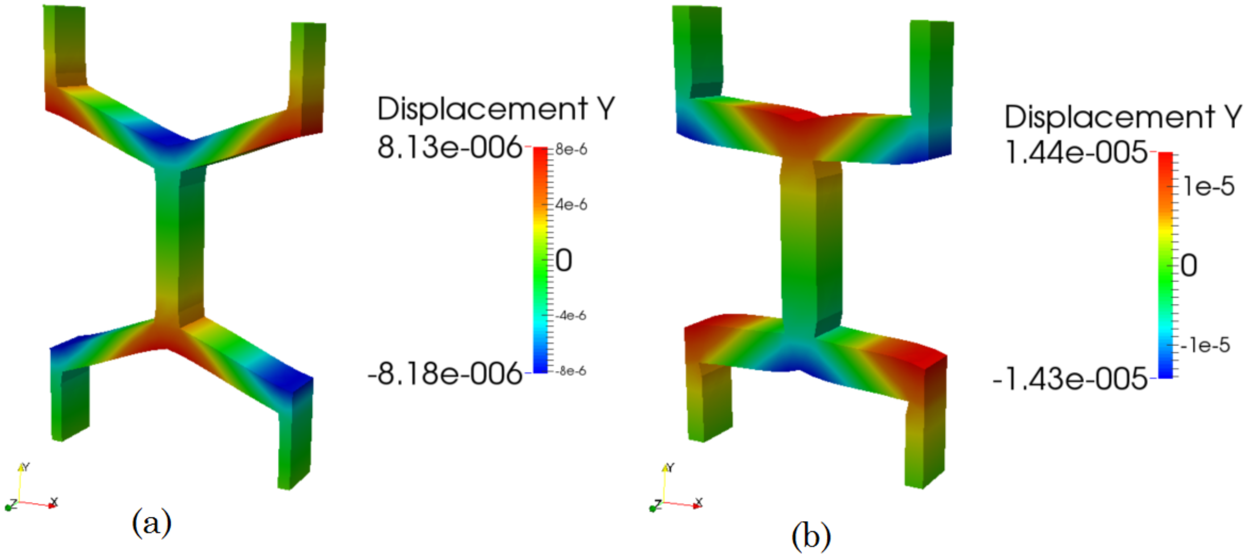

(a) (b)

Figure 4.32: Comparison of the displacements in the y direction of a wood cell (a) desorption (b) adsorption

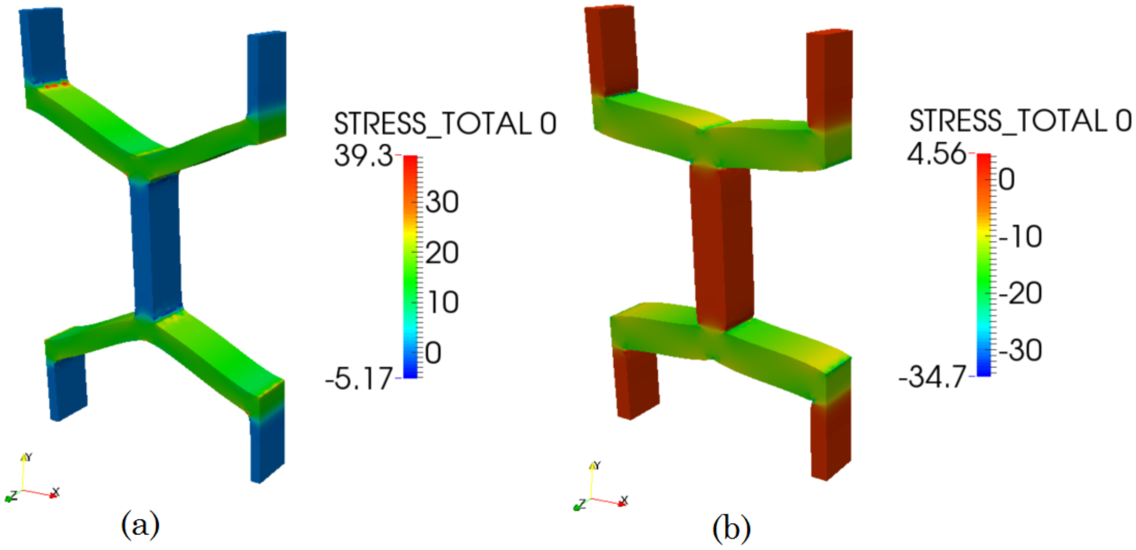

(a) (b)

Figure 4.33: Total stress, σ_{xx} (MPa) within a wood cell in (a) desorption (b) adsorption

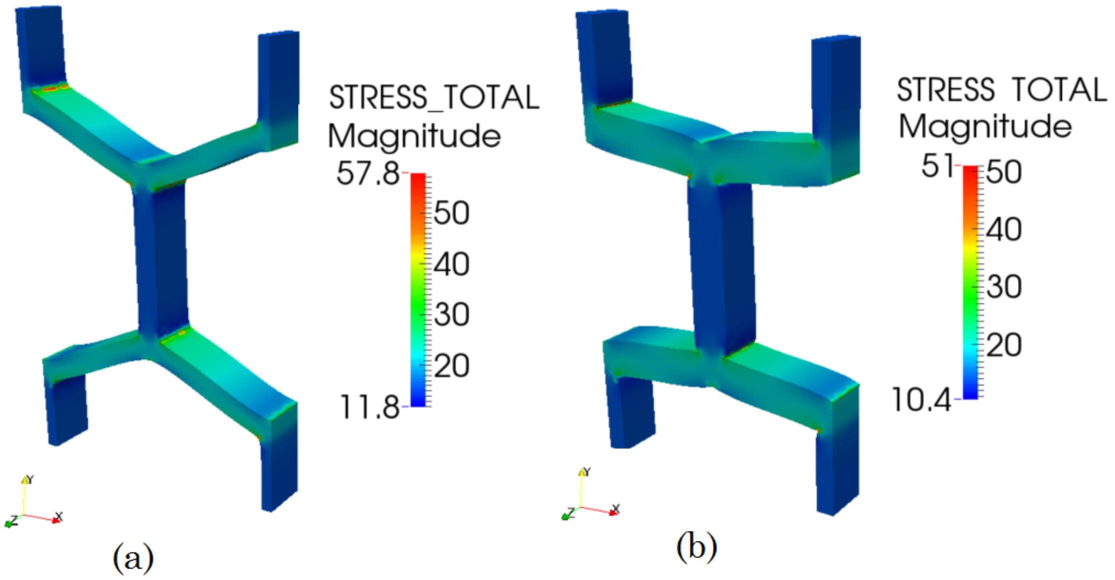

(a) (b)

Figure 4.34: Normal stress, σ_n (MPa) within a wood cell in (a) desorption (b) adsorption

The lowest stress appears in the sections of cell aligned in the y-direction, which are undergoing some slightly constrained swelling due to the connection to the angled members above and below. As such these angled members offer the highest stress within due to the constraint in the x direction and the bending stress associated with the increasing/decreasing angle of the connection.

4.3.3 Isotropic Latewood Cell

To look at the effect of cell wall thickness the cell is modified, giving it dimensions more representative of a typical latewood cell, which are typically characterised by a thicker cell wall and smaller lumens within. The angle remained the same as the earlywood cell, in order to view only the effect of the different cell wall width. The boundary conditions were applied in the same manner as the previous example and the effective length of diffusion in this case was 100 μm.

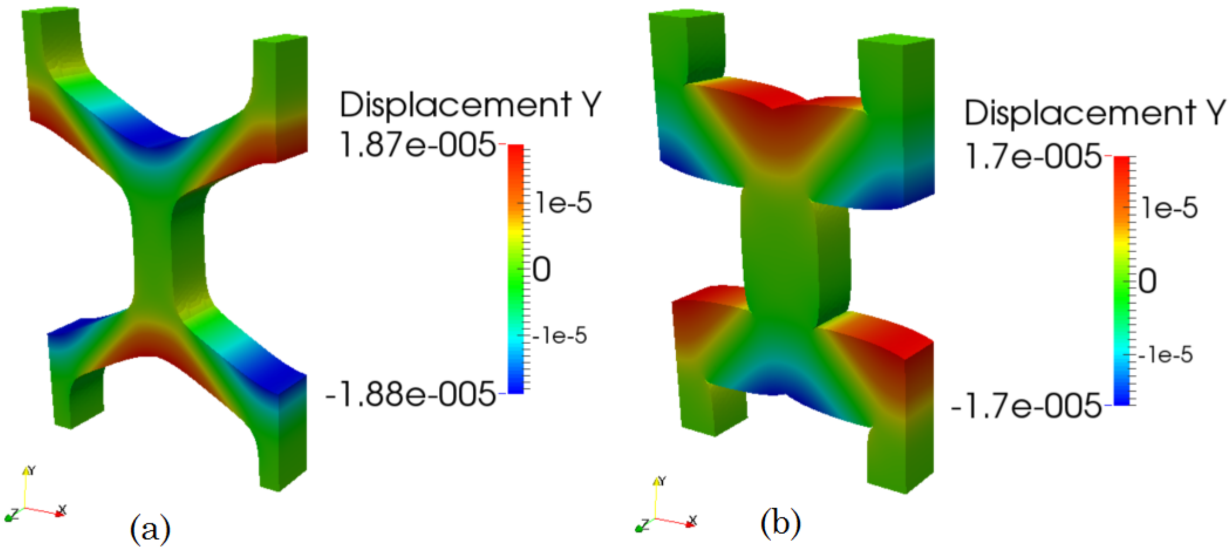

Figure 4.35: Deformation, in the y direction, of a wood cell (a) desorption (b) adsorption

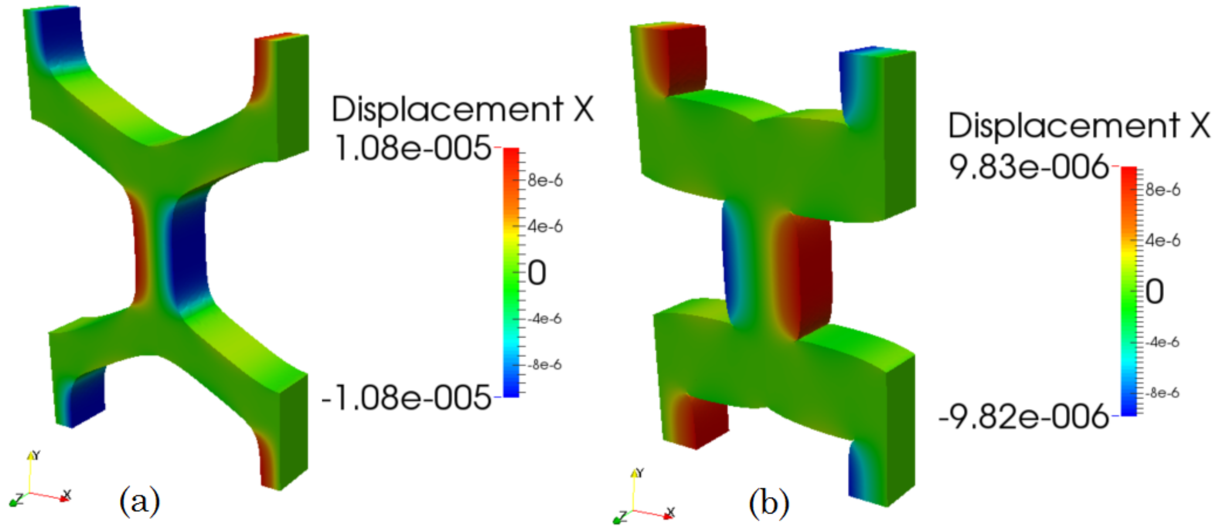

Figure 4.36: Deformation in the x direction of a latewood cell (a) desorption (b) adsorption

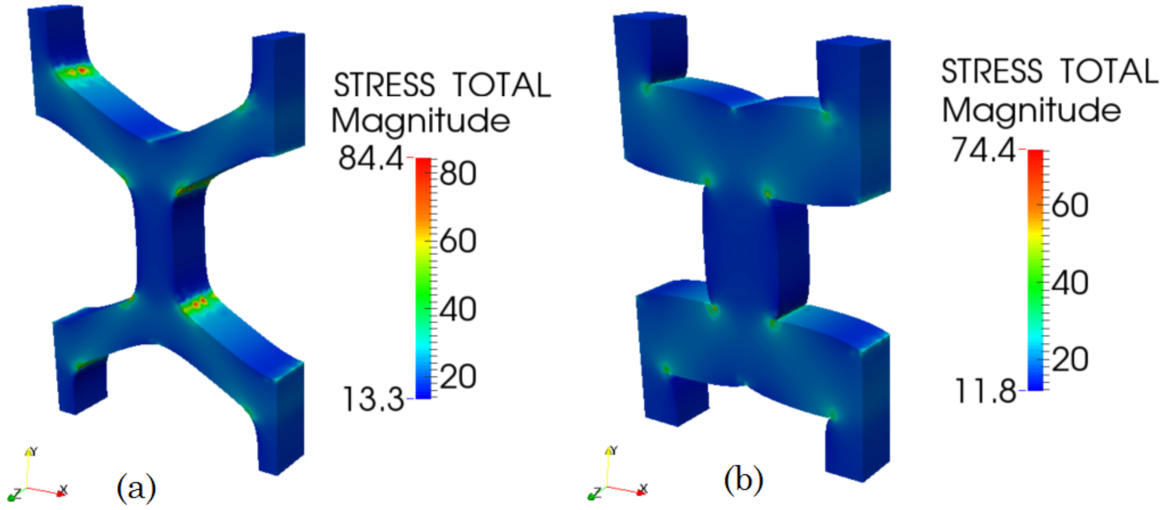

Figure 4.37: Normal stress, σ_n (MPa) within a latewood cell in (a) desorption (b) adsorption

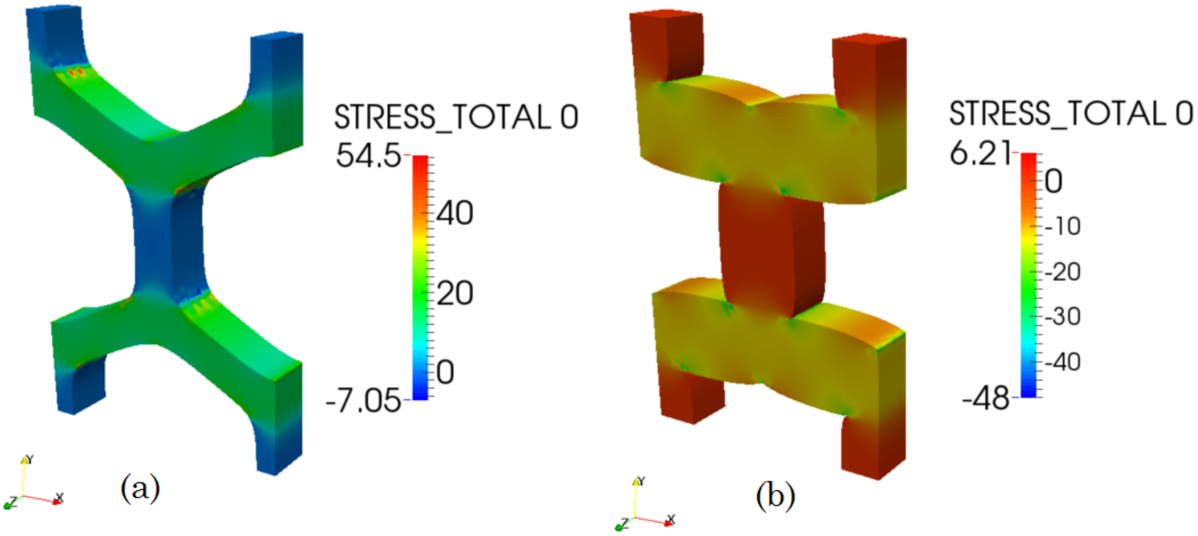

Figure 4.38: Stress, σ_{xx} (MPa) within a latewood cell in (a) desorption (b) adsorption

The displacements shown in Figures 4.35 and 4.36, demonstrate an increase in the displacements due to the change in climatic conditions, when compared to the earlywood cell unit in the previous sections. This was due to the extra polymer material interacting with the water, allowing a larger uptake for the same change in conditions. The stress was higher than it was for the earlwood cell (Figures 4.33 and 4.34), shown in Figures 4.37 and 4.38.

4.3.4 Conclusions of the Sorption Test on a Constrained Wood Cell

It is clear from the results of the wood cell test that the rate limiting step in the sorption kinetics within the range of humidity studied (35-45%) is the viscoelastic response of the material. This has been established using material properties for viscoelastic material behaviour within wood cell polymers, obtained from multi-scale modelling [30], and diffusion coefficients specific to bound water transport within wood cell polymers [95]. The wood cell is a thickness similar to that of typical wood cells and as such the characteristic diffusion time must be close to that actual value. Therefore it is a reasonable conclusion to reach, that viscoelastic processes are limiting the solvent uptake. As such this means the diffusion in this case is not Fickian in nature.

However this material behaviour could, and most likely would, change as the moisture content changes over a wider range. To implement this in a correct manner, an understanding between the dashpot viscosity and the moisture content and stress duration would need to be gained. This would allow the viscoelastic behaviour to change, depending upon how much moisture is within the cell wall. The expectation is the dashpot would provide more resistance to relaxation in drier environments and less when close to saturation conditions.

Within the range of studied humidity in this test (35% to 45%) there is no hysteresis observed. However this does not mean that hysteresis can be ruled out as significant within this range, as experimental results have indicated. Rather it highlights the importance that the cellulosic fibres may have in the longitudinal direction and it could be either these undergoing a slower relaxation or intrifibril shear that are contributing to the sorption hysteresis phenomena. A full multi-scale approach would be necessary to investigate this phenomena.

A size dependent factor has been observed with the wood cells, i.e. the smaller but thicker latewood cells undergo a higher degree of swelling. As such this shows the capability of the model to move towards more complex problems on the macro-scale, where layers of latewood and earlywood cells swell in ways which can cause viscoelastic deformations within sawn lumber. This model could be used to study this phenomena in more depth in the future.

Chapter 5

Conclusions

Within this thesis a 3D model has been presented that can be applied to many different polymeric gels, and thus can have applications ranging from wood and ligno-cellulosic materials to perhaps the food and medical industries.

The novel aspect of the work in this thesis is the additional internal variable that takes into account time dependent viscoelastic processes such as creep and relaxation, as proposed by Hu and Suo [60], as well as the addition of hydrogen bond theory [80] to account for softening of the constituent polymers.

The motivation behind the polymeric gel approach to wood-water interactions is to model wood and other ligno-cellulosic polymers, to closely analyse the interactions with water in the environment and perhaps apply to more complex multi-scale problems in the future. The formulation in terms of Helmholtz free energy allows the use in isothermal problems in wood engineering, such as mechano-sorptive creep and moisture induced swelling. The formulation of the environment in terms of Gibb's free energy, a commonly used approach when describing isothermal diffusion [95, 98], allows the coupling between the mechanical stresses and the chemical potential of the water within the cell wall polymers. The addition of Fick's 2nd law, describing the transient flux of the chemical field allows time-dependent analysis to be carried out on the moisture transport processes within the cell wall polymers.

The model was implemented using the 3D finite element method within MoFEM. A stable solution is ensured using hierarchical approximation of basis functions in order to allow a higher order of approximation to be applied to the displacement field than the flux field. This approach has allowed a novel implementation of a model which captures both poroelastic and viscoelastic processes concurrently.

Within Chapter 3 it was demonstrated that the model has a wide variety of potential uses. Both the creep test on a rectangular element and the complex compressive loading case on a hollow cylinder demonstrated an ability to induce deformations due to viscoelastic creep processes, whilst the free-swelling test demonstrates creep induced entirely by the changes in environmental conditions, although only when material properties are interplaying within the correct range. This will allow predictions of cases where changing material properties will induce different viscoelastic behaviours at various times. The multi-layer test provided particularly interesting results and displayed the most complex behaviour. It was demonstrated that the viscoelastic deformations can be induced not only by materials with different values of stiffness, but also by materials in which the solvent transfers through at different rates, leading to a viscoelastic deformation that was dependent upon the time of differential swelling between the two layers. The multi-layer test demonstrates the potential for the model to be used in the analysis of complex multi-layered structures and for studying the complex mechano-sorptive behaviour of individual wood cells.

The question of whether or not sorption hysteresis, within wood and other ligno-cellulosic materials, is due to viscoelastic effects within the polymers during the adsorption and desorption process has been widely debated over the last few decades [28, 33, 42, 50, 52, 52, 111–113]. The complex interplay between the different processes has also given rise to the theory of viscoelastically limited solvent migration within cell wall polymers during adsorption and desorption processes [33, 50–52, 54, 108, 111, 112, 116]. The model presented within this paper provides answers to both questions. Firstly with regards to hysteresis, the model presented demonstrates the link between viscoelasticity in the polymers and the sorption hysteresis effect during sorption cycles, demonstrated using parameters that represent the ligno-hemicellulosic matrix within the wood cell wall. This provided alongside experimental results and conclusions from Hill and Xie and theories provided by Vrentas et al, provides good evidence of such a link. Furthermore the results in Chapter 3, particularly the free-swelling response to an environmental change, and the wood cell in Chapter 4, display a possible link between substrate swelling and the rate of diffusion. More specifically it outlines the case where viscoelastic and diffusive processes interplay to cause viscoelastically limited solvent migration within the polymer substrate. This is based upon theories surrounding material behaviour around the glass transition and the transformation of the material response from glassy to rubbery [46, 108, 111, 112] and as such is based upon well known material knowledge. Thus it can be concluded, that sometimes the viscoelastic deformation of the polymer substrate, and thus the creation of new space in which bound-water can migrate, does control the rate of solvent uptake within the material. However this only happens when the time of diffusion and the viscoelastic relaxation time are similar, giving a corresponding Deborah number close to unity. To confirm this theory, we would suggest more work is undertaken with regards to relaxation behaviour and the relationship with the hydrogen bond. The hydrogen bond is the key component within the system, especially when considered over a range of moisture contents [80–82]. Thus the interplay between the elastic softening and the increasing material viscosity will determine at which moisture contents the rate of moisture uptake is determined by the viscoelastic processes.

In its current form the model takes into account stiffness changes due to hydrogen bonding, for the cellulose and hemicellulosic polymers. The question of whether or not lignin also undergoes softening is debatable, with evidence pointing towards both, with mechanical testing, not insitu, and hydrogen bond theory backing the softening theory [25, 81]. There is also good reason to believe lignin undergoes minimal softening when insitu [92]. However, even in the case where it is assumed lignin undergoes softening, the contribution is minimal when compared with the amorphous cellulose and hemicellulose, the polymers which contain the majority of the hydroxyl groups and therefore sorption sites. With the current approach to the hydrogen bonding, the current model compares well when sorption isotherms are plotted below the glass transition, and the hysteresis observed is very promising with regards to use in future multi-scale modelling, and perhaps even life-cycle analysis of sections of timber. The model could also be used, within a multi-scale framework, for the prediction of warping of greenwood during the first drying cycle, a process which often leads to large deformations and warping and sometimes even splitting of the timber. This process, a product of the arrangement of the different types of cells (earlywood and latewood), is hard to predict and as such would be a good area to implement such modelling make design and construction more efficient and therefore economical. This is of particular importance as timber presents a low carbon alternative to other materials such as concrete and steel and its increased use can lead to increased sustainability in construction in the future.

5.1 Recommendations for Future Work

Included here is a short section of recommendations on the direction of future research required to build upon the model and theories presented within this thesis. Within this recommendations are made for advancements of the polymeric gel modelling field, based upon the framework presented here and work previously carried out by other authors in the field, and advancements in the context of wood and multi-scale material modelling.

5.1.1 Sorption Behaviour

The work presented in this thesis covers a new approach to modelling the wood cell wall polymers and their interaction with the external environment. In its current state the work is limited to sorption below the glass transition and cannot yet accurately represent the desorption process due to the lack of the sorption hysteresis phenomena.

It has been theorised that the hysteresis in wood polymers is as a result of water molecules being trapped within pores as they collapse during desorption, the same pores as have been previously created during the adsorption process. However, Nissan's theory on h-bond dissociation [80] extends to the relaxation process. Through this a process of intramolecular hydrogen bonds breaking down when stress is applied for longer periods. It further goes on to explain that, when the stress is released, the sample locks into the new configuration, at which point the dashpot recovers to its previous stiffness, although with the sample in a new configuration.

Through this description, it may be possible to incorporate sorption hysteresis within the wood polymers. As the material evolves through its different states, the shear modulus of the dashpot is the parameter that determines the behaviour. As this softens, a complex interplay between the softening of the dashpot and the softening of the two springs happens, introducing varying amounts of dashpot relaxation at different moisture contents within the samples.

It has been demonstrated in Chapters 3 and 4 that the model can capture viscoelastic dimensional changes within the polymers, and as such it should be possible to extend this to a full range of relative humidity and implement as a predictive process. This ability to determine the hysteresis and therefore moisture induced stress and warping is a key stage to building a predictive model for lifecycle analysis of timber members, and the hydrogen bonding network is the key factor in determining that behaviour. Similar additions could solve the problem of selecting cuts for drying timber in the forestry industry. During the first drying phase after the felling of the tree, the stresses incurred as the timber is kiln dried can cause moisture induced warping and as such wastes resources. The pattern of rings across the timber member is potentially what causes such warping.

5.1.2 Extension to Hyperelastic Material Description

The model presented within this thesis is based upon small engineering strains and as such limits description of materials, under a strong influence of the internal hydrogen bonding behaviour, to below the glass transition temperature, due to the large strains encountered beyond this point.

Within the small strain model it has been shown that the relationship of coupled stress and diffusion, with the additional viscoelastic internal variable, can capture viscoelastically limited solvent migration and sorption hysteresis effects. As such this provides enough evidence to suggest a full hyperelastic description would give rise to a material description across all ranges of relative humidity encountered by hydrogen bond dominated polymers. However, several issues need to be considered before a more complex hyperelastic model, for instance a neo-hookean description, can be implemented.

The coupling between the stress and concentration fields set up in the current description, where any change in the volumetric strain is due to a corresponding change in the number of solvent molecules within the polymer. As such this can lead to issues within the chemical potential field description. As demonstrated within the cylinder test in Chapter 3, the chemical potential field under loading can produce negative chemical potential when the strains are sufficiently large and the initial chemical potential within the sample is sufficiently small. The negative value of chemical potential implies that there is a negative water content within the sample, which is of course impossible. This is due to the model incorrectly assuming that the material remains compressible when

$\mu \leq 0$. In reality, as the chemical potential, μ, approaches zero, the incompressibility condition should be imposed, ensuring that negative values of chemical potential do not arise.

Additional Heat of Mixing Term

Within this thesis, a 3D finite element model has been implemented based upon the theory of viscoelasticity and poroelasticity in elastomeric gels [60]. This theory is based upon the assumption of small strains where an assumption of full-swelling is applied. Govindjee and Simo describe this as a simple relation between the Jacobian and the concentration, similar to the assumption used in this model linking the volumetic strain to the concentration (Eqn. 2.13). However, the authors believe this to be a violation of the two primary field variables, i.e. the concentration and the stress field. Hong et al also take the view that this simple relationship between the two fields is erroneous [58]. They take the view that the commonly used analogy between a polymeric gel and a sponge is misleading. They base this opinion on the fact that when fluid leaves a sponge the pores are filled with air but on the other hand when fluid leaves a polymeric gel the long chain molecules seeks to close all the pores within due to the molecular forces.

Within both theories, i.e. Hong et al and Govindjee and Simo, they suggest achieving coupling through the addition of a heat of mixing term and keeping both the concentration and stress fields as independent of each other. Hu et al also share a theory of finite deformation in which they keep the two fields as seperate entities, allowed to evolve independently of each other due to complications within the free energy function at large strains [60]. As such any future extension to Hyperelastic theory should be accompanied by the inclusion of a free-energy of mixing term, within which the Jacobian describes the concentration of the solvent. Therefore any deformation caused by external loading would impact on the chemical potential field only through the free energy term.

5.1.3 Considerations of the Hydrogen Bond Effect

The ability of the model to capture the complex interplay of viscoelastic stress and diffusion processes allows for the implementation of the model through a fully multi-scale framework. Within the suggested framework we have already implemented softening of the cellulosic and hemicellulosic polymers, with the question or whether or not lignin undergoes significant softening still up for discussion. The implementation used at present uses the theory of hydrogen bond dissociation in hydrogen bond dominated solids to determine the hydrogen bond interactions of both the cellulose and hemicelluloses. This is connected to the chemical potential field and is therefore linked to the relative humidity. This is a simplification but it is done for several reasons.

The theory of hydrogen bonding as presented by Nissan [80] is based upon cellulose, and the associated stiffness curve obtained when reproducing the data is shown in Figure

4.6. When compared to the hemicellulose stiffness plots determined by Cousins it displays a very similar pattern of softening with respect to the relative humidity when under free-swelling. Cousins [24] also made the link between moisture content, relative humidity and the softening curve and suggested this as a means to predict softening under different environmental conditions. Furthermore, the sorption isotherms produced by Cousins show the same sigmoidal shape connected with the environmental humidity as expected from wood and cellulosic materials, albeit with a dramatically higher corresponding moisture content.

This poses an interesting question with regards to the sorption behaviour of the individual polymers. Is the softening behaviour linked with the sample concentration or the relative humidity? Without a relationship for the hemicellulose softening as a function of the concentration there is a lack of data from which to work with, and with the concentration and cooperative index information unknown for hemicellulose, we took the approach of linking softening to the chemical potential field. This works sufficiently in the free-swelling example for the pure polymer as the swelling from the environmental change is uninhibited and that the clustering of water molecules within the sorption sites are determined by the relative humidity. However, this assumption needs to be addressed in further detail.

With the addition of external loading and/or a complex multi-layer structure with fibres that constrain the swelling, the softening and glass transition may also change. For instance, in theory if the polymer is compressed, the space between the molecules will decrease leaving less space for the water in the interlocked polymer environment. However this assumption is not that simple. For instance if a load is applied quickly, and the molecules forced into a dense configuration, does the water already within become trapped, allowing a higher relative humidity. Theories of trapped moisture within the pores causing hysteresis exist in the literature [50]. However, it may be that it only changes the rate of diffusion and that the clustering of molecules reaches equilibrium with the environmental humidity. However, it is know that the effect of compressing the polymer in this manner would certainly increase the chemical potential within [98] due to the abundance of water molecules already held within. The description of chemical potential flux for the chemical field will mean this water will leave the system, yet the number of hydroxyl groups will remain the same. As such it is expected that the clustering of water at each site will reduce within the polymer. If this is not the case then perhaps the assumption of incompressibility of the water molecules would need to be reconsidered, this is unlikely however.

In the current framework deformations are relatively small, hence the changes in glass transition are not expected to be that large and the current description through the chemical potential field is satisfactory. This does mean however, that any extension to hyper elasticity would mean a careful consideration of this formulation would be needed. It is therefore suggested that a move towards cleary elucidating the hydrogen bond breakdown behaviour of each polymer whilst insitu is made. For instance the hemicelluloses have no clear relationship for hydrogen bond breakdown and the effects on the stiffness other than experimental observations on not insitu samples [24]. Recent work by Kulansinski et al [65, 66] provides a potentially promising solution using molecular dynamics. Once the cooperative behaviour is determined for each polymer, a concentration based relationship can be used within the cell and thus effects such as the constraint of other polymers and the effects of large deformation can be taken into account. One further problem of a volumetric, and therefore full-swelling description, of the polymer softening within a hyperelastic framework is the assumption that the deformation is entirely due to the presence of bound-water. For this reason it may also be advantageous to keep the softening relationship as a function of the chemical potential field.

5.1.4 Multi-Scale Modelling

The model in its current state only describes the mechanics of the polymer matrix within the wood cell wall layers. To fully describe the cell wall behaviour however, a multi-scale approach is required, where the different layers of fibres within the cell wall interact with each other. Each cell wall layer has a different composition of the main constituent polymers and a different percentage of crystalline fibres as well as different microfibril angles. The different constitutive polymers will lead to different rates of diffusion stiffness properties along each axis. This complex arrangement will also mean different degrees of softening at moisture contents, which when the material goes through the glass transition will have a large effect. The microfibrils may also have an effect on moisture hysteresis as the microfibrils themselves are largely unaffected by moisture, and therefore they are likely to undergo viscoelastic relaxation at a far slower rate than the associated amorphous polymers within the cell wall in which the fibres are embedded. This could explain why hysteresis is still present in wood cells and other associated cellulosic materials, despite observations that hysteresis disappears in glassy polymers above the glass transition.

References

[1] MoFEM finte element code. http://mofem.eng.gla.ac.uk/mofem/html/index.html.

[2] U. P. Agarwal. Raman imaging to investigate ultrastructure and composition of plant cell walls: distribution of lignin and cellulose in black spruce wood (picea mariana). *Planta*, 224(5):1141–1153, 2006.

[3] U. P. Agarwal and S. A. Ralph. Ft-raman spectroscopy of wood: identifying contributions of lignin and carbohydrate polymers in the spectrum of black spruce (picea mariana). *Applied spectroscopy*, 51(11):1648–1655, 1997.

[4] M. Åkerholm, B. Hinterstoisser, and L. Salmén. Characterization of the crystalline structure of cellulose using static and dynamic ft-ir spectroscopy. *Carbohydrate Research*, 339(3):569–578, 2004.

[5] M. Åkerholm and L. Salmén. Interactions between wood polymers studied by dynamic ft-ir spectroscopy. *Polymer*, 42(3):963–969, 2001.

[6] C. M. Altaner and M. C. Jarvis. Modelling polymer interactions of the molecular velcrotype in wood under mechanical stress. *Journal of theoretical biology*, 253(3):434–445, 2008.

[7] T. K. Bader, K. Hofstetter, C. Hellmich, and J. Eberhardsteiner. The poroelastic role of water in cell walls of the hierarchical composite softwood. *Acta mechanica*, 217(1-2):75–100, 2011.

[8] S. Balay, S. Abhyankar, M F. Adams, J. Brown, P. Brune, K. Buschelman, L. Dalcin, V. Eijkhout, W D. Gropp, D. Kaushik, M G. Knepley, L C. McInnes, K. Rupp, B F. Smith, S. Zampini, and H. Zhang. PETSc users manual. Technical Report ANL-95/11 - Revision 3.6, Argonne National Laboratory, 2015.

[9] T. A. Barbari. Dual-mode free volume model for diffusion of gas molecules in glassy polymers. *Journal of Polymer Science Part B: Polymer Physics*, 35(11):1737–1746, 1997.

[10] J. R. Barnett and V. A. Bonham. Cellulose microfibril angle in the cell wall of wood fibres. *Biological reviews*, 79(2):461–472, 2004.

[11] A. Bergander, J. Brändström, G. Daniel, and L. Sahnen. Fibril angle variability in earlywood of norway spruce using soft rot cavities and polarization confocal microscopy. *Journal of Wood Science*, 48(4):255–263, 2002.

[12] M. Bergenstråhle, K. Mazeau, and L. A. Berglund. Molecular modeling of interfaces between cellulose crystals and surrounding molecules: Effects of caprolactone surface grafting. *European Polymer Journal*, 44(11):3662–3669, 2008.

[13] J. Berthold, J. Desbrieres, M. Rinaudo, and L. Salmén. Types of adsorbed water in relation to the ionic groups and their counter-ions for some cellulose derivatives. *Polymer*, 35(26):5729–5736, 1994.

[14] J. Berthold, M. Rinaudo, and L. Salmeń. Association of water to polar groups; estimations by an adsorption model for ligno-cellulosic materials. *Colloids and surfaces A: physicochemical and engineering aspects*, 112(2):117–129, 1996.

[15] M. A. Biot. Theory of deformation of a porous viscoelastic anisotropic solid. *Journal of Applied Physics*, 27(5):459–467, 1956.

[16] M. A. Biot. Theory of stability and consolidation of a porous medium under initial stress. 1963.

[17] J. Boutelje. Juvenile wood with particular reference to northern spruce. *SVENSK PAPPERSTIDNING-NORDISK CELLULOSA*, 71(17):581, 1968.

[18] J. D. Boyd. An anatomical explanation for visco-elastic and mechano-sorptive creep in wood, and effects of loading rate on strength. In *New perspectives in wood anatomy*, pages 171–222. Springer, 1982.

[19] J. Brändström. Micro-and ultrastructural aspects of norway spruce tracheids: a review. *Iawa Journal*, 22(4):333–353, 2001.

[20] J. Brändström, S. L. Bardage, G. Daniel, and T. Nilsson. The structural organisation of the s1 cell wall layer of norway spruce tracheids. *IAWA Journal*, 24(1):27–40, 2003.

[21] S. Brunauer, P. H. Emmett, and E. Teller. Adsorption of gases in multimolecular layers. *Journal of the American chemical society*, 60(2):309–319, 1938.

[22] A. Célino, S. Fréour, F. Jacquemin, and P. Casari. Characterization and modeling of the moisture diffusion behavior of natural fibers. *Journal of Applied Polymer Science*, 130(1):297–306, 2013.

[23] S. A. Chester and L. Anand. A coupled theory of fluid permeation and large deformations for elastomeric materials. *Journal of the Mechanics and Physics of Solids*, 58(11):1879–1906, 2010.

[24] W. J. Cousins. Elastic modulus of lignin as related to moisture content. *Wood science and technology*, 10(1):9–17, 1976.

[25] W. J. Cousins. Young's modulus of hemicellulose as related to moisture content. *Wood science and technology*, 12(3):161–167, 1978.

[26] K. De Borst, C. Jenkel, C. Montero, J. Colmars, J. Gril, M. Kaliske, and J. Eberhardsteiner. Mechanical characterization of wood: an integrative approach ranging from nanoscale to structure. *Computers & Structures*, 127:53–67, 2013.

[27] R. W. Dent. A multilayer theory for gas sorption part i: sorption of a single gas. *Textile Research Journal*, 47(2):145–152, 1977.

[28] F. Dubois, JM. Husson, N. Sauvat, and N. Manfoumbi. Modeling of the viscoelastic mechano-sorptive behavior in wood. *Mechanics of Time-Dependent Materials*, 16(4):439–460, 2012.

[29] J. Eitelberger, T. K. Bader, K. De Borst, and A. Jäger. Multiscale prediction of viscoelastic properties of softwood under constant climatic conditions. *Computational Materials Science*, 55:303–312, 2012.

[30] J. Eitelberger and K. Hofstetter. Prediction of transport properties of wood below the fiber saturation point–a multiscale homogenization approach and its experimental validation: Part i: Thermal conductivity. *Composites science and technology*, 71(2):134–144, 2011.

[31] J. Eitelberger, K. Hofstetter, and S. V. Dvinskikh. A multi-scale approach for simulation of transient moisture transport processes in wood below the fiber saturation point. *Composites Science and Technology*, 71(15):1727–1738, 2011.

[32] E. T. Engelund. *Wood-water interactions.* Dissertation, Technical University of Denmark, Kgs. Lyngby, 2011.

[33] E. T. Engelund, L. G. Thygesen, S. Svensson, and C. AS. Hill. A critical discussion of the physics of wood–water interactions. *Wood Science and Technology*, 47(1):141–161, 2013.

[34] P. Eronen, M. Österberg, S. Heikkinen, M. Tenkanen, and J. Laine. Interactions of structurally different hemicelluloses with nanofibrillar cellulose. *Carbohydrate Polymers*, 86(3):1281–1290, 2011.

[35] J. Fahlén and L. Salmén. Cross-sectional structure of the secondary wall of wood fibers as affected by processing. *Journal of materials science*, 38(1):119–126, 2003.

[36] D. Fengel. The ultrastructure of cellulose from wood. *Wood Science and Technology*, 3(3):203–217, 1969.

[37] D. Fengel and M. Stoll. Variation in cell cross-sectional area, cell-wall thickness and wall layers of spruce tracheids within an annual ring. *Holzforschung*, 27(1):1–7, 1973.

[38] A. N. Fernandes, L. H. Thomas, C. M. Altaner, P. Callow, V. T. Forsyth, D. C. Apperley, C. J. Kennedy, and M. C. Jarvis. Nanostructure of cellulose microfibrils in spruce wood. *Proceedings of the National Academy of Sciences*, 108(47):E1195–E1203, 2011.

[39] G. K. Fleming and W. J. Koros. Dilation of polymers by sorption of carbon dioxide at elevated pressures. 1. silicone rubber and unconditioned polycarbonate. *Macromolecules*, 19(8):2285–2291, 1986.

[40] E. I. S. Flores, E. A. de Souza Neto, and C. Pearce. A large strain computational multi-scale model for the dissipative behaviour of wood cell-wall. *Computational Materials Science*, 50(3):1202–1211, 2011.

[41] P. J. Flory and J. Rehner Jr. Statistical mechanics of cross-linked polymer networks i. rubberlike elasticity. *The Journal of Chemical Physics*, 11(11):512–520, 1943.

[42] S. Fortino, F. Mirianon, and T. Toratti. A 3d moisture-stress fem analysis for time dependent problems in timber structures. *Mechanics of time-dependent materials*, 13(4):333–356, 2009.

[43] L. J. Gibson. The hierarchical structure and mechanics of plant materials. *Journal of the Royal Society Interface*, 9(76):2749–2766, 2012.

[44] N. Gierlinger, M. Schwanninger, A. Reinecke, and I. Burgert. Molecular changes during tensile deformation of single wood fibers followed by raman microscopy. *Biomacromolecules*, 7(7):2077–2081, 2006.

[45] F. Gouanve, S. Marais, A. Bessadok, D. Langevin, C. Morvan, and M. Métayer. Study of water sorption in modified flax fibers. *Journal of applied polymer science*, 101(6):4281–4289, 2006.

[46] S. Govindjee and J. C. Simo. Coupled stress-diffusion: Case ii. *Journal of the Mechanics and Physics of Solids*, 41(5):863–887, 1993.

[47] P. U. A. Grossman. Requirements for a model that exhibits mechano-sorptive behaviour. *Wood science and technology*, 10(3):163–168, 1976.

[48] J. J. Harrington. Hierarchical modelling of softwood hygro-elastic properties. 2002.

[49] H. W. Haslach Jr. The moisture and rate-dependent mechanical properties of paper: a review. *Mechanics of time-dependent materials*, 4(3):169–210, 2000.

[50] C AS. Hill, B A. Keating, Z. Jalaludin, and E. Mahrdt. A rheological description of the water vapour sorption kinetics behaviour of wood invoking a model using a canonical assembly of kelvin-voigt elements and a possible link with sorption hysteresis. *Holzforschung*, 66(1):35–47, 2012.

[51] C. AS. Hill, A. Norton, and G. Newman. The water vapor sorption behavior of natural fibers. *Journal of Applied Polymer Science*, 112(3):1524–1537, 2009.

[52] C. AS. Hill, A. Norton, and G. Newman. Analysis of the water vapour sorption behaviour of sitka spruce [picea sitchensis (bongard) carr.] based on the parallel exponential kinetics model. *Holzforschung*, 64(4):469–473, 2010.

[53] C. AS. Hill, A. J. Norton, and G. Newman. The water vapour sorption properties of sitka spruce determined using a dynamic vapour sorption apparatus. *Wood Science and Technology*, 44(3):497–514, 2010.

[54] C. AS. Hill and Y. Xie. The dynamic water vapour sorption properties of natural fibres and viscoelastic behaviour of the cell wall: is there a link between sorption kinetics and hysteresis? *Journal of materials science*, 46(11):3738–3748, 2011.

[55] B. Hinterstoisser, M. Åkerholm, and L. Salmén. Effect of fiber orientation in dynamic ftir study on native cellulose. *Carbohydrate Research*, 334(1):27–37, 2001.

[56] P. Hoffmeyer and R. W. Davidson. Mechano-sorptive creep mechanism of wood in compression and bending. *Wood Science and Technology*, 23(3):215–227, 1989.

[57] K. Hofstetter, B. Hinterstoisser, and L. Salmén. Moisture uptake in native cellulose– the roles of different hydrogen bonds: a dynamic ft-ir study using deuterium exchange. *Cellulose*, 13(2):131–145, 2006.

[58] W. Hong, Z. Liu, and Z. Suo. Inhomogeneous swelling of a gel in equilibrium with a solvent and mechanical load. *International Journal of Solids and Structures*, 46(17):3282–3289, 2009.

[59] W. Hong, X. Zhao, J. Zhou, and Z. Suo. A theory of coupled diffusion and large deformation in polymeric gels. *Journal of the Mechanics and Physics of Solids*, 56(5):1779–1793, 2008.

[60] Y. Hu and Z. Suo. Viscoelasticity and poroelasticity in elastomeric gels. *Acta Mechanica Solida Sinica*, 25(5):441–458, 2012.

[61] A. Ishikawa, T. Okano, and J. Sugiyama. Fine structure and tensile properties of ramie fibres in the crystalline form of cellulose i, ii, iii i and iv i. *Polymer*, 38(2):463–468, 1997.

[62] T. Joffre, P. Isaksson, P. J. J. Dumont, S. R. du Roscoat, S. Sticko, L. Orgéas, and E. K. Gamstedt. A method to measure moisture induced swelling properties of a single wood cell. *Experimental Mechanics*, 56(5):723–733, 2016.

[63] B. Jozsef et al. *Mechanics of wood and wood composites.* 1982.

[64] L. M. J. Kroon-Batenburg, J. Kroon, and M. G. Northolt. Chain modulus and intramolecular hydrogen bonding in native and regenerated cellulose fibers. *Polymer Communications*, 27(10):290–292, 1986.

[65] K. Kulasinski, R. Guyer, D. Derome, and J. Carmeliet. Water adsorption in wood microfibril-hemicellulose system: Role of the crystalline–amorphous interface. *Biomacromolecules*, 16(9):2972–2978, 2015.

[66] K. Kulasinski, S. Keten, S. V. Churakov, D. Derome, and J. Carmeliet. A comparative molecular dynamics study of crystalline, paracrystalline and amorphous states of cellulose. *Cellulose*, 21(3):1103–1116, 2014.

[67] K. Lewandowski X. Meng X. Zhou C. Pearce L. Kaczmarczyk, Z. Ullah. Mofem-v0.5.42, March 2017. http://mofem.eng.gla.ac.uk/mofem/html/.

[68] I. Langmuir. The adsorption of gases on plane surfaces of glass, mica and platinum. *Journal of the American Chemical society*, 40(9):1361–1403, 1918.

[69] M. Li, C. Jin, and J. Zhou. Finite element implementation of poroelasticity theory for swelling dynamics of hydrogels. *Theoretical and Applied Mechanics Letters*, 3(5):054009, 2013.

[70] J. F. Matthews, C. E. Skopec, P. E. Mason, P. Zuccato, R. W. Torget, J. Sugiyama, M. E. Himmel, and J. W. Brady. Computer simulation studies of microcrystalline cellulose iβ. *Carbohydrate research*, 341(1):138–152, 2006.

[71] K. Mazeau, C. Moine, P. Krausz, and V. Gloaguen. Conformational analysis of xylan chains. *Carbohydrate research*, 340(18):2752–2760, 2005.

[72] P. Mazzanti, J. Colmars, J. Gril, D. Hunt, and L. Uzielli. A hygro-mechanical analysis of poplar wood along the tangential direction by restrained swelling test. *Wood science and technology*, 48(4):673–687, 2014.

[73] G. Meshitsuka and J. Nakano. Structural characteristics of compound middle lamella lignin. *Journal of Wood Chemistry and Technology*, 5(3):391–404, 1985.

[74] K. Nakamura, T. Hatakeyama, and H. Hatakeyama. Studies on bound water of cellulose by differential scanning calorimetry. *Textile research journal*, 51(9):607–613, 1981.

[75] P. Navi, V. Pittet, and C. J. G. Plummer. Transient moisture effects on wood creep. *Wood Science and Technology*, 36(6):447–462, 2002.

[76] R. C. Neagu, E. K. Gamstedt, S. L. Bardage, and M. Lindström. Ultrastructural features affecting mechanical properties of wood fibres. *Wood Material Science and Engineering*, 1(3-4):146–170, 2006.

[77] A. Negi. Turbulence in the wood system with small and short stresses. *Wood science and technology*, 33(3):209–214, 1999.

[78] RM Nelson Jr. Diffusion of bound water in wood. *Wood science and technology*, 20(4):309–328, 1986.

[79] G. Némethy and H. A. Scheraga. *Chemical Physics*, 36(12):3382–3400, 1962.

[80] A. H. Nissan. H-bond dissociation in hydrogen bond dominated solids. *Macromolecules*, 9(5):840–850, 1976.

[81] A. H. Nissan. The elastic modulus of lignin as related to moisture content. *Wood Science and Technology*, 11(2):147–151, 1977.

[82] A. H. Nissan and S. S. Sternstein. Cellulose as a viscoelastic material. *Pure and Applied Chemistry*, 5(1-2):131–146, 1962.

[83] A. Olsson and L. Salmén. The association of water to cellulose and hemicellulose in paper examined by ftir spectroscopy. *Carbohydrate research*, 339(4):813–818, 2004.

[84] M. A. Palin and J.A Petty. Permeability to water of the cell wall material of spruce heartwood. *Wood Science and Technology*, 15(3):161–169, 1981.

[85] R. C. Pettersen. The chemical composition of wood. *The chemistry of solid wood*, 207:57–126, 1984.

[86] C. Plomion, G. Leprovost, and journal= Stokes, A. Wood formation in trees.

[87] A. Ranta-Maunus. The viscoelasticity of wood at varying moisture content. *Wood science and technology*, 9(3):189–205, 1975.

[88] I. Sakurada, Y. Nukushina, and T. Ito. Experimental determination of the elastic modulus of crystalline regions in oriented polymers. *Journal of Polymer Science*, 57(165):651–660, 1962.

[89] E. P. Saliklis and S. J. Kuskowski. Constitutive modeling of paper accounting for rate of load and transient relative humidity effects. *Tappi journal*, 81(2):181–188, 1998.

[90] L. Salmén. Micromechanical understanding of the cell-wall structure. *Comptes rendus biologies*, 327(9):873–880, 2004.

[91] L. Salmén and E. Bergström. Cellulose structural arrangement in relation to spectral changes in tensile loading ftir. *Cellulose*, 16(6):975–982, 2009.

[92] L. Salmén and A-M. Olsson. Interaction between hemicelluloses, lignin and cellulose: structure-property relationships. *Journal of pulp and paper science*, 24(3):99–103, 1998.

[93] L. Salmen, A-M. Olsson, J. Stevanic, J. Simonović, and K. Radotić. Structural organisation of the wood polymers in the wood fibre structure. *BioResources*, 7(1):0521–0532, 2011.

[94] S. Q. Shi. Diffusion model based on ficks second law for the moisture absorption process in wood fiber-based composites: is it suitable or not? *Wood Science and Technology*, 41(8):645–658, 2007.

[95] J. F. Siau. *Transport processes in wood*, volume 2. Springer Science & Business Media, 2012.

[96] J. F. Siau et al. An investigation of the external and internal resistance to moisture diffusion in wood. *Wood science and technology*, 21(3):249–256, 1987.

[97] W. T. Simpson. Predicting equilibrium moisture content of wood by mathematical models. *Wood and fiber science*, 5(1):41–49, 2007.

[98] C. Skaar. Wood-water relations. *Springer Verlag: Berlin, etc*, 283:352–3, 1988.

[99] P Solin, K Segeth, and I Dolezel. *Higher-order finite element methods*. CRC Press, 2003.

[100] A. J. Stamm. Bound-water diffusion into wood in the fibre direction. *Forest Products Journal*, 20(9):27–32, 1959.

[101] A. J. Stamm et al. Bound-water diffusion into wood in across-the-fibre directions. *Forest Products Journal*, 10(10):524–8, 1960.

[102] A. J. Stamm et al. Wood and cellulose science. *Wood and cellulose science.*, 1964.

[103] H. W. Starkweather. *Macromolecules*, 8:476–479, 1975.

[104] L. C. E. Struik. The mechanical and physical ageing of semicrystalline polymers: 1. *Polymer*, 28(9):1521–1533, 1987.

[105] K. Tashiro and M. Kobayashi. Theoretical evaluation of three-dimensional elastic constants of native and regenerated celluloses: role of hydrogen bonds. *Polymer*, 32(8):1516–1526, 1991.

[106] N. L Thomas and A. H. Windle. A theory of case ii diffusion. *Polymer*, 23(4):529–542, 1982.

[107] J. Tyrväinen. Wood and fiber properties of norway spruce and its suitability for thermomechanical pulping. 1995.

[108] G. K. Van der Wel and O. C. G Adan. Moisture in organic coatingsa review. *Progress in organic coatings*, 37(1):1–14, 1999.

[109] J. S. Vrentas, J. L. Duda, and H. C. Ling. Antiplasticization and volumetric behavior in glassy polymers. *Macromolecules*, 21(5):1470–1475, 1988.

[110] J. S. Vrentas, J. L. Duda, and H-C Ling. Influence of the glass transition on solvent self-diffusion in amorphous polymers. *Journal of Polymer Science Part B: Polymer Physics*, 26(5):1059–1065, 1988.

[111] J. S. Vrentas, C. M. Jarzebski, and J. L. Duda. A deborah number for diffusion in polymer-solvent systems. *AIChE Journal*, 21(5):894–901, 1975.

[112] J. S. Vrentas and C. M. Vrentas. Sorption in glassy polymers. *Macromolecules*, 24(9):2404–2412, 1991.

[113] J. S. Vrentas and C. M. Vrentas. Hysteresis effects for sorption in glassy polymers. *Macromolecules*, 29(12):4391–4396, 1996.

[114] A. Walther and A. Griewank. Getting started with adol-c. *Combinatorial scientific computing*, 20121684, 2012.

[115] Y. Xie, C. AS. Hill, Z. Jalaludin, S. F. Curling, R. D. Anandjiwala, A. J. Norton, and G. Newman. The dynamic water vapour sorption behaviour of natural fibres and kinetic analysis using the parallel exponential kinetics model. *Journal of Materials Science*, 46(2):479–489, 2011.

[116] Y. Xie, C. AS. Hill, Z. Jalaludin, and D. Sun. The water vapour sorption behaviour of three celluloses: analysis using parallel exponential kinetics and interpretation using the kelvin-voigt viscoelastic model. *Cellulose*, 18(3):517–530, 2011.

[117] S. L. Zelinka, M. J. Lambrecht, S. V. Glass, A. C. Wiedenhoeft, and D. J. Yelle. Examination of water phase transitions in loblolly pine and cell wall components by differential scanning calorimetry. *Thermochimica acta*, 533:39–45, 2012.